Universidad De Concepción
Facultad de Ciencias Físicas y Matemáticas
Magíster en ciencias con mención en física

The Ionospheric Spectral Imager (ISI): A digital spectrometric Riometer

Por: GONZALO ANDRÉS BURGOS FUENTES

Tesis presentada a la Facultad de Ciencias Físicas y Matemáticas de la Universidad de Concepción para optar al grado de Magíster en ciencias con mención en física

Profesor Guía: Rodrigo Andrés Reeves Díaz

30 de agosto de 2023
Concepción, Chile

With love to my parents, family and friends.

Acknowledgment

I would like to express my heartfelt gratitude to my parents, Maria Fuentes and Manuel Burgos, who have provided me with unwavering support and boundless love throughout the years. To my brother Roberto and my sisters Isaura, Jhona, Margarita, and Carmen, your presence and encouragement have meant the world to me.

I am immensely thankful to my friends for standing by me during my most challenging moments. Their presence has been a beacon of light, and I can confidently say that these years of hard work wouldn't have been the same without them.

I am indebted to my esteemed teachers, Dr. Rodrigo Reeves, Dr. Alberto Foppiano, and Dr. Rafael Rodríguez, for their exceptional guidance, valuable advice, and unwavering support. Your mentorship has been invaluable in shaping my academic and professional journey.

My sincere appreciation extends to the Departments of Physics and Astronomy at the Universidad de Concepción for their significant contributions to my growth and development. To the members of the CePIA laboratory, I am grateful for the positive and collaborative environment you have fostered. The camaraderie, laughter, and encouragement have been integral to my work. A special thank you goes to Cristian Calquin for his invaluable assistance in the final implementation of the analog system I designed, and to Nicolas Lastra for his dedicated work on the mechanical aspects.

Abstract

Radiometric systems' theory and application are fundamental to human progress, holding significance in telecommunications, electronics, medical devices, and beyond. In our investigation, they play a vital role in studying the universe, characterizing planetary atmospheres, and investigating the space weather of our solar system. This document thoroughly delves into these aspects to provide a comprehensive understanding of their application across these three topics.

Beginning with the subject's importance, the introduction delves into the characteristics and behavior of cosmic radiation, the Earth's ionosphere, their interplay, and their reliance on local space weather conditions. The discussion also encompasses the current state-of-the-art radiometric system designed for studying this phenomenon, referred to as the RIOMETER (Relative Ionospheric Opacity Meter for Extra-Terrestrial Emissions of Radio Noise). This system is capable of generating an intensity map of Relative Ionospheric Opacity using cosmic radiation at 38 MHz. Around 2004, roughly twelve instances of this system were set up in South America as part of the South America Riometer Network (SARINET). This aimed to study the South Atlantic Magnetic Anomaly (SAMA), where Earth's magnetic field strength significantly reduces, creating a gradient. One instance was implemented at Universidad de Concepción, operational but limited in producing sensitive ionospheric information.

Building on the theoretical framework, I proposed upgrading RIOMETER's data generation. Shifting from a total power receiver, the proposal involves a spectrometric system enabling multi-spectral image creationan advancement known as ISI-RIOMETER. This involves an overall upgrade of electric and electronic components using modern tech like surface-mount devices and field-programmable gate arrays. It enhances ionospheric understanding, space weather insights, and opens new exploration dimensions.

Analyzing ISI generated data for three weeks confirms its operational capability and capacity to produce a multi-spectral image using radio noise signals across 87 different pixels. Theoretical calculations and simulations project an expected 25-degree angular resolution and sensitivity near 0.01 dB.

Keywords – RIOMETER, CRN, Beamforming, SMT, FPGA y DSP

Contents

List of Tables

List of Figures

Chapter 1

Introduction

RIOMETERs are passive radiometric systems designed to study the relative opacity of the ionosphere and have undergone several improvements over time. The opacity parameter is derived from the intensity variability in the signal of Cosmic Radio Noise they measure. Its variation is associated with the interaction of electromagnetic waves from the source and the electron density of the ionospheric plasma. This interaction can be estimated using the ionospheric model from magnetohydrodynamic theory and the radiative transfer equation, leading to the Cosmic Noise Absorption method and the necessary development of RIOMETERs to study this phenomenon. This topic will be explored further in this chapter(A.P.Mitra et al., 1953; Beynon and Brown, 1957; Brekke, 2012; Browne et al., 1995; C.G. Little et al., 1959; Detrick, 1990; Honary et al., 2011; Hargreaves, 1995; Nielsen et al., 2004; Bittencourt, 2004; Rosenberg et al., 1993; S.Browne et al., 1995; K.A.Zawdie et al., 2017).

1.1 Science and state of the art

In order to comprehend the necessity and capabilities of both the old and new RIOMETERs, we present the spectral shape of the radiation source detected by the RIOMETERs. We then move on to the theoretical framework used to describe the ionosphere and its absorption coefficient k_ν, as well as the impact of the South American Magnetic Anomaly (SAMA) region on the electronic distribution in the area. Continuing, we explore the radiative transfer equation and its relationship with k_ν and the cosmic noise absorption (CNA) method. Finally, we conclude by

examining the historical evolution of the RIOMETER.

1.1.1 Radiation source

The Cosmic Radio Noise (CRN) used by the RIOMETER to characterize the ionosphere is better known in astronomy as the Cosmic Radio Background (CRB). This radiation is a small part of the entire electromagnetic spectrum of the cosmic background, composed of all photons emitted in the universe. Figure 1.1.1 illustrates the reconstruction of the universe's spectrum and its various components between 10^8 to 10^{25} Hz, using available data (Hill et al., 2018).

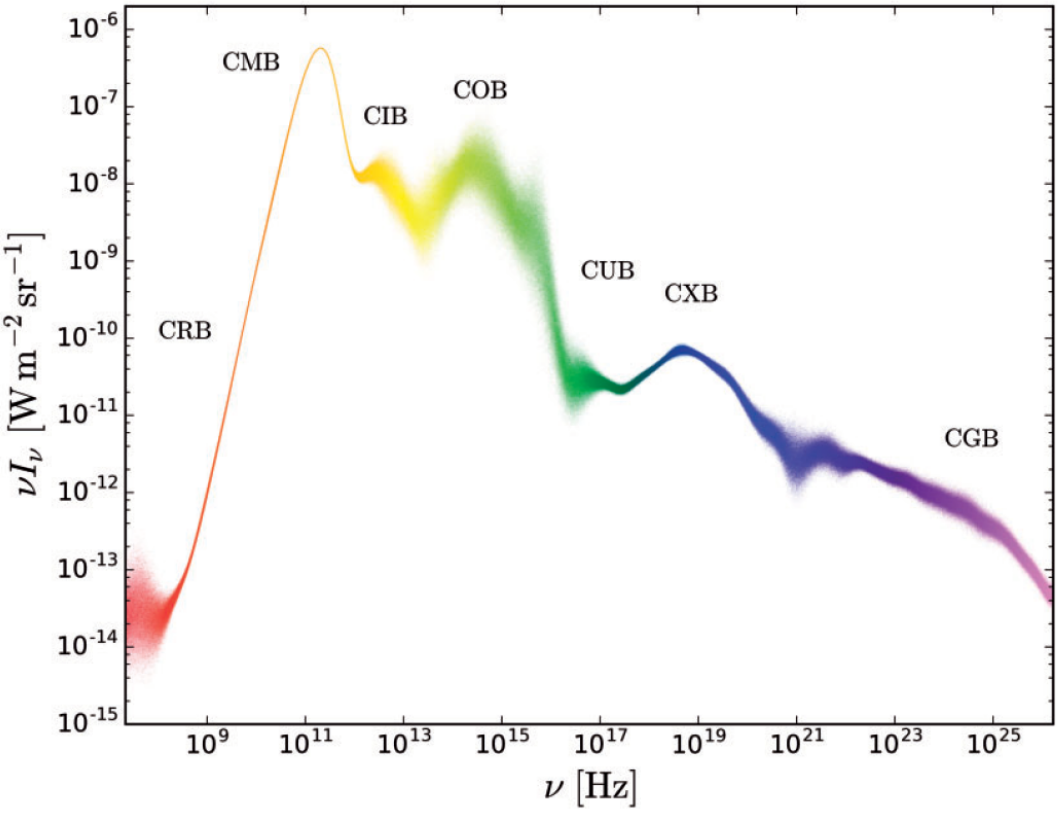

Figure 1.1.1: Estimation of the brightness intensity of the spectrum of the cosmic background radiation from observational data (Hill et al., 2018).

The CRN perceived on Earth is mainly composed of the synchrotron emission from our galaxy's magnetic field and the electrons rotating around it, the emission of the active galactic nuclei (AGN), the H1 emotion at high redshift and an even smaller portion of the CMB at these frequencies (Hill et al., 2018).

This signal was first measured and described by the physicist and engineer Karl

Guthe Jansky in 1932. He was searching for an explanation for the source of interference in the telecommunications link of Bell Laboratories. However, recent observations indicate that its brightness or intensity temperature ranges from around 1000 to 96000 Kelvins for frequencies below 74 MHz, providing a reference for the design of the system.(Browne et al., 1995; Dowell et al., 2017; A.Naparstek, 1963; Guzmán et al., 2011; Jansky, 1982b,a).

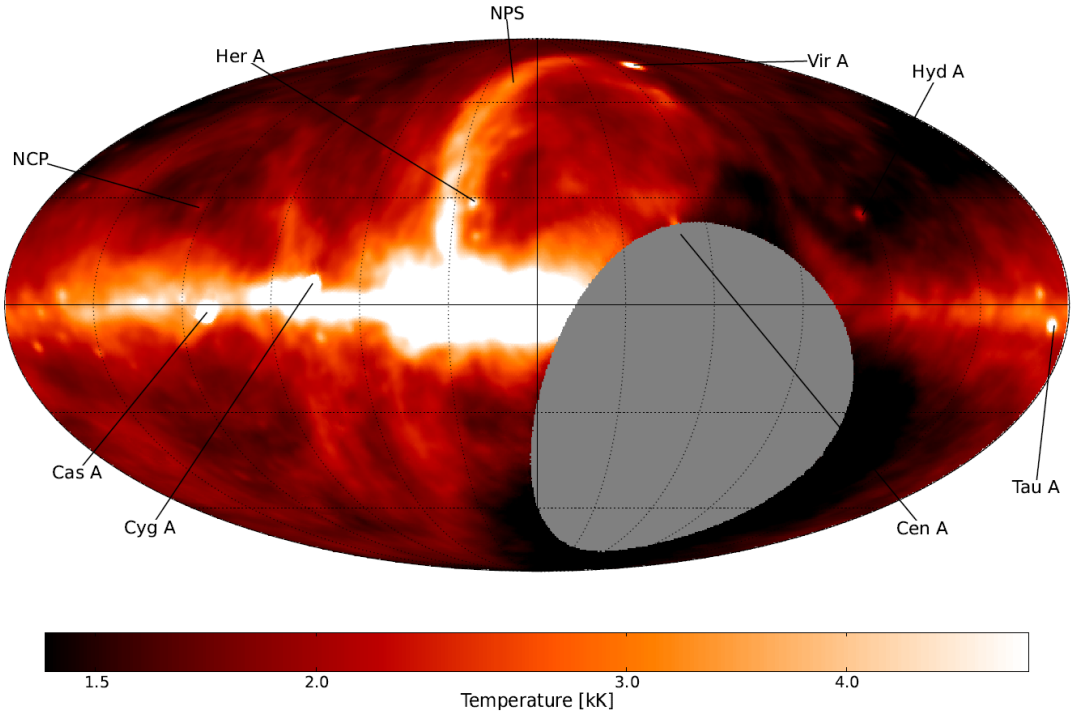

Figure 1.1.2: 74-MHz map imaged over 1 MHz of bandwidth. The map is displayed with a Mollweide projection in Galactic coordinates with latitude and longitude marked every 30. The colour scaling is logarithmic and the beam size at this frequency is 2.2°. Prominent sources, such as Cygnus A and Cassiopeia A, are labelled, along with the north celestial pole (NCP) and the north polar spur (NPS). The systematically lower temperatures near the South Galactic Pole are likely a result of limitations in the dipole response model and the corrections for the missing spacings(Dowell et al., 2017).

1.1.2 Atmospheric opacity and ionisation

The presence and distribution of molecules and atoms in Earth's atmosphere disturb the propagation of waves and matter through various processes, often resulting in partial or total interference[1]. In the context of electromagnetic waves,

[1]In many cases, these processes are responsible for supporting life on Earth.

their behavior is characterized by their transmission or transmittance in the medium. This is illustrated in Figure 1.1.3, which depicts the effects on different frequencies. (Thomas L. Wilson, 2009).

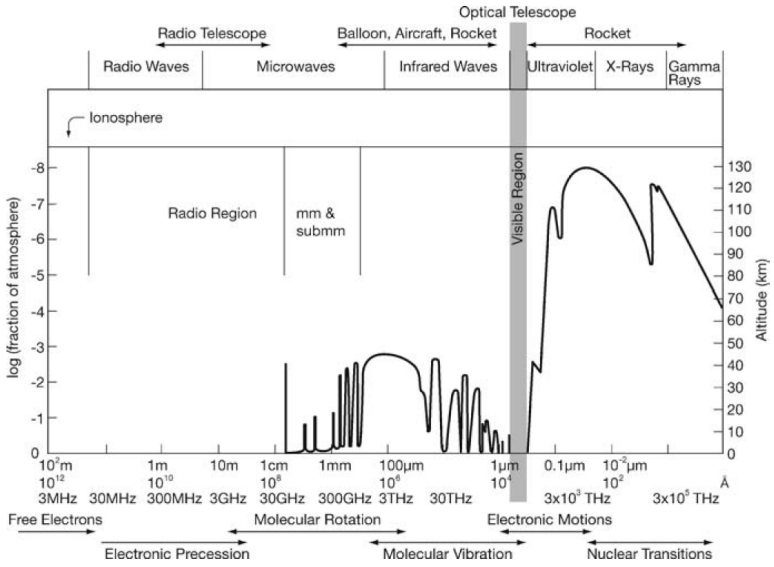

Figure 1.1.3: The transmission of the Earths atmosphere for electromagnetic radiation. The diagram gives the height in the atmosphere at which the radiation is attenuated by a factor 1/2 (Thomas L. Wilson, 2009).

The region in the spectrum with the least transmission is the high-frequency region (Ultraviolet, X-Rays and Gamma Rays), where the signal is weakly transmitted to the ground due to the process of photoionization and photodissociation of atmospheric gases, as illustrated in Figure 1.1.4. This process ionizes the medium, releasing electrons from atoms and molecular bonds. These electrons later contribute to the formation of the ionosphere as they concentrate at higher altitudes.(Brekke, 2012; McFadden et al., 2007; Hargreaves, 1992; Ratcliffe, 1970).

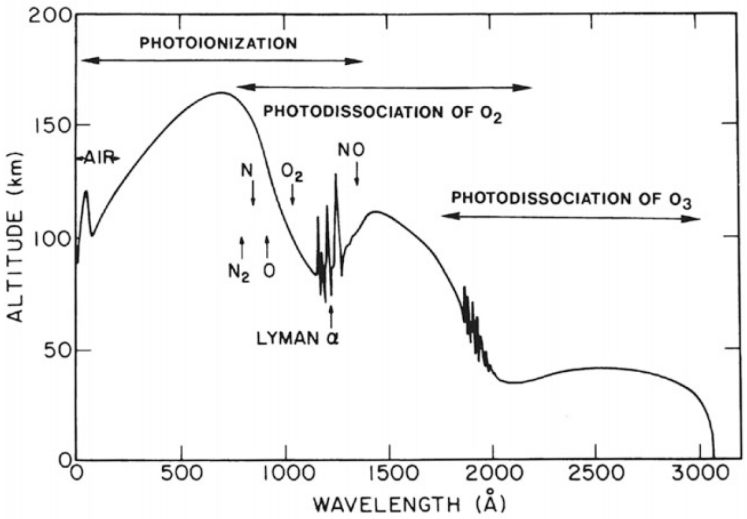

Figure 1.1.4: The altitude of unit optical depth in the wavelength region below 3,000A° (300 nm). This corresponds to the level where maximum energy is dissipated at each wavelength. The arrows indicate at what wavelength region the most typical ionization and dissociation processes take place. (Brekke, 2012).

1.1.3 Ionosphere

The processes of photoionization and photodissociation are primarily triggered by solar radiation, which is the principal source of energy in the solar system. As a result, variations in electron density occur both globally and locally, influenced by the solar cycles. This relationship is depicted in Figure 1.1.5, illustrating density profiles in relation to altitude.

These density profiles divide the ionosphere into three primary layers: the D layer, spanning from 60 to 80 km in altitude, with a density ranging between 10^8 and 10^{10} [e/m^3]; the E layer, extending from 80 to 110 km in altitude, with a density ranging between 10^9 and 10^{11} [e/m^3]; and the F layer, covering altitudes above 110 km, with a density between 10^{10} and 10^{12} [e/m^3] (Beynon and Brown, 1957; Brekke, 2012; Bittencourt, 2004; Hargreaves, 1992; Rishbeth and Garriott, 1969; Ratcliffe, 1970; Davies, 1990; K.A.Zawdie et al., 2017).

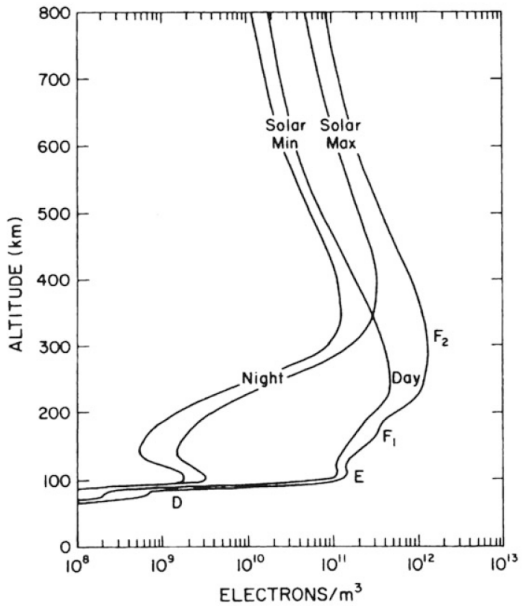

Figure 1.1.5: Typical mid-latitude ionospheric electron density profiles for sunspot maximum and minimum conditions at daytime and night-time. The different altitude regions in the ionosphere are labeled with the appropriate nomenclature (Brekke, 2012).

1.1.3.1 South American Magnetic Anomaly (SAMA)

The South Atlantic Magnetic Anomaly (SAMA), also known as SAA, is a distinct area within Earth's magnetic field situated in the South Atlantic Ocean. In this region, the strength of Earth's magnetic field experiences a significant reduction, resulting in a noticeable gradient in magnetic intensity as one moves southward from the South American continent, as illustrated in the figure. 1.1.6 form Finlay et al. (2020). The anomaly garners significant scientific interest due to its connection with Earth's dynamics, stemming from the interaction between the terrestrial magnetic field and electric currents within the ionosphere. Investigating the South Atlantic Magnetic Anomaly (SAMA) offers valuable insights into understanding the composition and behavior of the ionosphere and his opacity, as well as phenomena associated with geophysical activities and space weather in the South American region, which have effects in telecommunication and satellites. This study subsequently motivated the creation of the South America Riometer Network (SARINET), which we will delve into further later as a part of the project (Finlay et al., 2020).

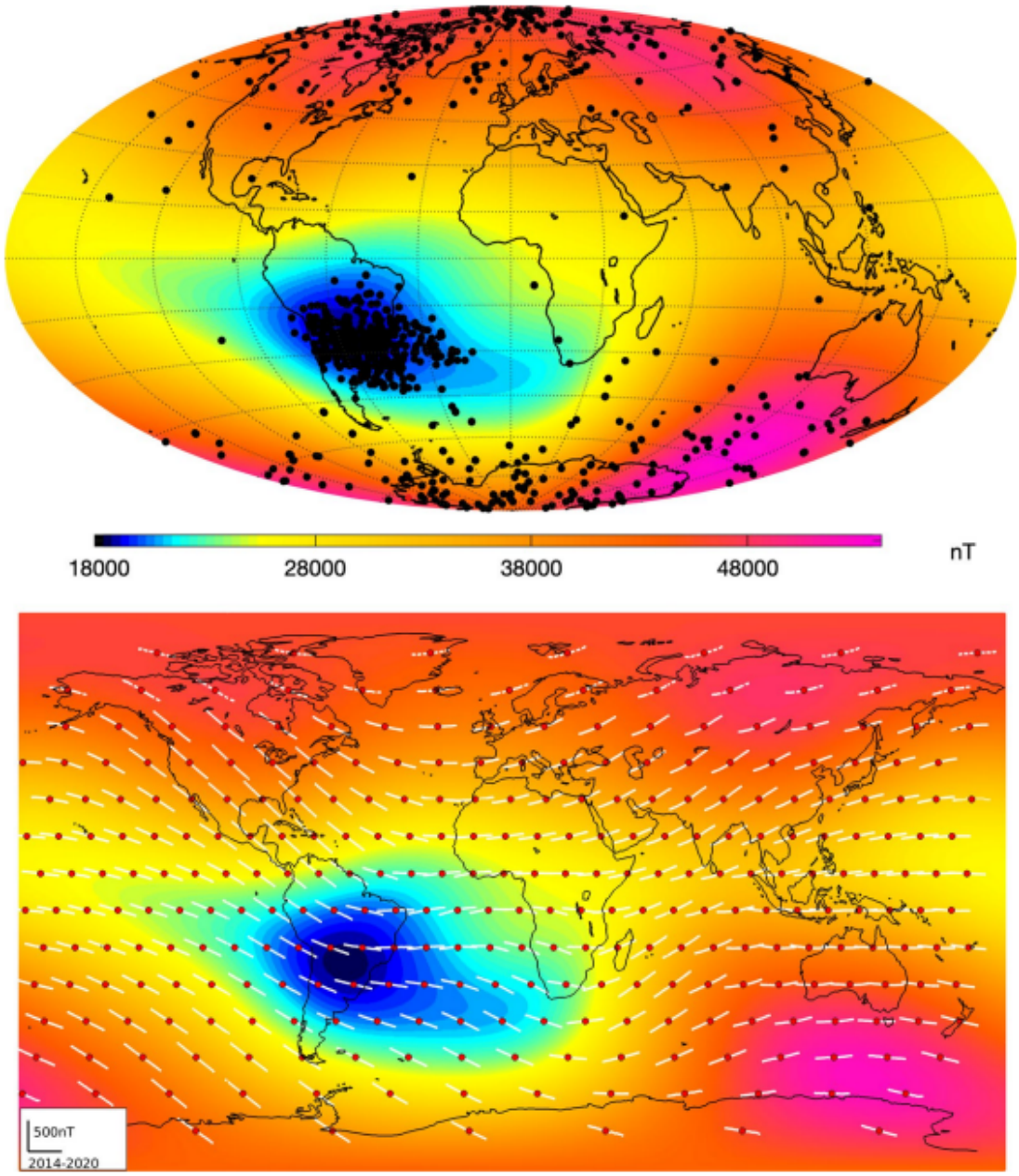

Figure 1.1.6: Top: locations of single-event upsets (SEUs) registered onboard the Swarm satellites between November 2013 and August 2019 (blackdots) plotted on top of the feld intensity at 450-km altitude in August 2017 according to the CHAOS-7 model. Bottom: feld intensity from the CHAOS-7 feld model in August 2017 at 450-km altitude with local time series of feld intensity, constructed using the geomagnetic virtual observatory approach, shown in white for the 300 equal-area distributed positions marked by the red dots. The mean value has been removed from each feld intensity series and the maximum feld change is 492 nT (Finlay et al., 2020).

1.1.3.2 Opacity

The ionosphere serves as an opaque medium, absorbing the energy carried by electromagnetic waves originating from the Cosmic Radio Noise (CRN). This absorption emerges from the interplay between electrons within the ionospheric plasma and the waves. This intricate interaction results in energy transfer to the medium through scattering processes. Within the atmosphere, this energy absorption takes place through two distinct mechanisms: collisions between electrons and neutral particles, as well as pseudo-collisions that encompass interactions among the electrons themselves.(Brekke, 2012; Hargreaves, 1992; Ratcliffe, 1970; Davies, 1990; Rishbeth and Garriott, 1969; K.A.Zawdie et al., 2017).

These phenomena are described by the Magneto-ionic theory, which incorporates all the interaction variables into Appleton's formula for the absorption coefficient k_ν. In the absence or low presence of magnetic fields[2], k_ν (expressed in dB/Km) can be given as:

$$k_\nu = \frac{e^2}{2\varepsilon_0\, mc\, \mu} \frac{N\nu_p}{\omega^2 + \nu_p^2} \tag{1.1.1}$$

Where ε_0 represents the vacuum permeability, N stands for the electronic density, ν_p signifies the collision frequency of electrons, ω denotes the frequency of incident signals, and μ corresponds to the fundamental part of the medium's permeability index. Considering all the variables in equation 1.1.1 and historical studies, the critical region for absorption is the D layer, where non-deviant absorption occurs below the GHz range. In this range, it is possible to approximate $\mu \approx 1$ and $\omega^2 \gg \nu^2$ (Figure 1.1.7 and 1.1.5), leading to the absorption coefficient k_ν as

$$k_\nu = \frac{e^2}{2\varepsilon_0\, mc} \frac{N\nu_p}{\omega^2} \tag{1.1.2}$$

[2]This approximation is valid at low latitudes, as the intensity of Earth's magnetic field lines decreases away from the poles. This is significant since the project is situated at a latitude where this approximation holds (36ř4622S and 73ř0347W)

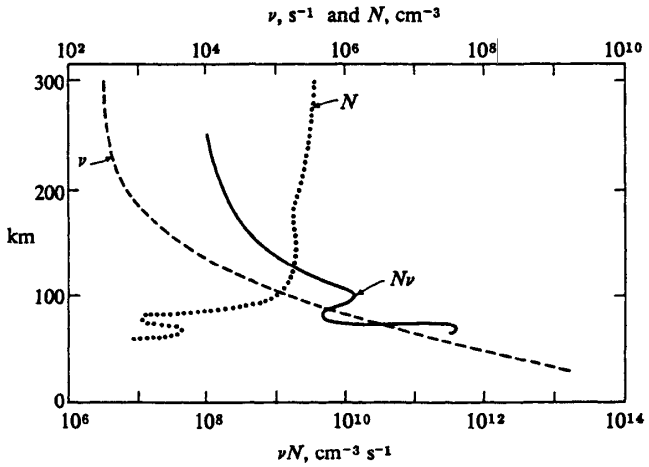

Figure 1.1.7: Variation with height of the electron collision frequency ν, electron density N, and the product $N\nu$, which is a measure of the nondeviative absorption of a radio signal passing through the layer (Davies, 1990).

1.1.4 Radiative transfer equation

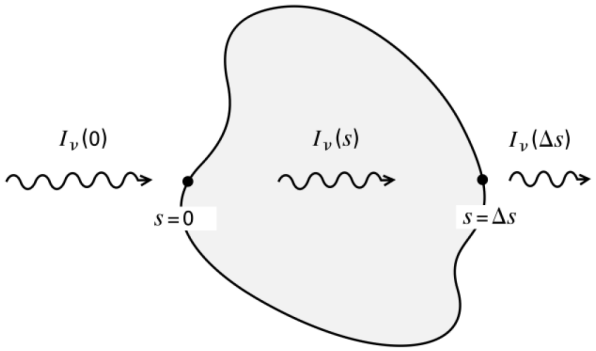

Figure 1.1.8: Schematic used to illustrate the path of a brightness intensity through a medium. (Image taken from the notes of Prof. Stefano Bovino)

To express and quantify the impact of each medium on each frequency signal ω at a macroscopic level, electromagnetic theory employs interface conditions to describe fluctuations. The total fluctuation is calculated using the radiative transfer equation (refer to figure 1.1.8), which takes into account three inputs and one output. These inputs include the intensity of the input signal I_ν, the absorption coefficient k_ν, and the emissivity coefficient ε_ν of the medium. The output corresponds to the differential intensity after passing through a differential segment of the medium (Beynon and Brown, 1957; Bittencourt, 2004; NRAO, 2018; Rishbeth and Garriott, 1969; Davies, 1990; K.A.Zawdie et al., 2017; Thomas

L. Wilson, 2009).

$$\frac{dI_\nu}{ds} = -k_\nu I_\nu + \varepsilon_\nu \tag{1.1.3}$$

In the specific case of the ionosphere, the emissivity coefficient ε_ν is negligible, allowing the equation to be simplified to:

$$\boxed{\frac{dI_\nu}{ds} = -k_\nu I_\nu} \tag{1.1.4}$$

resulting in the following solution to the equation:

$$\boxed{I_\nu(s) = I_\nu(s_0) \exp\left(-\int_{s_0}^{s} k_\nu(s) ds\right)} \tag{1.1.5}$$

1.1.4.1 Characterization Method

Combining the insights from the preceding two subsections, one can grasp and deduce the Cosmic Noise Absorption (CNA) method employed by the riometer to characterize the ionosphere. It's noteworthy that this method stands as the sole passive approach developed thus far. The term "Cosmic Noise Absorption" is derived from the utilization of the Cosmic Radio Noise (CRN) as a radiation source. It defines the relative absorption or opacity, denoted as L_a (dB), concerning the variability of CNA while traversing the ionosphere. This relationship is established by comparing the power measurement from the antenna, denoted as P_0, to the medium's value P extracted from the data (A.P.Mitra et al., 1953; Davies, 1990; K.A.Zawdie et al., 2017).

$$L_a = -10 \log(P_0/P) \tag{1.1.6}$$

The absorption in neper[3] is obtained using the same concept applied to the equation. 1.1.5 .

$$\ln\left(\frac{I}{I_0}\right) = -\int k ds \tag{1.1.7}$$

Taking into account that 1 neper is equivalent to 8.686 dB and the correlation between power and intensity, equation 1.1.7 can be reformulated to be equal to equation 1.1.6, providing us with a formulation for the relative opacity L_a(dB) in

[3]The base of the natural or Neperian logarithm, in gain analysis equivalent to decibel, which is calculated in base 10

terms of the absorption coefficient k_ν.

$$\boxed{L_a = -8.686 \int k_\nu ds} \tag{1.1.8}$$

1.1.4.2 Sensitivity and precision

The instrument's sensitivity to the observable extends from the formulation of the observable itself as a function of the powers detected by the instrument. Therefore, considering equation 1.1.6 derived from the powers measured by the instrument, in accordance with the observation methodology and the radiative transfer equation, it follows that P represents the average value of the detected power and P_0 represents the current measurement value. This allows us to express P_0 as $P+dP_u$, where dP represents the infinitesimal variations of power with respect to the mean value P. With this, equation 1.1.6 can be redefined as:

$$L_a = 10log\left(1 + \frac{dP}{P}\right) \tag{1.1.9}$$

This leads to the derivation of what is recognized and defined in receiver theory as the signal-to-noise ratio (SNR) of the receiver. In the case of a linear receiver, such as the one used in this project, the SNR takes the form of SNR= $\sqrt{\tau \times B}$, as indicated by Thomas L. Wilson (2009), where τ represents the integration time and B signifies the bandwidth of the instrument. This formulation defines the sensitivity of the instrument as:

$$L_a = 10log\left(1 + \frac{1}{\sqrt{\tau \times B}}\right) \tag{1.1.10}$$

and its precision as 2 times L_a (Nielsen et al., 2004; Thomas L. Wilson, 2009). It's worth noting that for the values of B=850 KHz and τ=1 s, the maximum sensitivity of the instrument will be approximately 0,01 dB. (A.P.Mitra et al., 1953; Nielsen et al., 2004; Davies, 1990; K.A.Zawdie et al., 2017).

1.1.5 Riometer's

The history of RIOMETER began with the publication of the Cosmic Noise Absorption (CNA) method formulated by A.P.Mitra et al. (1953). Subsequently,

the design and construction of Riometers has advanced, particularly in regions close to the poles, within latitudes above 65ř north and south (Hunsucker, 1991; Honary et al., 2011,?). The initial design, presented by C.G. Little et al. (1959), utilized a single antenna and a straightforward chain of analog components for signal detection and calibration at 38 MHz with a bandwidth of 200 kHz, as illustrated in the figure. 1.1.9

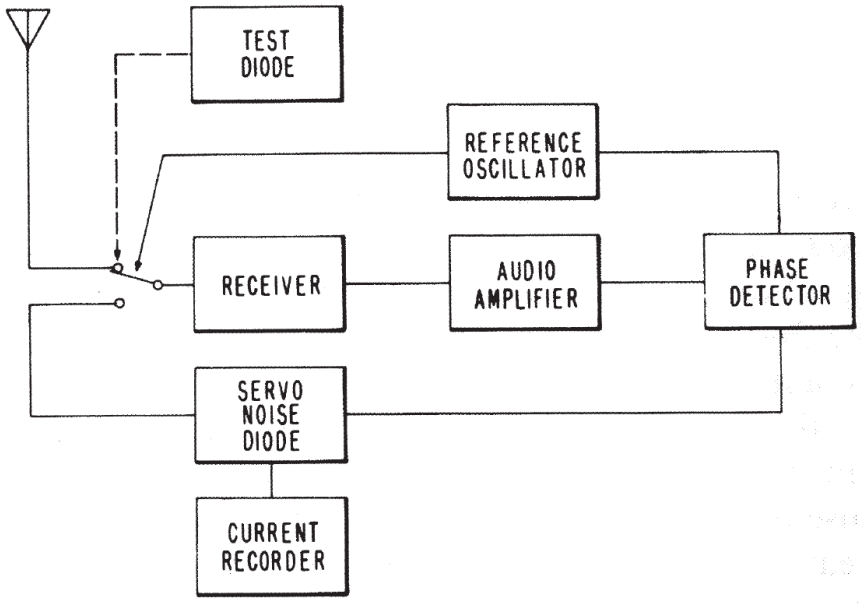

Figure 1.1.9: Simplified block diagram (Hunsucker, 1991).

After validating this concept, RIOMETERs have undergone updates to enhance their resolution, aiming to generate improved images of the ionospheric relative opacity. These updates involve the incorporation of more elements and techniques, such as beamforming and correlators, which integrate the response of all antennas to create images with enhanced resolution and greater sensitivity. The comprehensive information regarding these advancements has been consolidated by Honary et al. (2011) in a table on the subsequent page, encompassing all the intricate details of the diverse system enhancements. References for further exploration of each of these developments in this field are provided in the references section of this work, with specific focus on the research conducted by C.G. Little et al. (1959); S.Browne et al. (1995); Browne et al. (1995); Detrick (1990); Murayama et al. (1997); Rosenberg et al. (1993); M.V.Stepanovaa et al. (2005)

TABLE I. Comparison of various imaging riometer systems. The first part of the table contains general system specifications. The second part of the table provides information regarding the susceptibility to scintillation, which is dependent upon location, thus details for a specific station are given.

System type	IRIS	PENGUIN IRIS	Poker flat	ARIES	AIRIS	Ny-Ålesund	4 × 4
System specifications							
First deployed	January 1988[a]	December 1992	September 1995	January 2006	January 2006	October 2008	February 2010
System type	filled array	filled array	filled array	Mills cross	filled array	filled array	filled array
Beam-forming method	analogue Butler matrix	analogue Butler matrix	analogue Butler matrix	digital Butler matrix and cross-correlation	digital Butler matrix	digital Butler matrix	digital Butler matrix
Number of antennas	64	16	256	63	64	64	16
Number of receivers	7	4	16	63	64	64	16
Number of imaging beams	49	16	256	1024	49	49	16
Number of usable imaging beams	49	16	208	556	49	49	16
Footprint (m^2)	1544 (39.3 × 39.3)	557 (23.6 × 23.6)	3795 (61.6 × 61.6)	1985 (2 perpendicular arms, (each 129.6 × 7.9)	1544 (39.3 × 39.3)	1544 (39.3 × 39.3)	557 (23.6 × 23.6)
Operating frequency (MHz)	38.2	38.2	38.2	38.235	38.235	38.235	38.235
Receiver bandwidth (kHz)	200	200	200	1000	250	1000	250
Computational requirements:							
multiplications (M/s)	…	…	…	6810	358	358	90
additions (M/s)	…	…	…	3494	246	246	112
Beam width at zenith (°)	12.8	26.3	6.60	6.56[b]	12.8	12.8	26.3
at 90 km altitude (km)	20.2	42.1	10.4	10.3	20.2	20.2	42.1
Beam separation at zenith (°)	14.2	27.0	7.21	3.53	14.2	14.2	27.0
at 90 km altitude (km)	22.4	43.3	11.3	5.55	22.4	22.4	43.3
Cadence (s)	1	12	1	1	1	1	1
Integration time[c] (ms)	95[d]	550[d]	40	952	952	952	952
Bandwidth time product	19 000	110 000	8000	952 000	238 000	952 000	238 000
Theoretical precision (dB)	0.063	0.026	0.048	0.097	0.0089	0.0045	0.0089
Measured precision (dB)	0.076	…	…	0.045	0.010	0.0072	0.0093
Scintillation details							
Station	Kilpisjärvi, Finland	AGO-P2, Antarctica	Poker Flat, Alaska	Ramfjordmoen, Norway	Andøya, Norway	Ny-Ålesund, Svalbard	Maitri, Antarctica
Latitude (°)	69.05°N	85.67°S	65.10°N	69.64°N	69.15°N	78.92°N	70.77°S
Longitude (°)	20.79°E	46.38°W	147.50°W	19.49°E	16.03°E	11.94°E	11.73°E
Data affected by Cassiopeia A (%)	1.42	0	0.394	0.481	1.42	1.44	0
Beams affected by Cassiopeia A	12	0	32	94	12	14	0
Data affected by Cygnus A (%)	1.28	0	0.410	0.278	1.28	1.19	0
Beams affected by Cygnus A	15	0	56	80	15	14	0
Data affected by Sagittarius A* (%)	0	2.62	0	0	0	0	2.28
Beams affected by Sagittarius A*	0	8	0	0	0	0	6

[a]The first IRIS system was deployed at the South pole in January 1988. The Kilpisjärvi IRIS system was deployed in September 1994.
[b]With the standard cosine tapering.
[c]Integration time at stated cadence.
[d]Excluding effect of 50% duty cycle in noise-balancing receiver.

1.1.5.1 SARINET and Universidad de Concepcion

In 2004, Professor Alberto Foppiano from the Geophysics Department at the Universidad de Concepción (UdeC), Chile, along with Dr. K. Makita from the University of Takushoku, Japan, implemented a RIOMETER as part of SARINET. They were allocated a budget of approximately 30000 USD to establish a site within UdeC's forest (-36.84ř S, -73.03ř W). The RIOMETER featured a phased array with sixteen dipole antennas arranged in a 4x4 distribution, as depicted in Figure 1.1.10a. Each antenna had a central frequency of 38 MHz. The signals from the antennas were integrated using a Butler matrix BM-16-38, serial number 30521-004, manufactured by the Japanese company RK LTD[4] (Figure 1.1.10b). The fourth output signal from the Butler matrix was digitized using four IC-R8500 receivers from the Icom company (Figure 1.1.10c). The overall system response provides a bandwidth of 200 kHz at a central frequency of 38 MHz, similar to the IRIS riometer, which boasts a theoretical precision of 0.063 dB for an integration time of 95 ms. (Nishino and Monreal, 2004).

(a) Phase array **(b)** butler Matrix. **(c)** Digitizer Icom.

Figure 1.1.10: Image of the array in 2004, picture of the butler matrix and digitizer Icom which component the riometer UdeC (Nishino and Monreal, 2004).

The measurements conducted in March of 2004 using the Riometer were documented by Nishino and Monreal (2004), demonstrating the functionality of the system. These measurements enable the assessment of relative ionospheric opacity, with potential applications for studying the ionospheric effects of the South Atlantic Magnetic Anomaly (SAMA). The initial measurements captured the quiet curve of the cosmic radio noise (CRN). Subsequently, the collected data was used to generate synthesized images employing the Cosmic Noise Absorption method (CNA), as illustrated in the figure 1.1.11a and 1.1.11b.

[4]these devices were discontinued after 1999

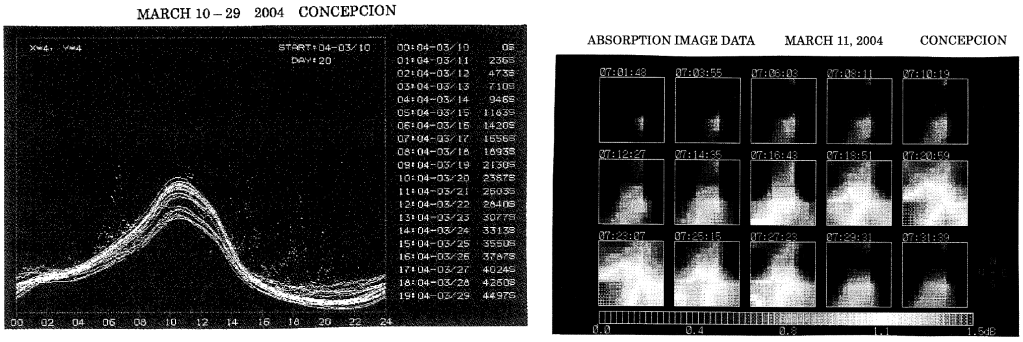

(a) Quiet curve of the data taken from 10 to 29 march 2004 in Concepción.

(b) Absorption event from 7:01 to 7:31.

Figure 1.1.11: Data taken for the professor Foppiano and Makita in Concepcion in 2004 (Nishino and Monreal, 2004).

Professor Foppiano has pointed out that the data lacks sufficient precision and exhibits excessive dispersion in the quiet curve (Figure 1.1.11a), making it challenging to proceed with observations without a reliable reference for the Cosmic Radio Noise. Consequently, the system was abandoned, and after nearly two decades (by 2019), the dipole arrays are now reclaimed by nature. This revelation presents us with a distinctive opportunity to refurbish and enhance the hardware, utilizing technologies and techniques that are more advanced by over 30 years compared to its predecessor.

1.2 Hypothesis

Previous studies indicate that ionospheric characterization becomes more challenging as one approaches the equator using conventional riometers. Building upon the findings of Dr. Makita and Prof. Foppiano, it is postulated that obtaining relative opacity measurements at low latitudes is possible and can be improved by completely restructuring the analog-digital processing system of the UdeC riometer. This restructuring aims to fully exploit the antenna bandwidth and implement spectral decomposition of its frequency band.

This approach will enable a comprehensive analysis of both Cosmic Radio Noise (CRN) and Cosmic Noise Absorption (CNA) signals across all spectral channels generated through band decomposition. This endeavor materializes in the ISI-RIOMeter, which seeks to offer enhanced capabilities for ionospheric research and

provide valuable insights into ionospheric behavior at low latitudes close to the SAMA region.

1.3 Project objectives

1.3.1 General objective

The primary goal of this project is to evaluate, design, simulate, implement, and characterize a novel Riometer instrumental prototype, known as the ISI-Riometer (Ionospheric Spectral Imager Riometer). This prototype aims to offer high sensitivity and spectral analysis capabilities for precise measurements of Cosmic Radio Noise (CRN).

1.3.2 Specific objectives

- Conduct a comprehensive characterization and simulation of the antenna array used in the ISI-Riometer to optimize its performance and effectiveness.
- Develop new analog hardware components for the ISI-Riometer, including design, simulation, implementation, and characterization processes to ensure enhanced sensitivity and accuracy in CRN measurements.
- Develop new digital hardware for the ISI-Riometer, involving design, simulation, implementation, and characterization steps to enable advanced spectral analysis capabilities.
- Integrate the newly designed antennas, analog hardware, and digital hardware into the ISI-Riometer system to create a cohesive and functional instrument.
- Perform data acquisition of the quiet curve of the Cosmic Radio Noise (CRN) using the ISI-Riometer prototype. This data will serve as a reference for future CRN measurements and analysis.

By accomplishing these specific objectives, the project aims to develop a state-of-the-art instrument that significantly enhances our ability to measure and analyze CRN, leading to a deeper understanding of ionospheric behavior and related phenomena.

Chapter 2

Theoretical framework

The following chapters consolidate the essential theory and parameters needed to comprehend the radiation source utilized by the RIOMETER and the radio system's components. This approach forms a unified framework by merging electromagnetic theory and quantum mechanics. This synergy enables us to model the source, understand wave propagation, and develop the tools for signal reception and processing, resulting in a comprehensive understanding of the RIOMETER's function and its significance in ionospheric research Maxwell (1865); Pozar (2005); Thomas L. Wilson (2009); Greiner and Bromley (2000); Walter Greiner (1998); Ulaby (2007); Arfken (1985); Pozar (2005).

2.1 Radiation source

To understand and determine the radiation's intensity and geometry that we expect to detect using this system, it's essential to define the signal's emission magnitude from the source, often represented by the brightness intensity B_ν modeled by a blackbody, as well as the wavefront's propagation geometry.

2.1.1 The Black-Body

The black body is a theoretical model of a body capable of absorbing all radiation and emitting radiation across the entire electromagnetic spectrum as a function of its temperature in thermodynamic equilibrium, following the Planck distribution defined by equation 2.1.1). This behavior is illustrated in figure 2.1.1 for different

body temperatures.(Rishbeth and Garriott, 1969; Beynon and Brown, 1957; Brekke, 2012; Greiner and Bromley, 2000; Walter Greiner, 1998; Thomas L. Wilson, 2009).

$$B_\nu(T) = \frac{2\hbar\nu^3}{c^2} \frac{1}{e^{\frac{\hbar\nu}{k_b T}} - 1} \tag{2.1.1}$$

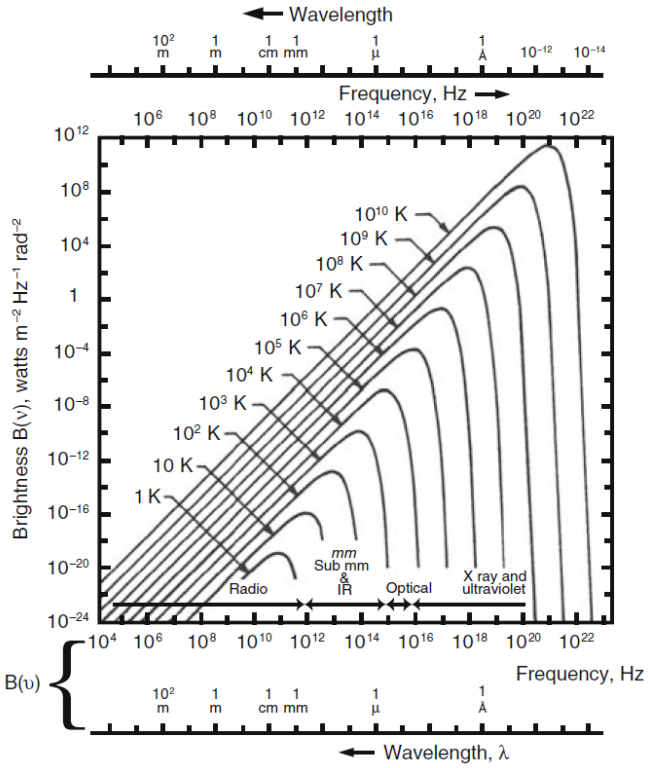

Figure 2.1.1: Planck spectrum for different blackbody temperatures(Thomas L. Wilson, 2009).

In the context of electromagnetic radiation, the term B_ν represents brightness intensity[1] emitted per unit area, unit bandwidth, and solid angle of a black body. In this equation, $\hbar$ denotes Planck's constant, approximately equal to 6.62×10^{-34} [Js]. The symbol ν corresponds to the frequency in cycles per second or hertz [Hz], while k_b stands for Boltzmann's constant, approximately equal to 1.38×10^{-23} [J/K]. The letter C represents the speed of light, approximately equal to 3×10^8 [m/s], and T represents the absolute temperature in kelvins of the black body in thermodynamic equilibrium (Thomas L. Wilson, 2009; Greiner and Bromley, 2000; Walter Greiner, 1998; Ulaby, 2007; Arfken, 1985; Pozar, 2005)

[1]Note: also referred to as power intensity, specific brightness, or specific brightness intensity. Please note that it denotes the value of the generated electromagnetic field's intensity

2.1.1.1 Rayleigh Jeans approximation

Considering the frequency range and temperature of the signal, we can make an approximation of the Planck law using the classic limit known as the Rayleigh-Jeans approximation ($h\nu/kT \ll 1$), which means:

$$\boxed{B_\nu = \frac{2h\nu^3}{c^2}\frac{kT_b}{h\nu} \approx \frac{2kT}{\lambda^2}\left[\frac{\mathbf{J}}{m^2}\right]} \tag{2.1.2}$$

where we obtain values ranging from $8.62906 \cdot 10^{-34}$ to $1.72581 \cdot 10^{-35}[J/m^2]$ for the maximum and minimum of the CRN.

2.1.2 Light propagation and wavefront

When light is emitted by a source, it propagates as an electromagnetic wave in all directions. A wavefront is defined by points with coherent phases in the signal propagation. Initially and in most cases, the geometry is spherical (depending on the source's geometry), but as the distance increases, the curvature decreases, changing to a planar wavefront or more complex geometries depending on changes in the medium and interface conditions. From the source's perspective, the distance is astronomical and using that approximation doesn't cause any issues. However, to apply this approximation in a radio system, the wavefront needs to travel at least the distance of Fraunhofer (Eq.2.1.3), a critical point that considers the aperture's diameter (D) and the wavelength () of the signal (Griffiths, 2012; Pozar, 2005; G. Rubilar and others., 2020; Thomas L. Wilson, 2009).

$$d_f = \frac{2D^2}{\lambda} \tag{2.1.3}$$

In the case of our dipole array, the Fraunhofer distance is approximately 136.4 meters, which needs to be considered to ensure that we are in the Fraunhofer region.

2.2 Signal reception and Antennas

To capture the CRN signal, we utilize antennas made from high-conductivity materials, which act as transducers by converting the electromagnetic potential of

waves within the radio and microwave frequency ranges into an electromagnetic potential that can propagate within an electric circuit. The fundamental characteristics of an antenna are shaped by its geometry and the materials employed in its construction. The choice of material impacts the antenna's efficiency in electromagnetic induction, while the geometry determines the tuning frequency and resolution size during observations. These values can be calculated by considering the retarded potential of the antenna and its corresponding Poynting vector. .(Pozar, 2005; Ulaby, 2007; Walter Greiner, 1998; Thomas L. Wilson, 2009).

2.2.1 The retarded potential and Poynting's theorem

The retarded potential $V(R)$ (Eq. 2.2.2) and $\tilde{A}(R,t)$ (Eq.2.2.1) represent the electromagnetic potential resulting from the superposition of the electrostatic potential generated by a charge moving an infinitesimal distance in an infinitesimal time across a volume. For an antenna conductor, this phenomenon is linked to the motion of its electronic density (ρ_v and J_v) within its conduction band and is influenced by its geometry ($\int_v' dv'$).

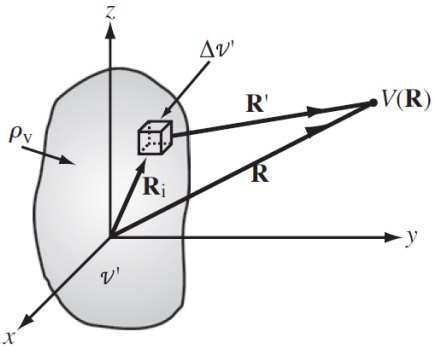

Figure 2.2.1: Schematic of electromagnetic potential generated by charge distribution ρ_ν over the volumeν'(Ulaby, 2007).

$$V(R) = \frac{1}{4\pi\epsilon}\int_{\nu'}\frac{\rho_v(R_i, t-R'/u_p)}{R'}d\nu' \ (V) \tag{2.2.1}$$

$$A(R,t) = \frac{\mu}{4\pi}\int_{\nu'}\frac{J_v(R_i, t-R'/u_p)}{R'}d\nu' \ (Wb/m) \tag{2.2.2}$$

This enables us to compute the electromagnetic fields ($\tilde{H}$ and $\tilde{E}$) generated by charges in the antenna conductor at any point R in space using the Lorentz gauge.

These calculations are usually carried out for harmonic potentials, which are similar to the signals we anticipate receiving.(Thomas L. Wilson, 2009; Pozar, 2005; G. Rubilar and others., 2020; Griffiths, 2017; Walter Greiner, 1998).

$$\boxed{\tilde{H} = \frac{1}{\mu_0}\nabla \times \tilde{A}} \tag{2.2.3}$$

$$\boxed{\tilde{E} = \frac{1}{j\omega\epsilon}\nabla \times \tilde{H}} \tag{2.2.4}$$

The energy carried by this electromagnetic field to the point R in space is calculated using the work-energy theorem of electrodynamics, expressed in Poynting's theorem and computed using the Poynting vector (S), which represents the energy per unit time and per unit area. It's important to note that the concept underlying this formulation is symmetric for both the emission and reception of radiation due to the conservation law and let us derivate the radiometric characteristics of the antennas. (Overby, 2022; Kittel, 2005; G. Rubilar and others., 2020; Ulaby, 2007; Griffiths, 2017; Walter Greiner, 1998).

$$P(r,t) = \frac{1}{\mu}\int_S [(\tilde{E} \times \tilde{H^*}) \cdot \hat{n}] d\Omega \tag{2.2.5}$$

$$S(r,t) = \frac{1}{\mu}[(\tilde{E} \times \tilde{H^*}) \tag{2.2.6}$$

2.2.2 Radiometric characteristics

The electromagnetic potential and the Poynting vector are foundational concepts that guide the design of the antenna conductor's geometry and the material selection. These concepts empower us to unravel the spatial dispersion of signal intensity or radiation pattern, pinpoint the solid angle encompassing over 50% of the signal's presence, quantify the average power within this region, evaluate the antenna's gain and directivity, gauge its effective temperature, and outline its equivalent circuitry and radiation resistance. (Thomas L. Wilson, 2009; Pozar, 2005; G. Rubilar and others., 2020; Griffiths, 2017; Walter Greiner, 1998; Ulaby, 2007).

2.2.2.1 Radiation pattern

The radiation pattern $P_n(\theta, \phi)$ is defined as the normalised Poynting vector and can be expressed in lineal (Eq. 2.2.8) or logarithmic scale (Thomas L. Wilson, 2009; Pozar, 2005; G. Rubilar and others., 2020; Griffiths, 2017; Walter Greiner, 1998).

$$F_n(\theta, \phi) = \frac{S(\theta, \phi)}{S_{max}(\theta, \phi)} \tag{2.2.7}$$

This parameter enables us to visualize and compare the intensity and direction of signal emissions or receptions using our antenna with an ideal isotropic antenna that emits and receives signals with the same intensity in all directions. The conversion from linear to logarithmic scale is achieved using the corresponding equation 2.2.8

$$P_n(\theta, \phi)_{dbi} = 10log(F_n(\theta, \phi)) \quad [dBi] \tag{2.2.8}$$

It is important to highlight that $P_n(\theta, \phi)$ represents the energy distribution of the wavefront. Therefore, it is customary to visualize and express it in terms of θ and ϕ on a polar coordinate plane.

2.2.2.2 Beamwidth

The beamwidth offers a practical estimation of the region where the majority of signals are concentrated. It serves to define the antenna's angular resolution and the size of observation pixels. The extent of the beamwidth is ascertained by the point at which P_n diminishes to 50% of its maximum value on a linear scale, or -3 dB on a logarithmic scale (Thomas L. Wilson, 2009; Pozar, 2005; Ulaby, 2007).

2.2.2.3 Effective aperture

The effective aperture A_e serves as a measure of the antenna's efficiency in converting electromagnetic waves into electrical signals at its interfaces. It can be determined by establishing the relationship between the power ($P_i[W]$) transmitted or received by the antenna and the flux ($S_i\ [W/m^2]$) passing through it (Thomas L. Wilson, 2009; Pozar, 2005; Ulaby, 2007).

$$A_e = \frac{P_{int}}{S_i} \quad [m^2] \tag{2.2.9}$$

2.2.2.4 Average power

The average power refers to the power generated by the antenna at its terminals and can be estimated based on its characteristics and the intensity of the source. This estimation takes into account the effective aperture A_e, the power flux at each frequency (expressed in terms of the brightness intensity $B_\nu(\theta, \phi)$ of the source), and the radiation pattern $P_n(\theta, \phi)$ of the antenna across the entire sphere (Thomas L. Wilson, 2009; Pozar, 2005; Ulaby, 2007).

$$\boxed{P_{avg} = \frac{1}{2} A_e \int \int B_\nu(\theta, \phi) P_n(\theta, \phi) d\Omega} \tag{2.2.10}$$

2.2.2.5 Antenna temperature

The antenna temperature $T_A(\theta_0, \phi_0)$ is an approximation of the temperature generated by the flux within the antenna, as if the antenna were an impedance radiator with a brightness temperature $T_b(\theta_0, \phi_0)$ and a radiation pattern $P_n(\theta, \phi)$.

$$T_A(\theta_0, \phi_0) == \frac{\int T_b(\theta, \phi) P_n(\theta - \theta_0, \phi - \phi_0) \sin(\theta) d\theta d\phi}{\int P_n(\theta, \phi) d\Omega} \tag{2.2.11}$$

This enables us to represent the average power in terms of the brightness temperature, as shown in equation 2.2.12, where K represents Boltzmann's constant. (Thomas L. Wilson, 2009; Pozar, 2005; Ulaby, 2007).

$$P_{avg} = K T_A \tag{2.2.12}$$

2.2.2.6 Directivity

Antenna directivity (D) is a parameter used to assess the antenna's ability to distinguish the intensity originating from the maximum of its radiation pattern compared to the overall average radiation pattern. It is defined as the ratio between the two. (Thomas L. Wilson, 2009; Pozar, 2005; Ulaby, 2007).

$$\begin{aligned} D &= \frac{P_{max}}{P_{Prom}}, \\ &= \frac{1}{\frac{1}{4\pi} \int \int_{4\pi} P(\theta, \phi) d\Omega}, \end{aligned}$$

$$\boxed{D = \frac{4\pi}{\Omega_p}}. \tag{2.2.13}$$

and can be expressed in term of the flux

$$D = \frac{4\pi R^2 S_{max}}{P_{rad}} = \frac{S_{max}}{S_{prom}}. \tag{2.2.14}$$

2.2.2.7 Gain

The antenna gain (G) is a parameter used to estimate the relation between the maximum flux (S_{max}) in the antenna and the transmission power (P_t) to the antenna

$$G = \frac{4^2 S_{max}}{P_t} d\Omega, \tag{2.2.15}$$

The equation for the antenna gain is similar to that of the antenna directivity (D), and these parameters are intrinsically related by the efficiency (ξ) of the antenna.

$$\xi = \frac{P_{rad}}{P_t}, \tag{2.2.16}$$

This enables us to express the antenna gain (G) in terms of antenna directivity (D).

$$G = \xi D. \tag{2.2.17}$$

Please note that the gain enables us to calculate the harmonic losses, while the directivity characterizes the spatial energy distribution.

2.2.2.8 Antenna equivalent circuit and radiation resistance

As previously discussed, the antenna can be conceptualized as an impedance or load with the temperature of the radiation source at its tuned frequency, referred to as the antenna temperature (T_A). This concept can be further explained in terms of equivalent Thévenin's circuits, as illustrated in the figure

2.2.3 Antenna array and beamforming

An antenna array is one of the options to enhance the response and sensitivity of the radio system. It consists of multiple antennas arranged in a specific geometry, which operate in tandem and combine their responses to synthesize an antenna

with improved characteristics (Barott et al., 2011; B.D.Van Veen, 1988; S.Nordebo et al., 1994; M.T.Ma, 1974; Observatory, 2021; Creative, 2021; H.Unz, 1960, 1956).

2.2.3.1 Beamforming

The beamforming algorithm represents the superposition of electromagnetic fields generated by the retarded potentials of each antenna in the array. It is expressed through the summation of signals with coherent phases. These algorithms necessitate a reference system and the precise positioning of each element within that framework to define the wavefront to be measured (B.D.Van Veen, 1988; M.T.Ma, 1974; Barott et al., 2011).

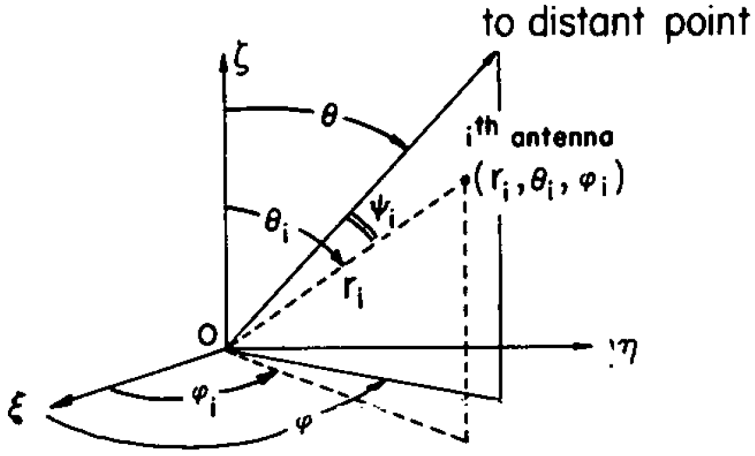

Figure 2.2.2: Reference system for a distribution of "i" elements (M.T.Ma, 1974).

Hence, the resultant electromagnetic fields constitute the cumulative sum of each individual field generated by all antennas at the specific point under observation, relative to the chosen reference system. This relationship can be expressed using the following equation 2.2.18

$$E_t(\theta, \varphi) = \sum_{i}^{n} f(\theta, \varphi) I_i \exp[j(kr_i \cos(\psi_i) + \alpha_i)] \tag{2.2.18}$$

In this context, I_i and α_i stand for the signal's amplitude and phase excitation, respectively. These values play a crucial role in establishing the specific direction (θ, ϕ) from which we aim to capture the wavefront.

2.3 Analog system

As electromagnetic waves convert into electrical potential at antenna terminals, the resulting electrical signal can be propagated through transmission lines and processed using resonant active and passive circuits, selected based on the specific application of the radio frequency (RF) receptor.

While delving into the detailed analysis and theory of these components goes beyond the project's scope due to their complex scientific nature, it remains crucial to acknowledge their significance. The lumped-element model serves as a fundamental representation of the transmission line, rooted in its geometry and constitutive parameters. The transmission line equation facilitates circuit exploration by considering the transmission of current ($\tilde{I}$), voltage ($\tilde{V}$), and power ($\tilde{P}$) along the line. This examination encompasses an evaluation of the reflection coefficient (Γ) effects. The active and passive resonant circuit theories contribute to understanding the complete response of the analog system, playing a pivotal role in its characterization. (Pozar, 2005; Ulaby, 2007; Bowick et al., 2007).

2.3.1 Transmission line

According to transmission line theory, it's understood that a harmonic signal's current ($\tilde{I}$) and voltage ($\tilde{V}$) are connected by a first-order equation. However, they can be separated into two symmetric second-order equations (Pozar, 2005; Ulaby, 2007; Bowick et al., 2007).

$$\boxed{\frac{d^2\tilde{V}(z)}{dz^2} - \gamma^2\tilde{V}(z) = 0.} \tag{2.3.1}$$

$$\boxed{\frac{d^2\tilde{i}(z)}{dz^2} - \gamma^2\tilde{i}(z) = 0.} \tag{2.3.2}$$

Here, $\gamma_c = \alpha + j\beta$ represents the complex propagation constant, which is determined by the values of resistance R (ω/m), inductance L (H/m), conductance G (S/m), and capacitance C (F/m).

$$\boxed{\gamma_c = \sqrt{((R' + j\omega L')(G' + j\omega C'))}} \tag{2.3.3}$$

which solution is

$$\tilde{V}(z) = V_0^+ e^{-\gamma Z} + V_0^- e^{\gamma Z} \quad (V) \tag{2.3.4}$$

$$\tilde{I}(z) = I_0^+ e^{-\gamma Z} + I_0^- e^{\gamma Z} \quad (A). \tag{2.3.5}$$

from this we obtain

$$\tilde{I}(z) = \frac{\gamma}{R' + j\omega L'}[V_0^+ e^{-\gamma Z} - V_0^- e^{\gamma Z}] \tag{2.3.6}$$

and

$$\frac{V_0^+}{I_0^+} = Z_0 = \frac{V_0^-}{I_0^-} \tag{2.3.7}$$

where Z_0 is the characteristic impedance for the frequency ω

$$Z_0 = \frac{R' + j\omega L'}{\gamma} = \sqrt{\frac{R' + j\omega L'}{G' + j\omega C'}} \tag{2.3.8}$$

2.3.1.1 Interface between two transmission lines

Similar to the interface condition in wave propagation between two mediums with different impedances (η_1 and η_2), circuits exhibit voltage continuity at interfaces (z=0) between different impedances (Z_0 and Z_L). (Pozar, 2005; Ulaby, 2007; Bowick et al., 2007).

$$Z_L = \frac{\tilde{V}_L}{\tilde{I}_L} \tag{2.3.9}$$

$$\tilde{V}_L = \tilde{V}(z=0) = V_0^+ + V_0^- \tag{2.3.10}$$

$$\tilde{I}_L = \tilde{I}(z=0) = \frac{V_0}{Z_0} - \frac{V_0^-}{Z_0} \tag{2.3.11}$$

From this, it is deduced that the voltages at the interfaces are directly proportional to

$$\frac{V_0^-}{V_0^+} = \frac{Z_L - Z_0}{Z_L + Z_0} \tag{2.3.12}$$

defining the reflection (Γ) and transmission (τ_c) coefficients of the signal at the interface

$$\boxed{\Gamma_c = \frac{V_0^-}{V_0^+} = \frac{Z_L - Z_0}{Z_L + Z_0} = -\frac{I_0^-}{I_0^+}} \tag{2.3.13}$$

$$\boxed{\tau_c = 1 + \Gamma_c} \tag{2.3.14}$$

which in general is a complex number

$$\boxed{\Gamma = |\Gamma| e^{j\theta_r}} \tag{2.3.15}$$

and let rewrite the current and the voltage in the circuit like

$$\tilde{V}(z) = V_0^+(e^{-j\gamma z} + \Gamma e^{j\gamma z}) \tag{2.3.16}$$

$$\tilde{I}(z) = I_0^+(e^{-j\gamma z} - \Gamma e^{j\gamma z}) \tag{2.3.17}$$

and the $|\tilde{V}(z)|$

$$\begin{aligned} |\tilde{V}(z)| &= |V_0^+|[e^{2\alpha z} + |\Gamma|^2 e^{2\alpha z} + |\Gamma|(e^{-j(2\beta z+\theta_r)} + e^{j(2\beta z+\theta_r)})]^{1/2} \\ &= \boxed{|V_0^+|[e^{2\alpha z} + |\Gamma|^2 e^{2\alpha z} + 2|\Gamma|\cos(2\beta z + \theta_r)]^{1/2}} \end{aligned} \tag{2.3.18}$$

Now it becomes clear to observe the presence of maximum and minimum values in voltage and current when $2\beta z + \theta_r = 2n\pi$ and $2\beta z + \theta_r = (2n+1)\pi$ respectively, where $n \geq 0$. This results in the generation of a static wave pattern along the signal's propagation axis, characterized by the standing wave ratio (SWR).

$$SWR = \frac{1 + |\Gamma|}{1 - |\Gamma|} \tag{2.3.19}$$

and the values of the incident, reflected, and transmitted voltage signals at z=0 are:

$$\tilde{V}_i = V_0^+, \qquad \tilde{I}_i = \frac{V_0^+}{Z_0} \tag{2.3.20}$$

$$\tilde{V}_r = \Gamma V_0^+, \qquad \tilde{I}_r = \Gamma \frac{V_0^+}{Z_0} \tag{2.3.21}$$

$$\tilde{V}_t = \tau_c V_0^+, \qquad \tilde{I}_t = \tau_c \frac{V_0^+}{Z_0} \tag{2.3.22}$$

2.3.1.2 Phase velocity

The constitutive parameters of the transmission line simultaneously influence both the amplitude and the phase of the signal. Before examining their effects on amplitude and phase, it's important to recall that wave velocity is determined by

the constants μ and ε, and in a vacuum, the phase velocity u_p equals the speed of light $C \approx 3 \times 10^8$ m/s [1][2][3].

$$u_p = C = f\lambda = \frac{1}{\sqrt{\mu\varepsilon}} \tag{2.3.23}$$

In other scenarios, this velocity is adjusted by the relative permittivity ε_r of the medium.

$$u_p = f\lambda = \frac{1}{\sqrt{\mu\varepsilon\varepsilon_r}} = \frac{C}{\sqrt{\varepsilon_r}} \tag{2.3.24}$$

As the frequency remains constant, equation 2.3.23 reveals that the wavelength λ transforms to λ_0 under the modulation of ε_r.

$$\lambda = \frac{u_p}{f} = \frac{\lambda_0}{\sqrt{\varepsilon_r}}. \tag{2.3.25}$$

This alteration directly amplifies the effective wavelength and consequently induces changes in phase propagation in transmission lines.

2.3.1.3 Power

The power through the circuit is equal to the product of Voltage ($\tilde{V}$) and current ($\tilde{I}$) (Pozar, 2005; Ulaby, 2007; Bowick et al., 2007).

$$P(z,t) = \tilde{V}(z,t) \cdot \tilde{I}(z,t) \tag{2.3.26}$$

$$= \Re e\left[\frac{|V(z,t)|^2}{Z_0}\right] \tag{2.3.27}$$

In practical scenarios, it becomes necessary to quantify signal power within infinitesimal discrete time dt across a load Z_L, illustrated in Figure 2.3.1. Here, Z_g corresponds to Z_0. Within the "dt" interval, the measurement system registers the load's average instantaneous power (P_a^i) and reflected power (P_a^r). In other words, the system integrates power over the period $T = 1/f = 2\pi/\omega$ to capture the summarized power behavior. (Thomas L. Wilson, 2009; Pozar, 2005; Ulaby, 2007).

$$P_a^i = \frac{1}{T}\int_0^t P^i(t)dt = \frac{\omega}{2\pi}\int_0^{2\pi/\omega} P^i(t)dt \tag{2.3.28}$$

and integrated

$$P_a^i = \frac{|V_+|^2}{2Z_0} \quad (W) \tag{2.3.29}$$

and for the P_a^r

$$P_a^r = -|\Gamma|^2\frac{|V_+|^2}{2Z_0} = -|\Gamma|^2 Pi_{prom} \quad (W) \tag{2.3.30}$$

and the total average power in the load is

$$\boxed{P_a = P_a^i + P_a^r = \frac{|V_+|^2}{2Z_0}[1-|\Gamma|^2] \quad (W)} \tag{2.3.31}$$

2.3.2 Tool and parameters for RF system

The RF system comprises a transmission line, as well as active and passive resonant circuits. These components are analyzed through their power transmission or scattering parameters to define specific regions within the electromagnetic spectrum in which they operate. Subsequently, they are examined using the tools and parameters outlined below (Thomas L. Wilson, 2009; Pozar, 2005; Ulaby, 2007).

2.3.2.1 Scattering parameters

The scattering parameters, often referred to as S parameters, constitute a framework of concepts derived from reflection and transmission coefficients. These parameters provide a versatile means to comprehensively describe signal propagation through RF circuits (Pozar, 2005; Ulaby, 2007).

In two-port circuits (labeled as 1 and 2 in Figure 2.3.1), the S parameters establish a relationship between the inputs (V_1^+ and V_2^+) and the outputs (V_1^- and V_2^-) of the circuits. This relationship defines the scattering matrix of the two-port network, as illustrated below :

$$\begin{pmatrix} V_1^- \\ V_2^- \end{pmatrix} = \begin{pmatrix} S_{11} & S_{12} \\ S_{21} & S_{22} \end{pmatrix} \begin{pmatrix} V_1^+ \\ V_2^+ \end{pmatrix} \tag{2.3.32}$$

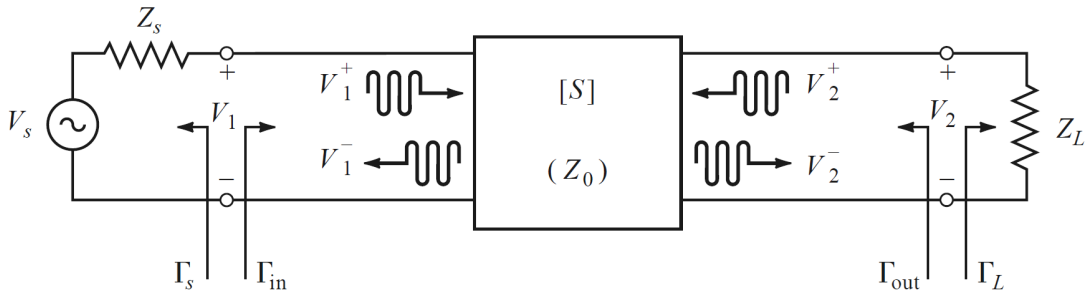

Figure 2.3.1: Two ports representation of RF circuit (Pozar, 2005).

where

$$\begin{aligned} S_{11} &= \frac{V_1^-}{V_1^+} \quad S_{12} = \frac{V_1^-}{V_2^+} \\ S_{21} &= \frac{V_2^-}{V_1^+} \quad S_{22} = \frac{V_2^-}{V_2^+} \end{aligned} \tag{2.3.33}$$

Furthermore, $S_{11} = \Gamma_{11}$ represents the reflection coefficient for port 1, and $S_{22} = \Gamma_{22}$ corresponds to the reflection coefficient for port 2. The parameters S_{21} and S_{12} denote the direct and reverse transmission gains, respectively. It's important to note that this analysis can be extended to circuits with multiple n-ports ($n \in \mathbb{N}$).

2.3.2.2 Smith chart

The Smith chart, developed in 1939, is a potent graphical tool meticulously crafted for impedance calculations, with a focused emphasis on the comprehension of reflection coefficients (Γ). It presents a visual depiction that greatly enhances the understanding of impedance matching within electrical circuits. For practical illustration, kindly direct your attention to Figures 2.3.2 and 2.3.3.

Moreover, it's important to note that the reflection coefficients (Γ) can be expressed as (Pozar, 2005; Ulaby, 2007)

$$\Gamma = |\Gamma| e^{j\theta_r} = \Gamma_r + j\Gamma_i \tag{2.3.34}$$

(2.3.35)

where

$$\Gamma_r = |\Gamma| \cos(\theta_r) \tag{2.3.36}$$

$$\Gamma_i = |\Gamma| \sin(\theta_r) \tag{2.3.37}$$

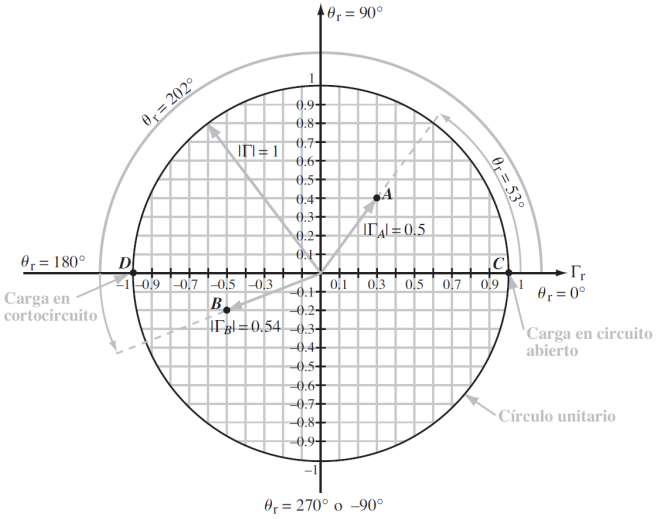

Figure 2.3.2: The complex Γ plane. Point **A** is at $\Gamma_a = 0.3 + j0.4 = 0.5e^{j53^\circ}$, and point **B** is at $\Gamma_B = 0.5 + j0.2 = 0.54e^{j202^\circ}$. The unit circle corresponds to $|\Gamma| = 1$. At point **C**, $\Gamma = 1$, corresponding to an open-circuit load, and at point D, $\Gamma = -1$, Corresponding to a short circuit (Ulaby, 2007)

To effectively utilize the Smith chart, it is essential to normalize the impedance of Γ based on the characteristic of the circuit or transmission line. This involves defining $z_L = Z_L/Z_0$. As a result, the reflection coefficients can be expressed as

$$\Gamma = \frac{Z_L/Z_0 - 1}{Z_L/Z_0 + 1} = \frac{z_L - 1}{z_L + 1} \tag{2.3.38}$$

and z_L

$$\boxed{z_L = \frac{1 + \Gamma}{1 - \Gamma}} \tag{2.3.39}$$

a complex variable that expresses the normalized load's resistance (r_L) and reactance (x_L).

$$r_L = \frac{1 - \Gamma_r^2 - \Gamma_i^2}{(1 - \Gamma_r)^2 + \Gamma_i^2} \tag{2.3.40}$$

$$x_L = \frac{2\Gamma_i}{(1 - \Gamma_r)^2 + \Gamma_i^2}. \tag{2.3.41}$$

For every combination of Γ_r and Γ_i, there exists a corresponding and unique pair of r_L and x_L. When one of the values, either r_L or x_L, is set, a distinctive family of curves emerges for Γ_r and Γ_i, defined by the following equations:

$$\left(\Gamma_r - \frac{r_L}{1+r_L}\right)^2 - \Gamma_i^2 = \left(\frac{1}{1+r_L}\right)^2 \tag{2.3.42}$$

$$(\Gamma_r - 1)^2 + \left(\Gamma_i - \frac{1}{x_L}^2 = \frac{1}{x_L}^2\right) \tag{2.3.43}$$

This approach enables the visualization of the variation of Γ in relation to the characteristic impedance of the transmission line. This variation is depicted through the curves outlined within the Smith chart.

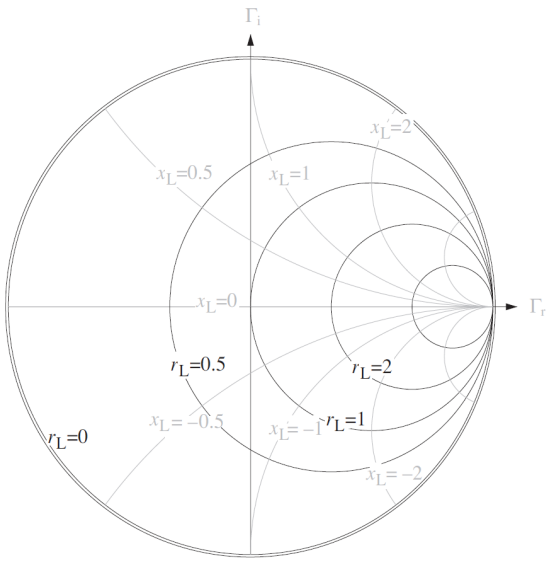

Figure 2.3.3: Families of r_L and x_L circles within the domain $|\Gamma|$ (Ulaby, 2007)

2.3.2.3 Decibel (dB)

The decibel is a mathematical expression used to describe the relationship between two magnitudes. It is commonly employed in circuits to express the linear magnitudes of power, gain, or loss on a logarithmic scale. Typically, milliwatts are used as a reference to express power in logarithmic scale (dBm). (Bowick et al., 2007; Ulaby, 2007; Pozar, 2005).

$$P_{db} = 10\log_1 0\left(\frac{P}{P_0}\right) \tag{2.3.44}$$

where P_0 represents 1 milliwatt. Another equivalent equation, used to express logarithmic potential as a function of voltage or current, is

$$P_{db} = 20 \log_{10} \left(\frac{V}{V_0} \right) \tag{2.3.45}$$

$$P_{db} = 20 \log_{10} \left(\frac{I}{I_0} \right) \tag{2.3.46}$$

where V_0 represents millivolts and A_0 represents milliamperes. It's important to note that if we use a reference magnitude for the input signal in the circuit, the equation can express gains and losses in dB. This concept is utilized in characterizing circuits with respect to a reference signal.

2.3.2.4 Bandwidth

When employing a logarithmic scale to express the transmission spectrum (S_{12}) of a circuit, the term 'Bandwidth' refers to the segment of the spectrum that decreases by -3 dB from its peak value between frequencies f_1 and f_2. The peak value is illustrated in Figure 2.3.4, and this measure is also known as the 'bandwidth at half power'.[2](Bowick et al., 2007; Ulaby, 2007; Pozar, 2005).

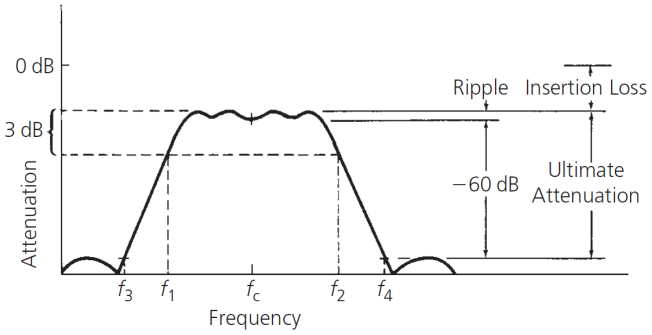

Figure 2.3.4: Practical approximation to a filter response(Bowick et al., 2007).

2.3.2.5 Q-factor

The Q-factor is a measurement of a circuit's selectivity. It is calculated as the ratio of the central frequency of the circuit to its bandwidth. A higher Q-factor

[2]Note: $-3, \text{dB} \approx 10 \log_{10}(0.5)$

indicates better selectivity.(Bowick et al., 2007; Ulaby, 2007; Pozar, 2005).

$$Q = \frac{f_c}{f_2 - f_1} \tag{2.3.47}$$

2.3.2.6 Ripple

The ripple measures gain fluctuations within the bandwidth and is expressed in dB. It is calculated as the ratio between the maximum and minimum values of the gain within the bandwidth. (Bowick et al., 2007; Ulaby, 2007; Pozar, 2005).

$$Ripple = max(G[f_1 - f_2]) - min(G[f_1 - f_2]) \tag{2.3.48}$$

Signal-to-noise ratio (SNR) The Signal-to-Noise Ratio (SNR) is a measure utilized for characterizing the relationship between the power of the signal (P_s) and the noise power (P_n) introduced by the components of the circuit (Bowick et al., 2007; Ulaby, 2007; Pozar, 2005).

$$SNR = \frac{P_s}{P_n} \tag{2.3.49}$$

in dB

$$SNR_{dB} = 10\log\left(\frac{P_s}{P_n}\right) = 10\log(P_s) - 10\log(P_n) \tag{2.3.50}$$

2.3.2.7 Insertion loss (IL)

The Insertion Loss is an indicator of resistive losses and is determined by the maximum gain of the passive chain within the bandwidth.(Bowick et al., 2007; Ulaby, 2007; Pozar, 2005).

$$IL = G_{max}[f_2 - f_1] \tag{2.3.51}$$

2.3.2.8 Noise factor (F)

and noise figure (NF) The noise factor and noise figure describe the SNR degradation at the terminals of any device within a circuit (Bowick et al., 2007; Ulaby, 2007; Pozar, 2005).

$$F = \frac{SNR_i}{SNR_o} \tag{2.3.52}$$

$$NF = 10\log(F) \tag{2.3.53}$$

2.3.2.9 Components noise temperature

The noise factor (F) and insertion loss (IL) of the active and passive components within the system are expressions of the noise they introduce. Expressing these factors in terms of temperature is beneficial, as it allows for the inclusion of the temperature of each component within the system chain.

$$T_e = (F-1)T_0 \tag{2.3.54}$$

$$T_e = (IL-1)T_0 \tag{2.3.55}$$

Here, T_e represents the noise temperature of each component, while T_0 represents the physical temperature of each component. (Bowick et al., 2007; Ulaby, 2007; Pozar, 2005).

2.3.2.10 Friis equation

La ecuación de Friis es posiblemente una de las ecuaciones más cruciales en el diseño de circuitos. Permite el cálculo de la contribución total de la temperatura de ruido del receptor de radio, teniendo en cuenta la distribución de los componentes dentro del sistema de radio (Bowick et al., 2007; Ulaby, 2007; Pozar, 2005).

$$T_R = T_1 + \frac{T_2}{G_1} + \frac{T_3}{G_1 G_2} + ... + \frac{T_n}{G_1 ... G_n} \tag{2.3.56}$$

In this context, T_R signifies the equivalent temperature of the receiver. Meanwhile, T_1, T_2, ..., T_n represent the T_e values of the components, and G denotes the gain or loss associated with each component within the receiver.

2.3.2.11 Output power of the receptor

Finally, building upon the complex analysis presented earlier, the system's output power is calculated using the following equation:

$$P = KT_{sys}G\Delta\nu = K(T_A + T_R)G\Delta\nu \tag{2.3.57}$$

Where T_{sys} stands for the total system temperature, T_A represents the temperature of the antenna, T_R signifies the temperature of the receptor, G denotes the gain, and $\Delta\nu$ corresponds to the bandwidth of the receiver.

2.4 Digital system

The digital system, serving as the Riometer's final component, manages data measurements of signal power derived from the analog system's output. It transforms analog signals into digital format, enabling processing through digital logic. While this text introduces fundamental concepts, it acknowledges the subject's comprehensive nature, limiting an in-depth exploration in line with the project's focus.

However, it's important to note that the chosen technology is the Field-Programmable Gate Array (FPGA), selected for its distinct advantage over other digital hardware due to its modular configuration. This allows modules to synchronize operations using a signal clockan attribute unattainable in hardware like Central Processing Units (CPUs) or graphics processing units (GPUs), which process tasks sequentially (Moss, 2017; Trimberger, 2015; Thomas L. Wilson, 2009; Lizhe Tan Ph.D. Electrical Engineering University of New Mexico, 2018; Maxfield, 2008).

2.4.1 Digital Hardware

In the realm of digital hardware, three crucial components come into play: the analog-to-digital converter (ADC), the FPGA, and a computer designated for the tasks of configuration, compilation, programming, and the management of both the FPGA and ADC. Below, each of these components will be expounded upon.

2.4.1.1 Analog to Digital Convert (ADC)

The ADC, or analog-to-digital converter, is a digital system designed to measure voltage at its input port. The majority of ADCs operate using a common logic structure composed of four key elements: a Comparator, a Digital-to-Analog Converter (DAC), a register, and a control unit, as illustrated in Figure 2.4.1.

The ADC employs the comparator to compare the input signal V_A with the signal

V_{AX} generated by the DAC. This generation is done by utilizing a reference charge stored in the register, under the control of the unit that operates at the signal clock's velocity. This process associates the value of V_A with the value in the register, ultimately generating the digital output value of the ADC. (Moss, 2017).

Hence, the performance of the ADC is determined by the comparator's clock, the

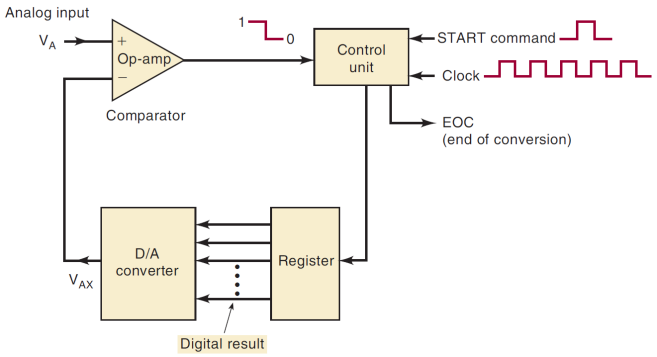

Figure 2.4.1: Graphical illustration of the ADC operation(Moss, 2017).

number of bits in the register (referred to as the sample rate), and the transfer function (illustrated in Figures 2.4.2a and 2.4.2b). These factors collectively define the resolution of the ADC, represented as $C_n = 2^{-N}V_{ref}$, where V_{ref} signifies the reference voltage for the DAC, and N represents the number of bits in the register.

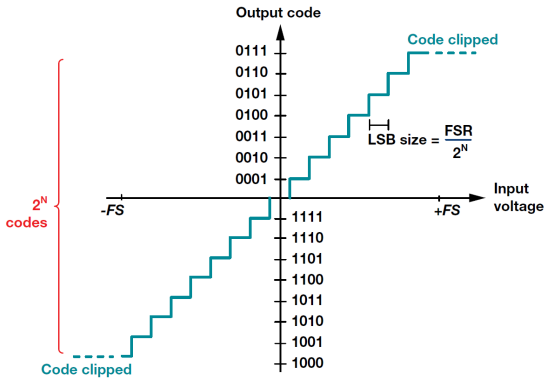

(a) An ADCs ideal transfer function(Lizon, 2020).

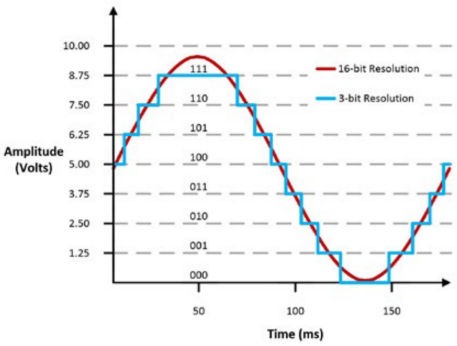

(b) Difference of a Waveform Between 16 Bits and 3 Bits of ResolutionNI (2021)

Figure 2.4.2: ADC performance.

2.4.1.2 Field-Programmable Gate Array

The FPGA (depicted in Figure 2.4.3) exhibits a hierarchical structure primarily comprised of Configurable Logic Blocks (CLBs) and interconnections. These

interconnections encompass external and internal connections to interfaces and supporting sub-systems (Moss, 2017; Trimberger, 2015; Maxfield, 2008). The

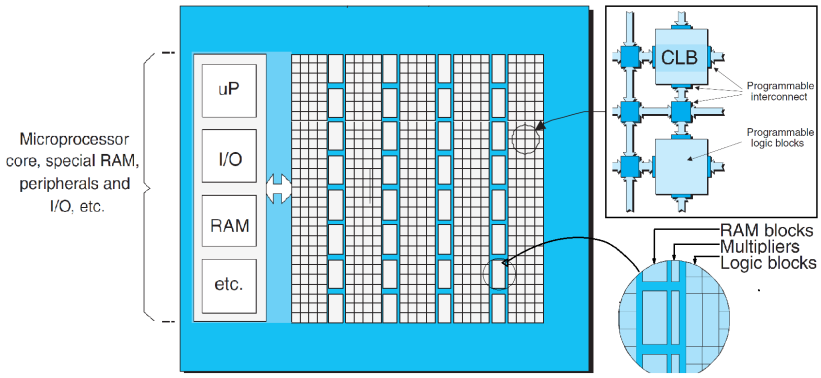

Figure 2.4.3: Simplified diagram of an FPGA. In reality, these are made up of hundreds and even millions of CLBs, accompanied by hundreds to thousands of peripheral support and interface systems.(Maxfield, 2008).

Configurable Logic Block (CLB) is at the core of the FPGA's structure. These CLBs are then subdivided into slices, which, in turn, comprise logic cells, the fundamental processing units within the FPGA (Moss, 2017; Trimberger, 2015; Maxfield, 2008).

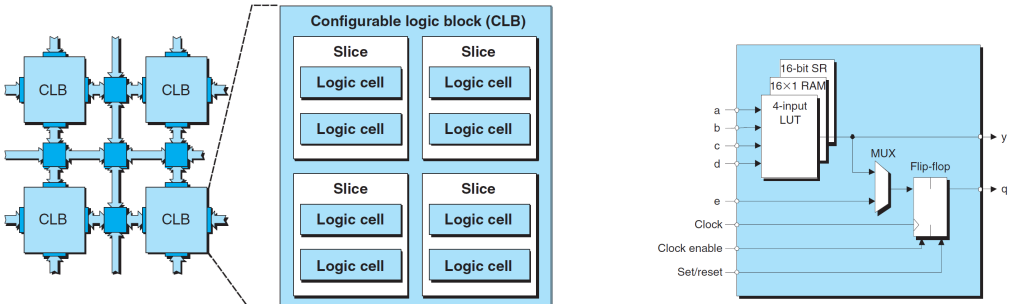

(a) Simplified diagram of an FPGA. Illustrated the composition of the CLBs and their Slices **(b)** Simplified diagram of an FPGA. Illustrating the composition of your Slices.

Figure 2.4.4: FPGA-Slices structure (Maxfield, 2008).

The Logic Cells (LCs) encompass fundamental structures for digital processing, such as Lookup Tables (LUTs), flip-flops, and multiplexers. All these components are managed and synchronized by a master clock and a control switch (enabling and resetting) (Moss, 2017; Trimberger, 2015; Maxfield, 2008).

2.4.1.3 Computer

The chosen FPGA hardware for digital processing is the ROACH2, a platform endorsed by the Collaboration for Astronomical Signal Processing and Electronics Research (CASPER). Its programming and implementation necessitate a specific computer setup and special software configuration, as detailed on the CASPER website. Below, you can find the key points:

- OS ubuntu 16.04/18.04
- matlab 2013a/b
- xilinx tools 14.7
- Python 2.7
- CASPER library

2.4.2 Digital logic

The FPGA hardware is specifically designed for real-time processing, and in this project, its role is to facilitate digital beamforming. This task involves two pivotal calculations. Firstly, there's the Fourier transform. Which needs to be executed for every signal received from the antennas and processed by the analog system. Secondly, determining the phase difference between each of these signals is essential for the overall process and the beamforming algorithms (Arfken, 1985; Griffiths, 2017; Walter Greiner, 1998; Greiner and Bromley, 2000; Pozar, 2005; Rubilar, 2019; G. Rubilar and others., 2020; Ulaby, 2007; Thomas L. Wilson, 2009).

2.4.2.1 The Fourier transform (FT)

The Fourier transform is a mathematical algorithm created by Joseph Fourier in the nineteenth century to convert the representation of a function from one domain to another. In most cases, from the time (t) domain to the frequency domain (ω). They are derived from the 'Fourier series,' which represents an objective function f(t) as a superposition of amplitudes a_ω and b_ω or c_n of the sinusoidal components at the frequency ω (Arfken, 1985; Rubilar, 2019). Meaning,

$$f(t) = \frac{a_0}{2} + \sum_{\omega=0}^{\infty} a_\omega \cos(\omega t) + \sum_{\omega=0}^{\infty} b_\omega \sin(\omega t) \tag{2.4.1}$$

or in a complex formulation with $n \in [-\infty, \infty]$

$$f(t) = \sum_{\omega=-\infty}^{\infty} C_\omega e^{j\omega t} \tag{2.4.2}$$

where

$$C_\omega = \frac{1}{2}(a_\omega - jb_\omega) \tag{2.4.3}$$

$$C_{-\omega} = \frac{1}{2}(a_\omega + jb_\omega) \quad \omega > 0 \tag{2.4.4}$$

$$C_0 = \frac{1}{2}a_0 \tag{2.4.5}$$

and from the orthogonality relation of sine and cosine

$$a_\omega = \frac{2}{T}\int_{-T/2}^{T/2} f(t)\cos(\omega t)dt, \tag{2.4.6}$$

$$b_\omega = \frac{2}{T}\int_{-T/2}^{T/2} f(t)\sin(\omega t)dt, \quad \omega = 0, 1, 2, ... \tag{2.4.7}$$

$$c_\omega = \frac{1}{T}\int_{-T/2}^{T/2} f(t)e^{(-j\omega t)}dt \tag{2.4.8}$$

where f(t) is continued and square-integrable, meaning it satisfies the Dirichlet conditions. The Fourier transform of f(t) is defined as the complex amplitudes of the Fourier series of f(t) for each frequency in the Fourier space. Similarly, the inverse Fourier transform allows us to recover the original function f(t) from its frequency domain representation F() (Arfken, 1985; Rubilar, 2019).

$$\tilde{f}(\omega) \equiv \int_{-\infty}^{\infty} f(t)e^{-j\omega t}dt \tag{2.4.9}$$

And its inverse:

$$f(t) \equiv \int_{-\infty}^{\infty} \tilde{f}(\omega)e^{j\omega t}d\omega \tag{2.4.10}$$

2.4.2.2 Discrete and fast fourier transform

The Fourier Transform (FT) is a powerful tool, but it needs to be discretized to be used in a computer or digital system. To achieve this, it's necessary to consider N

symmetrical time samples (Arfken, 1985; Rubilar, 2019; Cooley and Tukey, 1965)

$$t_k = \frac{kT}{N}, \quad k = 0, 1, 2, ..., (N-1) \tag{2.4.11}$$

The orthogonality relations of sine and cosine are preserved, allowing the spectral frequencies in the symmetrical space of the transform to be defined as:

$$\omega_p = \frac{2\pi p}{T}, \quad p = 0, 1, 2, ..., (N-1) \tag{2.4.12}$$

However, the transform is from -T/2 to T/2, and the output frequencies range from -ω/2 to ω/2, or just 0 to ω/2, due to the symmetry of the FT and the Nyquist Theorem.

$$F(\omega_p) = \frac{1}{N} \sum_{k=0}^{N-1} f(t_k) e^{-j\omega_p t_k} \tag{2.4.13}$$

And its inverse:

$$f(t_k) = \frac{1}{N} \sum_{k=0}^{N-1} F(\omega_p) e^{j\omega_p t_k} \tag{2.4.14}$$

When given N time samples t_k or N frequency samples ω_p, N^2 computations (sine and cosine calculations) are needed to obtain the FT results. However, by leveraging the parity of sine and cosine functions along with segmentation and computation reduction of repetitive calculations in the process, it's possible to reduce the computation complexity to $Nlog(N)$. This algorithm is known as the Fast Fourier Transform (FFT), and it is implemented using a butterfly algorithm based on graph theory to solve the assignment problem of the transformation. (Cooley and Tukey, 1965) .

2.5 Noise and Efficiency of the receiver

The previous section illustrates the ideal performance of a radiometric system. However, in reality, the situation is distinct due to the presence of intrinsic noise that modify and constrain the system's performance (Pozar, 2005; Thomas L. Wilson, 2009; Kendal and Jørgensen, 2011; Cohen, 1982).

2.5.1 Radiometer equation

The Radiometer equation defines the minimum detectable temperature value, denoted as ΔT_{rms} o σ_T, that the system can measure. This relationship is contingent upon several parameters: the system's temperature (T_{sys}), the total gain (G) and its variation (ΔG), the integration time (τ), and the reception bandwidth ($\Delta\nu$) (Thomas L. Wilson, 2009; Allan, 1987; D.B. Sullivan, 1990).

$$\sigma_\tau = \Delta T_{RMS} = T_{sys}\sqrt{\frac{1}{\tau\Delta\nu} + \left(\frac{\Delta G}{G}\right)^2} \tag{2.5.1}$$

In this context, ΔG is the result of the product of voltage, current, and temperature variations within the analog system. τ represents the integration time determined by the digital system, while $\Delta\nu$ characterizes the bandwidth of the analog system.

To determine the optimal integration time (t_m) for the system, a prevalent approach involves performing a linear fit of the Gain, expressed as $(\Delta G/G)^2 = \gamma_0 + \gamma_1\tau$.

$$\tau_m = \frac{1}{\sqrt{\gamma_1\Delta\nu}} \tag{2.5.2}$$

2.5.2 Electronic noise

The electronic noise in a radiometric system originates from four primary sources. Some of these sources are linked to environmental conditions, while others have an unidentified origin. (Kendal and Jørgensen, 2011; Thomas L. Wilson, 2009; Cohen, 1982).

- Thermal noise is generated by the thermal agitation of charged particles within the circuit.
- Shot noise is a phenomenon characterized by a Poisson distribution and is

associated with fluctuations in the flow of electric charge in a current.

- Pink noise, also known as 1/f noise, is a type of noise characterized by a frequency dependence and environmental conditions, yet lacking a known identifiable source.
- G-R noise is noise related to the fluctuations of charge carriers moving between the valence and conduction bands.

Figure 2.5.1 represents all analogical noise types, which can vary between different technologies while still exhibiting typical behaviors.(Thomas L. Wilson, 2009; Cohen, 1982; Kendal and Jørgensen, 2011; Cohen, 1982).

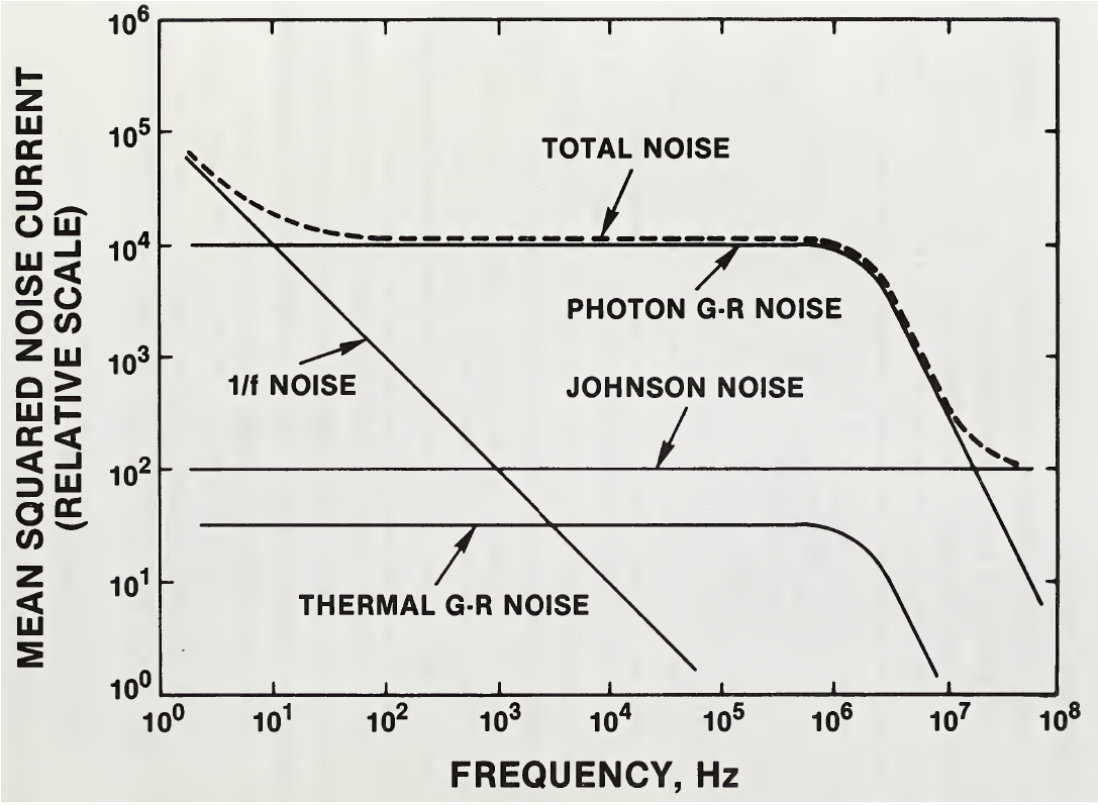

Figure 2.5.1: Illustration of the contribution of various noise sources to spectral noise (Cohen, 1982).

2.5.3 Digital noise

Digital noise arises from both the signal and the noise inherent in the analog system's output during the process of digitization. In this context, the limitations posed by the number of bits (n-bit) and the digitization frequency define the

minimum noise floor and shape the digital system's ability to differentiate between high and low frequencies, as governed by the Nyquist theorem. This phenomenon leads to the emergence of various noise types, encompassing aliasing, input-referred noise and Noise-Free (Flicker-Free) noise. The information about each type of noise can be found in the references mentioned Kester (2006a); Lizon (2020); NI (2021). Since our primary objective is to determine the system's noise floor, more detailed explanations will be presented below.

2.5.3.1 Noise floor

The cumulative noise contribution can be visualized through the power spectral density, which is indicative of the system's noise floor. This is characterized in relation to the number of bits (N) and the effective number of channels (M/2) within the digitizer's frequency range ($f_s/2$), as depicted in the figure.

$$SNR = 6.02N + 1.76 + 10log_{10}\left(\frac{M}{2}\right) \ [dB] \tag{2.5.3}$$

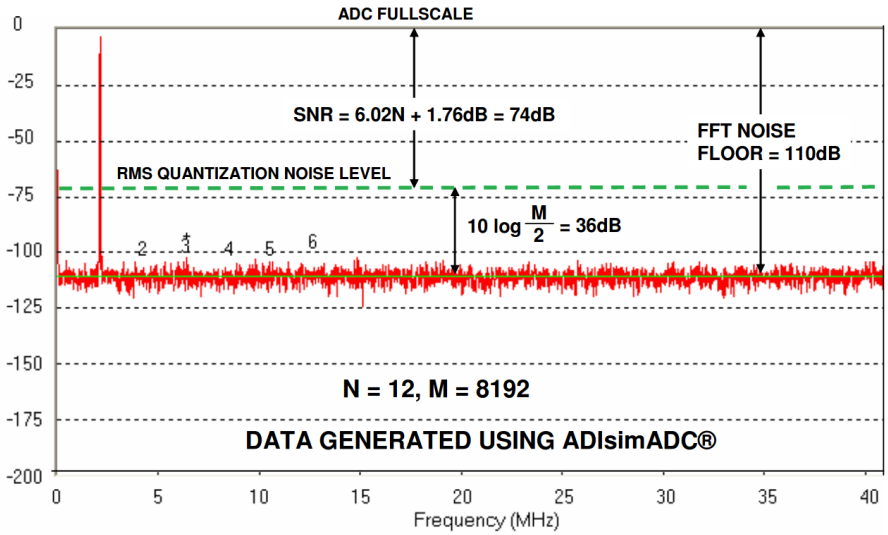

Figure 2.5.2: FFT output data for a 12-Bit ADC deal, an input signal at 2.111MHz, f_s = 82MSPS, 5 averages of FFTs and M = 8192Kester (2006b)

Chapter 3

ISI-RIOMETER develoment

This chapter provides an in-depth overview of the methodology employed to calculate, simulate, fabricate, program, and implement each component of the ISI-RIOMeter. It begins by offering detailed insights into the analysis, calculation, and simulation of the antenna array. Subsequently, it delves into the intricacies of designing the analog receptor, incorporating simulation, fabrication, and characterization processes. The chapter then advances to encompass the configuration, implementation, and characterization of the digital system ROACH 2. Finally, it concludes by presenting data measurements of the Cosmic Radio Noise (CRN) alongside images generated through beamforming techniques at the array's location.

3.1 Antenna

The antennas within the array have undergone extensive examination, beginning with fundamental principles. The initial phase included calculating the parameters for a single element using a numerical approach in both Matlab and Python. Subsequently, comprehensive simulations were conducted using the FEKO software, which employed the Method of Moments (MOM) to solve the Maxwell equations for the entire array. Consequently, the software generated parameters for diverse distributions and quantities of elements.

3.1.1 Ideal dipole

The antennas employed in the array are half-wavelength dipoles. This configuration entails two conductive arms with a combined length equivalent to half of the spatial and temporal resonant frequency wavelength (Thomas L. Wilson, 2009; Ulaby, 2007; Pozar, 2005).

3.1.1.1 Analytical solution

Solving for the retarded potential $\tilde{A}(R)$ generated at a point $Q(R, \theta, \phi)$ by the dipole connected to a source operating at a frequency of $\omega = 38$ MHz.

$$\tilde{A}(R) = \frac{\mu_0}{4\pi} \int_v' \frac{\tilde{J} e^{-jkR}}{R} dv' \tag{3.1.1}$$

Taking into account the z-y plane or when $\phi = 90$ (Fig. 3.1.1)

This is defined as a surface current density $\tilde{J}$ over the dipole arms with a length of $z = \pm\lambda/4 = \pm 1.873$, where $k = 2\pi/\lambda$, and it is generated by the source within the conductor.

$$\tilde{J} = \hat{z}\tilde{I}/s, \tag{3.1.2}$$

$\tilde{I}$ represents the current generated by the source and can be defined as the real part of a phasor.

$$\tilde{I} = i(t) = \Re e[I_0 \cos(kz) e^{j\omega t}] = I_0 \cos(kz) \cos(\omega t) \tag{3.1.3}$$

By employing equation 2.2.2, we derive the phasor of the retarded potential $\tilde{A}(s)$ at a distance 's' from each segment (dz) of the antenna, with respect to the point $Q(R, \theta, \phi)$, in the following manner:

$$\tilde{A}(s) = \hat{z} \frac{I_0 \cos(kz) \mu_0}{4\pi} \frac{e^{-jks}}{s} l \tag{3.1.4}$$

Where $\frac{e^{-jks}}{s}$ represents a propagation factor that indicates the linear decay of the field and phase variations with distance. Utilizing the spherical coordinate system

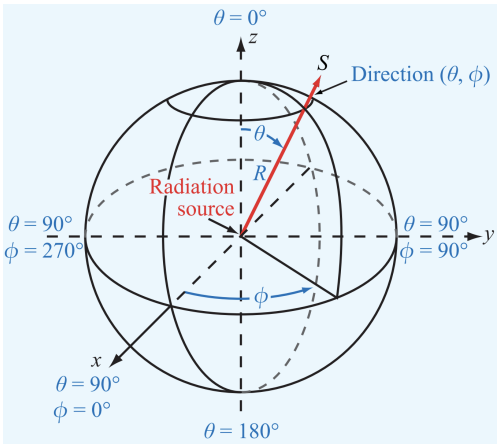

(a) Spherical and cartesian coordinate system

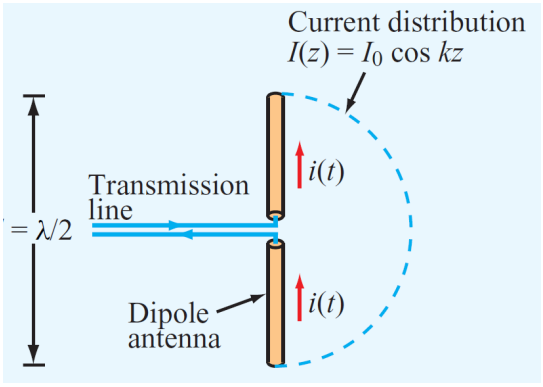

(b) Dipole in the plane z-y

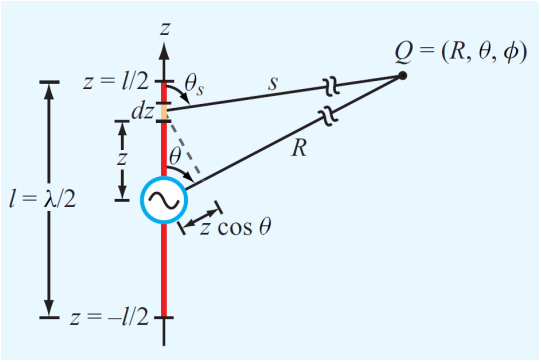

(c) representation of the dipole in the plane z-y and the point Q.

Figure 3.1.1: Cartesian and spherical coordinate system, used for the representation of the antennas and the generated fields with respect to the referent system(Ulaby, 2007).

(R, θ, ϕ), we can express $\tilde{A}(s)$ as follows:

$$\tilde{A}_R = \frac{I_0 \mu_0 l}{4\pi} \cos(kz) \cos(\theta) \frac{e^{-jks}}{s} \tag{3.1.5}$$

$$\tilde{A}_\theta = -\frac{I_0 \mu_0 l}{4\pi} \cos(kz) \sin(\theta) \frac{e^{-jks}}{s} \tag{3.1.6}$$

$$\tilde{A}_\phi = 0. \tag{3.1.7}$$

from which we obtain the value of the electric and magnetic field using the

equations 2.2.3 y 2.2.4 in the far field approximation ($s = R - z\cos(\theta)$) as

$$\tilde{H}_\phi = \frac{-jI_0}{2\pi}\left[\frac{\cos(\pi/2\cos(\theta))}{(\theta)}\right]\left(\frac{e^{jkR}}{R}\right), \tag{3.1.8}$$

$$\tilde{E}_\theta = \frac{j\eta_0}{2\pi}\tilde{I}_0\left[\frac{\cos(\pi/2\cos(\theta))}{(\theta)}\right]\left(\frac{e^{-jkR}}{R}\right), \tag{3.1.9}$$

which means that the power density, as defined in equation 2.2.5, is

$$S(R,\theta) = \frac{\eta_0\tilde{I}_0^2}{2\pi R^2}\left[\frac{\cos(\pi/2\cos(\theta))}{(\theta)}\right] \quad (W/m^2) \tag{3.1.10}$$

defining $S_0 = \frac{\eta_0\tilde{I}_0^2}{2\pi R^2}$

$$S(R,\theta) = S_0\left[\frac{\cos(\pi/2\cos(\theta))}{(\theta)}\right]^2 \quad (W/m^2) \tag{3.1.11}$$

and the normalized radiation pattern

$$P(\theta,\phi) = \left[\frac{\cos(\pi/2\cos(\theta))}{(\theta)}\right]^2 \tag{3.1.12}$$

Graphing the solution of the equation (Fig. 3.1.2) in the θ plane at the $\phi = 90$ cut, the blue line represents it, and the red segmented line indicates the Full Width at Half Maximum (FWHM) of approximately 78 degrees. The directivity and gain are 1.64 or 2.15 dB, the radiation resistance is 73 Ω, and the effective aperture is 7.33087 [m^2].

All the results obtained from calculations and antenna parameters are presented in Table 3.1.1.

3.1.1.2 Software solution

The FEKO software empowers us to define the three-dimensional geometry of the antenna and its associated electrical parameters. Additionally, the software allows us to establish a mesh to discretize the space and subsequently integrate the response of each infinitesimal mesh division (Fig. 3.1.3). Finally, the software uses this information to solve the equations and provide us with information about the electromagnetic field E, the Gain, the Directivity, and the scattering parameter S_{11} of the antenna in the far-field.

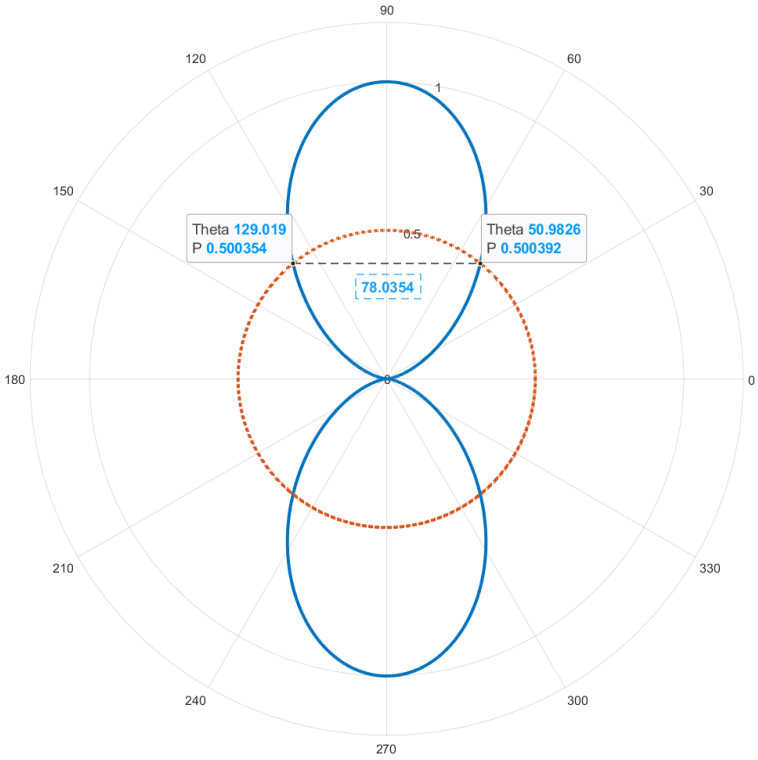

Figure 3.1.2: Polar graph of the radiation pattern of the dipole with cut in $\theta = 0$, self-made source matalabR2021a

Parameter	Value	Parameter	Value
λ	7.89 [m]	Antenna length	3.95 [m]
Center frequency	38 MHz	Arm length L($\lambda/4$)	1.97 [m]
Directivity	1.64	Arm length R($\lambda/4$)	1.97 [m]
ξ	1	FWHM	78.0354°
Gain	1.64	Effective aperture g	8.12 [m^2]
G and D [db]	2.15	Directivity	2.15 [m^2]

Table 3.1.1: Summary table of the arithmetic calculations of the parameters of a dipole antenna of $\lambda/2$

Continuing with the same methodology used for the numerical solution, an antenna was constructed comprising two copper conductor arms, each measuring $\lambda(37.075MHz)/4 = 1.972$ meters in length (yellow line). These arms are connected to the balanced source terminals (red and blue) across frequencies ω ($[0.38 - 224]$ MHz)[1].

[1]All simulation results are provided in the appendix 5

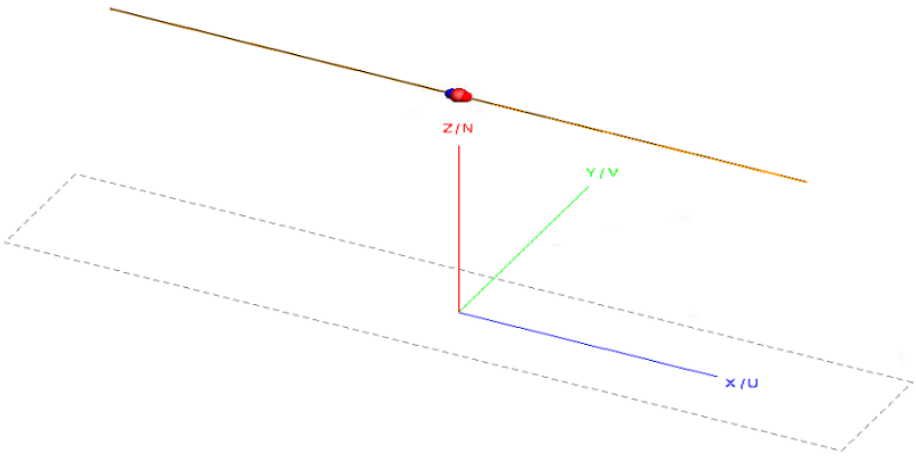

Figure 3.1.3: Graphic representation of the geometric structure of the dipole antenna, FEKO v2020.

The simulation outcomes offer insights into the antenna's behavior. The radiation pattern is visualized at the central frequency of the design through gain graphs (3.1.4 and 3.1.5). The magnitude of antenna mismatch is displayed across frequency points within the source bandwidth using the scattering parameter S_{11} graph (3.1.6). Furthermore, the ϕ and θ cuts of the gain graph for the frequency point with the best mismatch exhibit the antenna's FWHM in both ϕ and θ dimensions.

A comprehensive summary of the primary antenna parameters at the frequency ω = 37.075 MHz can be found in Table 3.1.4. The comparison between these results and the analytical solution highlights the suitability of the software for advancing the simulation.

Parameter	Value	Parameter	Value
λ	8.086 [m]	Antenna length	3.9445 [m]
ω	37.075 MHz	Arm length L(λ/4)	1.972 [m]
D	1.63734	Arm length R(λ/4)	1.972 [m]
ξ	1	FWHM θ y $\phi = [0, 90]$	[78.2378,78.2378] °
G	1.63734	FWHM ϕ	360°
Power at 1V	27.7718 [mW]	Effective opening	8.51915 [m^2]

Table 3.1.2: Summary table of the results obtained for the dipole $\lambda/2$ in Feko 2020.

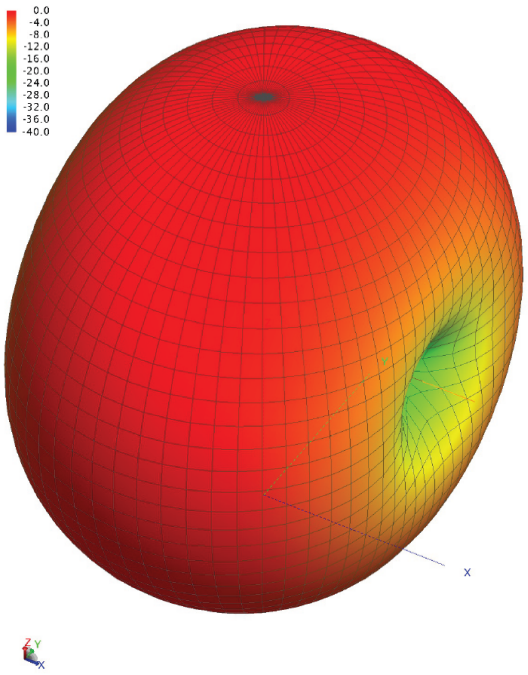

Figure 3.1.4: Gain results for the geometric structure of the ideal dipole, FEKO v2020.

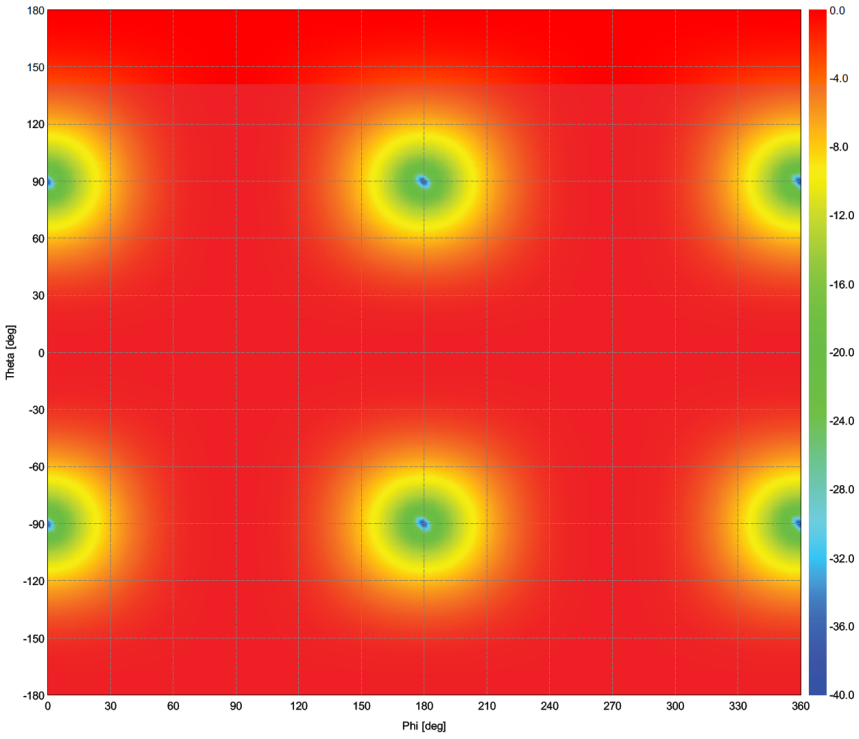

Figure 3.1.5: Normalised gain results in the θ, ϕ plane for the geometric structure of the ideal dipole, FEKO v2020.

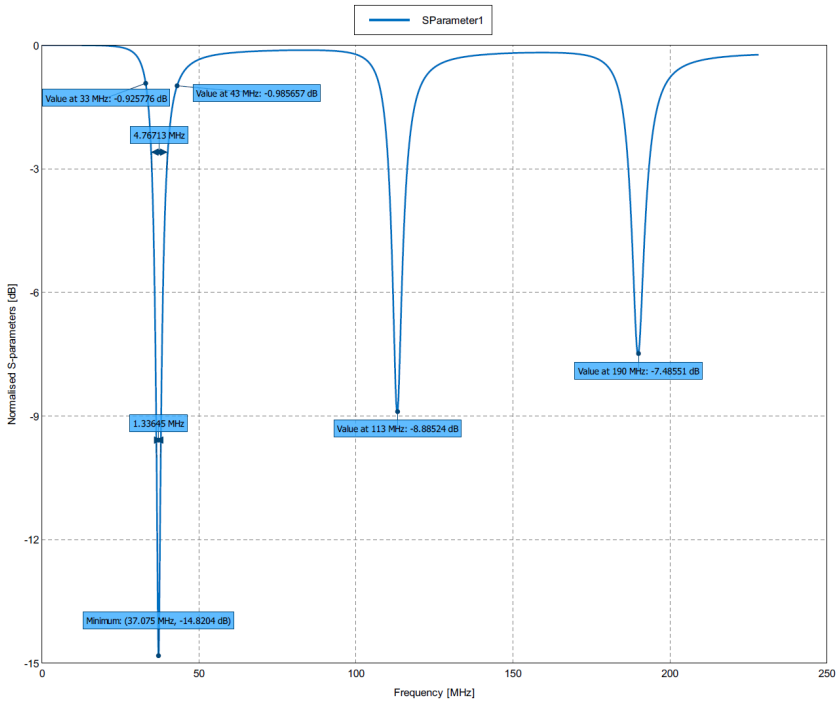

Figure 3.1.6: Results of the scattering parameters of the ideal dipole, FEKO v2020.

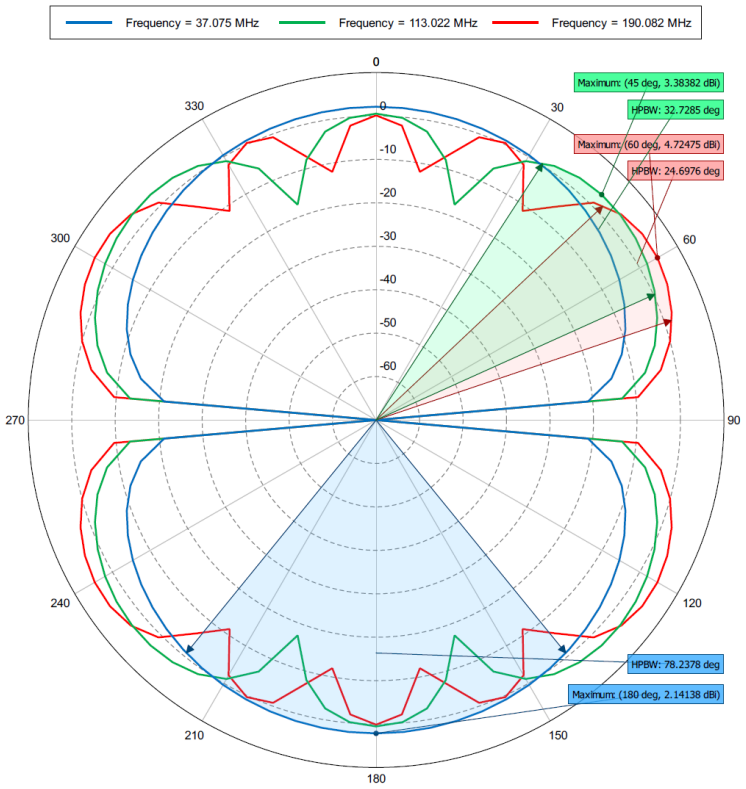

Figure 3.1.7: Result in the $\phi = 0$ axis of the gain for the geometric structure of the ideal dipole, FEKO v2020.

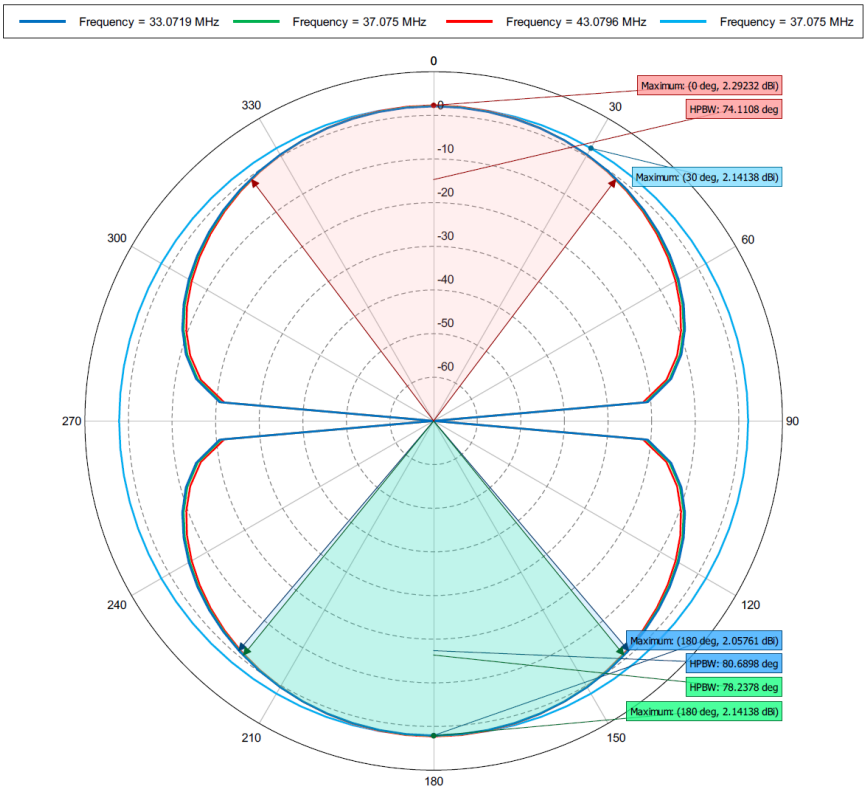

Figure 3.1.8: Results of the cut in the axis $\phi = 0$ (blue, green, red) and $\phi = 90$ (calypso) of the gain for the geometric structure of the ideal dipole, FEKO v2020.

3.2 Antenna Array

The successful execution of the project hinged on characterizing and simulating an antenna array that had been installed by Professor Foppiano. This array is arranged in a square pattern, rotated at a 45-degree angle with respect to the X-axis, as visually depicted in figures 3.2.1 and 3.2.2. The separation between antennas measures approximately $\lambda/2$, roughly equivalent to 1.97 meters. Furthermore, each antenna maintains a consistent elevation length. Notably, a critical aspect of this configuration is the adaptation of each individual antenna to a 50-ohm impedance through the implementation of a balun.

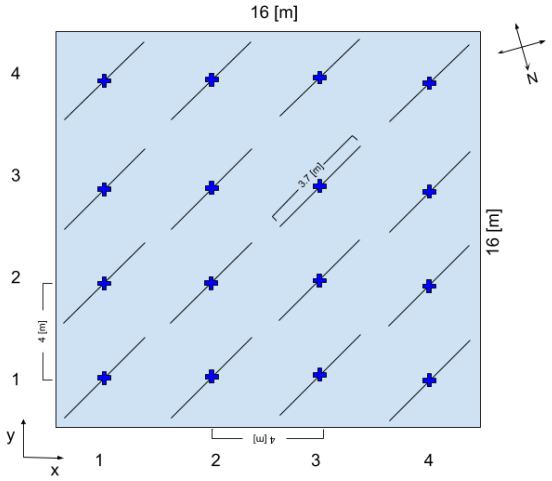

Figure 3.2.1: Element distribution (-36.84°S, -73.03°W).

Figure 3.2.2: Photograph of the array (-36.84°S, -73.03°W)

3.2.1 Characterization

The antennas, having a length of $\lambda/2$ (as shown in 3.2.3), are meticulously crafted using two copper cables, each with a diameter of 5mm. The extension of 1.92 meters is carefully allocated to each of the dipole arms (enclosed within the yellow box). These arms are subsequently linked to a balun model BL-40X (encased in the red box). This integration of a balun serves the dual purpose of achieving line balance and fine-tuning the antenna's impedance to the requisite 50 ohms. This impedance alignment is a prerequisite before the antennas can be seamlessly integrated into the coaxial transmission line.

Furthermore, an augmentation in the form of a dielectric extension, depicted by the green box, has been thoughtfully introduced across the arrays. This strategic extension serves a dual role: firstly, it provides augmented structural reinforcement to the antennas, and secondly, it proves instrumental in effectively absorbing lower frequencies, enhancing the overall performance of the setup.

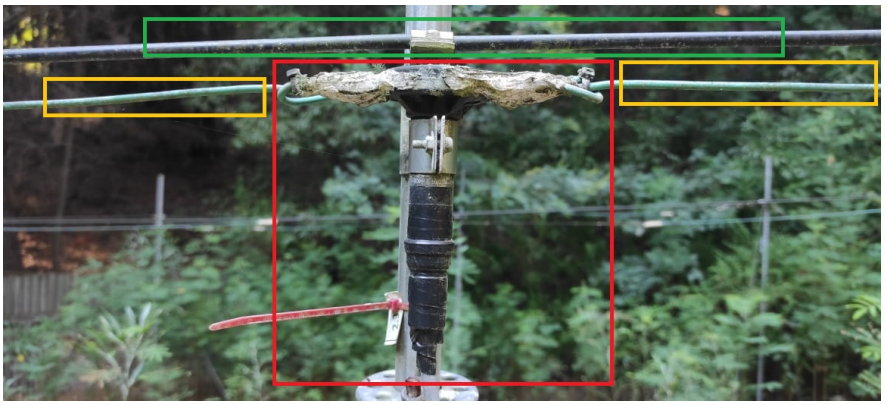

Figure 3.2.3: Photograph of the balun

The characterization of the antennas involves conducting two distinct measurements, each utilizing a different type of Vector Network Analyzer (VNA). Specifically, the measurements are performed using a FieldFox/Keysight model N9918A and a nanoVNA, as depicted in figure 3.2.4.

The initial measurement involved capturing the spectral power received by the antenna while the galaxies were positioned at the zenith, maximizing radiation. This measurement was conducted on February 4, 2021, at 1:01:39 PM (as illustrated in Fig. 3.2.5). The FieldFox VNA was employed in its spectrum analyzer mode, with a channel bandwidth of 65 KHz, a gain of 40dB, and a frequency range

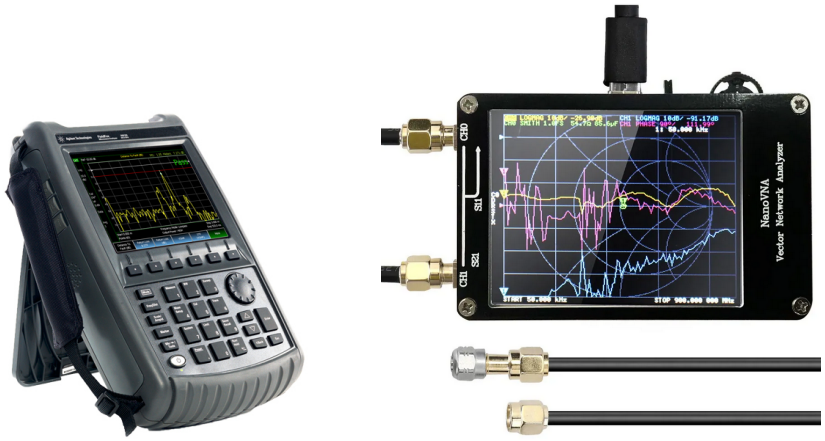

Figure 3.2.4: On the right the vector network analyzer model N9918A and on the left the NanoVNA

spanning from 0 to 80 MHz.

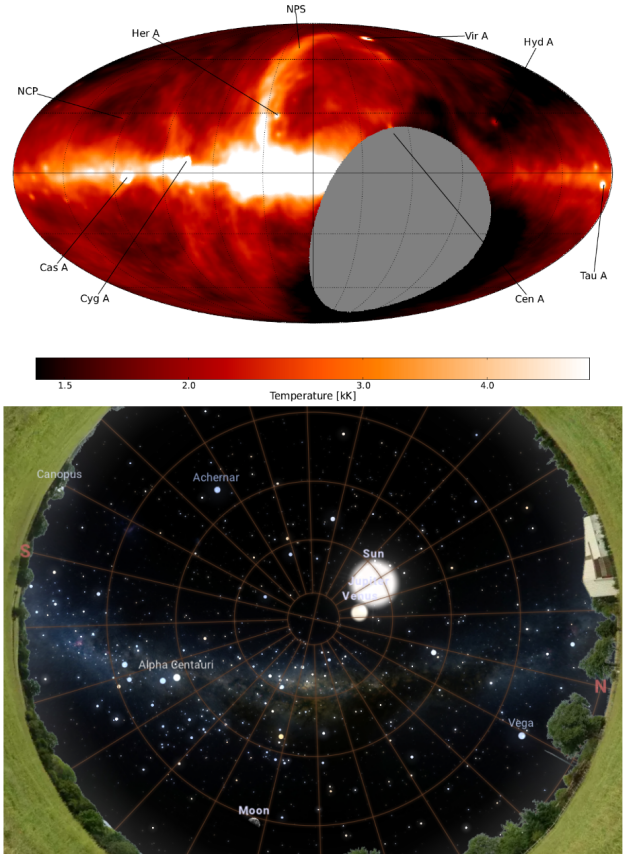

Figure 3.2.5: Comparative images of the CRN radiation and the position of the galaxy at the time of observation(Dowell et al.(2017) y Stelarium v2020)

.

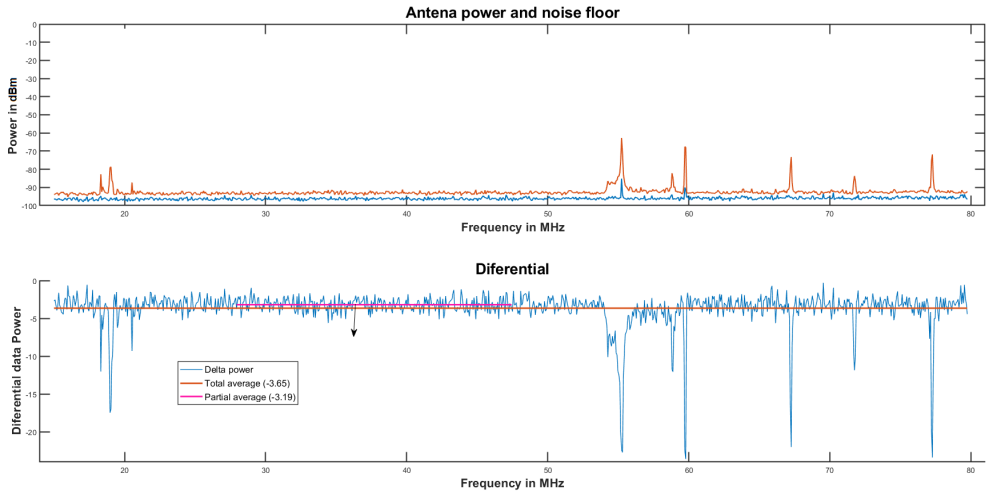

Figure 3.2.6: Spectral power measure using the FieldFox/keysight Vector network analyzer model N9918A

The results of this measurement are shown in figure 3.2.6. The VNA configuration generates a noise floor of -96.1127 dBm when connected to a 50-ohm load. When the antenna is connected to the VNA, the spectral power increases to a mean of -92.4607 dBm. Within the band of interest, the spectral power further increases to -92.9227 dBm, which closely approximates the expected value of -93.036 dBm for the maximum galaxy signal at Zenith.

The second measurement involved assessing the return loss, quantified through the spectral parameter S_{11}, utilizing a nano-VNA. The configuration allowed measurements across a bandwidth of 0 to 85 MHz, employing a spectral resolution of 600 KHz. The resulting graphs are labeled as 3.2.7, 3.2.8, 3.2.9, and 3.2.10, with the antenna's arrangement corresponding to columns along the x-axis, as depicted in figure 3.2.1.

The graphs illustrate that the antenna is well-tuned, particularly within the frequency range of 33 to 43 MHz. In this range, the return loss decreases to approximately -10 dB, indicating effective impedance matching, and about 90% of the signal is either integrated or transmitted.

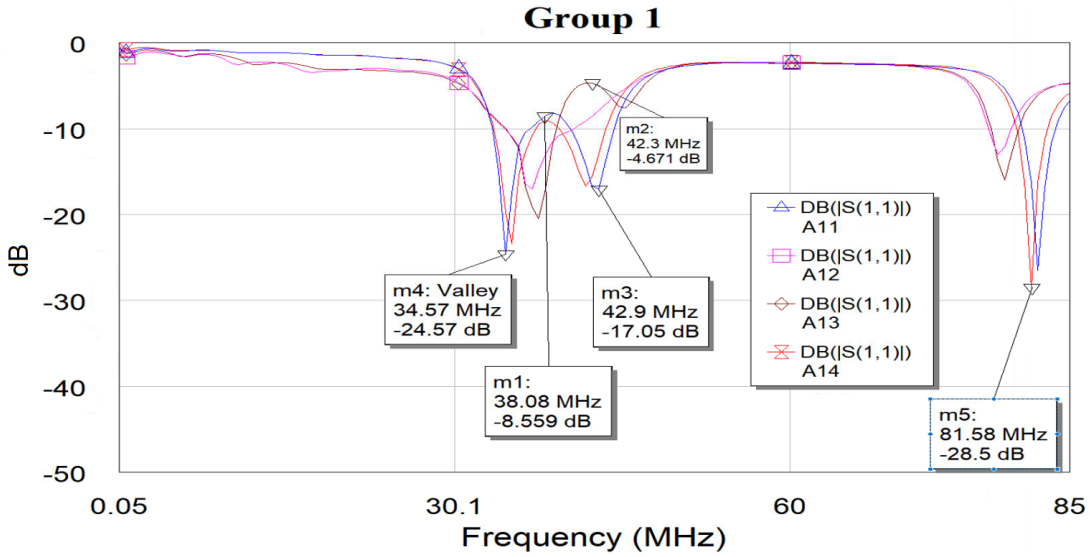

Figure 3.2.7: Spectral parameters S_{11} group 1 .

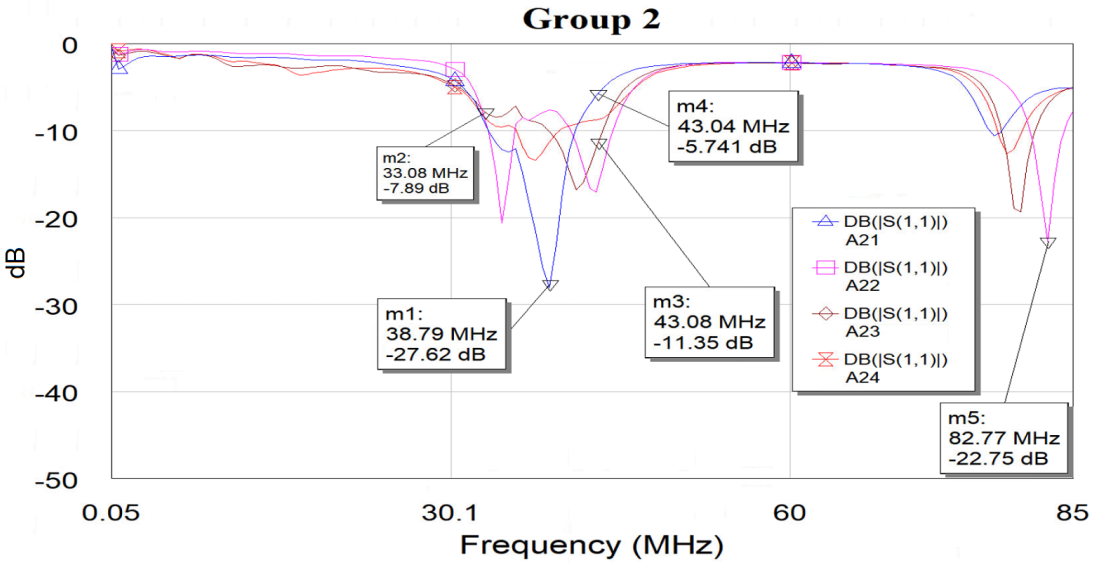

Figure 3.2.8: Spectral parameters S_{11} group 2.

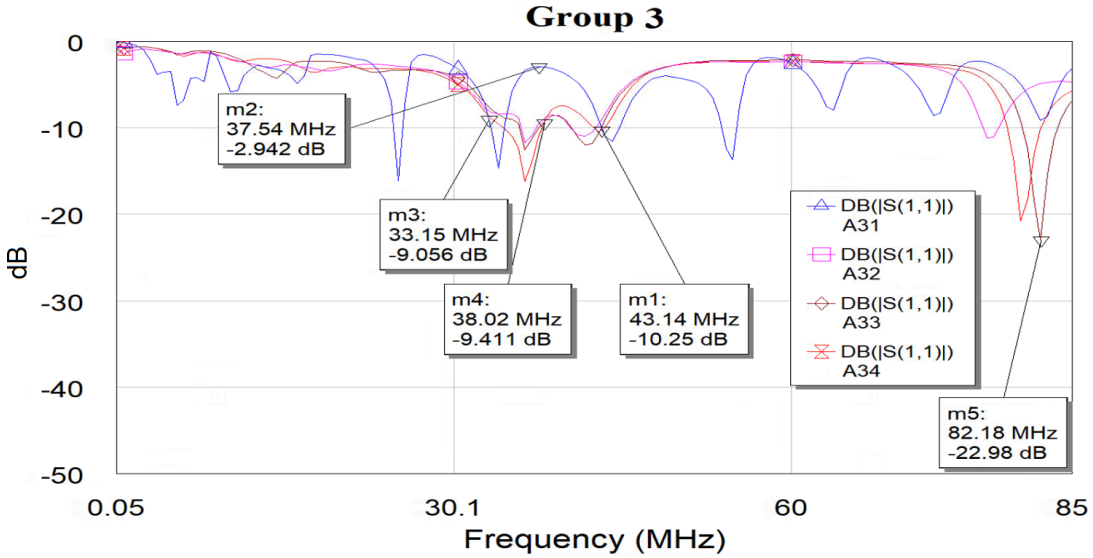

Figure 3.2.9: Spectral parameters S_{11} group 3.

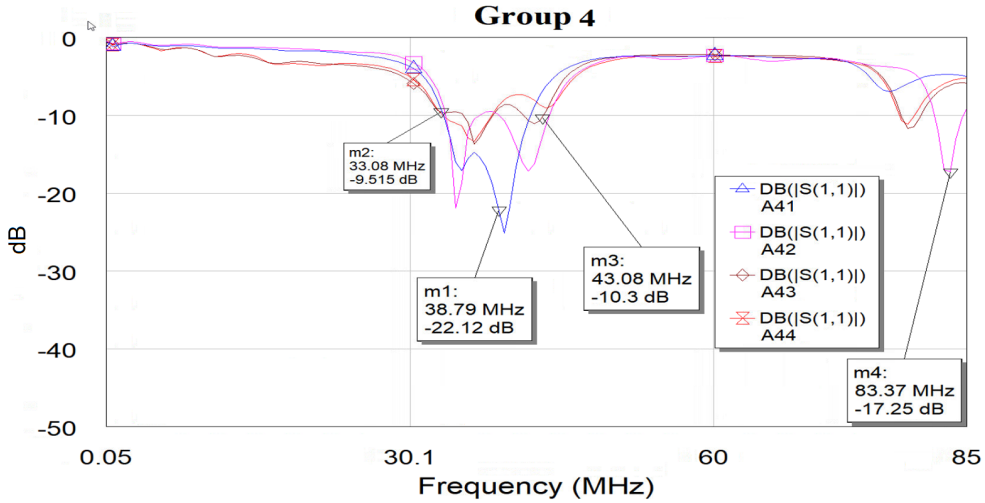

Figure 3.2.10: Spectral parameters S_{11} group 4.

3.2.2 Antenna array simulation

I conducted a complete simulation of the array using FEKO software. Taking into account one, fourth, and sixteenth elements and their distribution in a quadratic shape of 4 by 4. The simulation uses a source with a spectral bandwidth of [0.38-224] MHz and performs the beamforming using the calculations of M.T.Ma (1974) and Barott et al. (2011) for the array and different points of view.

3.2.2.1 One element

The simulation of a single element forms the foundation for comprehending the electric and radiometric performance of the antennas within the array. Figure 3.2.11 provides an illustration of the dipole and its spatial distribution. In this illustration, the copper calypso lines depict the conductor cable, the orange circle represents the source, the red and blue circles symbolize the electrical terminal connectors of the antenna, and the plain ochre background signifies the electrical ground plane.

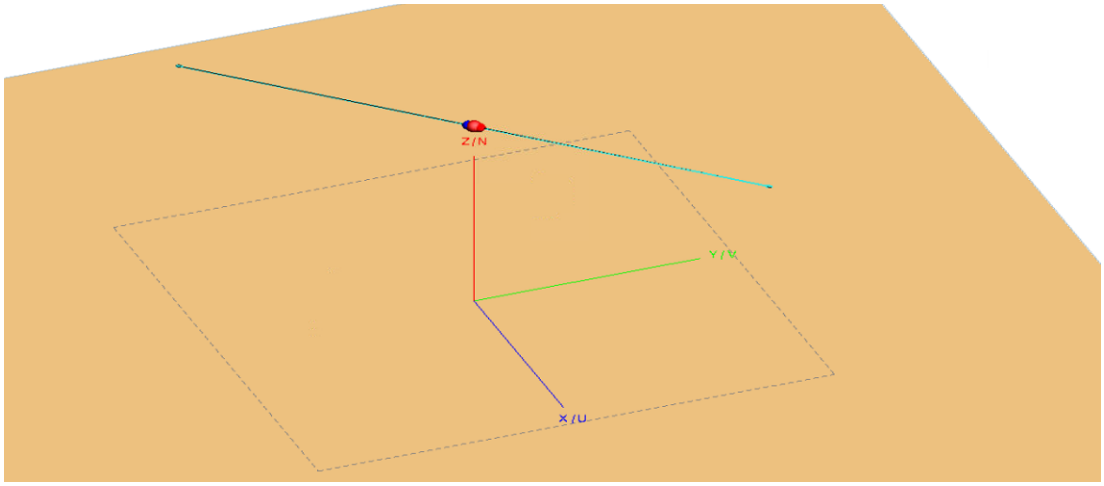

Figure 3.2.11: Graphical representation of the dipole in the FEKO software v2020.

All the results from this simulation are available in appendix 5. The most relevant results are presented below, including the gain graphs in three dimensions (3.2.12) and two dimensions (3.2.13), the scattering parameters S_{11} (3.2.14), the $\phi = [0, 90]$ cuts for the frequencies of interest (3.2.12 and 3.2.16), and a summary of the principal simulation parameters at approximately 38.1 MHz, as outlined in table 3.2.4.

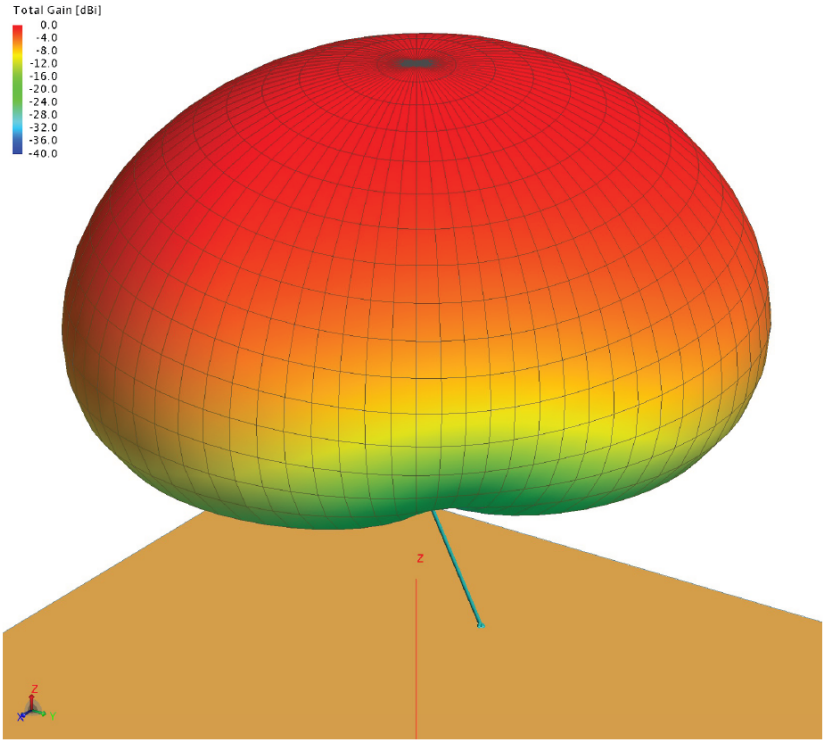

Figure 3.2.12: Gain results for the geometric structure of the real dipole, FEKO v2020.

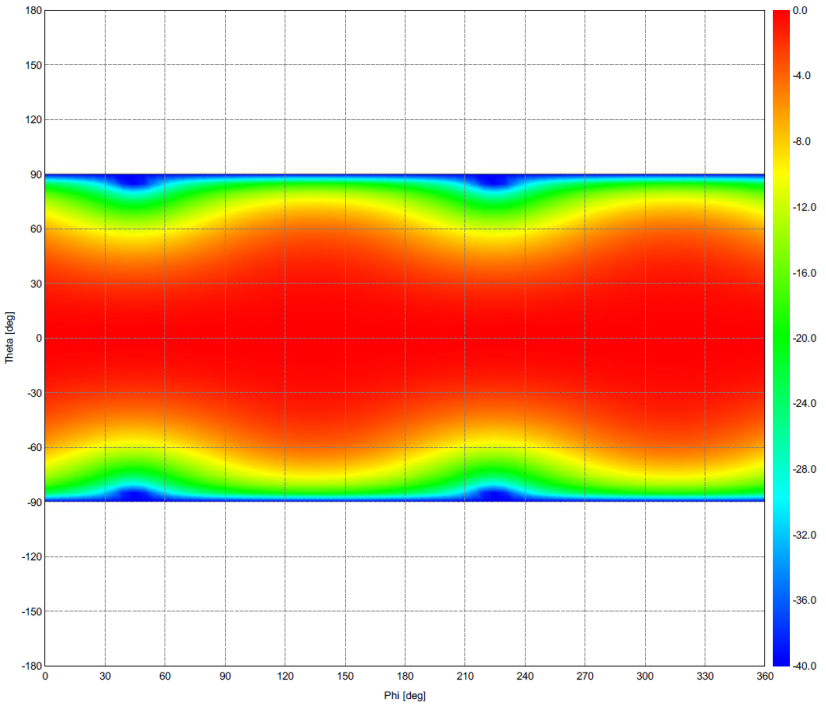

Figure 3.2.13: Normalised gain results for the geometric structure of one real dipole in the plane θ, ϕ FEKO v2020.

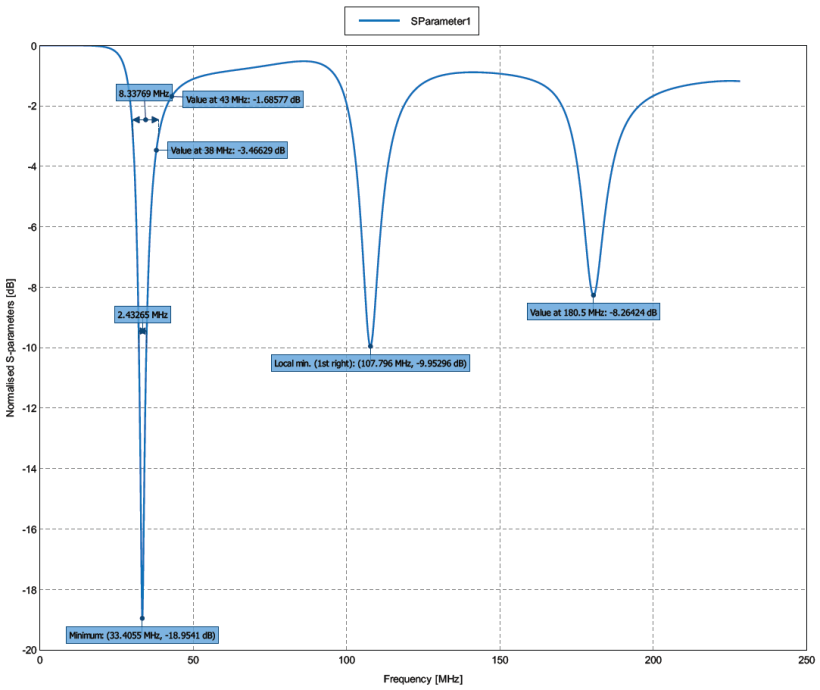

Figure 3.2.14: Results of the scattering parameters S_{11} of the real dipole, FEKO v2020.

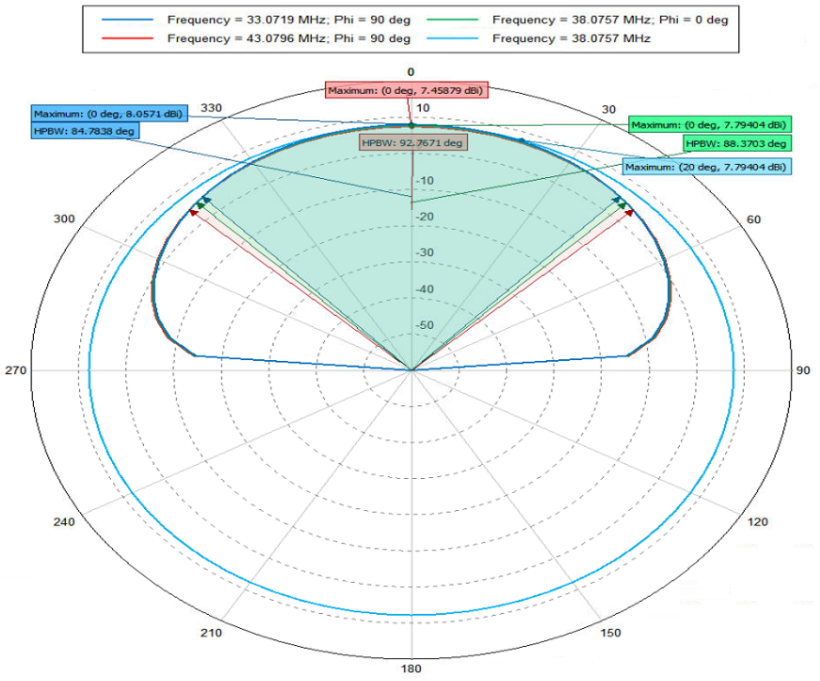

Figure 3.2.15: Results in the axis $\phi = 0$ (blue, green, red) of the gain of the real dipole, FEKO v2020.

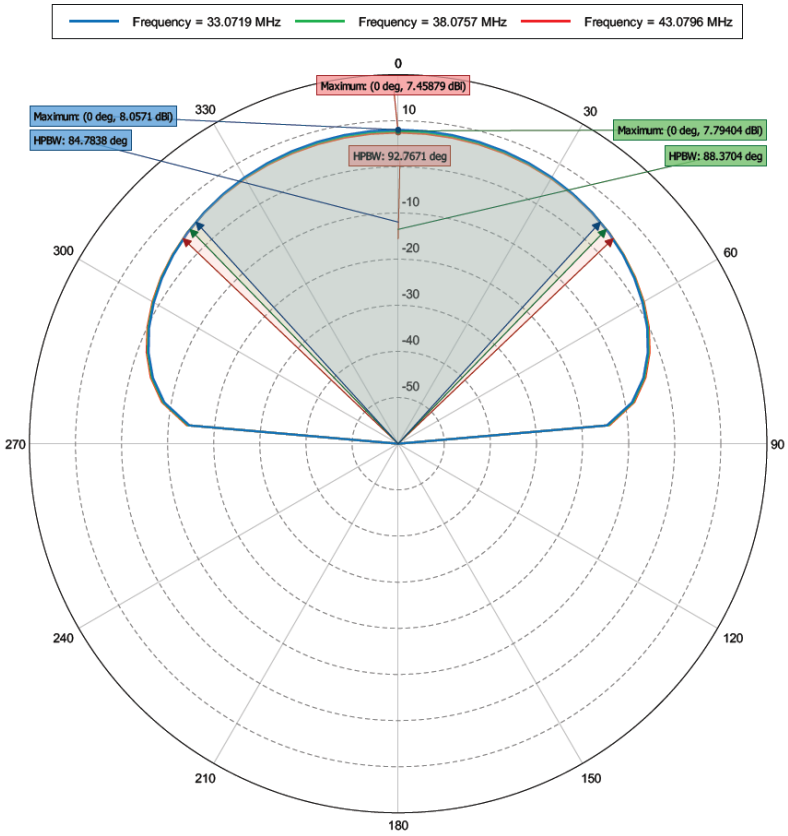

Figure 3.2.16: Results in the axis $\phi = 90$ (blue, green, red) of the gain of the real dipole, FEKO v2020.

Parameter	Value	Parameter	Value
λ	7.8735 [m]	Antenna length	3.81 [m]
ω	38.07575 [MHz]	Arm $\leftarrow$	1.83 [m]
D	7.79404	Arm $\rightarrow$	1.83 [m]
ξ	1	FWHM θ y $\phi = [0.90]$	88.3703° y 88.3704°
Gain (G)	7.79404	FWHM ϕ	360 [m^2]
Power	2.06636 [mW]	Effective opening	31.7271[m^2]

Table 3.2.1: Summary table of the results obtained for an element of the array.

3.2.2.2 Four elements simulation

By increasing the number of antennas to four and employing the beamforming technique to combine each of their individual responses (3.2.17), the simulation reveals alterations in the electrical and radiometric parameters within the far-field.

All the results of this simulation can be found in appendix 5. The most relevant

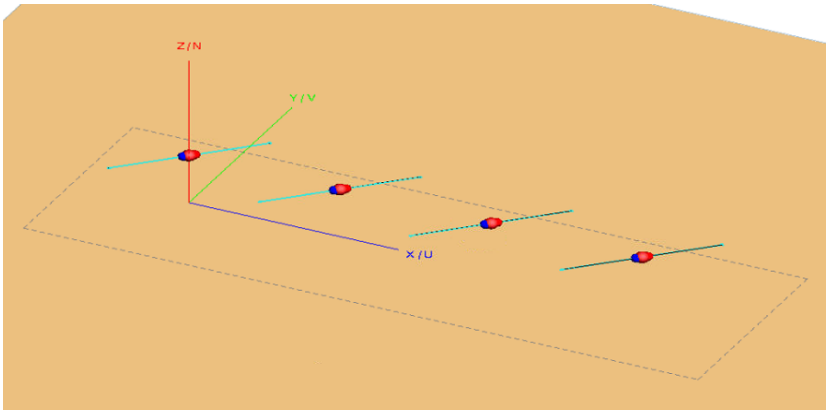

Figure 3.2.17: Graphical representation of 4 dipoles in the array, FEKO v2020.

ones are presented below, including the gain graph in three dimensions (3.2.18) and two dimensions (3.2.19), the S_{11} scattering parameters (3.2.20), the $\phi = [0, 90]$ cuts in the frequencies of interest (3.2.21 and 3.2.22), and table 3.2.4, which provides a summary of the principal parameters of the simulation at approximately 38.1 MHz.

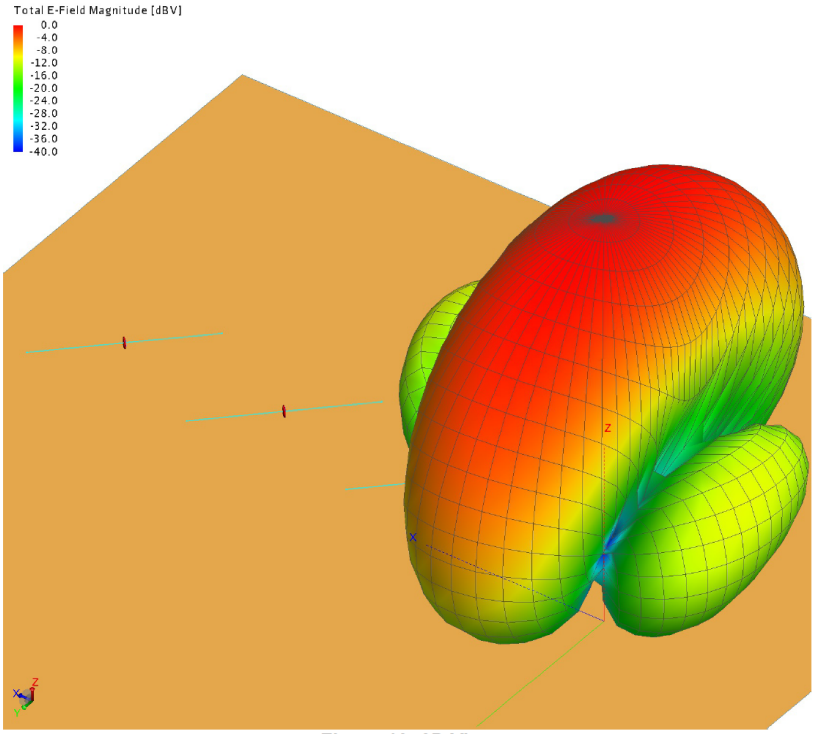

Figure 3.2.18: Gain results for the geometric structure of four real dipole, FEKO v2020.

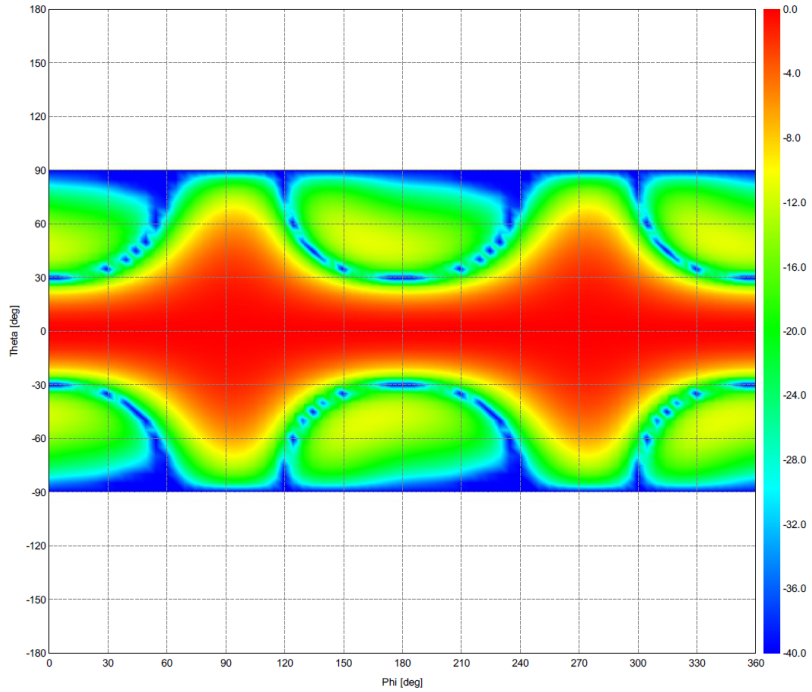

Figure 3.2.19: Normalised gain results for the geometric structure of four real dipole in the plane θ, ϕ FEKO v2020.

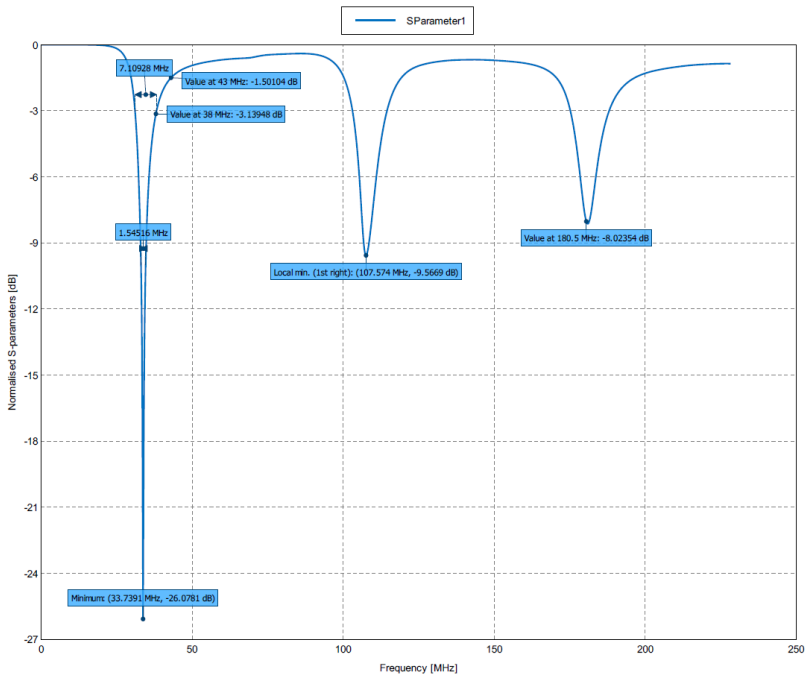

Figure 3.2.20: Results of the scattering parameters S_{11} of four real dipole, FEKO v2020.

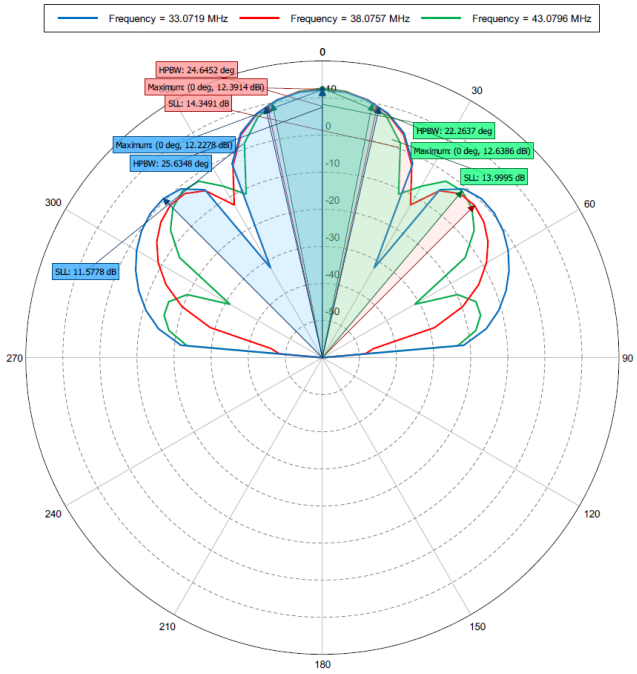

Figure 3.2.21: Results in the axis $\phi = 0$ (blue, green, red) of the gain for four real dipole, FEKO v2020..

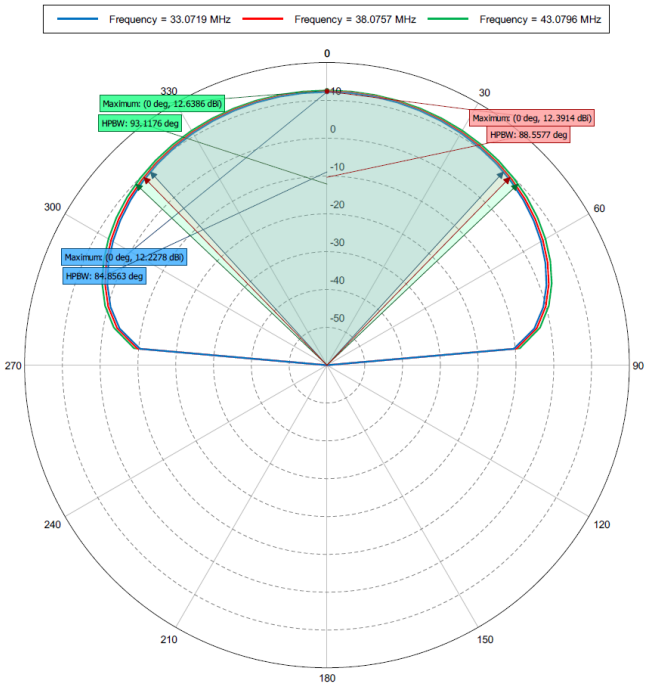

Figure 3.2.22: Results in the axis $\phi = 90$ (blue, green, red) of the gain for four real dipole, FEKO v2020.

Parameter	Value	Parameter	Value
λ	7.8735 [m]	Antenna length	3.81 [m]
ω	38.07575 [MHz]	Arm $\leftarrow$	1.83 [m]
D	12.3914	Brazo $\rightarrow$	1.972 [m]
ξ	1	FWHM θ y $\phi = [0, 90]$	24.6452° y 88.557°
G	17.344 [dbi]	FWHM ϕ	360°
Power	9.9971 [mW]	Apertura efectiva	64.4730[m^2]

Table 3.2.2: Summary table of the results obtained for four element of the array.

3.2.2.3 Sixteen elements simulation

The array comprises a total of sixteen elements, and conducting simulations for this configuration proves essential in uncovering the optimal radiometric performance potential of the Riometer. Illustrated in Figure 3.2.23, the array's geometric layout is showcased within FEKO 2020. The intricate arrangement is highlighted by calypso lines denoting copper conductor cables, an orange circle symbolizing the sources, and red and blue circles representing the electrical terminal connectors of the antenna. The plain ochre background serves as the electrical ground plane backdrop, collectively painting a comprehensive picture of the system's composition and structure. All the results of this simulation can be found in appendix 5. The most relevant results are shown below and include the gain graph in three dimensions (see 3.2.24 and 3.2.26), as well as in two dimensions (see 3.2.25 and 3.2.27) with different observation points synthesized using the beamforming algorithm. Additionally, the S_{11} scattering parameters (see 3.2.28), the $\phi = [0, 90]$ cuts in the frequencies of interest (see **??** and 3.2.31), and the total power (see 3.2.29) generated by the array using a 1V source in each one of the elements are examined. Table 3.2.4 provides a summary of the principal parameters of the simulation at around 38.1 MHz.

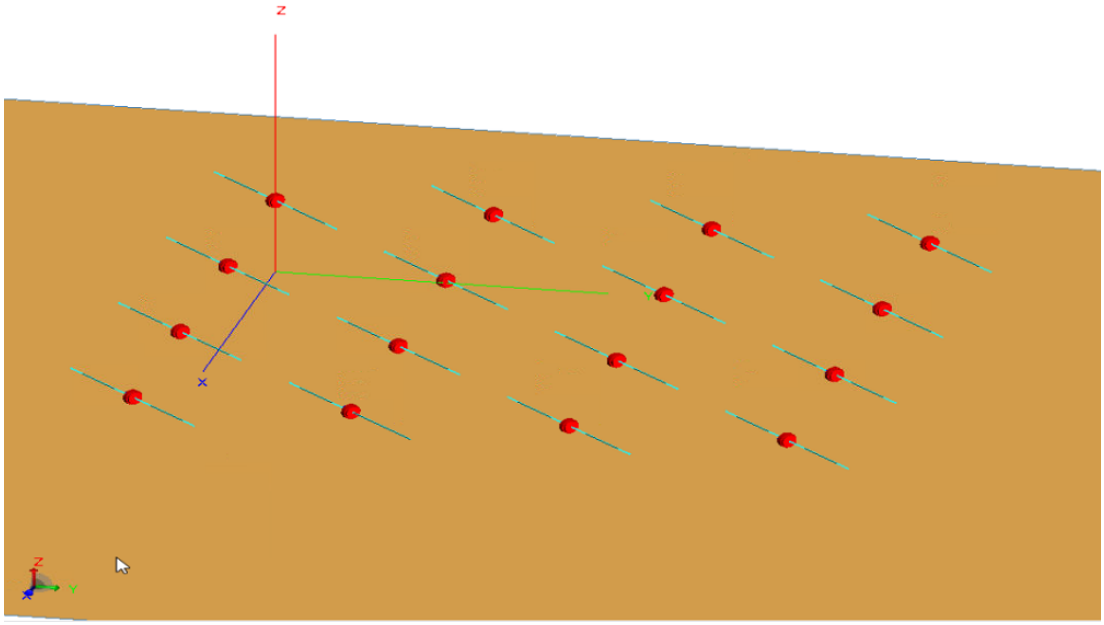

Figure 3.2.23: Graphical representation of 16 dipoles in the array, FEKO v2020.

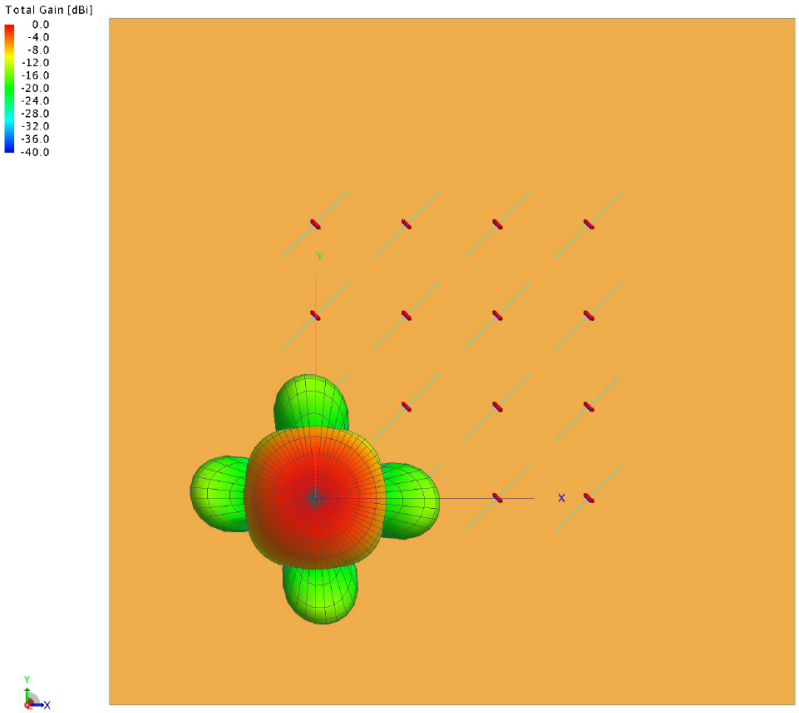

Figure 3.2.24: Gain result for geometry of sixteen elements in the array, without phase changes, FEKO v2020.

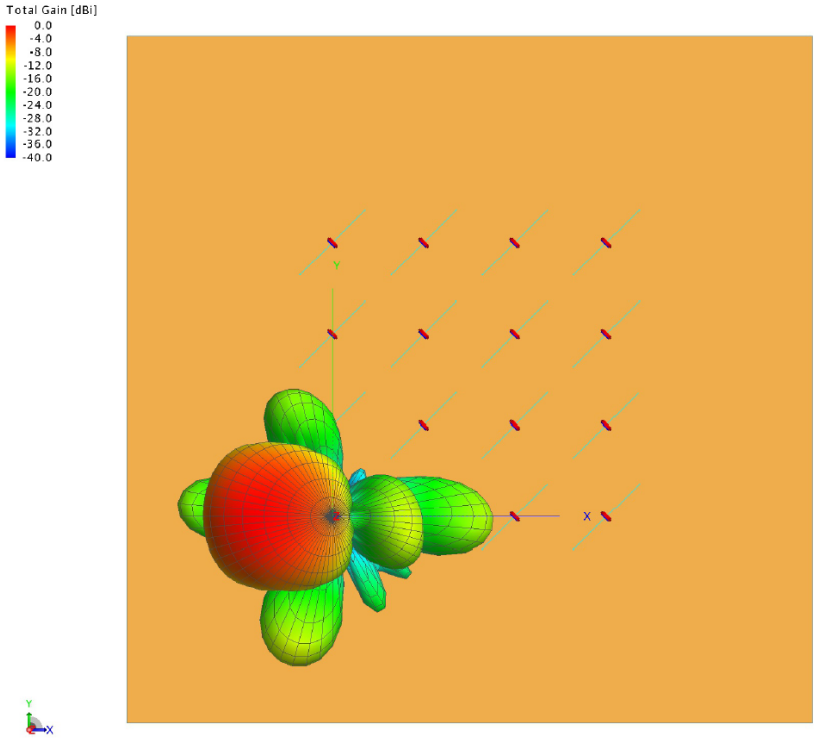

Figure 3.2.25: Gain result for geometry of sixteen elements in the array, with controlled phase changes, FEKO v2020.

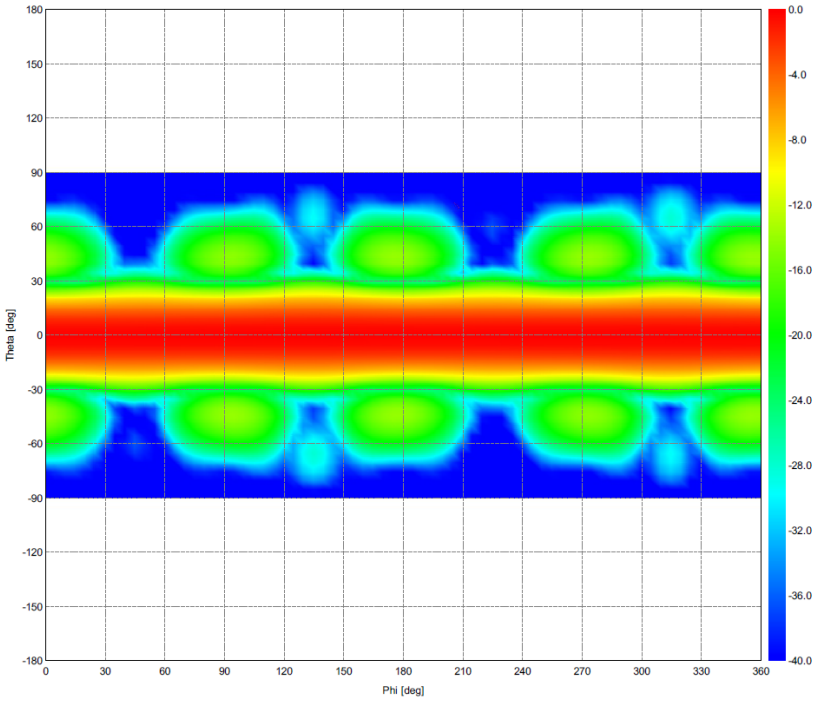

Figure 3.2.26: Normalised gain results for the geometric structure of sixteen real dipole in the plane θ, ϕ FEKO v2020.

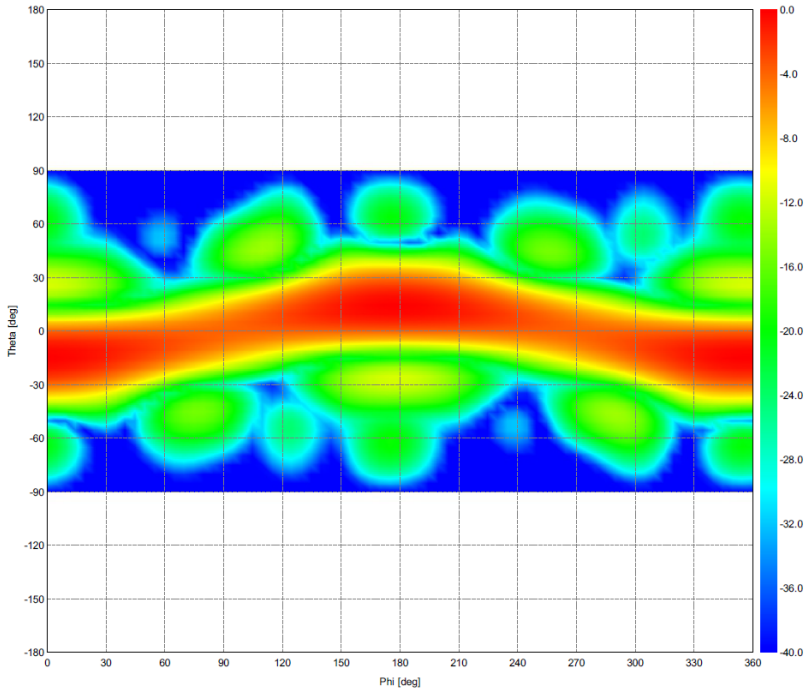

Figure 3.2.27: Normalised gain results for the geometric structure of sixteen real dipole in the plane θ, ϕ FEKO v2020.

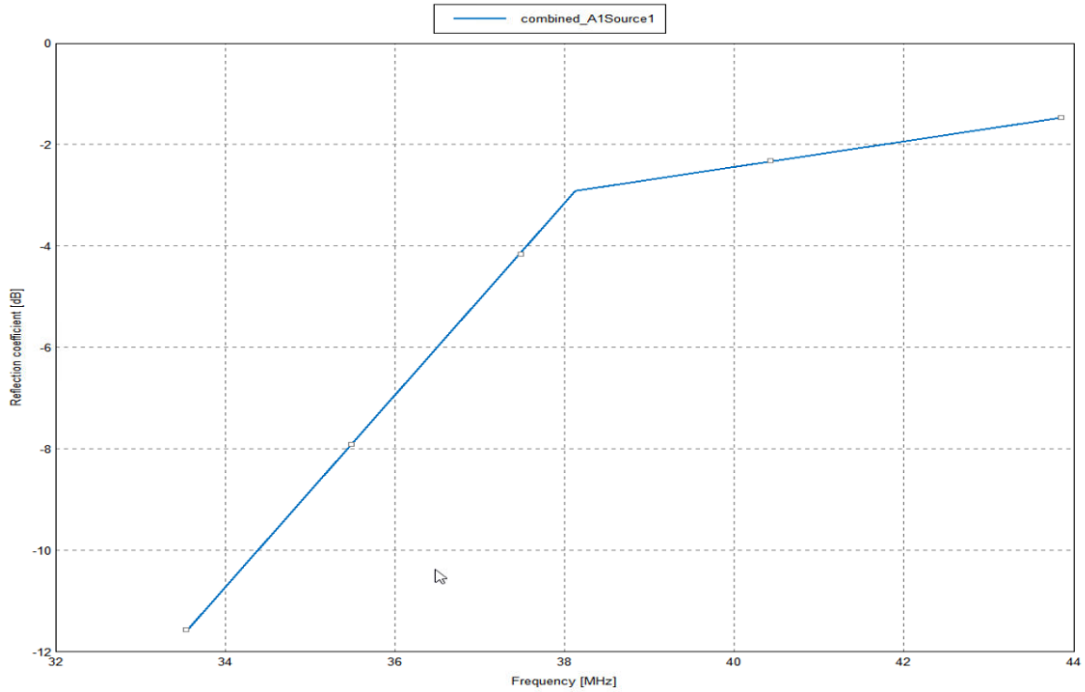

Figure 3.2.28: Results of the scattering parameters S_{11} for sixteen real dipole, FEKO v2020.

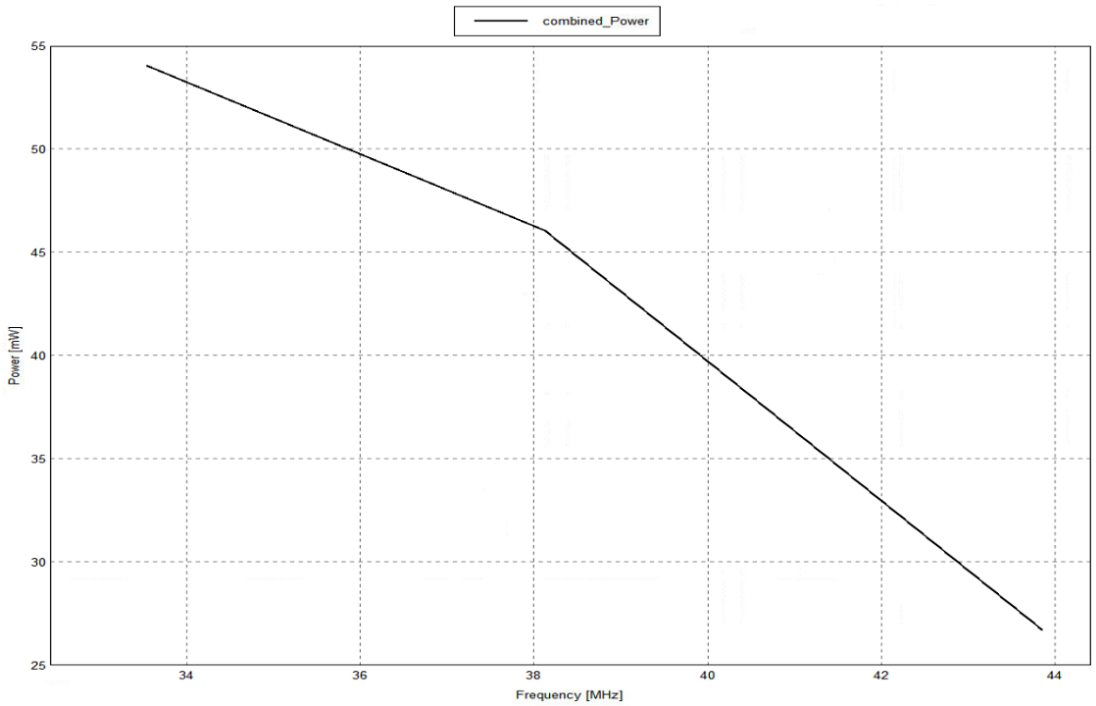

Figure 3.2.29: Results of the power generated by sixteen real dipole, FEKO v2020.

Parameter	Value	Parameter	Value
λ	7.8735 [m]	Antenna length	3.81 [m]
ω	38.07575 [MHz]	Arm $\leftarrow$	1.83 [m]
D	54.6009	Arm $\rightarrow$	1.972 [m]
ξ	1	FWHM θ y ϕ = [0.90]	24.6146° y 24.6146°
G	17.4364 [dbi]	FWHM ϕ	360°
Power	46.228 [mW]	Effective opening	284.091[m^2]

Table 3.2.3: Summary table of the results obtained for the arrangement pointing to $\theta = 0$ and $\phi = 0$ in Feko 2020.

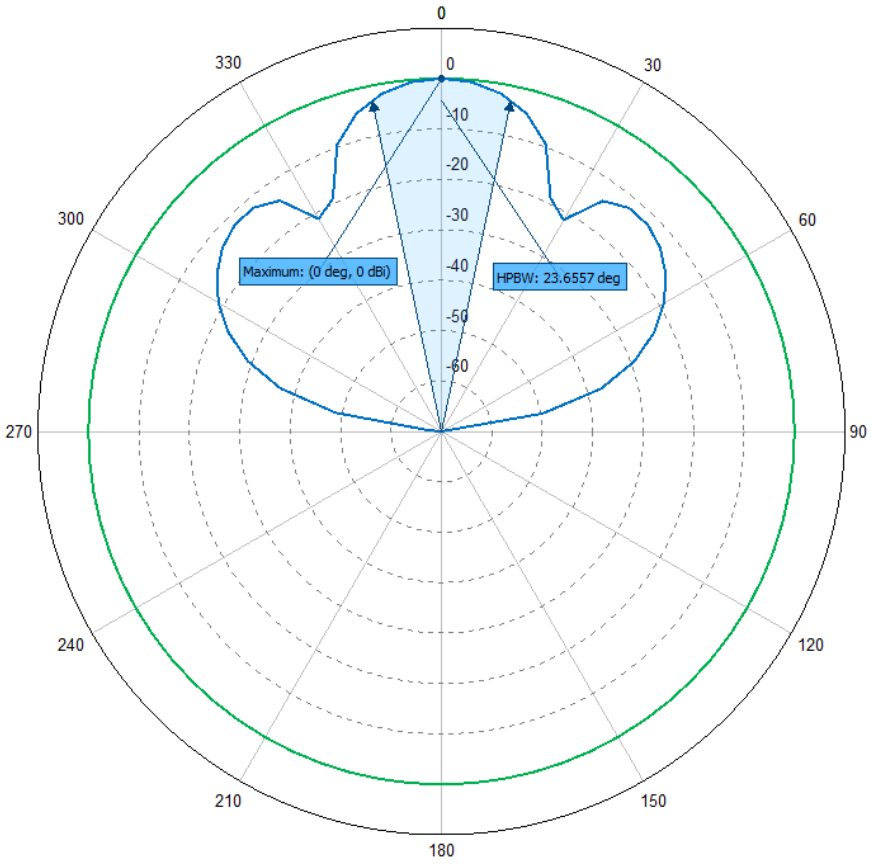

Figure 3.2.30: Results in the axis $\phi = 0$ (green) and $\theta = 0$ (blue) of the gain for four real dipole, FEKO v2020.

Parameter	Value	Parameter	Value
λ	7.8735 [m]	Antenna length	3.81 [m]
ω	38.07575 [MHz]	Arm $\leftarrow$	1.83 [m]
D	52.735	Arm $\rightarrow$	1.972 [m]
ξ	1	FWHM θ y $\phi = [0, 90]$	25.443° y 24.874°
G	17.3983 [dbi]	FWHM $\phi =$	104.672°
Power	46.228 [mW]	Effective opening	274.383[m^2]

Table 3.2.4: Summary table of the results obtained for the arrangement pointing to $\theta = 15$ and $\phi = 0$ in Feko 2020.

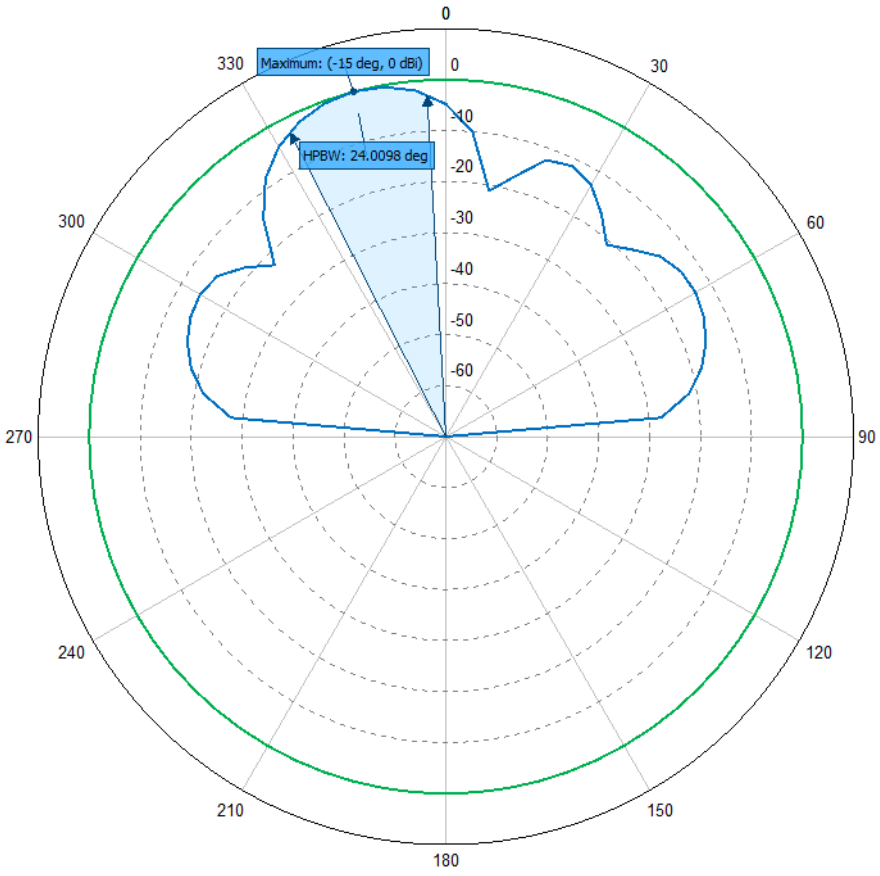

Figure 3.2.31: Results in the axis $\phi = 0$ (green) and $\theta = 0$ (blue) of the gain for four real dipole, FEKO v2020.

3.3 Analog system

Considering theory, literature, and prior measurements, the magnitude of the Cosmic Radio Noise (CRN) detected by the antennas has been established. This knowledge, combined with the chosen digital system for the project, delineates the optimal operating range of gain and bandwidth supported by the digital system. It also defines the performance specifications necessary for the analog system.

Table 3.3.1 summarizes all the parameters considered during the design, simulation, and fabrication of analog receptors. Meanwhile, Table 3.3.2 outlines the optimal working range for this specific application.

Parameter	value	Alternative unit
Bandwidth	10 [MHz]	-
Spectral resolution	781.25 [KHz]	-
Max input power	0.01 [W]	10 [dBm]
Noise floor	7.96×10^{-8} [W]	-70.9921 [dBm]
Minimum power CRN (1000K)	1.08×10^{-14} [W]	-109.673 [dBm]
Maximum power CRN (40000K)	4.31x10^{-}13 [W]	-93.652 [dBm]
Load power (298.15 K)	3.21×10^{-15} [W]	-115.002 [dBm]
Minimum power (1298.15 K)	1.40×10^{-14} [W]	-108.556 [dBm]
Maximum power (40298.15 K)	4.34×10^{-13} [W]	-93.620 [dBm]
Maximum power in the band	5.56×10^{-12} [W]	-82.548[dBm]
Analog SNR	3.42-137.342	-

Table 3.3.1: Summary of system parameters and expected powers.

Parameter	Valid Ranges	Default Value
Center frequency	35-45 [MHz]	38 [MHz]
Bandwidth	10-20 [MHz]	12 [MHz]
Gain	30-70 [db]	60 [db]

Table 3.3.2: Analogical system requirements and valid range.

3.3.1 Design and Simulation

The chosen technology for the analog receptor is Surface-mount technology (SMT) due to its compatibility with the system's frequency range. Guided by the gain and bandwidth prerequisites (tanle 3.3.2), we devised a streamlined configuration comprising three elements on a standard PCB board using FR4 material. This configuration involves two low noise amplifiers (LNA) and one filter, as depicted in Figure 3.3.1. The incorporation of Frizz equation into the design aids in minimizing the receptor's noise contribution effectively.

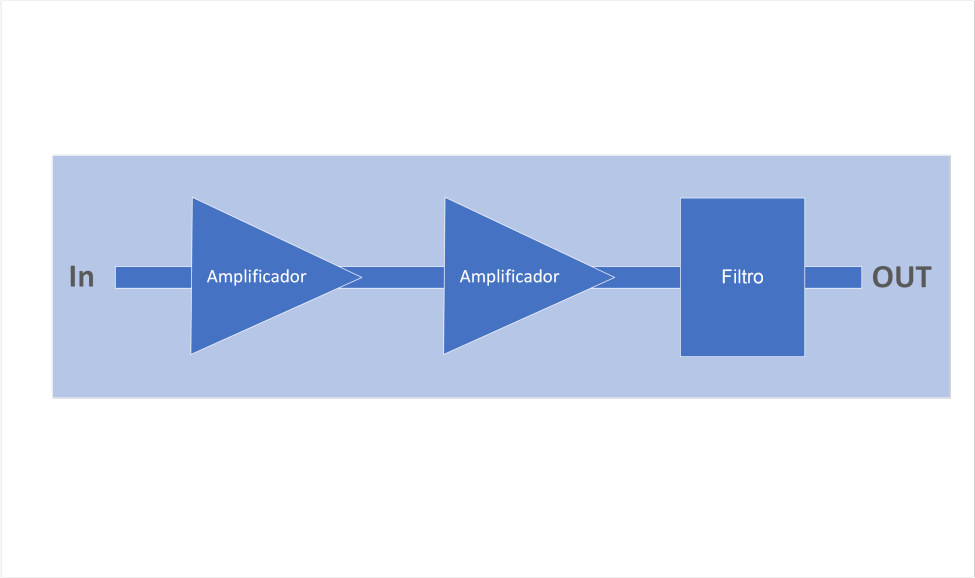

Figure 3.3.1: Simplified diagram of the analog system

The filter design is achieved through meticulous performance assessment, selecting from numerous options generated using the iFilter Filter Synthesis tool from Applied Wave Research (AWR) Software. This approach yields the anticipated performance characteristics (refer to Figure 3.3.3), along with a comprehensive list of components (refer to 3.3.3) required for the filter implementation.

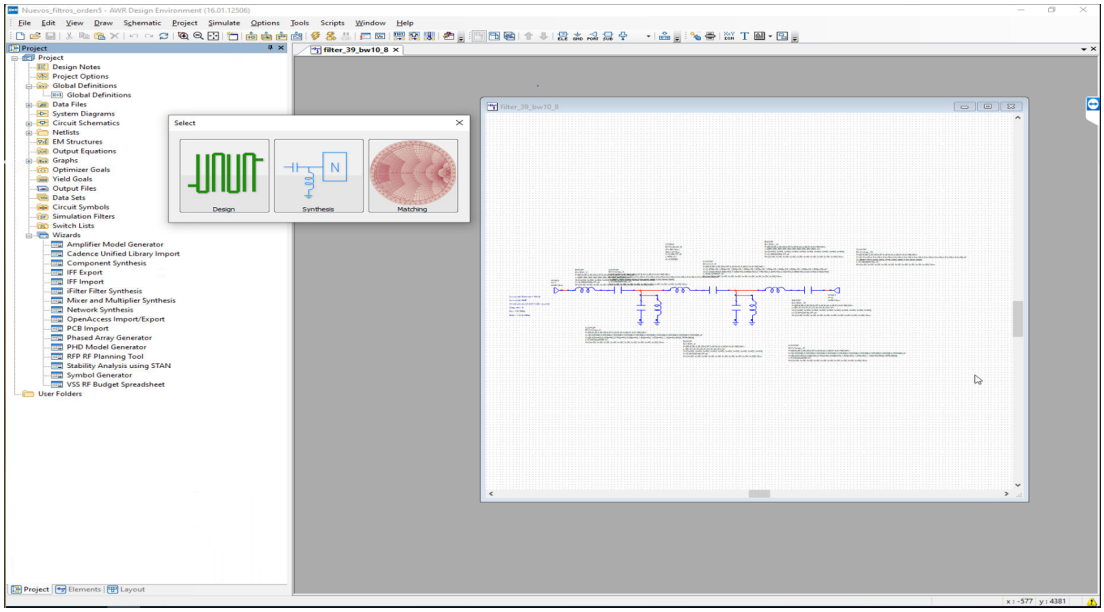

Figure 3.3.2: Software AWR y IFilter Filter syntesis

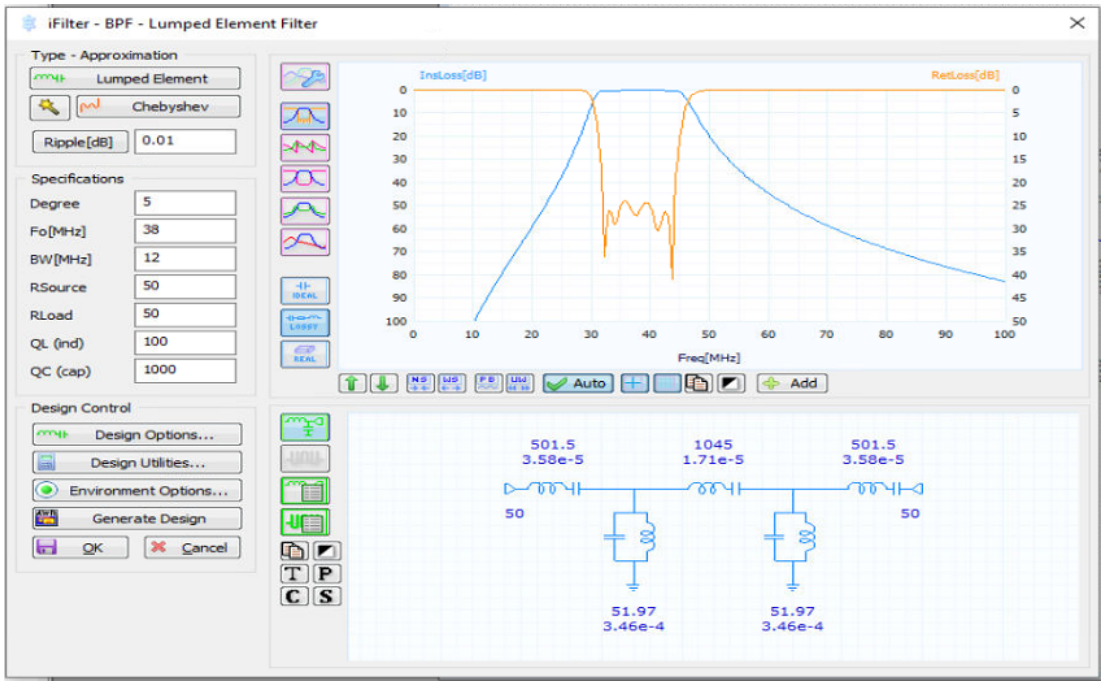

Figure 3.3.3: Configuration and synthesis window of IFilter Filter syntesis

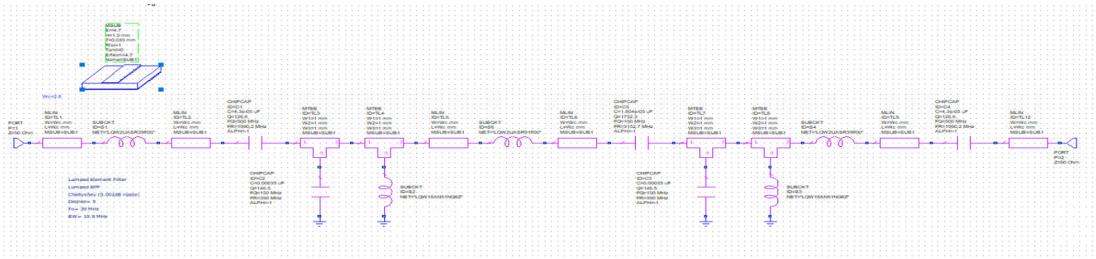

Figure 3.3.4: PCB filter simulation diagram

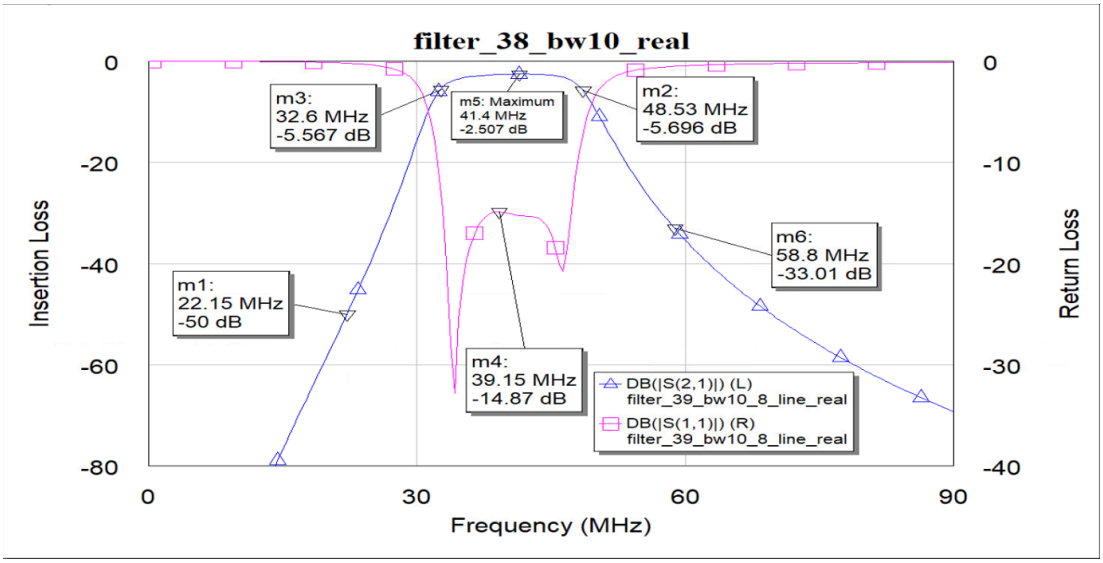

Figure 3.3.5: Answer filter simulation diagram on PCB

Component	Value	Quantity
Side inductors	390 nH	2
Ground Inductors 2	51 nH	2
Central inductor 3	910 nH	1
Side Capacitors 1	43 pF	2
Ground Capacitors2	330 pF	2
Center Capacitor	18 pF	1

Table 3.3.3: Summary of components for the filter extracted from awr.

To simulate a real filter is considered the availability of components in the market. All the specific components used can be found in the appendix 6

Simultaneously, utilizing the AWR software, the complete analog receiver is

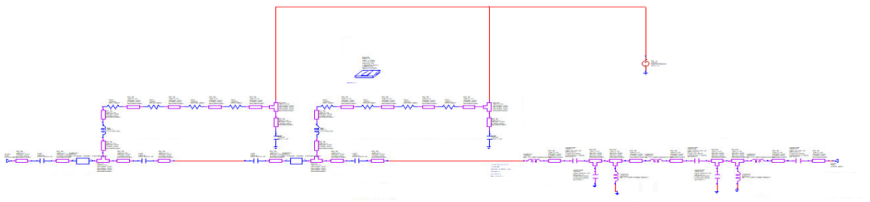

Figure 3.3.6: RF system simulation diagram on PCB

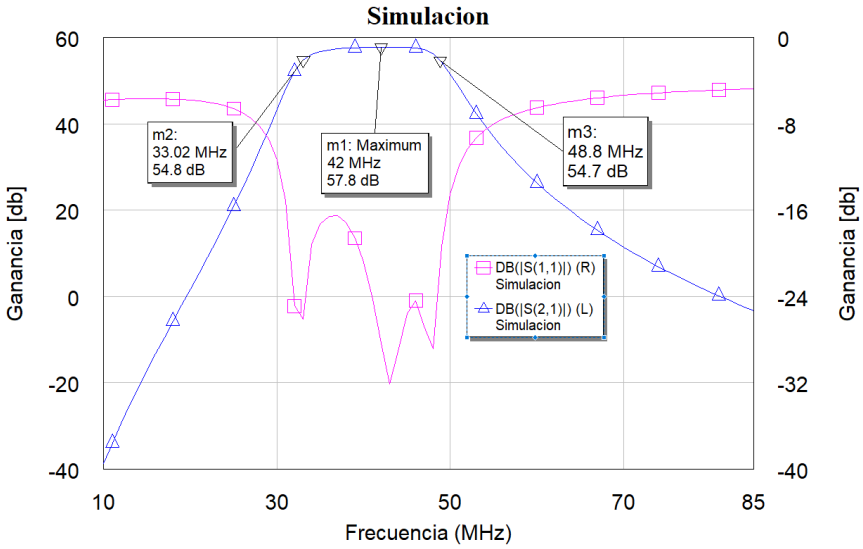

Figure 3.3.7: Response of RF system simulation on PCB

simulated, encompassing the LNAs MAR-8ASM+[2]. This simulation incorporates all the necessary components for the optimal functioning of the LNAs, as illustrated in Figure 3.3.6. The outcomes of this simulation duly demonstrate a performance that aligns with the anticipated behavior, as indicated in Figure 3.3.7.

[2]The simulation for this LNA has been successfully conducted and verified

3.3.2 Manufacture and Characterisation

The manufacturing process of the receiver has undergone several stages of evolution, as illustrated in Figure 3.3.8. Currently, we are showcasing the final stage where the system attains compliance with the international standards IPC 2221-B and IPC A-610.

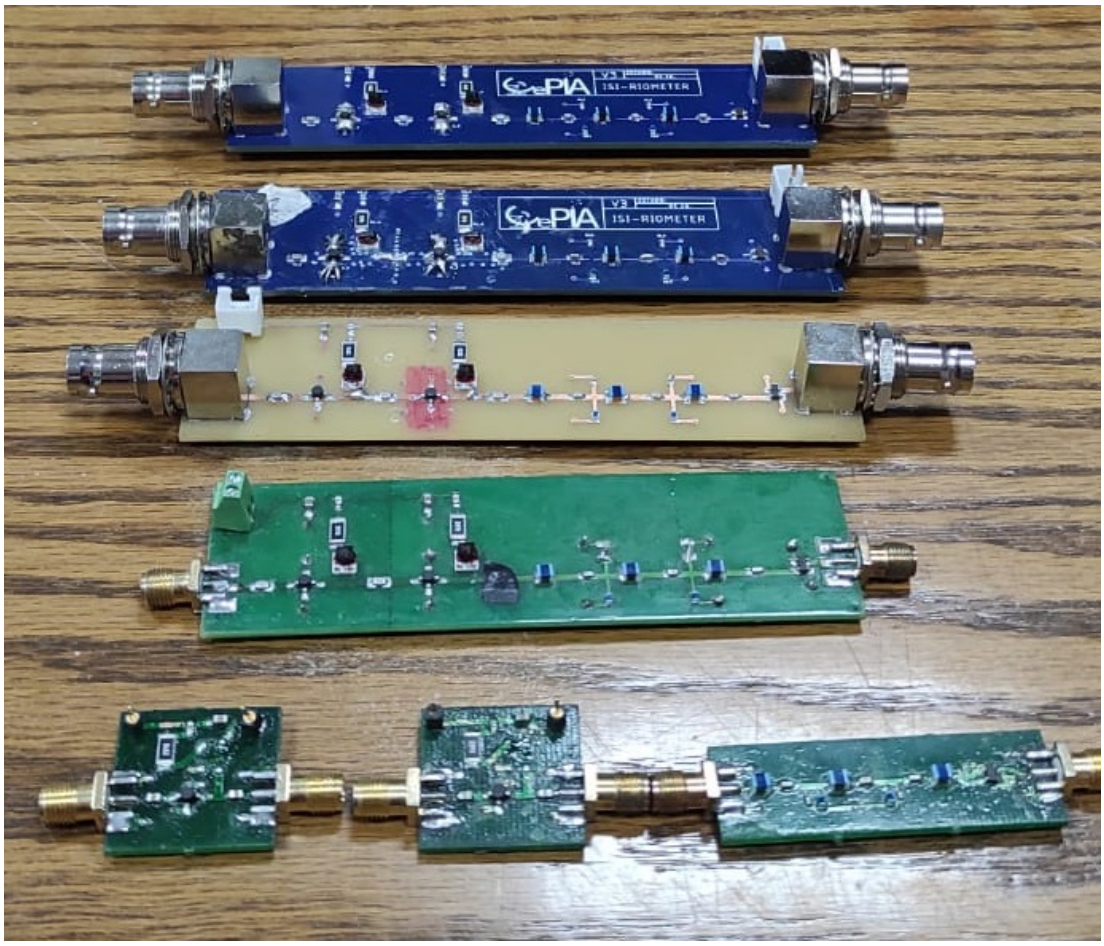

Figure 3.3.8: Diagram and photograph of the printing of the manufactured amplifiers.

In essence, the manufacturing process comprises three primary steps. It commences with the dissection of the printed file, where the architecture of each individual component is meticulously arranged on a PCB in accordance with the AWR simulation diagram. In this instance, EAGLE is employed, resulting in an outcome akin to that depicted in Figure 3.3.9.

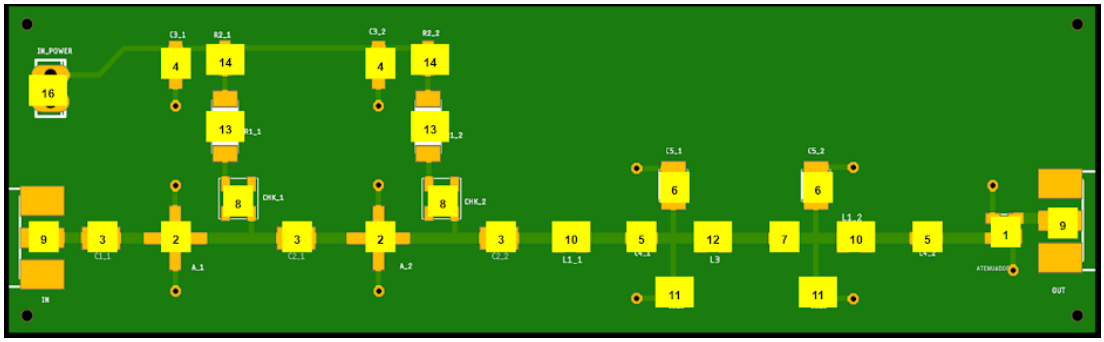

Figure 3.3.9: EAGLE Software plate printing scheme.

Once the printed file is generated, the subsequent step involves transferring the design onto the PCB. This can be achieved through various methods, such as Proto-laser or Etching. These processes culminate in a result resembling Figure 3.3.9. The final stride encompasses soldering the components onto the board, an illustration of which can be seen in Figures 3.3.11 and 3.3.13.

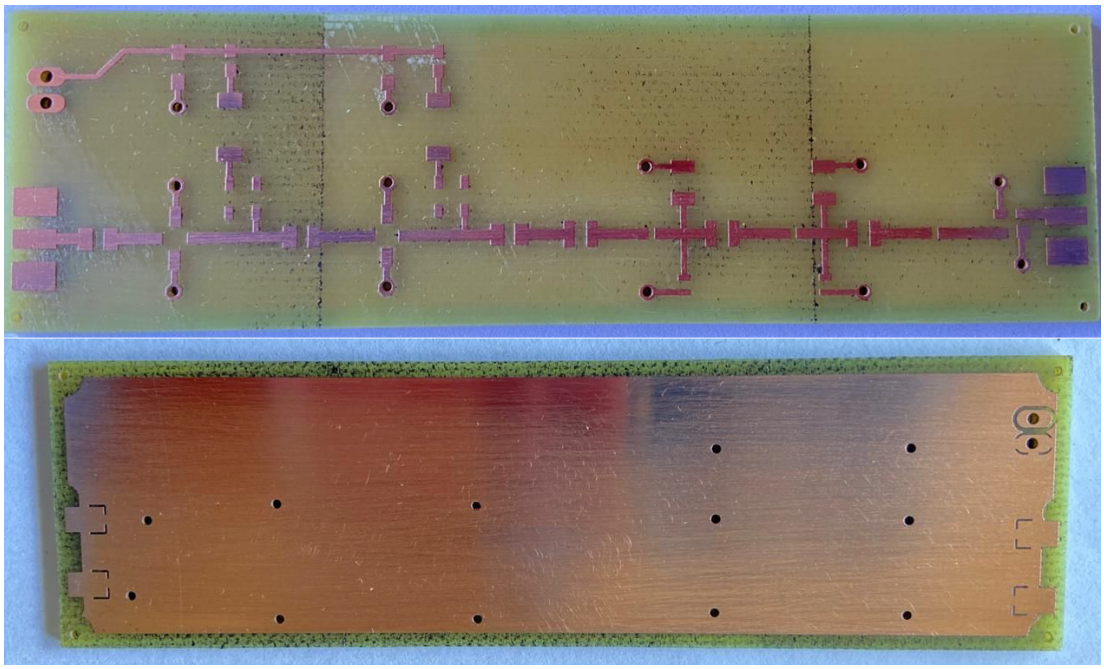

Figure 3.3.10: Printed plate photograph.

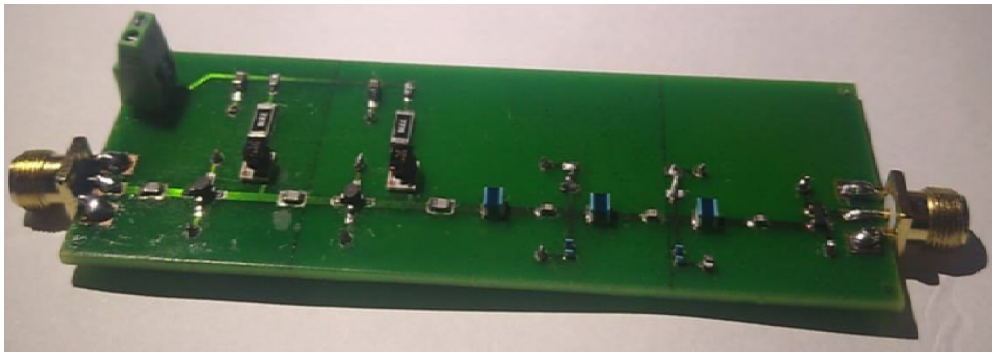

Figure 3.3.11: Photograph of the assembled PCB, dimensions 106.81 X 30.88 [mm].

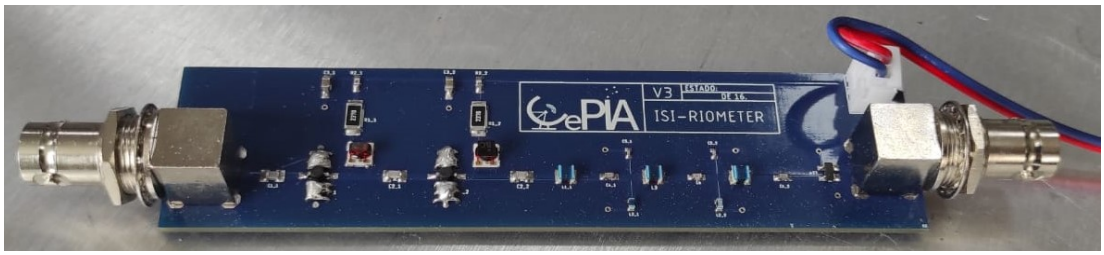

Figure 3.3.12: Photograph of the final assembled PCB, Dimensions 120 x 30 [mm]

Upon the completion of the manufacturing process, the next step involves utilizing the VNA to characterize the response of the receiver. This characterization facilitates a comparison between the data obtained from the AWR simulation and the actual measurements. This comparative analysis is illustrated in Figure 3.3.13, while a summarized overview of the principal parameters derived from the measurements is provided in Table 3.3.4.

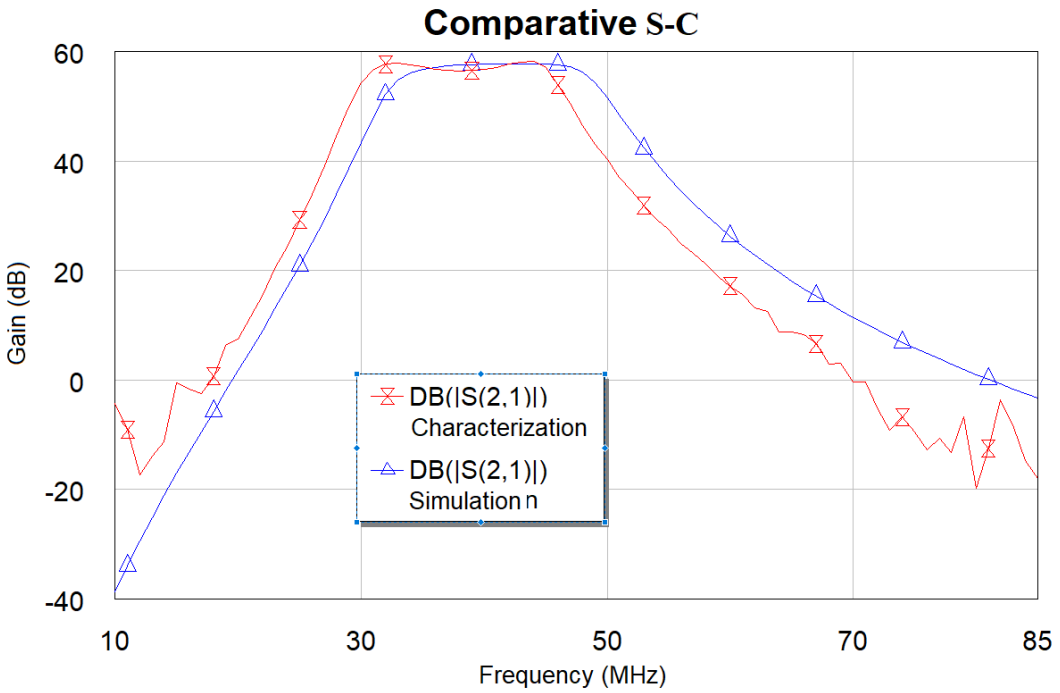

Figure 3.3.13: Comparison between Simulation and Characterization of an Analog Receiver PCB.

Parameter	Value heightMaximum Gain
58.3 dB -3dB Frequencies (55.3 dB)	(30.4, 45.57) MHz Bandwidth
15.16 MHz Central Frequency	37.89 MHz height

Table 3.3.4: Summary of analog system parameters.

The comprehensive study detailing the final iteration of the analog system is expounded within the thesis authored by Calquin (2021). This exceptional work, which played a pivotal role in their attainment of a degree in electronic execution engineering, serves as a valuable resource for comprehending the entirety manufacturing process.

3.4 Digital system

The final component of the system is the digital receiver, responsible for measuring the analog signal, performing digital fast Fourier transforms, calculating channel amplitudes and relative phases, as well as integrating the signal. To fulfill these functions, the chosen systems are the ROACH2 and the ADC16x250-8. These systems were supported by CASPER until 2018.

3.4.1 Digital Hardware

The configuration of the digital system required specific hardware and software to compile the code, configure, control, and extract the data from the FPGA card (see Figure 3.4.1). The specifications of the computer named 'Mr. Beam' are provided in Appendix 6, and the details about ROACH 2 are presented in the following sub-section.

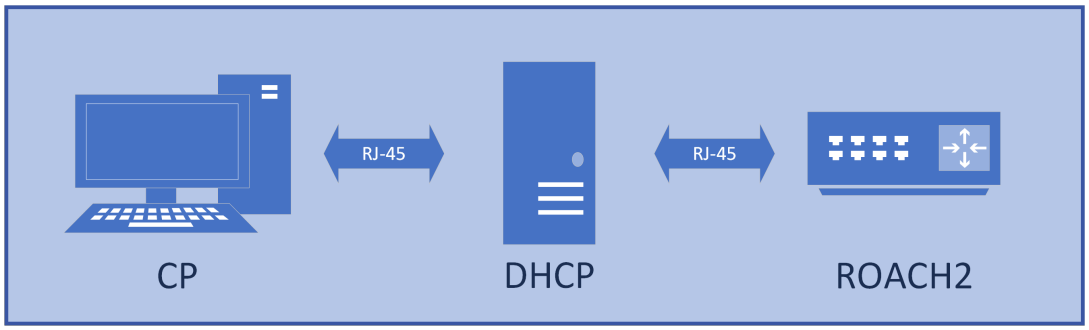

Figure 3.4.1: PC-server-ROACH connections diagram.

(a) Computer and DHCP server.

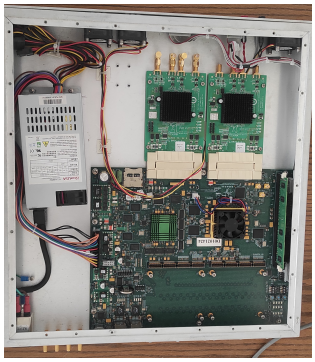

(b) ROACH2

Figure 3.4.2: Hardware Digital

Component	quantity
Logic cell	476,160
Slices	74400
DSP48E1 Slices	2,016
Distributed RAM	7640 Kb
Block RAM	38304 Kb
Clock managers	18
Max I/O	840
Ethernet MACs	4

Table 3.4.1: Feature summary of FPGA Virtex-6 XC6VSX475T

3.4.1.1 ROACH2 and digitizers

The ROACH2 (Fig. 3.4.2b) consists of an FPGA Virtex-6 SX475T on a PCB board IPC 6012 class 2, connected to all external peripherals as shown in Figure 3.4.3. The principal characteristics are presented below.

- Virtex-6 SX475T FPGA (XC6VSX475T-1FFG1759C)
- PowerPC 440EPx stand-alone processor to provide control functions
- 2 x Multi-gigabit transceiver break-out card slots, supporting up to 8x10Ge links which may be CX4 or SFP+
- 4 x 36 * 2M QDR II+ SRAMs connected to the FPGA
- A single 72-bit DDR3 RDIMM slot connected to the FPGA
- 2 x ZDOKs
- An FTDI FT4232H USB to JTAG, serial and IIC

The Virtex-6 SX475T is one of the most powerful members of its family, and its principal features are summarized in Table 3.4.1. The ADC16x250-8, shown in Figure 3.4.4, is a digitizer capable of transforming sixteen analog signals at a maximum rate of 250 Mega samples per second with eight bits of resolution. The ADC supports a maximum input power of +10 dBm (0.01 W) or 1-volt peak-to-peak at 50 ohms.

Both are in sync using a clock synthesizer, the Valon 5007, which generates two

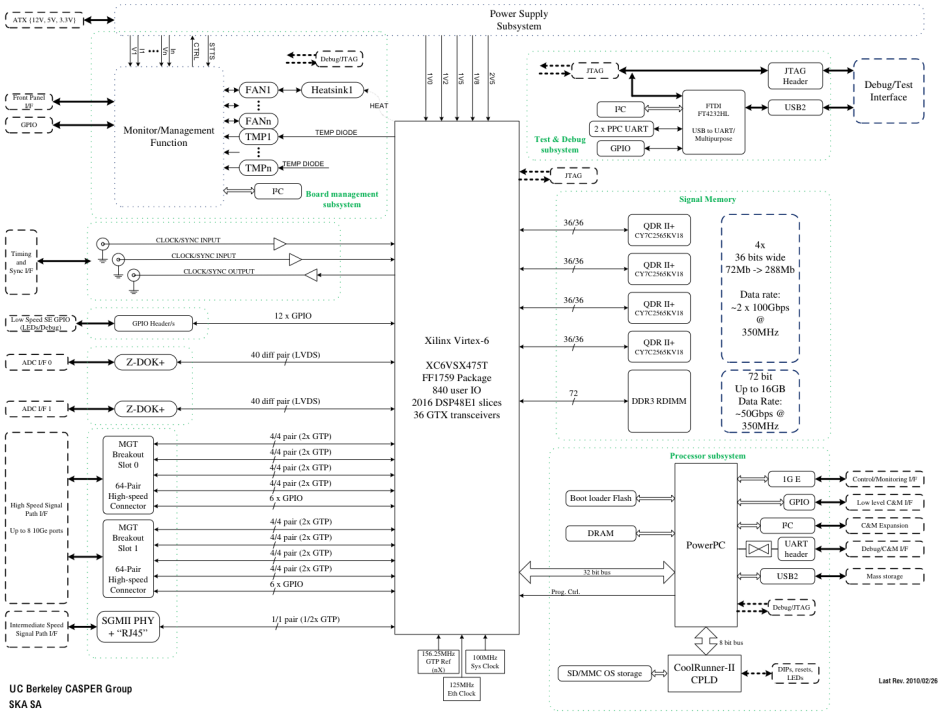

Figure 3.4.3: Block Diagram ROACH2 (Casper, 2010).

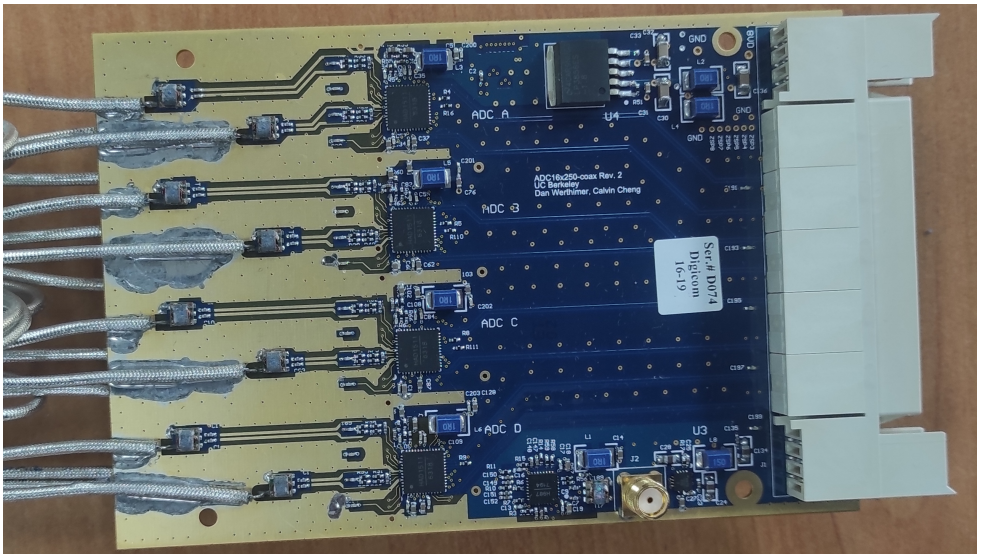

Figure 3.4.4: Picture of ADC16x250-8.

Figure 3.4.5: ROACH2, ADC16x250-8 and valon 5007.

out-of-sync signals and can be connected as shown in Figure 3.4.5.

3.4.2 Digital Software

The hardware required a specific tool flow for designing, simulating, compiling the code, and interacting with the hardware. The tool flow starts with the operating system Ubuntu 16.04, followed by the Simulink extension of Matlab 2013b and the libraries for ROACH2. Simulink provides an interface (see Figure 3.4.6) and an environment that makes programming the digital configuration for the hardware easy.

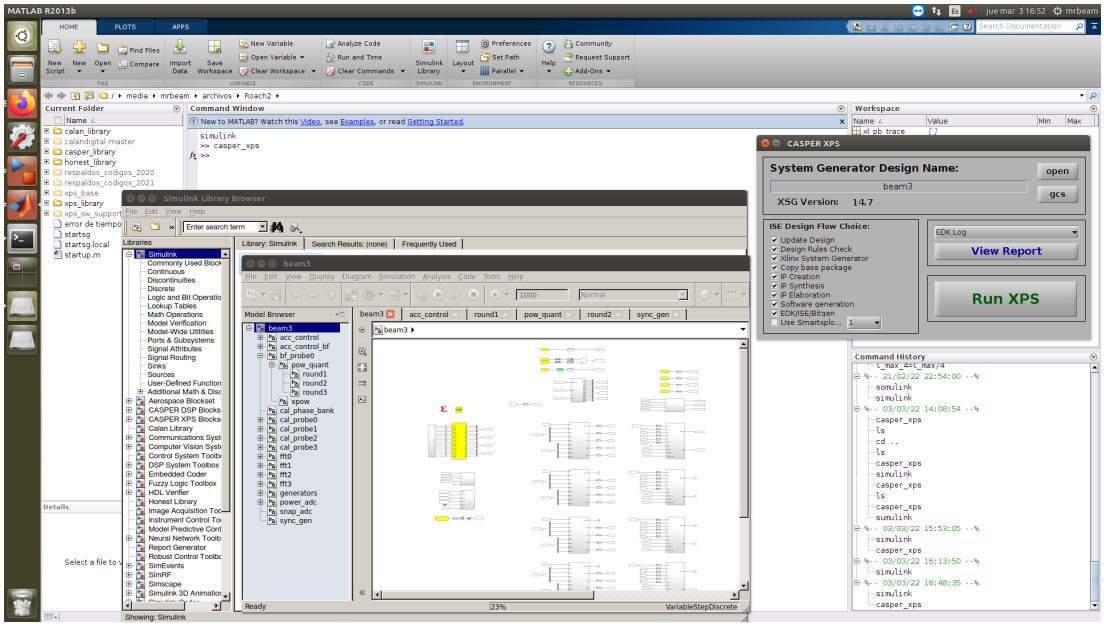

Figure 3.4.6: Toolflow diagram of matlan2013b.

Additionally, the tool flow utilizes Python 2.7 to interact with the hardware, extracting data and modifying parameters using libraries such as construct v2.5.3, katcp v0.5.5, numpy, scipy, matplotlib, pyserial, pyvisa, and corr. All of these libraries are installed and ready to use on the computer 'Mr. Beam'.

3.4.3 Configuration diagram

The tool flow and the hardware have been installed and configured. The next step is to validate the operation of this system for beamforming.

3.4.3.1 The beamforming

The beamforming implemented in this work is entirely digital. The logic of the system is depicted in Figure 3.4.8, which illustrates the signal flow. It starts with the ADC and its sixteen inputs, followed by a Polyphase Filter Bank (PFB) and FFT of two hundred fifty-two channels. These steps are utilized to reduce input noise and aliasing in each of the sixteen channels and transform signals into the spectral domain.

Afterwards, the signal is duplicated and routed into two different paths. The first path (upper path in the figure) calculates calibration values for amplitude and phase, which are stored for computer retrieval. This step is crucial for the accurate

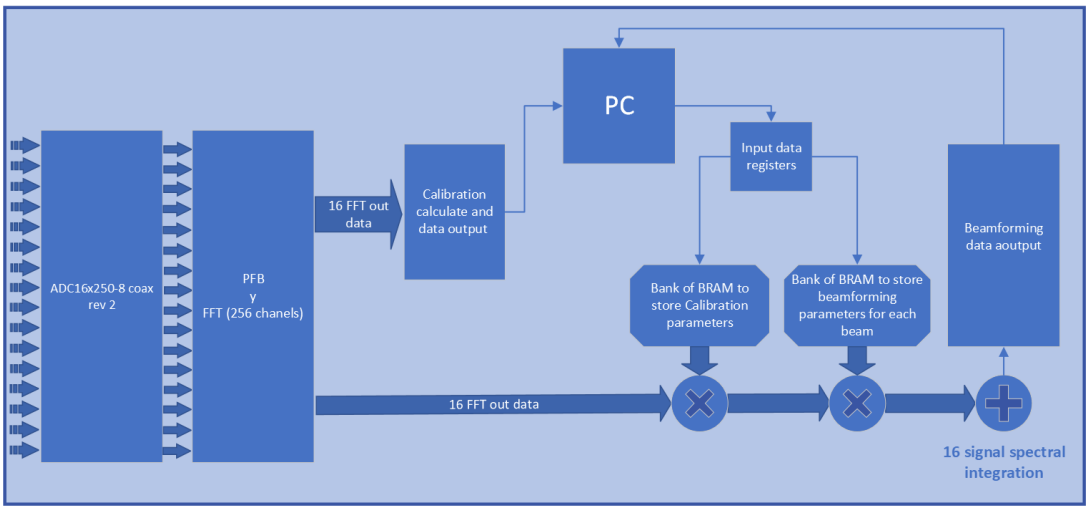

Figure 3.4.7: Schematic block of the digital signal processing

implementation of beamforming, as each input exhibits unique performance and must be standardized to a reference channel (pre-selected channel).

The second path (lower path in the figure) involves the beamforming process, which consists of three steps. The initial step standardizes each of the channels. The second step adjusts the phases of the channels using beamforming calculations. The third step integrates all channel responses and stores the resultant data for computer analysis.

Additionally, Figure 3.4.8 displays the block diagram created in Simulink Matlab 2013b.
The FPGA and the ADC operate at 200 MHz. The internal performance of the ADC allows generating useful spectral data from 0 to 50 MHz. The number of useful data channels is a quarter of the total, resulting in 64 channels. This equates to a total channel resolution of 781250 Hz in the first Nyquist zone. This implementation utilizes no more than 20% of the resources of the ROACH 2, as shown in the table.3.4.2.

3.5 Setup and characterization

The implementation of the system consists of two phases. The first phase takes place in the laboratory, where the analog and digital hardware are integrated and validated. The second phase involves the deployment of the system to a location

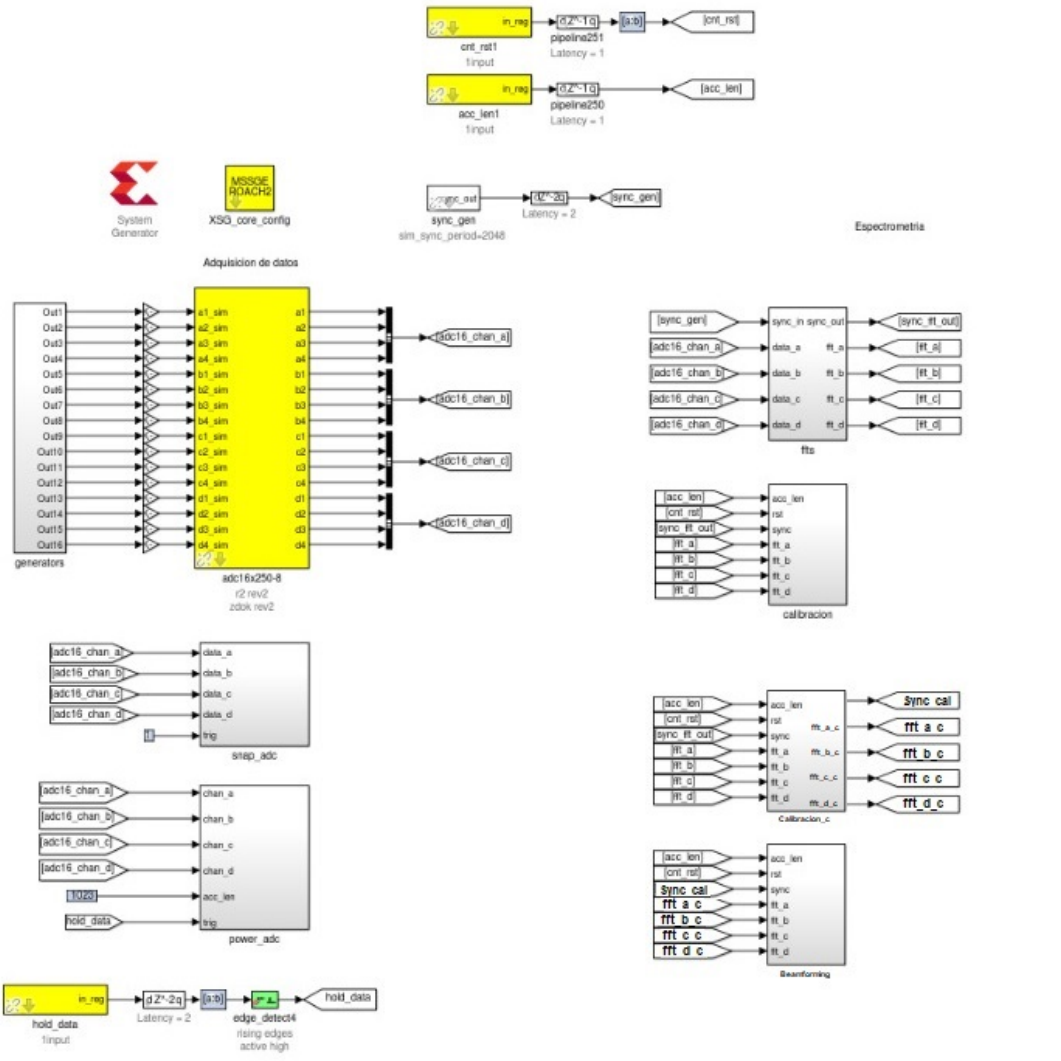

Figure 3.4.8: Schematic block diagram from Simulink

Slice Logic Utilization		
Slice Registers	74,318 out of 595,200	12%
Slice LUTs	52,282 out of 297,600	17%
Slice Logic Distribution		
Occupied Slices	16,937 out of 74,400	22%
Unused Flip Flop	8,870 out of 63,476	13%
Unused LUT	11,194 out of 63,476	17%
IO Utilization		
Bonded IOBs	142 out of 840	16%
Specific Feature Utilization		
RAMB36E1/FIFO36E1s	192 out of 1,064	18%
RAMB18E1/FIFO18E1s	172 out of 2,128	8%
BUFG/BUFGCTRLs	7 out of 32	21%
ILOGICE1/ISERDESE1s	127 out of 1,080	11%
OLOGICE1/OSERDESE1s	36 out of 1,080	3%
DSP48E1s	329 out of 2,016	16%
d IDELAYCTRLs	2 out of 27	7%
IODELAYE1s	32 out of 1,080	2%
MMCM-ADVs	2 out of 18	11%

Table 3.4.2: Device Utilization Summary:

within the dipole array. In this phase, a few problems needed to be solved, and both of these phases are described below.

3.5.1 Laboratory setup

The laboratory setup is used for characterizing the amplitude and relative phase measurements made by the analog and digital system created for ISI-RIOmerte. The setup includes a source of white noise created using a fifty-ohm load, with a spectral power of -114.98 dBm in each of the spectral channels of the FFT. A low noise amplifier, the ZFL-500LN+ model from Mini-Circuits, is also used, providing a gain of 24 dB. The output signal has a spectral power around -90.98 dBm per channel and is divided using a chain of 5 power dividers. This chain includes two 1x2 power dividers, two 1x4 power dividers (manufactured in CePIA), and one 1x8 power divider (Mini-Circuits 15542 zcsc-8-1), resulting in a total of sixteen divisions and a total loss per path of 24 dB. The output power of each of the divider's output paths is -114.98 dBm.

Next, each of the outputs from the dividers is connected to the analog receiver using different coaxial cables (see Figure 3.3.13). The analog receiver is powered using a 12-volt commercial medical source. This component filters and amplifies the signal by 60 dB within the bandwidth of 30 to 46 MHz, generating an output power of around -54.98 dBm per channel. Finally, the output signals are fed into the ADC16x250-8 through the RF Q9 connector (BNC male to SMB female).

(a) 50 ohm load **(b)** 4 db attenuator

Figure 3.5.1: Photograph of components used in the characterization of digital beamforming.

(a) 4 Power dividers

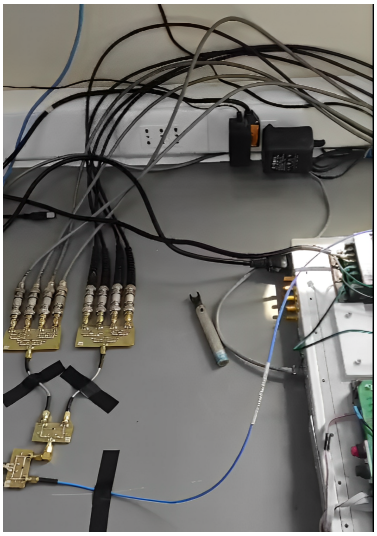

(b) 8 connection cables from source to analog System

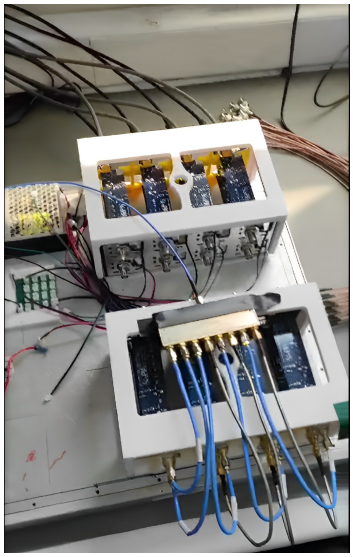

(c) Power divider and connection cables from source to analog System

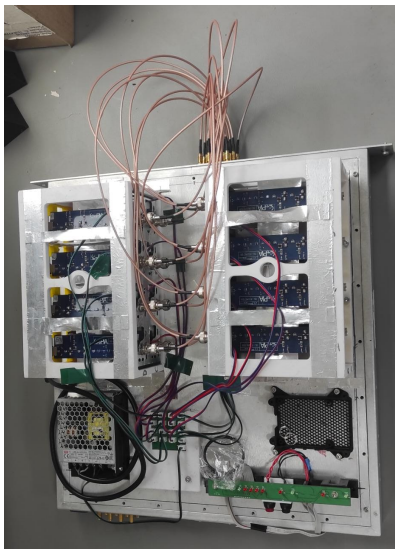

(d) Connection cables from analog System to digital system

Figure 3.5.2: Photograph of components used in the characterization of digital beamforming

The data measured with the Beamforming configuration on ROACH2 demonstrates the expected performance. The power measurement (see Figure 3.5.3) is around 55 dBm for all the input ports, and different phases (see Figure 3.5.4) are observed for each of the frequency channels. These phases are in relation to the length difference between the coaxial cables used to connect the power divider and the analog receiver.

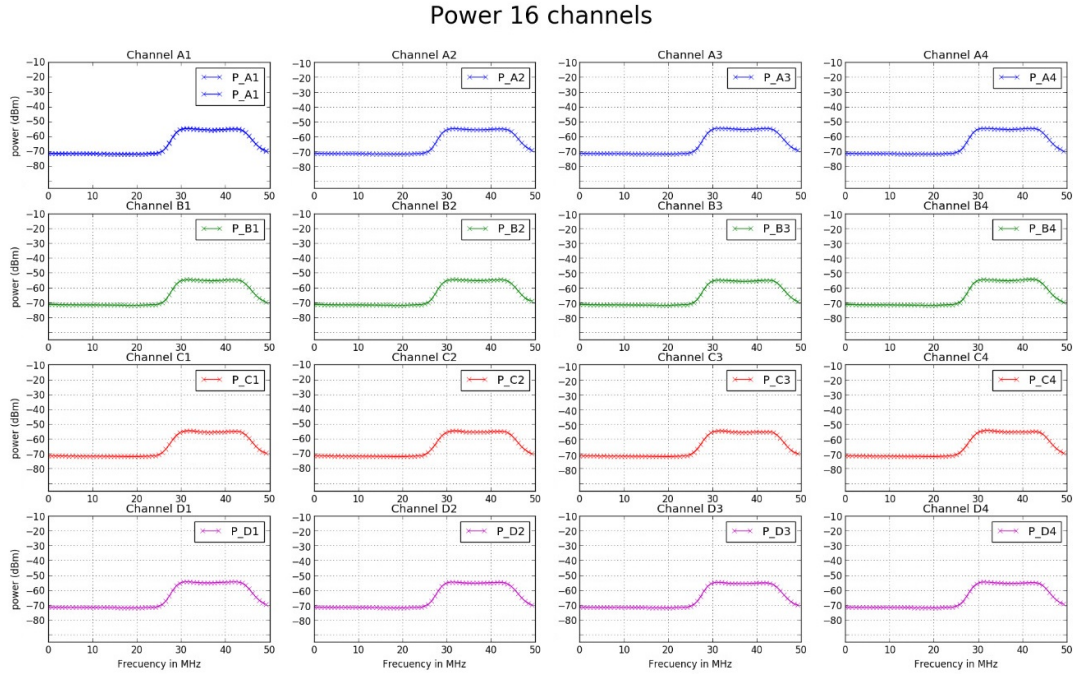

Figure 3.5.3: Graphic representation of the power measure with ROACH2.

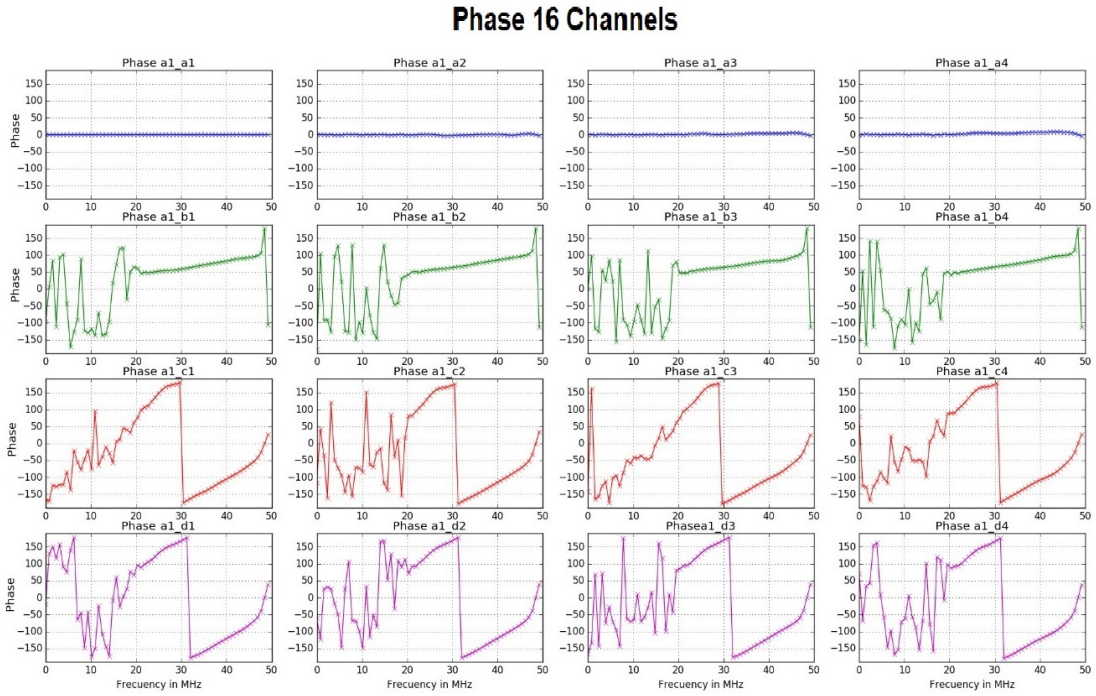

Figure 3.5.4: Graphic representation of the phase measure with ROACH2.

3.5.2 Field setup

The field setup is more complex than the one in the laboratory. This complexity arises from the need to establish power and Ethernet connections between the workstation and the location of the array (see Figure 3.5.5). Additionally, it was necessary to provide environmental protection for the hardware. These requirements were addressed by establishing a power and Ethernet connection spanning 70 meters and installing an IP55-rated metal enclosure (1000x800x300mm) within the array. This enclosure houses all the components of the ISI-RIOmeter system (see Figures 3.5.7 and 3.5.8).

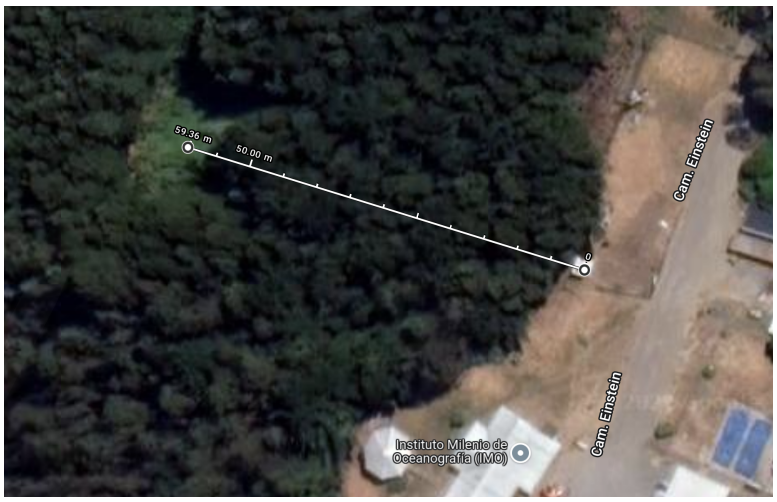

Figure 3.5.5: Picture of the location of workstation and the dipole array of ISI-RIOmeter

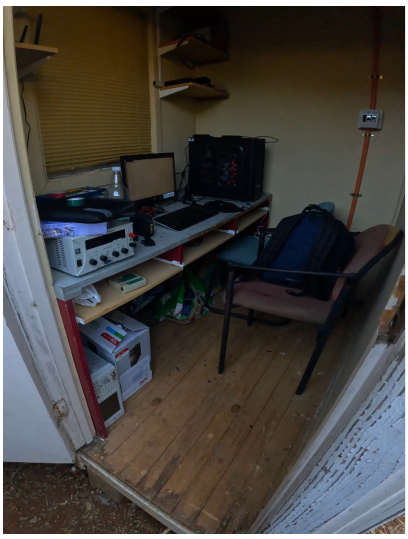

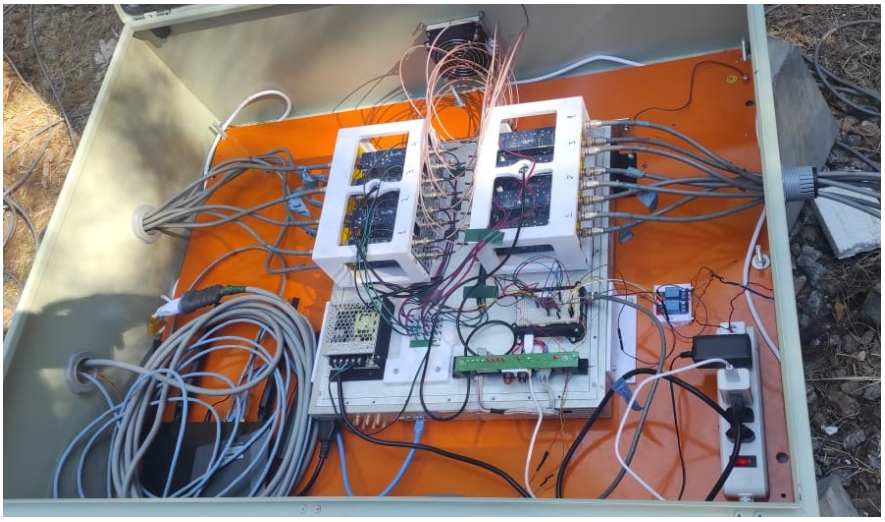

Figure 3.5.7: Picture of the setup of the analog and digital hardware of ISI-RIOmeter in the environment

Figure 3.5.8: Picture of the metal box for hardware of ISI-RIOmeter and external wood box to reduce the heating by sun radiation. .

The system collected data for approximately 3 weeks and generated 7 types of graphical results. Two of these graphs illustrate the instantaneous spectral phase and power detected by each antenna (figures 3.5.9 and 3.5.10). Another two are related to power and phase measurements in a single spectral channel over the course of a day (figures 3.5.11 and 3.5.12). The remaining three graphs are associated with spectral power of the beamforming output: one shows the spectral power of a single spectral channel throughout the day, another displays the simultaneous intensity of all spectral channels throughout the day, and the last one depicts an image generated with the beamforming, which has 87 pixels to cover the spatial range between $\theta \in [0, -30]0$ and $\phi \in [0, 360]$, based on the Nyquist theorem. This image includes the full width at half maximum (FWHM) of the central pixel and the magnitude of the side lobes. It's worth noting that these last images can be recreated for each useful spectral channel in the ISI-RIOmeter band using the data cube. Also, in figure 3.5.16, it is possible to see nine frames of the data where you can observe the passage of the galaxies over the antenna array.

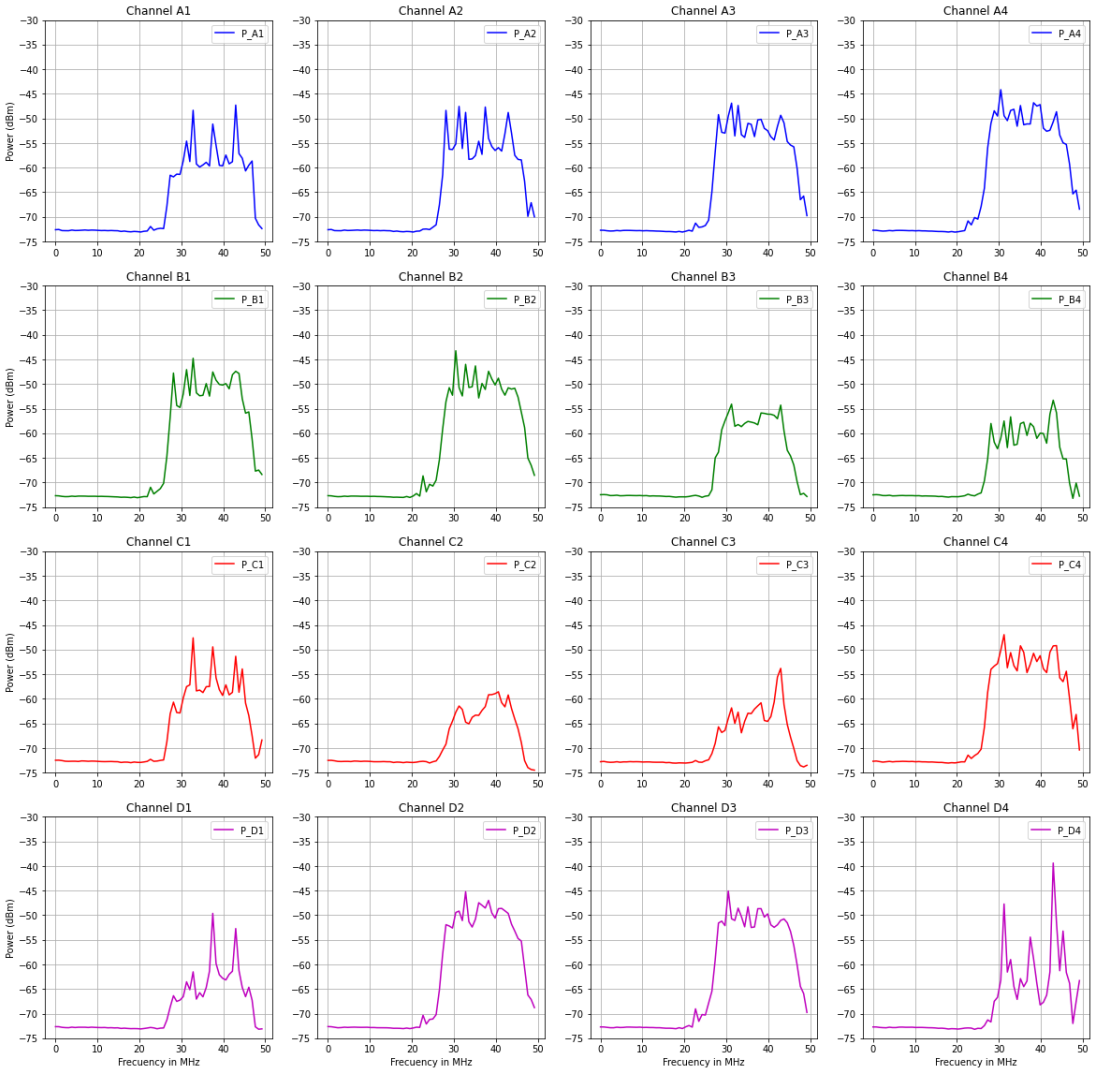

Figure 3.5.9: Instantaneous spectral power form 16 antenna dipole.

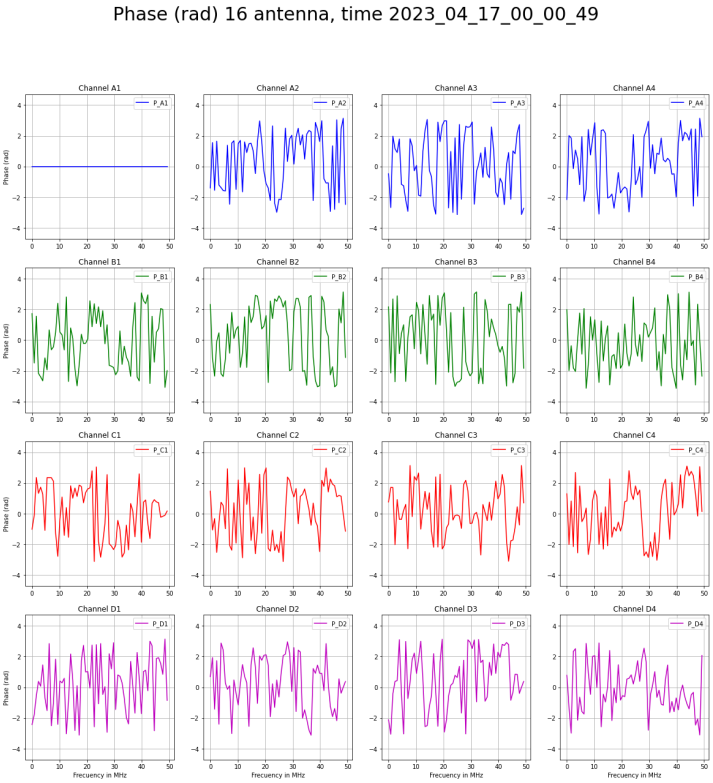

Figure 3.5.10: Instantaneous spectral phase form 16 antenna dipole.

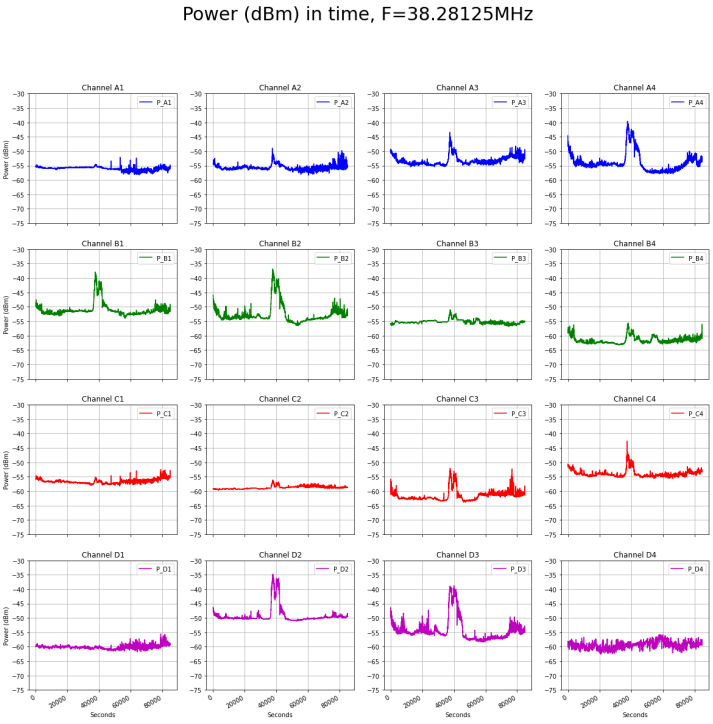

Figure 3.5.11: Spectral power of one day of data, with a integration time of 1s.

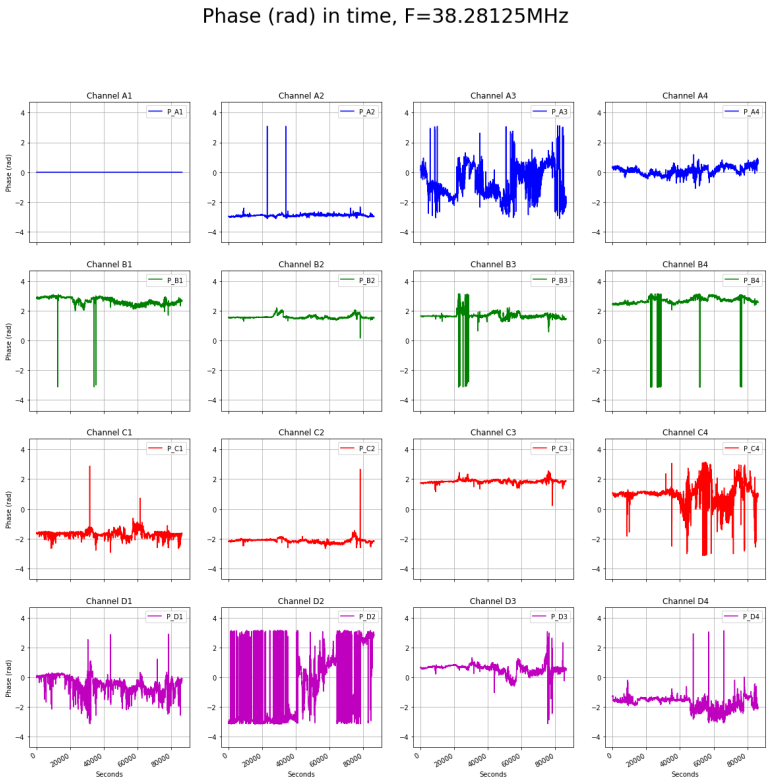

Figure 3.5.12: Relative phase of one day of data, with a integration time of 1s.

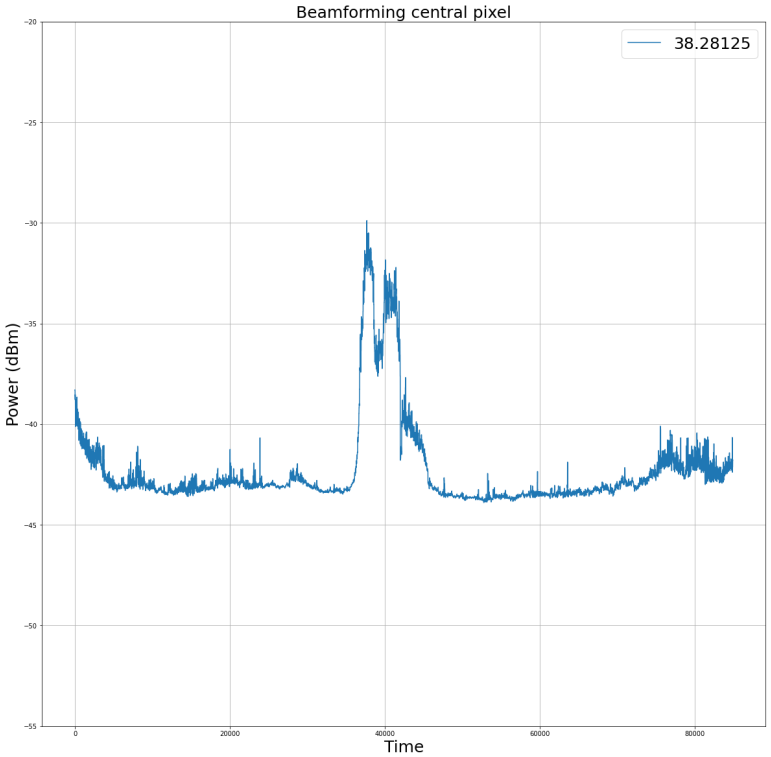

Figure 3.5.13: Beamforming spectral power output for central pixel in one frequency using one day of data.

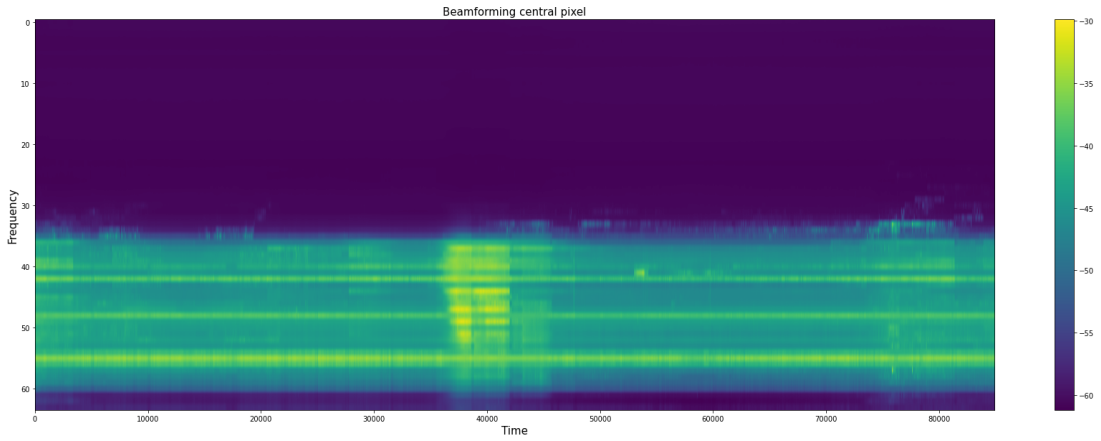

Figure 3.5.14: Beamforming spectral power output for the central pixel in all frequencies using one day of data. The plot shows the Center of the galaxy detection using the ISI-Riometer.

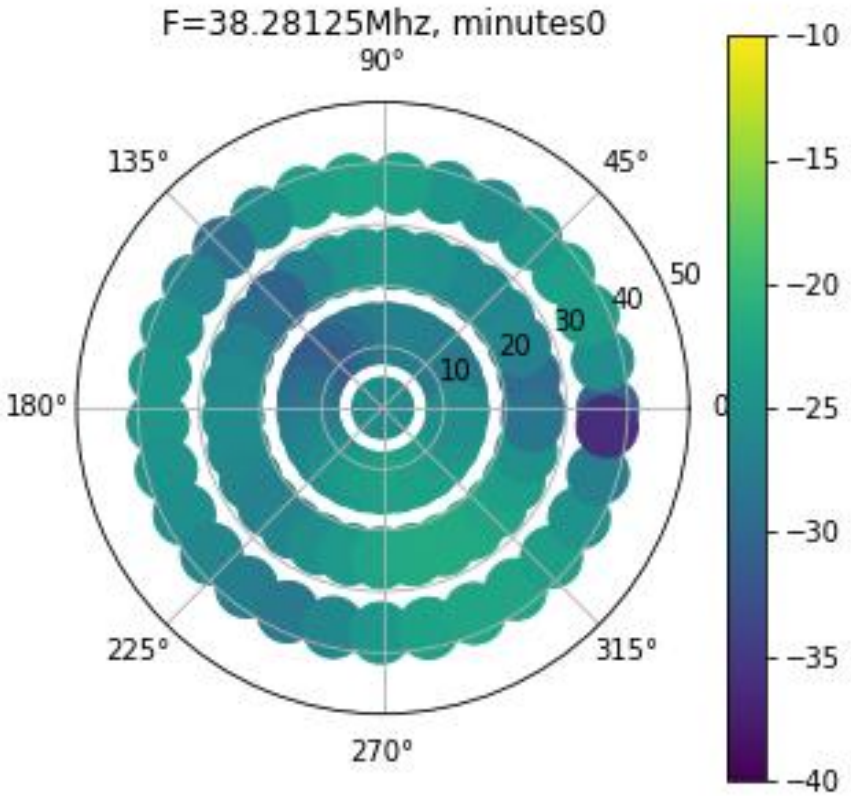

Figure 3.5.15: Image with 87 pixels generated using the beamforming technique and the data output of each one of the sixteen antennas.

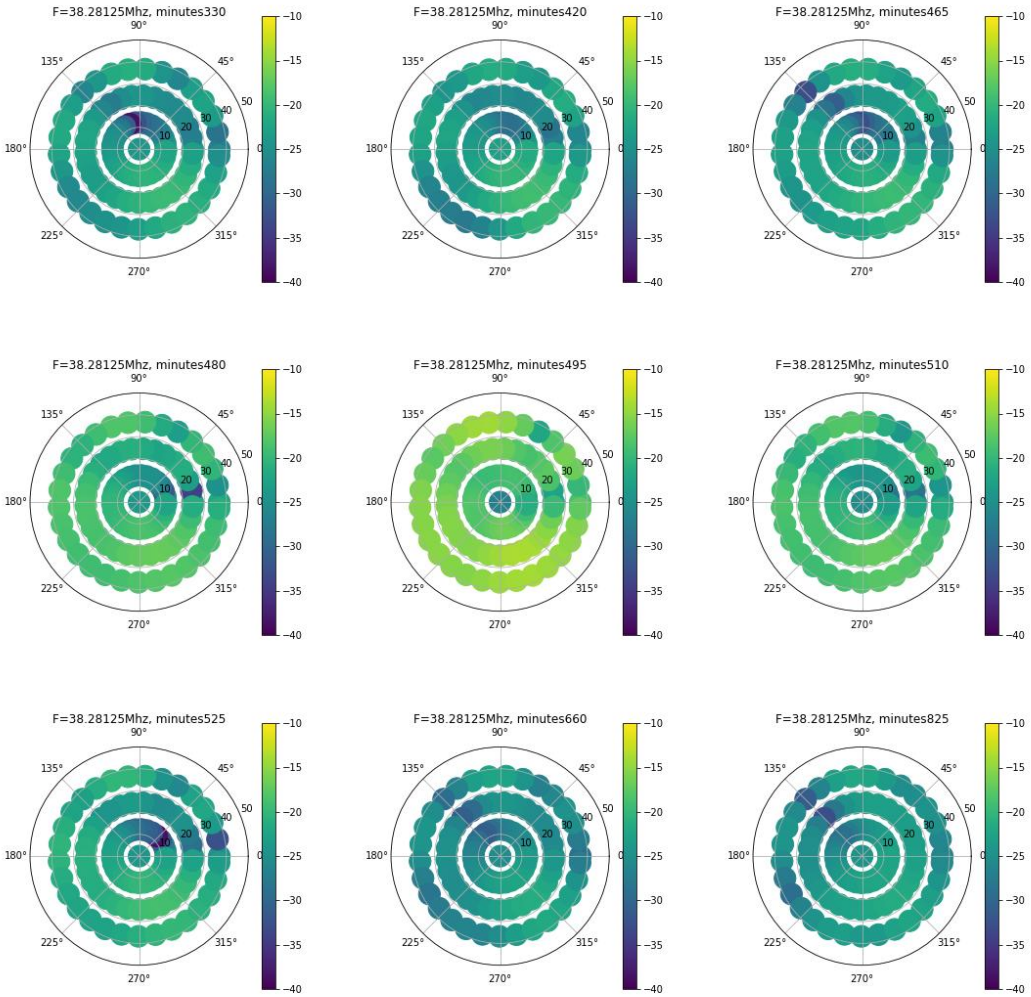

Figure 3.5.16: Center of the galaxy detection using the ISI-RIOmeter

Chapter 4

Analysis, conclusions and future works

The work undertaken in this thesis necessitates distinct analysis due to the presence of partial results for each of the sub-systems. This is essential to comprehend the comprehensive behavior of the integrated system and its deployment at the observation site, which are elucidated in the methodology chapter. This analytical journey culminates in concluding remarks and highlights future endeavors aimed at enhancing the performance of the ISI-RIOmeter.

4.1 Analysis

From the outset, the utilization of dispersion parameters, power, and phase is demonstrated to examine the performance of each individual system. These parameters are now employed to analyze and comprehend the obtained results.

4.1.1 Antennas

The analysis of the antennas commences with the numerical simulation of the ideal dipole using MATLAB 2020 (3.1.1) and FEKO 2020 (3.1.4). This step is taken to achieve an initial approximation and understanding of the antenna's behavior, as well as to observe the disparities between the analytical solution of Maxwell's equations implemented in MATLAB and the Method of Moments implemented in FEKO 2020. Both methods utilize a similar approach to solve

the equations, deriving the retarder potential from the geometrical distribution and subsequently inferring the remaining parameters.

The results from both simulations exhibit remarkable similarity, with minor discrepancies arising primarily from initial assumptions regarding the conductor materialperfect conductor in the MATLAB simulation and copper conductor in FEKO. These outcomes underscore that FEKO serves as a robust tool for analyzing antenna design and the complete array. Moreover, FEKO offers additional simulation options, including the ability to define antenna materials, segment space, determine mesh for numerical equation solutions, specify source intensity, and select the number of simulation frequencies.

Utilizing these initial outcomes and the information regarding the intensity of the Cosmic Radio Noise (CRN), the magnitude of the output spectral power from the antennas is calculated to be approximately -93.036 dBm. Employing the FieldFox VNA as a spectrometer with a noise floor at around -96 dBm enables the measurable observation of the CRN while also detecting any potential sources of noise or signals within or near the desired bandwidth.

To measure the noise floor, a fifty-ohm load was used in a bandwidth ranging from 10 MHz to 80 MHz. The obtained data reveals a value close to -96 dBm, with an uncertainty of around 0.1 dBm. The measurement of the output power from the antennas indicates an average spectral power of -92.9227 dBm within the bandwidth of 30 to 50 MHz. Outside this band, numerous high spectral points corresponding to unidentified sources are visible. These frequencies align with space research and operations, mobile and fixed telephony.

Another measurement conducted on the antennas involved characterizing the parameter S_{11}. It is evident from the results that the antennas exhibit a tuning of less than -3 dB within the expected bandwidth. Both sets of results confirm that the antennas are operational and capable of detecting signals both within and outside the desired bandwidth. Consequently, there is a need to implement bandwidth filtering before the analog-to-digital converter (ADC) in the analog receiver. This step is essential to enhance the system's performance and safeguard the ADC from potential issues.

Following the preliminary analysis to ensure the functionality of the system and conducting necessary repairs to the array, the subsequent step involved simulating

the complete array to derive radiometric parameters. The simulation initially focused on a single real element within the array. The results indicated an angular resolution of 88.3703° in θ over 360° in ϕ, along with a gain of 6.01733 dBi at the central frequency of 38 MHz. Evaluating extreme bandwidth sides revealed a variation of two degrees and 0.4 in linear gain, while maintaining the toroid-shaped radiation pattern.

Expanding the simulation to include four elements demonstrated a notable improvement in angular resolution (24° in θ over 88.5577° in ϕ) and gain (17.3436 dBi) at the central frequency. Variations of approximately 5 degrees were observed at the bandwidth limits, alongside a 1.01 linear gain variation that exhibited a flower petal-like pattern. A decrease of -12 dB was noted in secondary lobes.

The simulation with sixteen elements further improved angular resolution to 24.6146° in both θ and ϕ, while achieving a 54.6 dBi gain at the central frequency. Similar variations of approximately 5 degrees at the bandwidth limits and 15 in linear gain were observed. The radiation pattern exhibited four secondary lobes, differing by 11 dB from the main lobe.

These analyses and results establish a foundation for understanding the array's and its elements' performance, serving as a comparative framework for future modifications and endeavors. Furthermore, these findings underscore the necessity of integrating a filter into the analog receiver to eliminate undesired signals outside the bandwidth, which could potentially adversely affect the system.

4.1.2 Analog system

The design of the analog system considered the magnitude of the output signal from the antennas and the parameters of the digital back-end. This involved working with a maximum expected input spectral power of -93 dBm and a minimum of -113 dBm, with a spectral resolution of 0.8 MHz within the bandwidth from 33 to 43 MHz. This corresponds to integrated powers of -82.03 dBm and -92.03 dBm, respectively. The maximum integrated output power was +10 dBm, and the minimum was -49.92 dBm. The noise floor, determined through spectral analysis with the same resolution, reached -70.99 dBm. To ensure signal detectability, a gain of less than 45 dB and a bandwidth close to 10 MHz were deemed necessary. Based on these criteria, a validity range of 50 to 75 dB for gain and 10 to 20 MHz

for bandwidth was defined.

For the average values within the validity range of gain, bandwidth, and central frequency, a Surface-mount technology (SMT) approach over PCB FR4 was adopted. Component selection took into account cost and performance. For gain, the low noise amplifier 'MAR-8ASM+' was chosen, with a gain of 32 dB, a noise figure of 3.1 dB, and a bandwidth from DC to 1 GHz. The bandwidth was determined using AWR wizards iFilter Filter Synthesis. The filter, with a 5th order, fifty-ohm impedance, 38 MHz central frequency, and 12 MHz bandwidth, was created from scratch.

Using AWR Circuit schematics, a PCB FR4 simulation was implemented. This simulation included a microstrip transition line with pads for each SMT component. It was aimed at studying the behavior of the two amplifiers and the filter with commercial components, following the proposed design to achieve the desired gain and bandwidth. The simulation was successful and provided the green light for the analog receiver's manufacturing.

The manufacturing process was time-consuming and required iterations to create a successful system. The first iteration (V0) involved separate manufacturing of the amplifier and the filter at CePIA. The subsequent integrations (V1 and V2) were carried out at CePIA and encompassed the integration of all systems (two amplifiers and one filter). The final PCB iteration (V3) was manufactured in China by the company PCBWay, with element mounting performed at CePIA.

Results from the manufacturing process, as discussed in the previous chapter, reveal that the system response exhibited a bandwidth of 15.6 MHz, a gain of 58.3 dB, and a central frequency of 38 MHz. These results are outstanding, leading to a noise temperature of 1,001 for the analog receiver and an SNR consistently over 2

4.1.3 Digital system

The digital hardware comprises three components: the FPGA Roach2, the ADC16x250-8 converter, and the DualFrequency Synthesizer Board Valon 5007. The Synthesizer was configured to generate a synchronous 200 MHz signal with two outputsone connected to the FPGA and the other to the ADC. Simultaneously, the FPGA and ADC are linked through the ZDOK connector interface to facilitate

data transmission from the ADC to the FPGA. The ADC's configuration utilized the LVDS/RSDS interfaces, employing the RUBY language. This configuration allows the selection of operational modes (1, 2, or 4 channels, or 1 GSPS, 500 MSPS, or 250 MSPS) and the gain. For our case, all four channels were used with a gain equal to 1.

The FPGA's internal configuration encompasses a process chain designed to produce three types of data outputs. These outputs are stored in RAMs or registers for subsequent computer reading for each of the sixteen inputs. The first data path consists of the data output from the ADC, featuring values of 1 Vpp and 8 bits of resolution. This data is sent to RAMs for simultaneous reading. A duplicate of this data proceeds to the subsequent processing stage, where it undergoes Polyphase Filter Bank (PFB) implementation and Fast Fourier Transform (FFT) with 256 elements. These processes enhance bandwidth definition and facilitate the transition from the time domain to the frequency domain. Following this stage, the data divides into two paths: one path calculates amplitudes and phases, using RAMs to integrate and store information for 1 seconddata to be read by the computer. The other path employs a RAM for calibration and the implementation of beamforming weights. This generates pixel data, integrated over 1 second and stored in RAMs for computer reading.

Based on theory, spectral analysis was expected to yield a total bandwidth of 100 MHz. However, due to internal data transmission behavior, data was held for one cycle, resulting in a spectral outcome with two symmetrical Nyquist zones per spectral integration and an effective spectrum of just 50 MHz. Considering this, the final figure presented in the last section illustrates the system's corrected response. The system exhibited a noise floor of -70.99 dB, relative phase measurement precision of 0.0027 degrees between channels, and a bandwidth resolution of 0.78125 MHz per channel.

4.1.4 Integration

The implementation of the system in the laboratory works perfectly, yielding results with a variability of less than 0.001 dB in intensity and phases, with errors less than 0.001 degrees in relation to the electrical length of the cables and source used in pruves. On the other hand, the environment necessitated several complementary tasks, including establishing electrical and Ethernet connections,

utilizing a metal box for environmental protection, employing a wooden box to mitigate temperature fluctuations caused by solar radiation, and creating a local ground for the circuits. After several days of measurements and data analysis, the system demonstrated the potential to detect the maximum Cosmic Ray Noise (CRN) when the center of the galaxy was directly above the array's zenith. However, it also exhibited an inability to measure regions of the galaxy with lower power, without an apparent explanation.

The system's performance showcases ample sensitivity to measure variability down to 0.001 dB. The beamforming process aligns with expectations when the galaxy passes over the array, as depicted in the figures illustrating the instant plot and timeline plot of power and phase. From these plots, it is evident that certain elements are unable to detect the signal and phase, resulting in a significant amount of noise when the center of the galaxy is positioned outside the array's field of view.

4.2 Conclusions

The analysis of each of the results has led to several important conclusions. Among these conclusions, the most significant is the successful achievement of the objectives set forth at the outset of this work, which represent a notable evolution of RIOMETERs.

- The cosmic noise signal is spectrally detectable at low latitudes using the wide-bandwidth dipole antennas implemented by Professor Foppiano, which are still operational.
- The beamforming algorithm on the array improve the resolution from 98° to 24.6146° and the gain from 6 to 54.6 dBi, that is, to 25% and 910% respectively to a single element.
- The analog system complies with the imposed requirements and its noise contribution does not generate complications in signal detection, keepinh allways a SNR>3 to environment temperature (6-23 Celsius).
- The digital system is capable of integrating the response of the elements synthesizing the beamforming within its architecture, offering the possibility of multiple observations, with an almost negligible error, correctable in

calibration.

- the system can work for days and generate apartial detection of CRN.
- The cost of implementing the project is around 10,000 dollars, approximately 8 million pesos, without considering the work of the staff and previous or future efforts.

4.3 Future works

The successful implementation of the ISI-RIOMETER was a titanic task and produce a unique opportunity for the technology transfer and science to different fields like telecommunications, electrical, electronics, programming, and others associated with physics, astronomy, and geophysics. Because opens an opportunity in each of these fields to explore is stated of the art and prove the new concept in the current system of ISI. To give an idea about what is possible to do in the future, here we have a make a list in sequential order

1. Calibration proposal.
2. Data reduction Proposal.
3. Data analysis proposal.
4. Observational proposal.
5. New antenna array distribution.
6. Double polarisation antenna array.
7. New analog receiver dissing.
8. Auto-calibration analog receiver.
9. New digital receiver dissing.
10. Double polarisation digital receiver.
11. Auto-calibration digital receiver.
12. Correlator RIOMETER.
13. Less expensive digital architecture.

Bibliography

Allan, D. (1987). Time and frequency (time-domain) characterization, estimation, and prediction of precision clocks and oscillators. *IEEE Transactions on Ultrasonics, Ferroelectrics, and Frequency Control*, 34(6):647–654.

A.Naparstek (1963). Efective antena temperature from terrestrial and cosmic noise in the 0.1 to 40.0 gc band. Measure, Institute of Science and technology, The university of michigan.

A.P.Mitra, C. et al. (1953). The measurement of ionospheric absorption using observations of 18ů3 Mc/s cosmic radio noisen. *Journal of Atmospheric and Terrestrial Physics*, 4(4-5):204–218.

Arfken, G. B. (1985). *Mathematical methods for physicists*. Academic Press, 3rd ed edition.

Barott, W. C., Milgrome, O., Wright, M., MacMahon, D., Kilsdonk, T., Backus, P., and Dexter, M. (2011). Real-time beamforming using high-speed fpgas at the allen telescope array. *Radio Science*, 46(1).

B.D.Van Veen, K. B. (1988). Beamforming: a versatile approach to spatial filtering. *IEEE ASSP Magazine*, 5(2):4–24.

Beynon, W. J. G. and Brown, G. M. (1957). *IGY instruction manual: the ionosphere. / Editors : W. J. G. Beynon and G. M. Brown. Pref. by Edward Appleton*. Pergamon Press London, New York.

Bittencourt, J. A. (2004). *Fundamentals of Plasma Physics*. Third edition.

Bowick, C., Ajluni, C., and Blyler, J. (2007). *RF Circuit Design, Second Edition*. Newnes, USA, 2nd edition.

Brekke, A. (2012). *Physics of the Upper Polar Atmosphere*. Springer Atmospheric Sciences. Springer Berlin Heidelberg.

Browne, S., Hargreaves, J., and Honary, B. (1995). An imaging riometer for ionospheric studies. *Electronics and Communication Engineering Journal*, 7(5):209–217.

Calquin, C. (2021). Análisis de sistema análogo para riometer. Tesis, Instituto profecional, Virginio Gómez.

C.G. Little, H. et al. (1959). The Riometer-A Device for the Continuous Measurement of Ionospheric Absorption. *Proceedings of the IRE*, 47(2):315–320.

Cohen, J. (1982). Introduction to noise in solid state devices. TECHNICAL NOTE 1169, Center for Radiation Research, National Measurement Laboratory, National Bureau of Standards, Washington, DC 20234. 1169.

Cooley, J. W. and Tukey, J. W. (1965). Time resolution of cosmic noise observations with acorrelation experiment. *Annales Geophysicae*, 19:297–301.

Creative, C. (2021). Square kilometre array (ska). [Web; accedido el 01-06-2021].

Davies, K. (1990). *Ionospheric Radio*. The Institution of Engineering and Technology, London.

D.B. Sullivan, D.W. Allan, D. H. F. W. (1990). *Characterization of Clocks and Oscillators*. NIST Technical Note 1337. National Institute of Standards and Technology.

Detrick, D. L. Rosenberg, T. J. (1990). A phased-array radiowave imager for studies of cosmic noise absorption. *Radio Science*, 25(4):325–338.

Dowell, J., Taylor, G. B., Schinzel, F. K., Kassim, N. E., and Stovall, K. h. (2017). The LWA1 Low Frequency Sky Survey. , 469(4):4537–4550.

Finlay, C. C., Kloss, C., Olsen, N., Hammer, M. D., Tøffner-Clausen, L., Grayver, A., and Kuvshinov, A. (2020). The CHAOS-7 geomagnetic field model and observed changes in the South Atlantic Anomaly. *Earth, Planets and Space*, 72(1):156.

G. Rubilar, F. I. and others. (2020). Electrodinámica clásica. Technical report, Universidad de Concepción.

Greiner, W. and Bromley, D. (2000). *Queantum Mechanics an introduction*. springer.

Griffiths, D. J. (2012). *Introduction to Electrodynamics*. Pearson Education, 4th edition.

Griffiths, D. J. (2017). *Introduction to Electrodynamics*. Cambridge University Press, 4th revised edition.

Guzmán, A. E., May, J., Alvarez, H., Maeda, K., et al. (2011). All-sky Galactic radiation at 45 MHz and spectral index between 45 and 408 MHz. , 525:A138.

Hargreaves, J. K. (1992). *The solar-terrestrial environment: An introduction to geospace–the science of the terrestrial upper atmosphere, ionosphere, and magnetosphere*. Cambridge University Press, England.

Hargreaves, J. K. (1995). *The solar-terestrial environment. An introduction to geospace - the science of the terrestrial upper atmosphere, ionosphere and magnetosphere.* Cambridge University press.

Hill, R., Masui, K. W., and Scott, D. (2018). The Spectrum of the Universe. *Applied Spectroscopy*, 72(5):663–688.

Honary, F. M. et al. (2011). Invited Article: Digital beam-forming imaging riometer systems. *Review of Scientific Instruments*, 82(3):031301–031301–15.

Hunsucker, R. (1991). Radio Techniques for Probing the Terrestrial Ionosphere. Physics and Chemistry in Space. *Springer*.

H.Unz (1956). Linear arrays with arbitrarily distributed elements. Elect.Reac. Lab, Rept. 168, University of California, Berkeley.

H.Unz (1960). Linear Arrays with arbitrarily distributed elements. *IRE Transactions on Antennas and Propagation, IEEE*, 8(1):222–223.

Jansky, K. G. (1982a). *1932, Directional Studies of Atmospherics at High Frequencies*, volume 10, page 10.

Jansky, K. G. (1982b). *1933, Electrical Disturbances Apparently of Extraterrestrial Origin*, volume 10, page 23.

K.A.Zawdie, D. P. D. et al. (2017). Calculating the absorption of hf radio waves in the ionosphere. *Radio Science*, 52(6):767–783.

Kendal, W. S. and Jørgensen, B. (2011). Tweedie convergence: A mathematical basis for taylor's power law, $1/f$ noise, and multifractality. *Phys. Rev. E*, 84:066120.

Kester, W. (2006a). Adc input noise: The good, the bad, and the ugly. is no noise good noise? TECHNICAL NOTE 40-02, Analog Devices.

Kester, W. (2006b). Understand sinad, enob, snr, thd, thd + n, and sfdr so you don't get lost in the noise floor. TECHNICAL NOTE MT-003, Analog Devices.

Kittel, C. (2005). *Introduction to Solid State Physics*. Wiley, 8th ed edition.

Lizhe Tan Ph.D. Electrical Engineering University of New Mexico, J. J. P. E. E. U. o. N. M. (2018). *Digital Signal Processing: Fundamentals and Applications*. Academic Press, 3 edition.

Lizon, B. (2020). Fundamentals of precision adc noise analysis. TECHNICAL NOTE 40-02, Texas Instruments.

Maxfield, C. (2008). *FPGAs: Instant Access*. Newnes.

Maxwell, J. C. (1865). A dynamical theory of the electromagnetic field. *Phil. Trans. R. Soc. Lond.*, 155(https://doi.org/10.1098/rstl.1865.0008):459–512.

McFadden, L. A. A., Weissman, P. R., and Johnson, T. V. (2007). *Encyclopedia of the solar system*.

Moss, Gregory L.; Tocci, R. J. W. N. S. (2016;2017). *Digital systems: principles and applications*. Pearson, 12. edition edition.

M.T.Ma (1974). *Theory and Application of Antenna Arrays*. John Wiley Sons Inc.

Murayama, Y., Mori, H., Kainuma, S., Ishii, M., Nishimuta, I., Igarashi, K., Yamagishi, H., and Nishino, M. (1997). Development of a high-resolution imaging riometer for the middle and upper atmosphere observation program at poker flat, alaska. *Journal of Atmospheric and Solar-Terrestrial Physics*, 59(8):925–937. Imaging Riometers.

M.V.Stepanovaa, E.E.Antonovab, A. T. E. et al. (2005). Intermittency of riometer auroral absorptionobserved at South Pole. *Journal of Atmospheric and Solar-Terrestrial Physics*, 65(1):1718.

NI (2021). Instrument fundamentals: Complete guide. Technical note, National Instruments.

Nielsen, E., Honary, F., and Grill, M. (2004). Time resolution of cosmic noise observations with acorrelation experiment. *Annales Geophysicae*, 22(5):1687–1689.

Nishino, M.; Makita, K. F. A. and Monreal, R. (2004). NetworkObservationsof Imaging RiometersinSouthAmerica. *Bulletin of Science and Engineering Takushoku University*, (9):31–36.

NRAO (2018). Wave propagation in a plasma. https://www.cv.nrao.edu/ sransom/web/A4.html.

Observatory, A. (2021). Atacama large millimeter/submillimeter array (alma). [Web; accedido el 01-06-2021].

Overby, R. C. J. (2022). *Chemistry*. 14 edition.

Pozar, D. M. (2005). *Microwave engineering; 3rd ed.* Wiley, Hoboken, NJ.

Ratcliffe, J. A. (1970). *Sun, earth and radio: an introduction to the ionosphere and magnetosphere [by] J. A. Ratcliffe*. Weidenfeld Nicolson London.

Rishbeth, H. and Garriott, O. K. (1969). *Introduction to ionospheric physics [by] Henry Rishbeth [and] Owen K. Garriott*. Academic Press New York.

Rosenberg, T. J., Wang, Z., Rodger, A. S., Dudeney, J. R., and Baker, K. B. (1993). Imaging riometer and hf radar measurements of drifting f region electron density structures in the polar cap. *Journal of Geophysical Research: Space Physics*, 98(A5):7757–7764.

Rubilar, G. (2019). *Física Matematica II*. GPL v3.

S.Browne, J.K.Hargreaves, B. et al. (1995). An imaging riometer for ionospheric studies. *Electronics Communication Engineering Journal*, 7(5):209 – 217.

S.Nordebo, I.Claesson, S. et al. (1994). Adaptive beamforming: Spatial filter designed blocking matrix. *IEEE Journal of Oceanic Engineering*, 19(4):583–590.

Thomas L. Wilson, Kristen Rohlfs, S. H. a. (2009). *Tools of Radio Astronomy*. Astronomy and Astrophysics Library. Springer Berlin Heidelberg, 5th ed. edition.

Trimberger, S. M. (2015). Three ages of fpgas: A retrospective on the first thirty years of fpga technology. *Proceedings of the IEEE*, 103(3):318–331.

Ulaby, F. T. (2007). *Fundamentos de aplicaciones en electromagnetismo*. Prentice Hall / Pearson, México [etc.], 5ł ed. edition.

Walter Greiner, D. B. (1998). *Classical Electrodynamics*. Classical Theoretical Physics. Springer, 1 edition.

Chapter 5

FEKO

Dipolo ideal 0.38-224MHz

C:/Users/Cepia-beam/Documents/Feko/dipolo ideal
2022-03-15 11:58

S-parameter

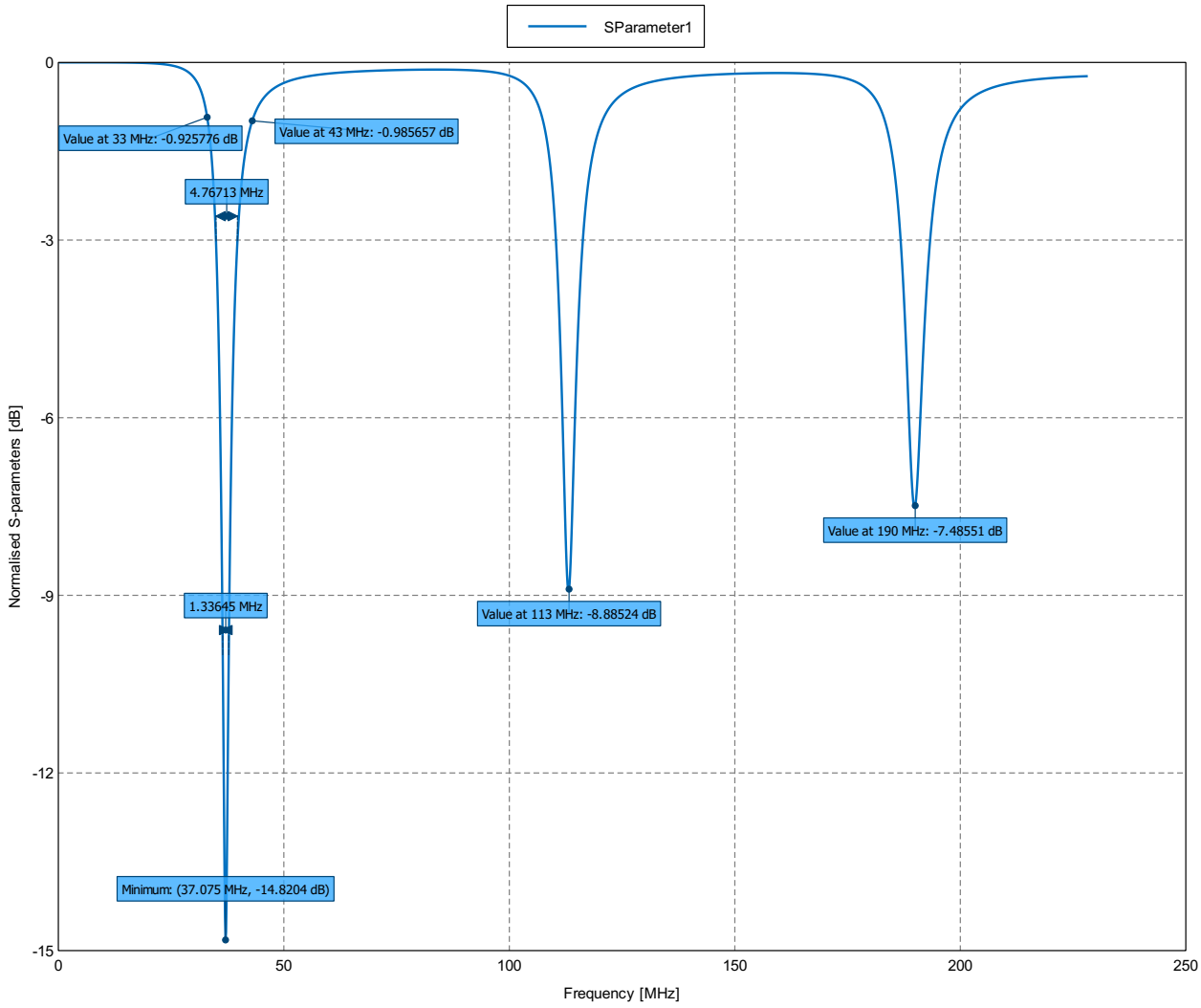

Figure 1: S-parameters Magnitude [dB] (S-parameter = S1,1) - Dipolo

Power

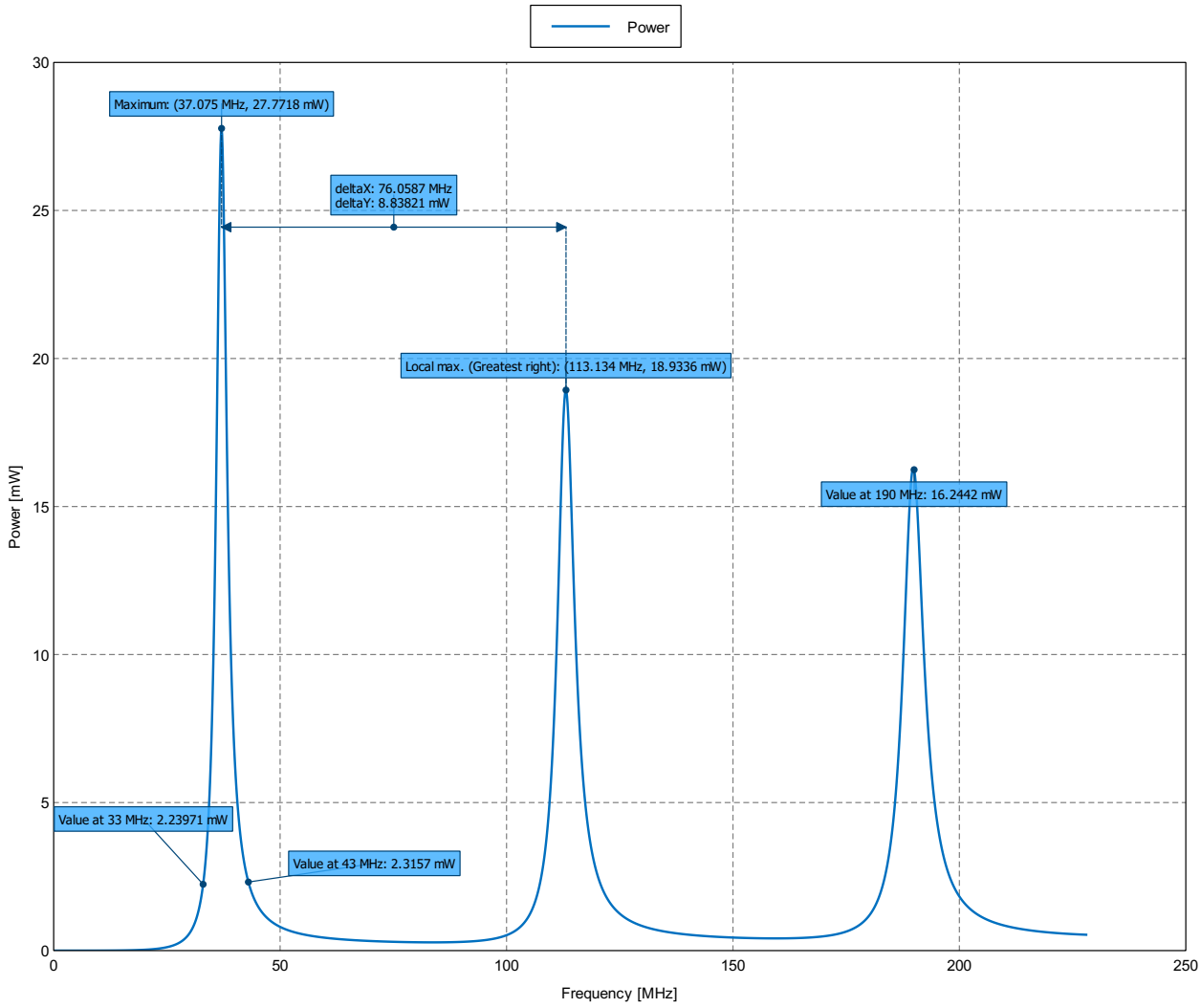

Figure 2: Active Power [mW] - Dipolo

Power db

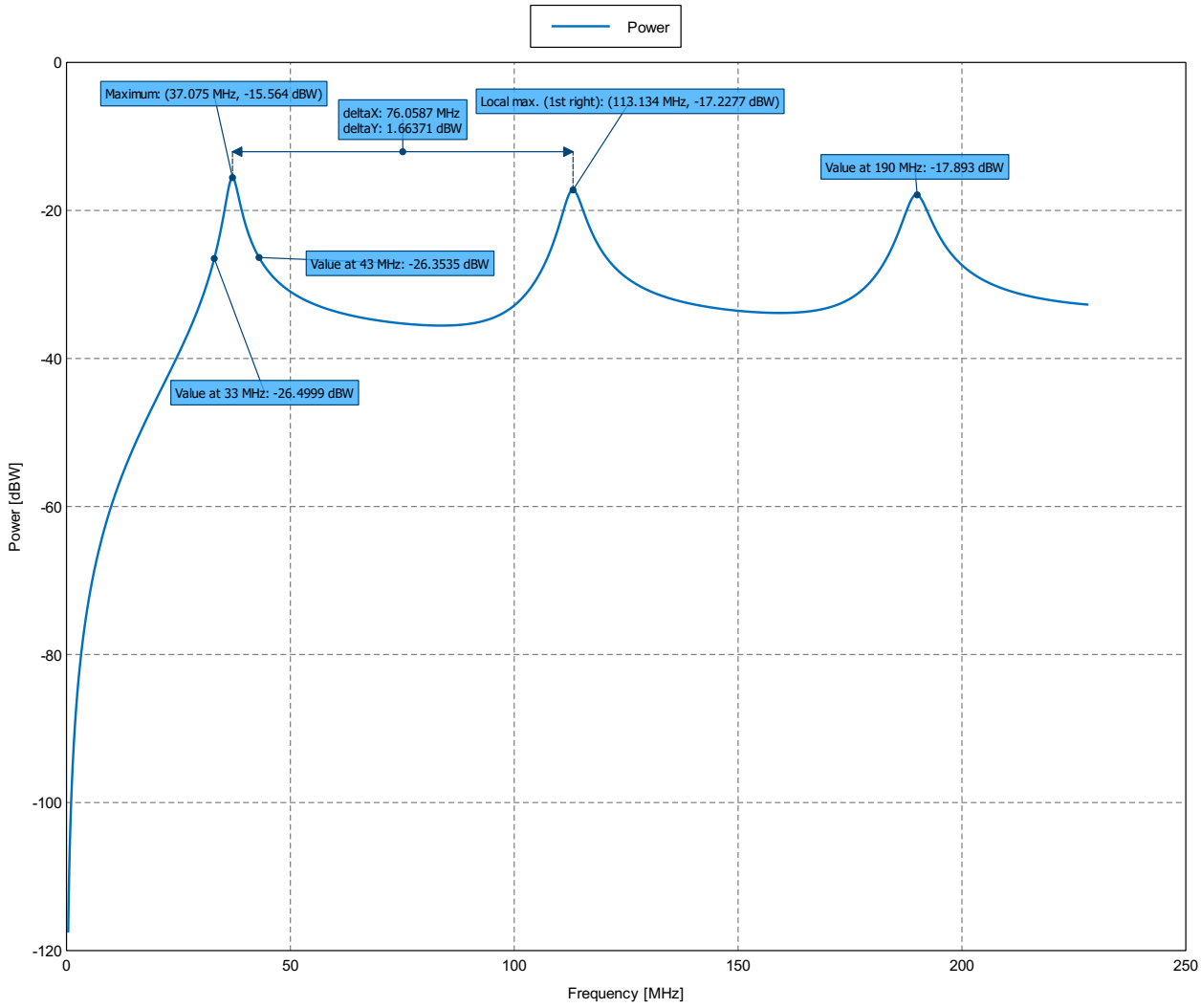

Figure 3: Active Power [dBW] - Dipolo

Far field: E

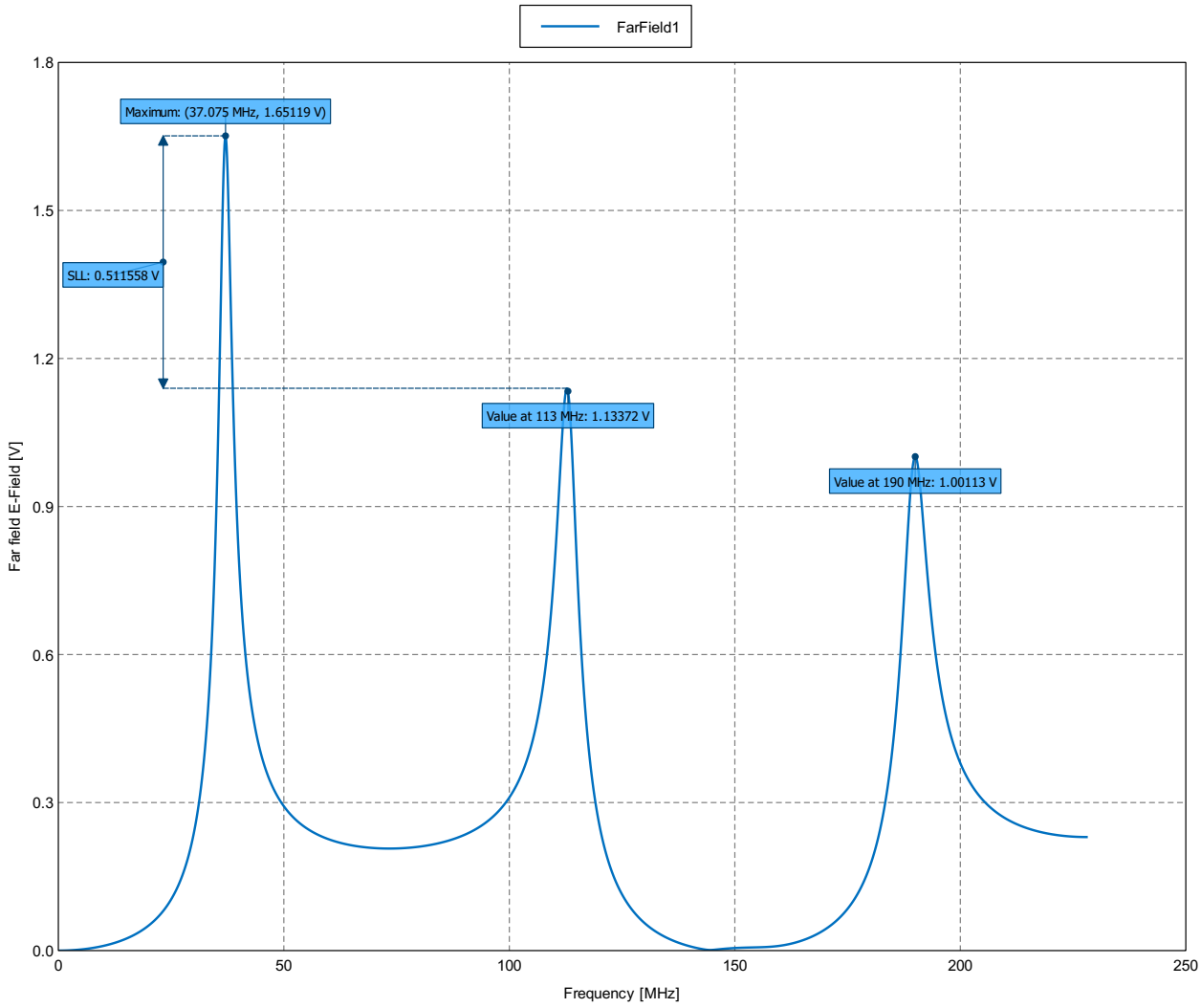

Figure 4: Total E-Field Magnitude [V] (Theta = 0 deg; Phi = 0 deg) - Dipolo

Far field: E_db

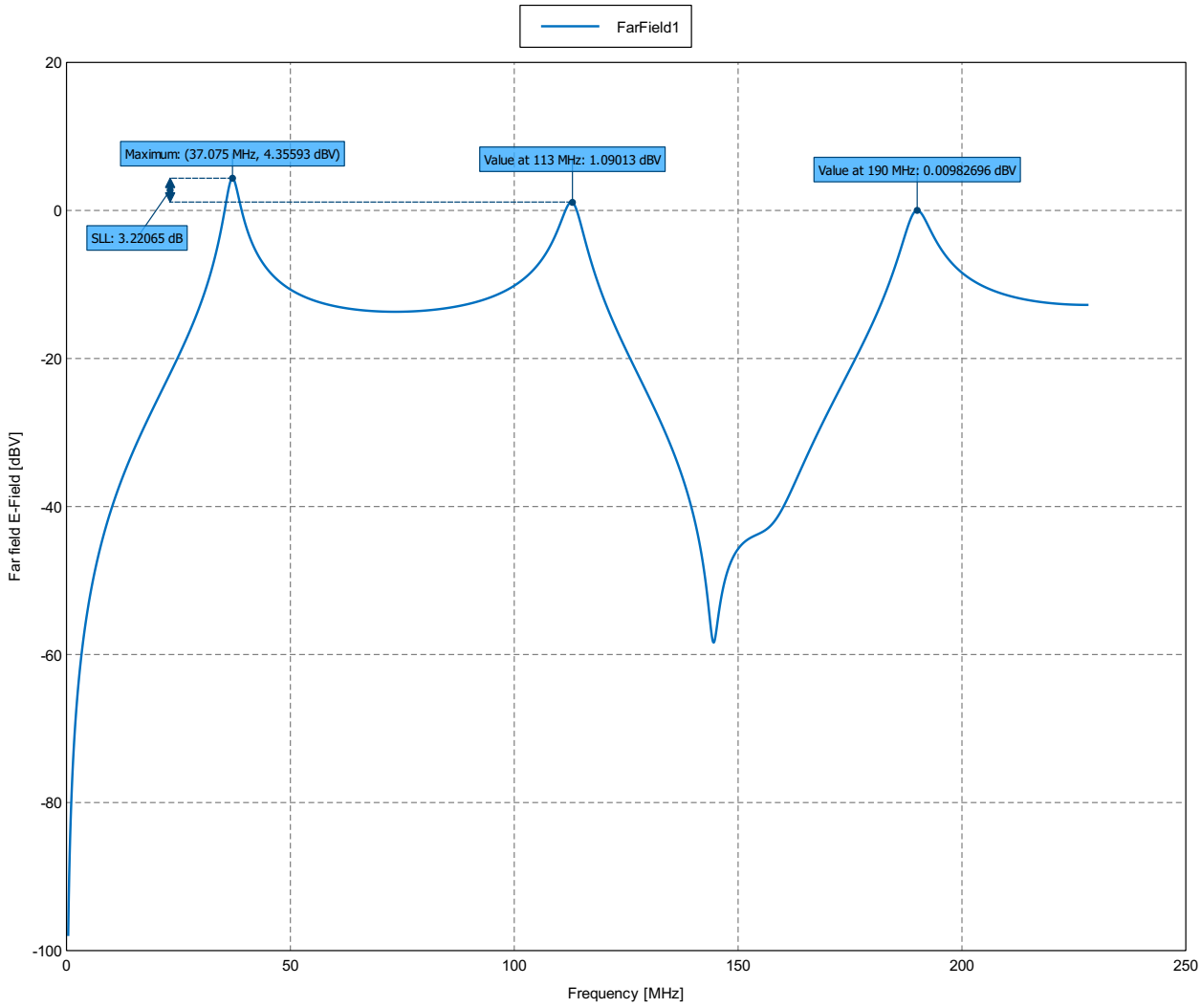

Figure 5: Total E-Field Magnitude [dBV] (Theta = 0 deg; Phi = 0 deg) - Dipolo

Far field: G

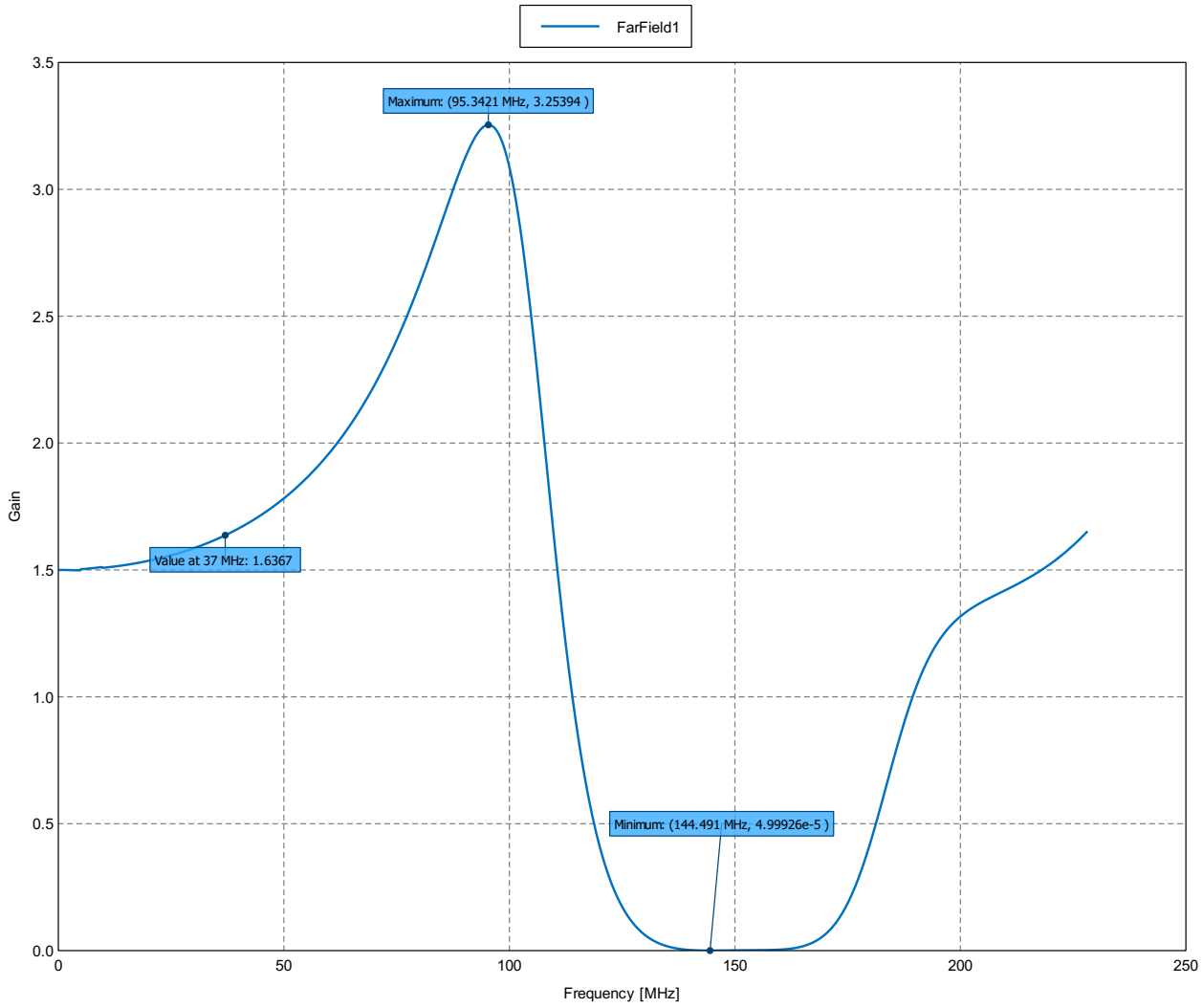

Figure 6: Total Gain (Theta = 0 deg; Phi = 0 deg) - Dipolo

Far field: G_dbi

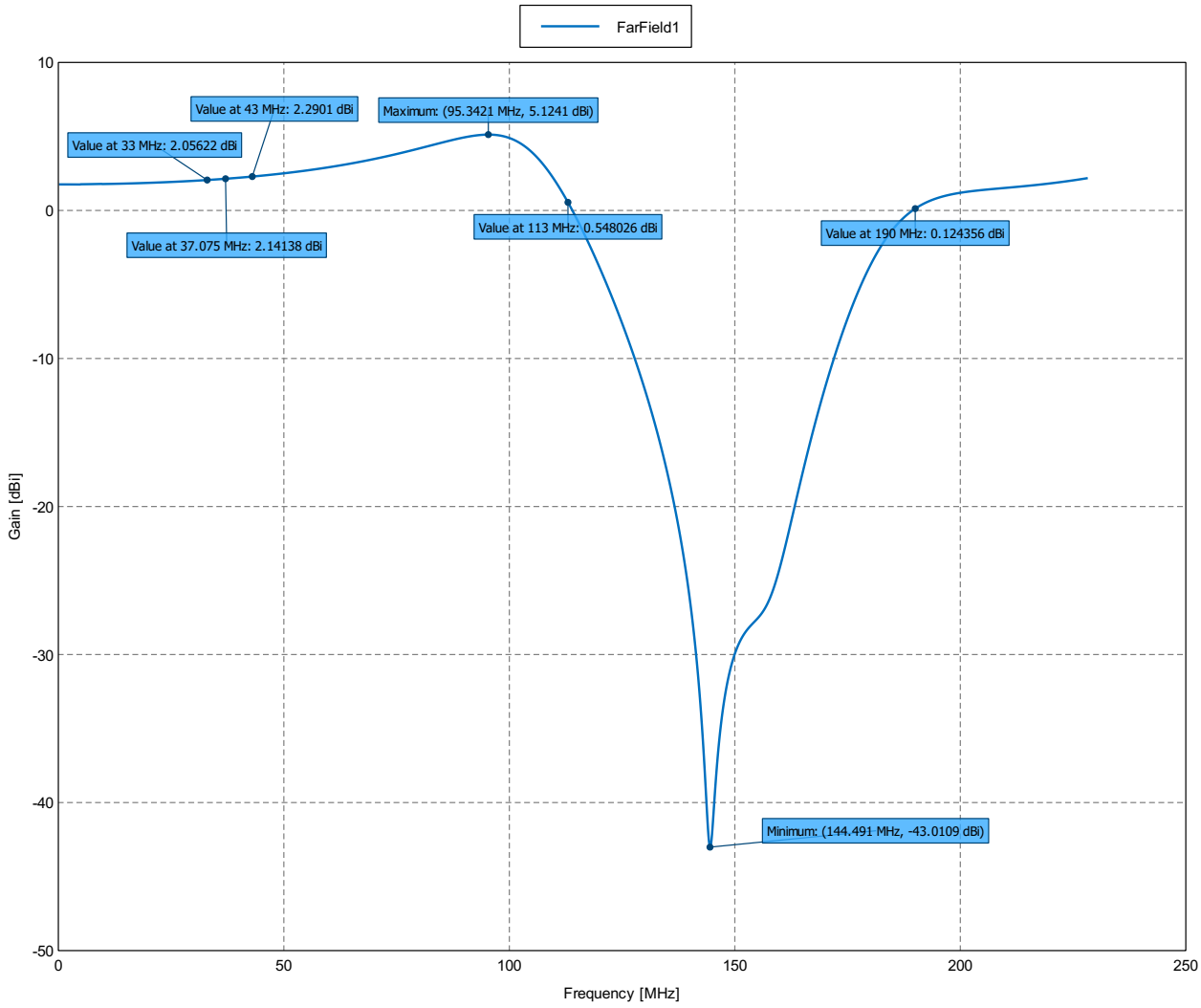

Figure 7: Total Gain [dBi] (Theta = 0 deg; Phi = 0 deg) - Dipolo

Far field: D

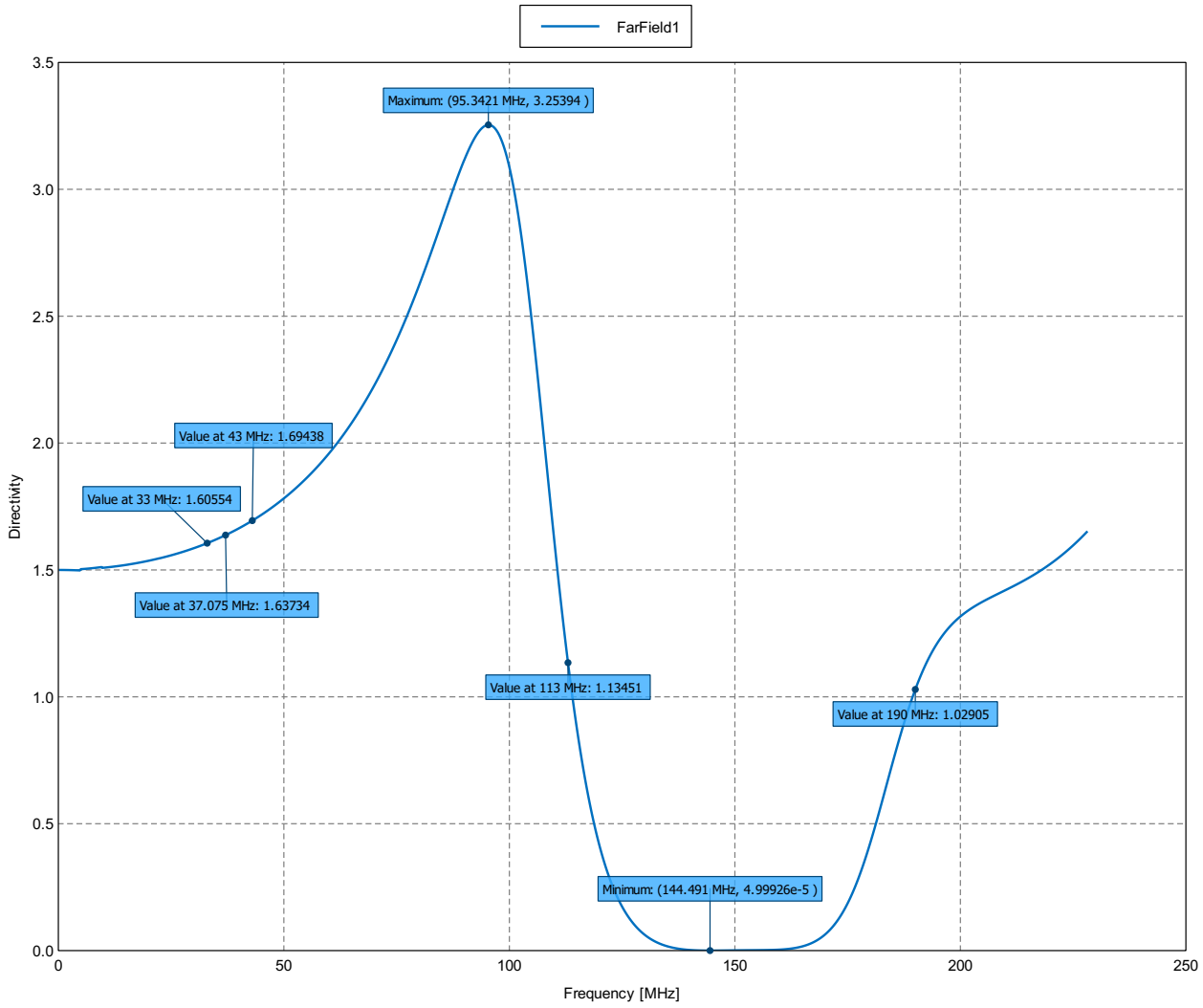

Figure 8: Total Directivity (Theta = 0 deg; Phi = 0 deg) - Dipolo

Far field: D_dbi

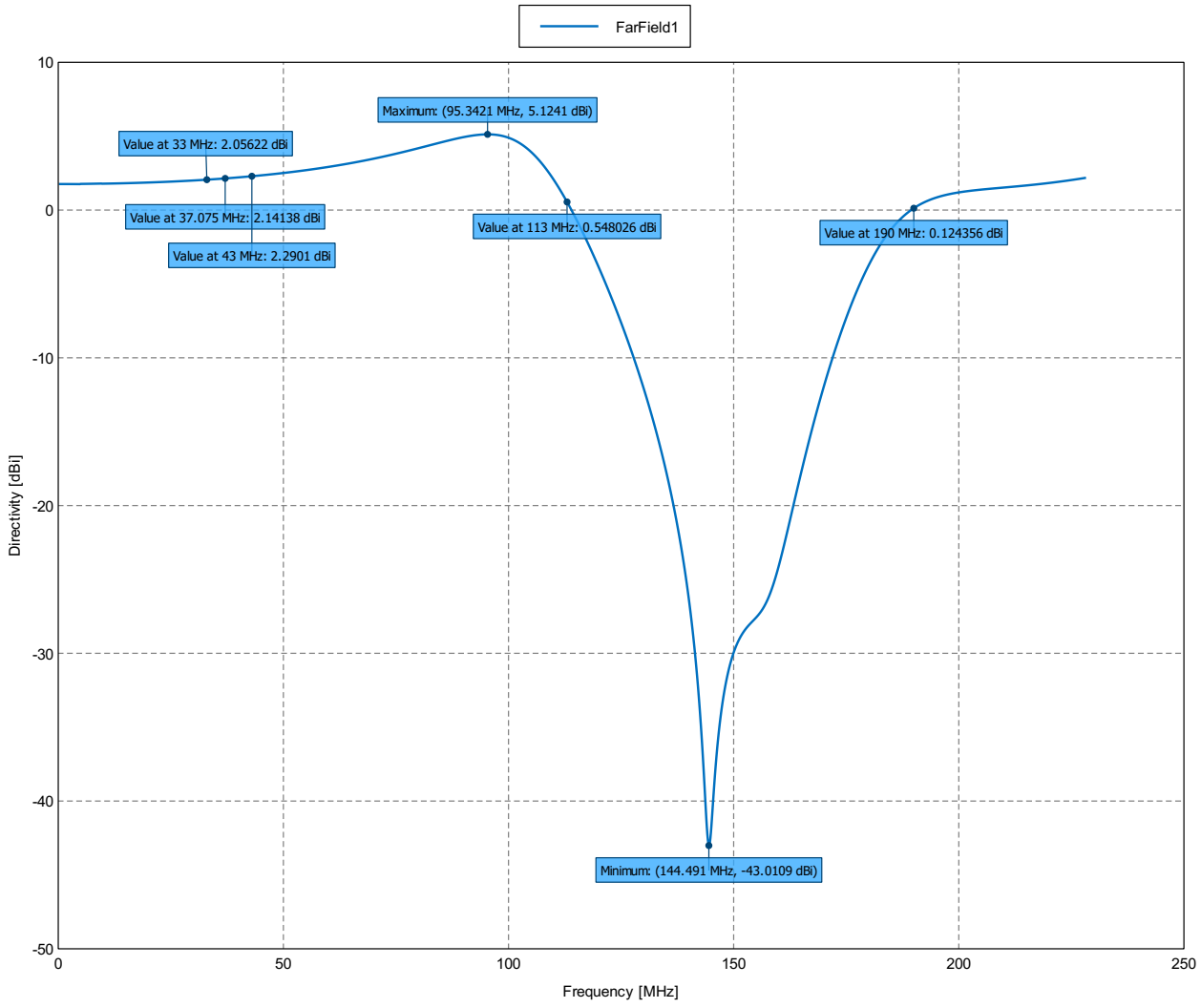

Figure 9: Total Directivity [dBi] (Theta = 0 deg; Phi = 0 deg) - Dipolo

E_n_db_37MHz

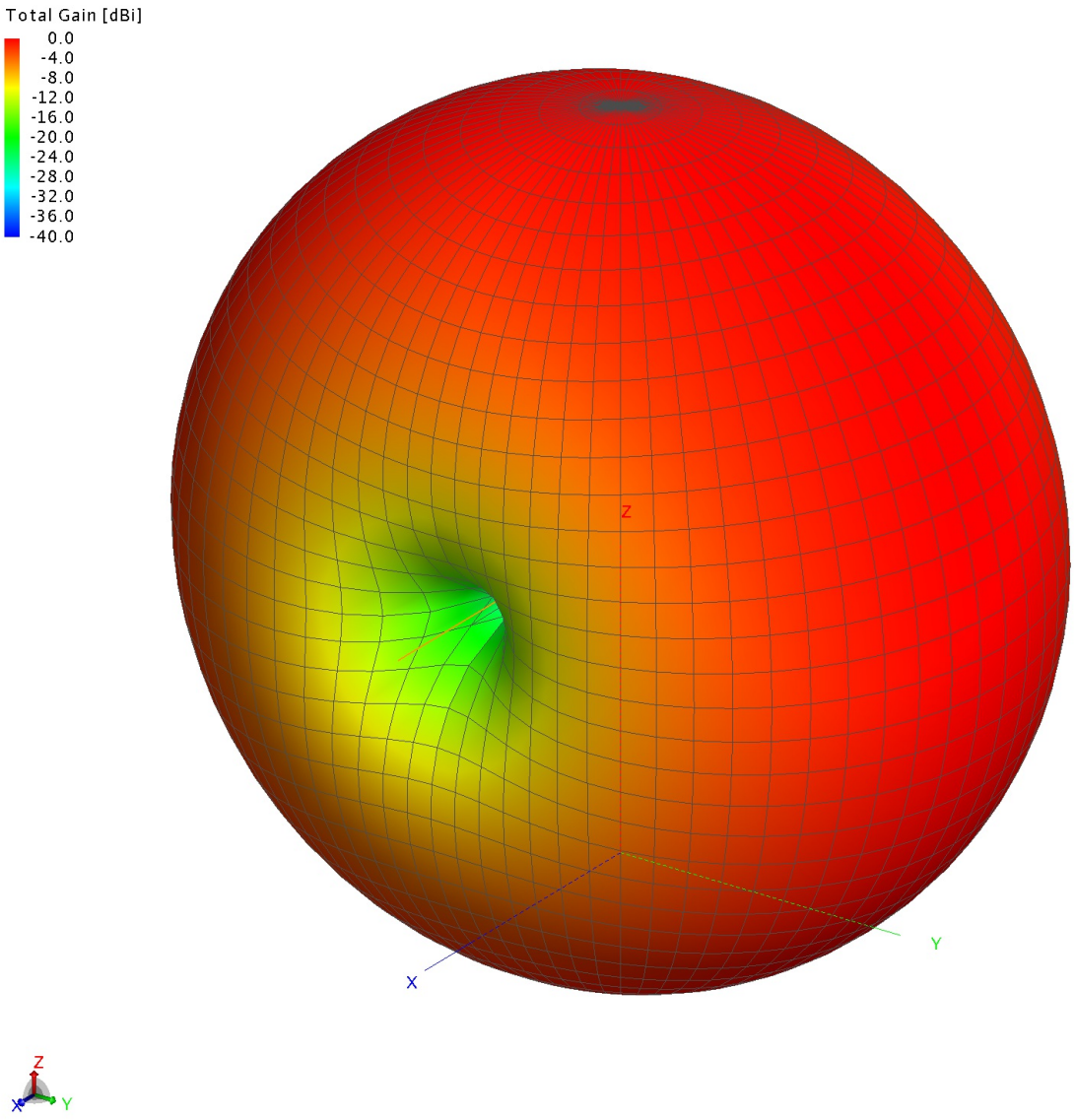

Figure 10: 3D View

G_n_dbi_37Mhz

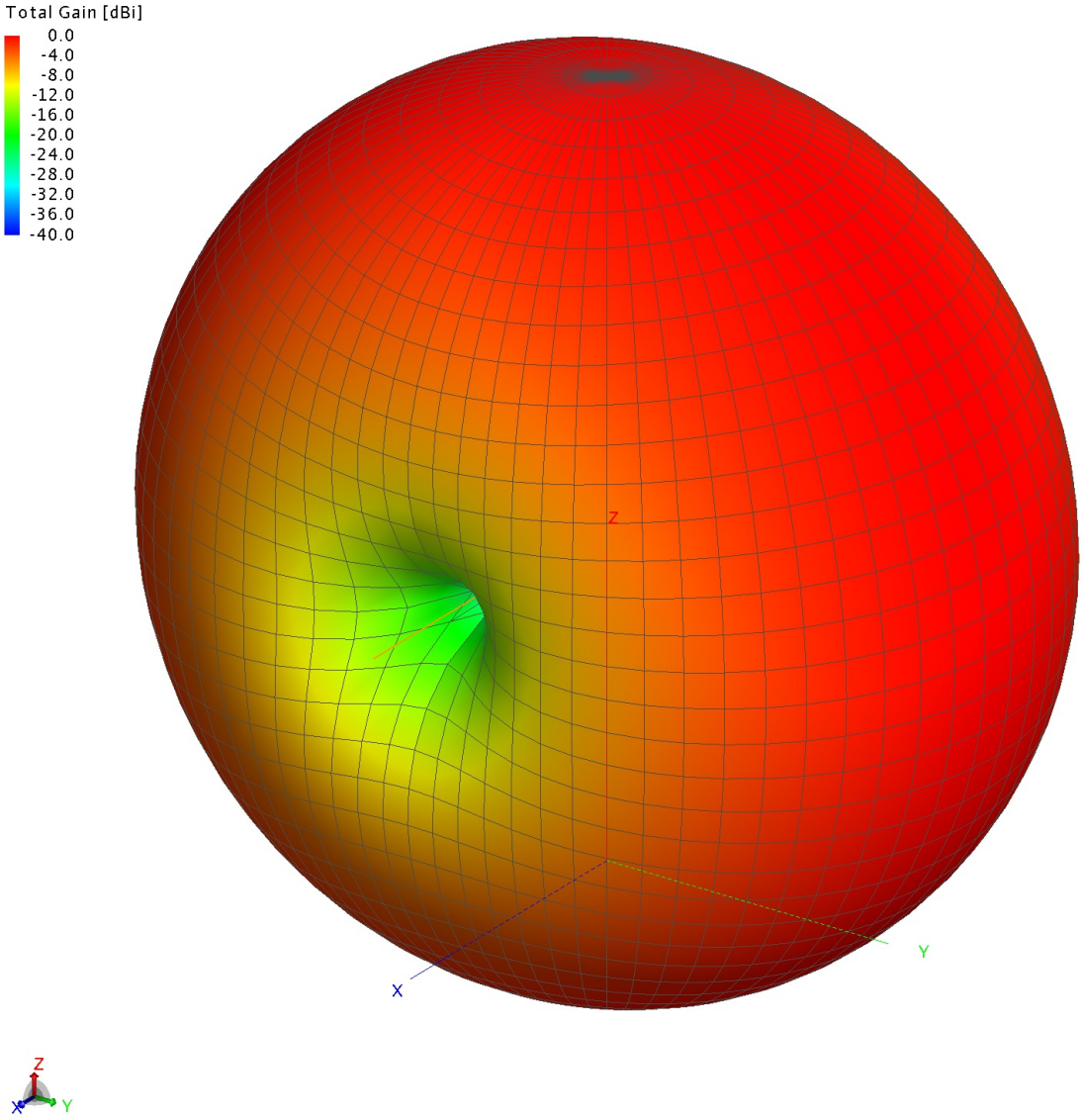

Figure 11: 3D View

D_n_db_37MHz

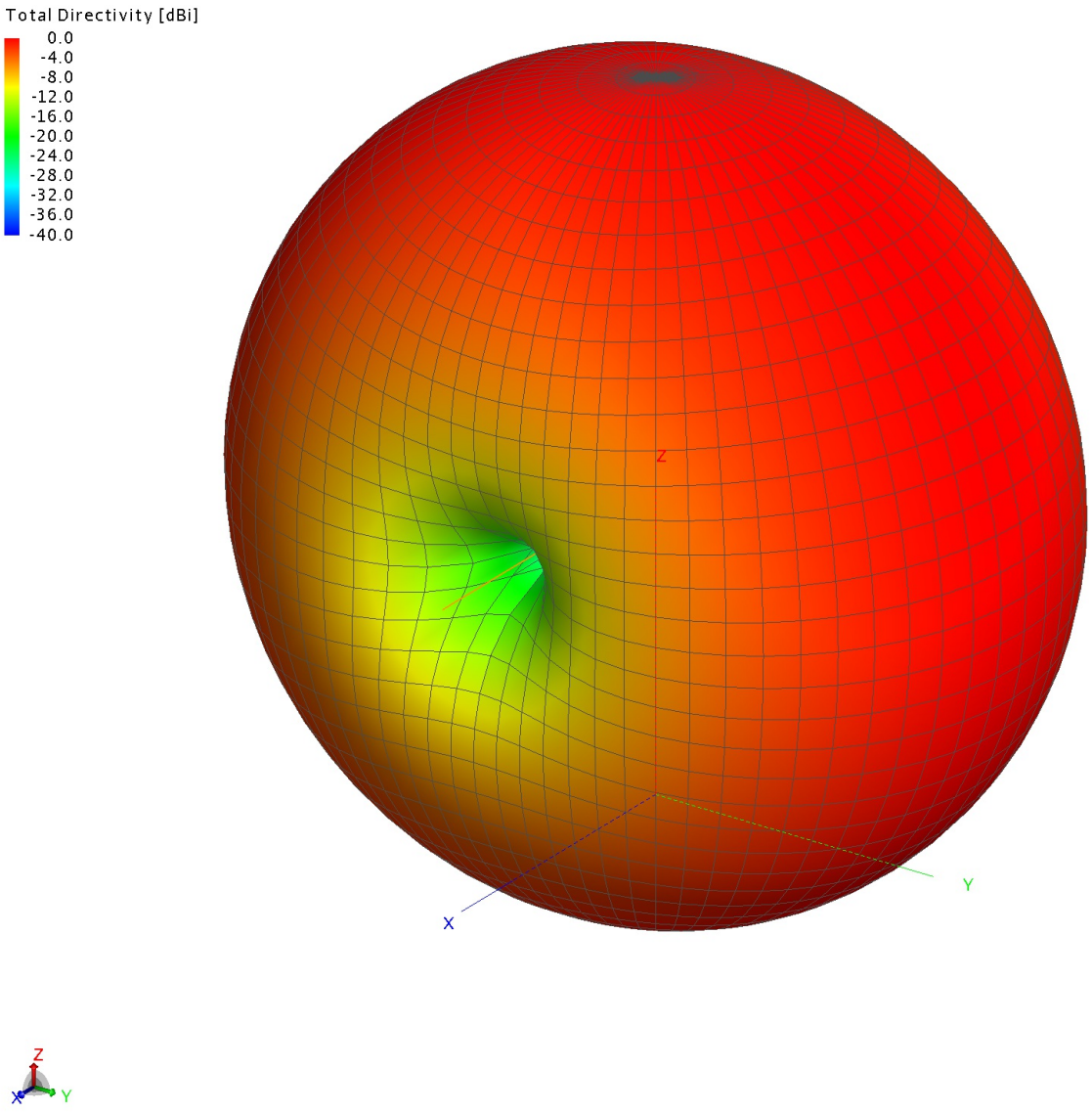

Figure 12: 3D View

FarField1: Total E-Field Magnitude [dBV]

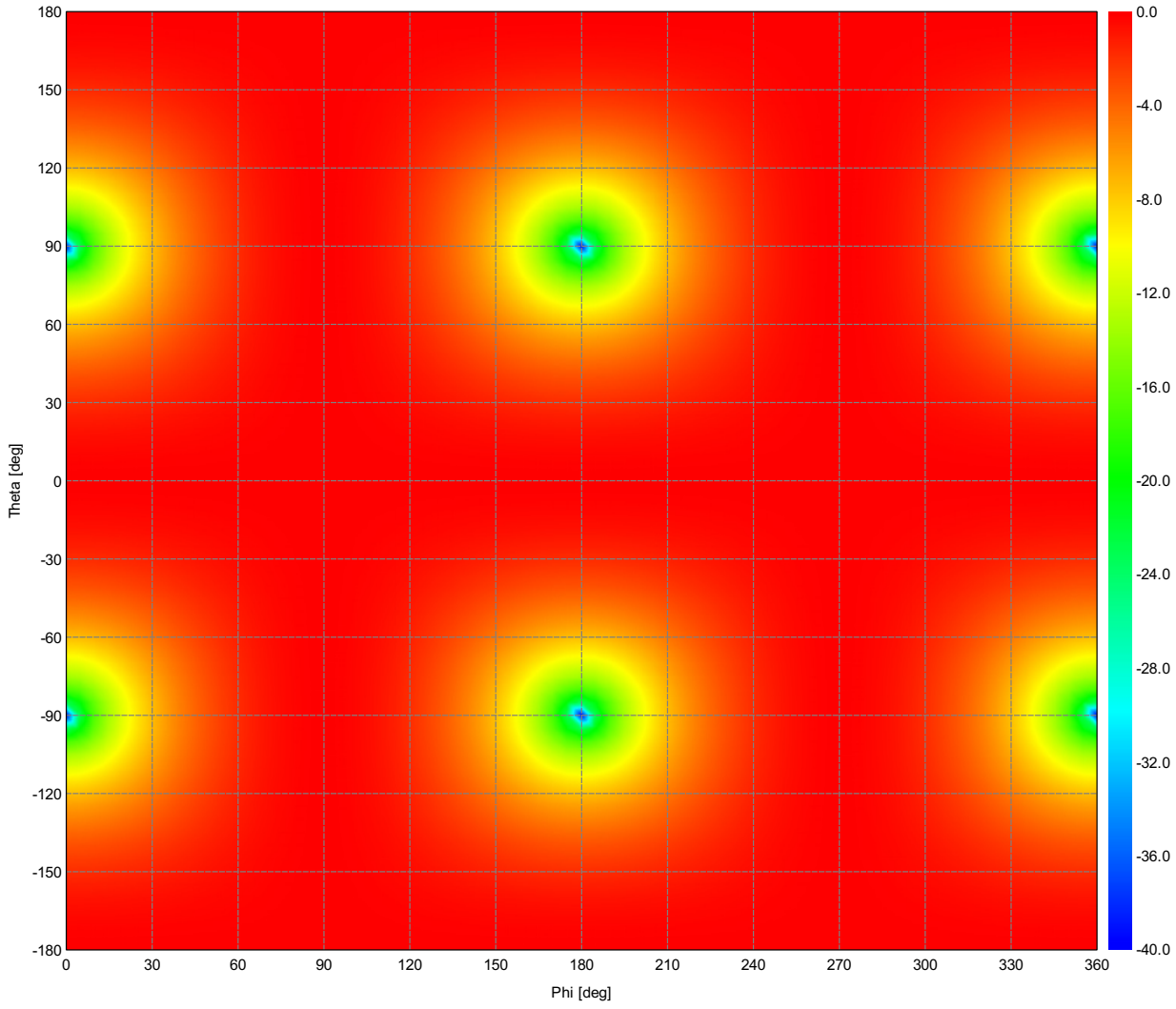

Figure 13: Total E-Field Magnitude (Frequency = 37.075 MHz) - Dipolo

FarField1: Total Gain [dBi]

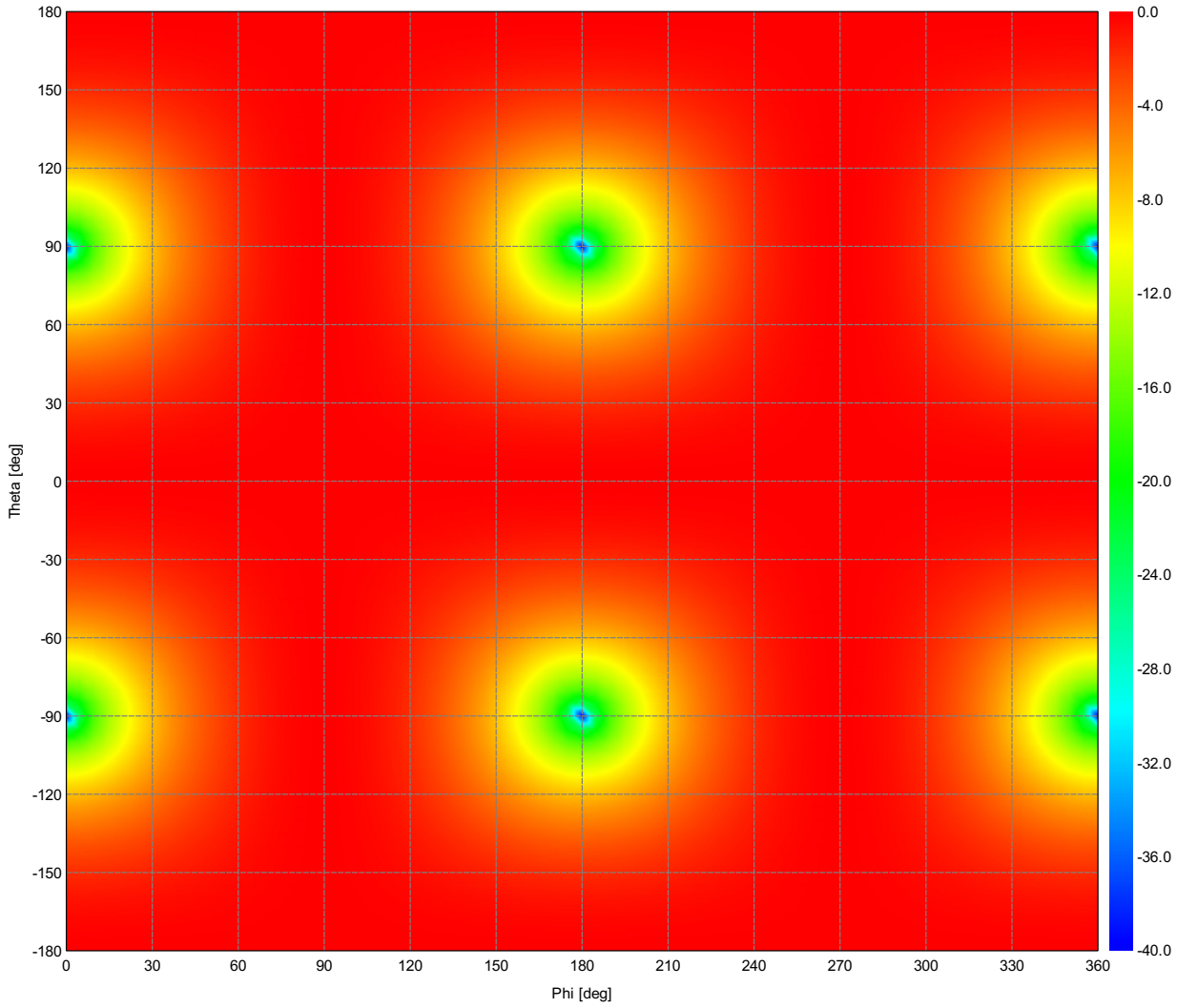

Figure 14: Total Gain (Frequency = 37.075 MHz) - Dipolo

FarField1: Total Directivity [dBi]

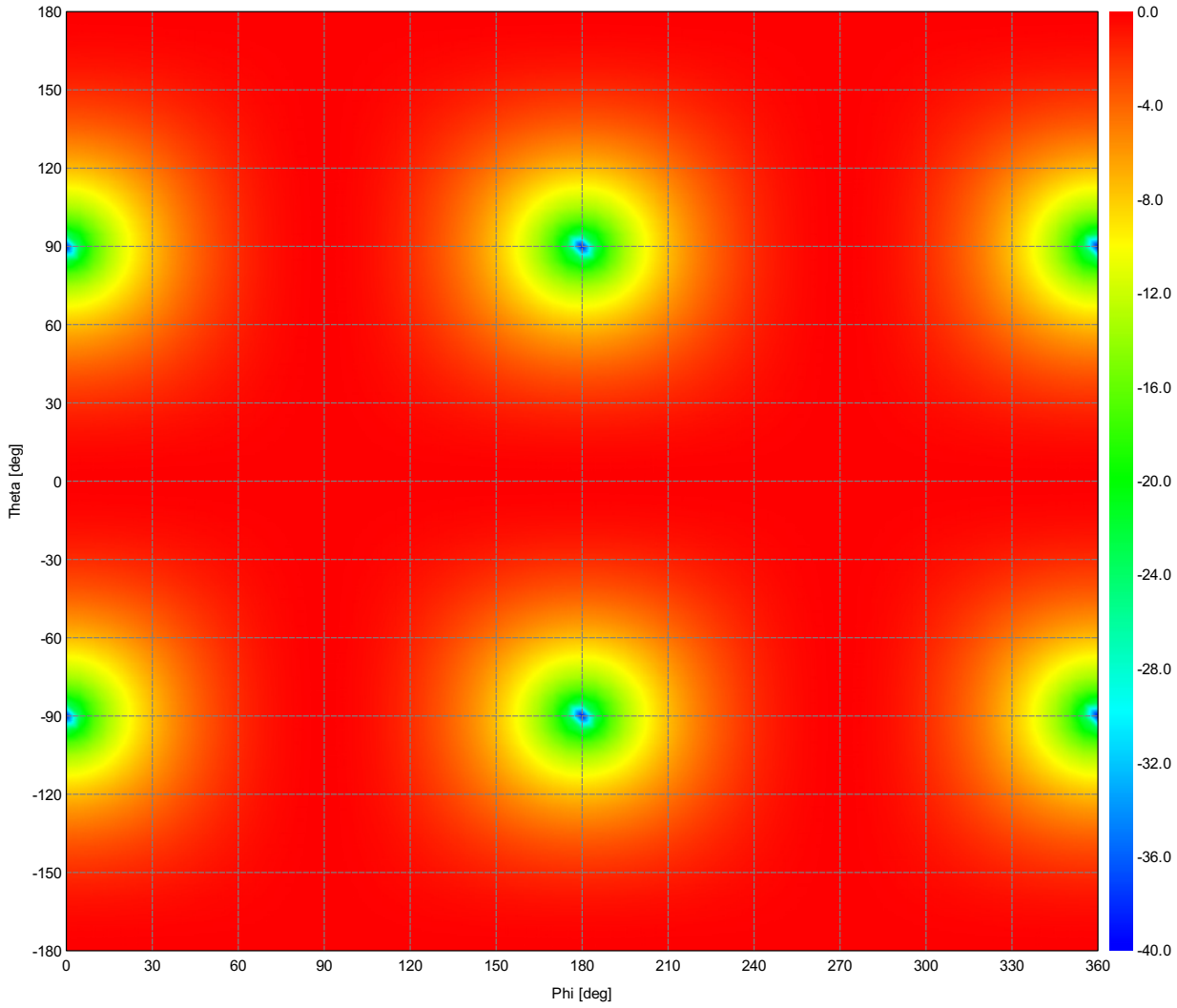

Figure 15: Total Directivity (Frequency = 37.075 MHz) - Dipolo

Far field: Minimos S_11

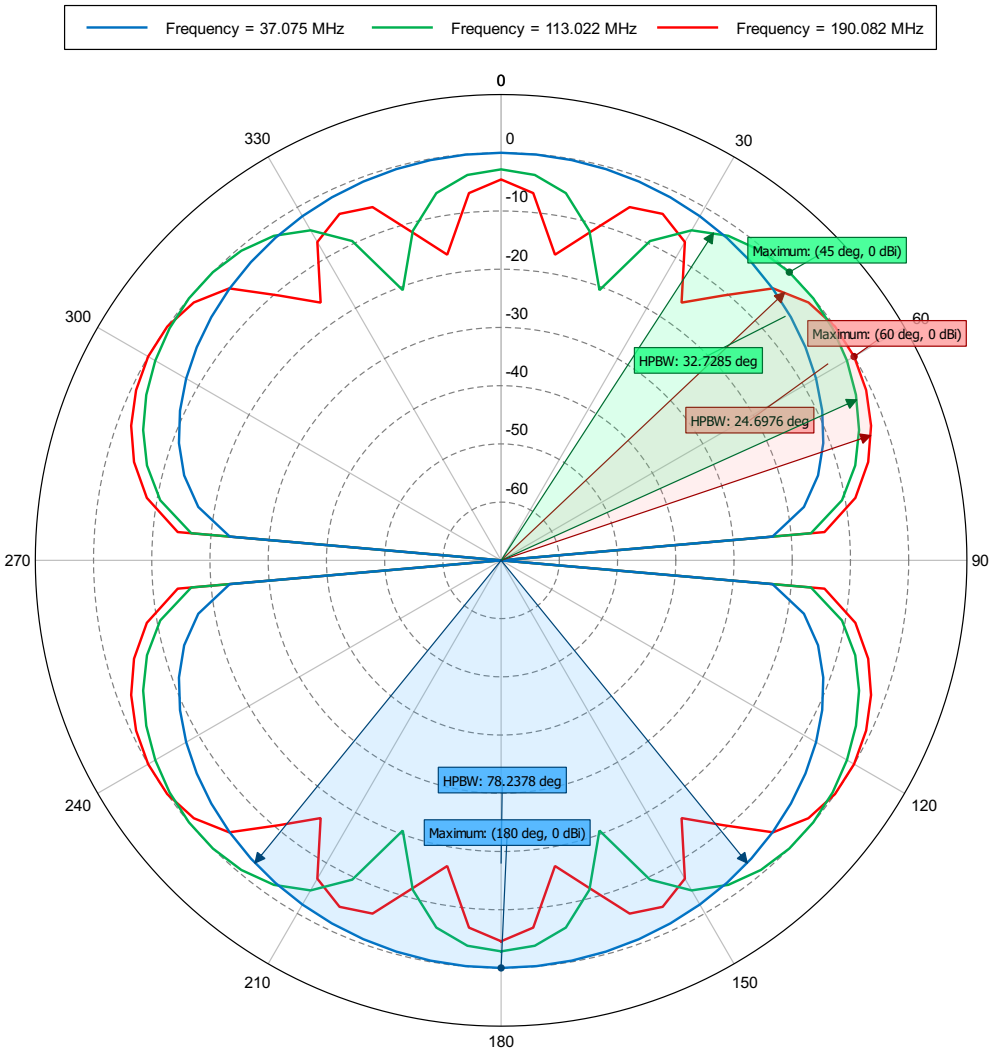

Figure 16: Total Gain (Phi = 0 deg) - Dipolo

Far field: Max gain

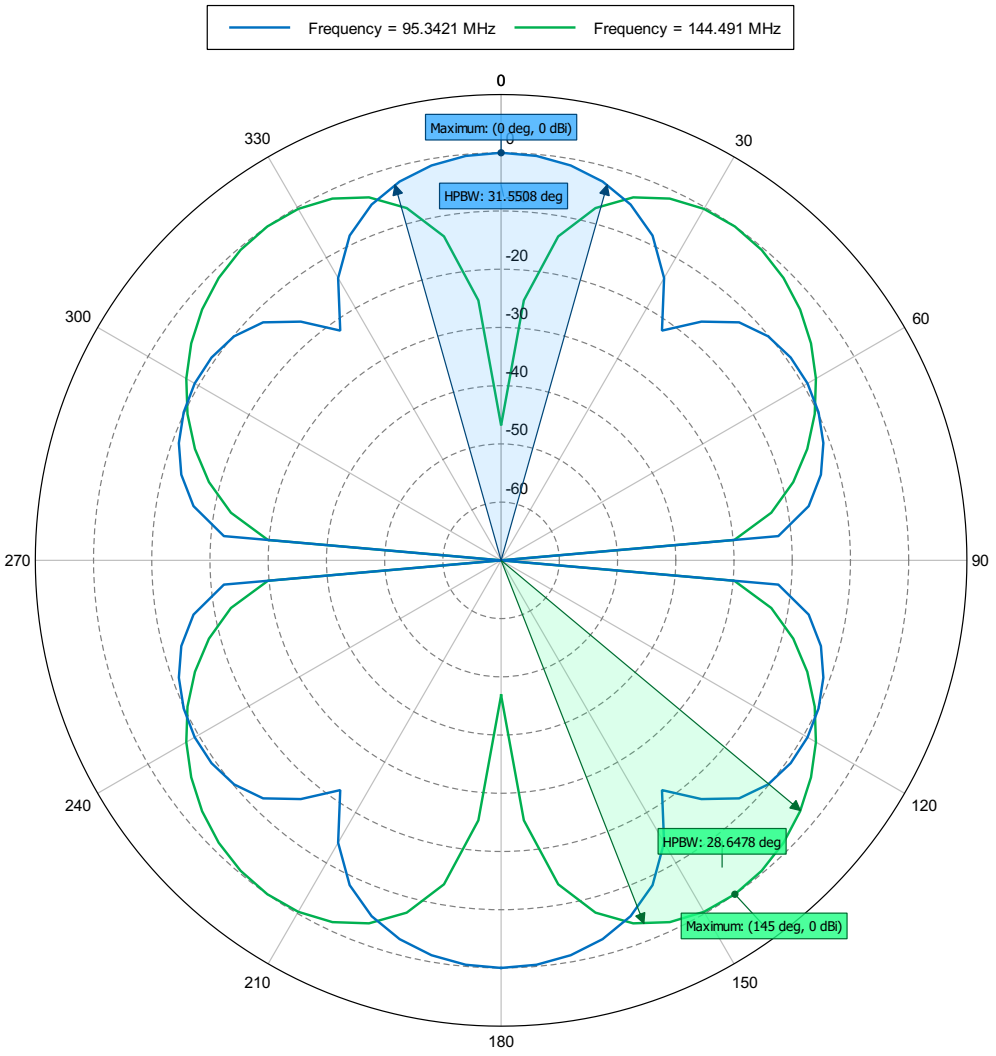

Figure 17: Total Gain (Phi = 0 deg) - Dipolo

Far field: BW 33-43MHz

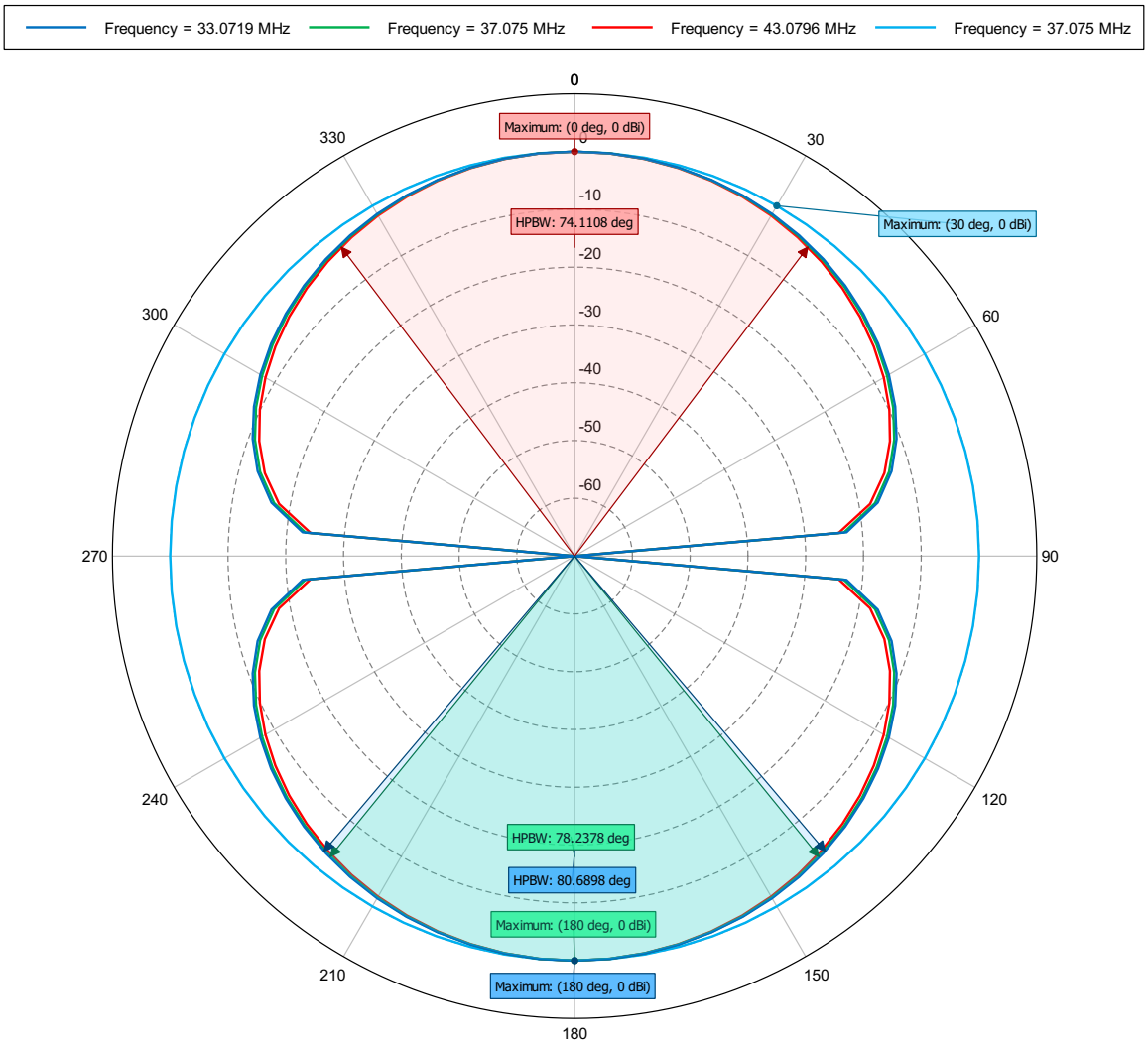

Figure 18: Total Gain (Theta = 0 deg; Phi = 0 deg) - Dipolo

S-parameter

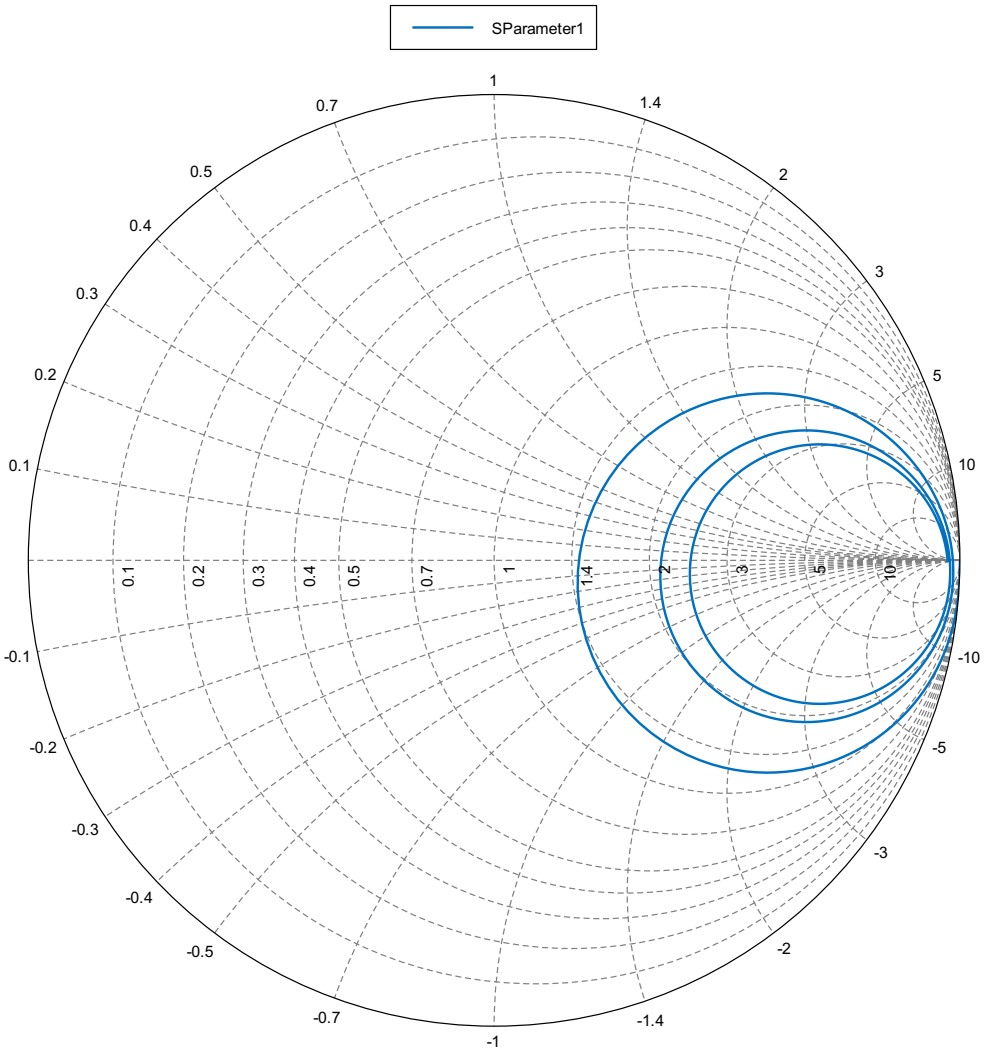

Figure 19: S-parameters (S-parameter = S1,1) - Dipolo

Dipolo real 0.38-224MHz

C:/Users/Cepia-beam/Documents/Feko/dipolo realista
2022-02-28 22:47

S-parameter

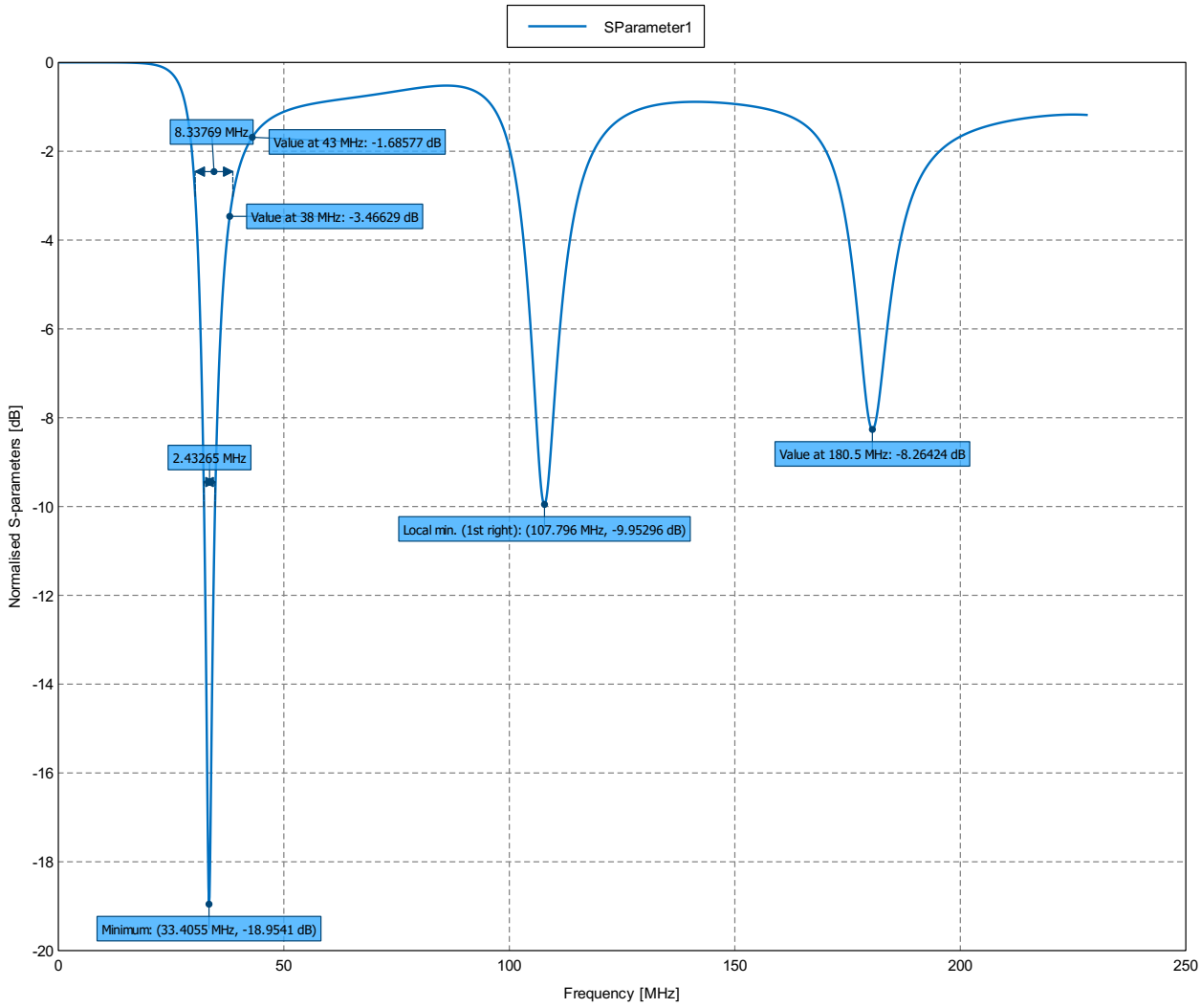

Figure 1: S-parameters Magnitude [dB] (S-parameter = S1,1) - Dipolo_real

Power

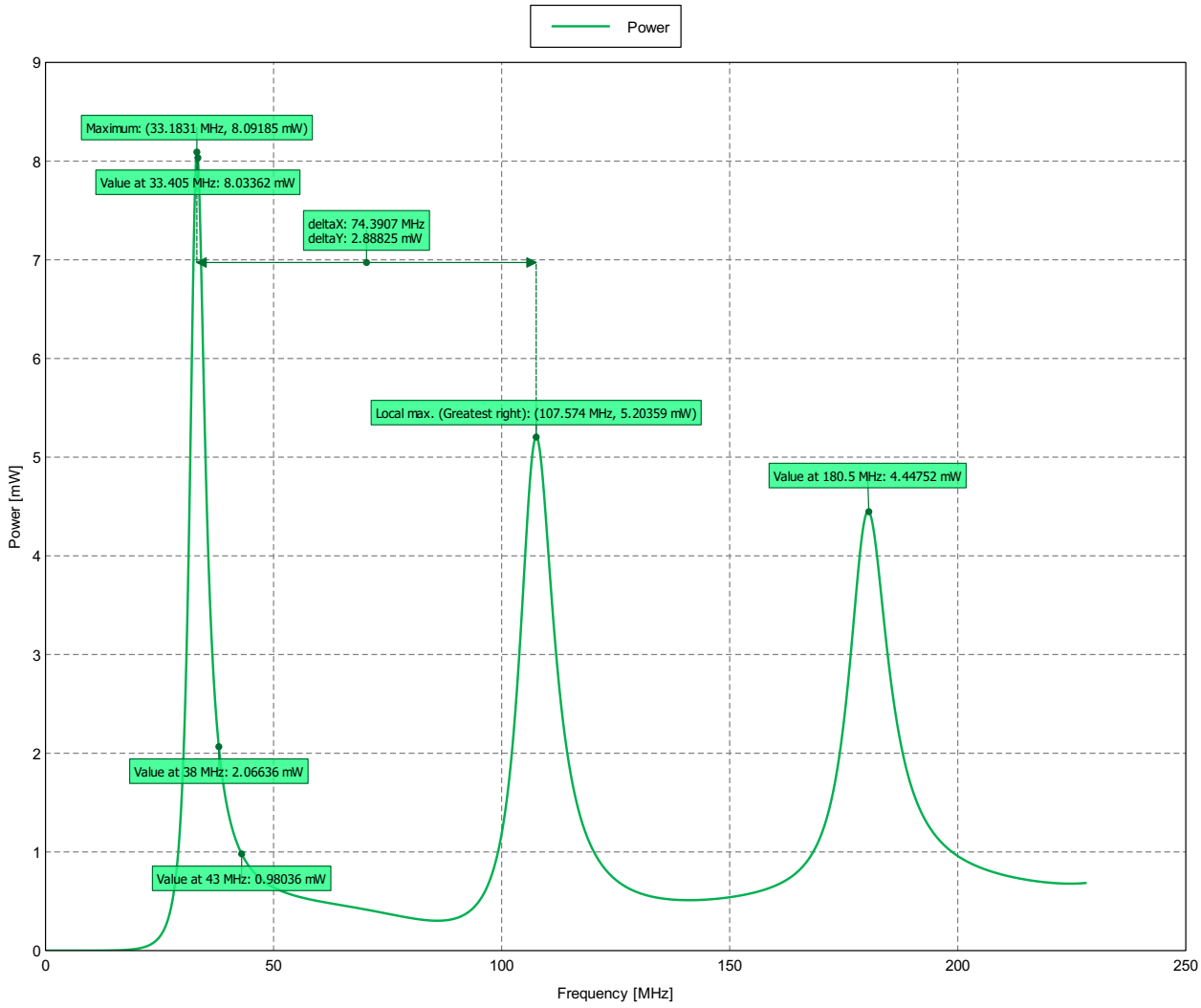

Figure 2: Active Power [mW] - Dipolo_real

Power dbW

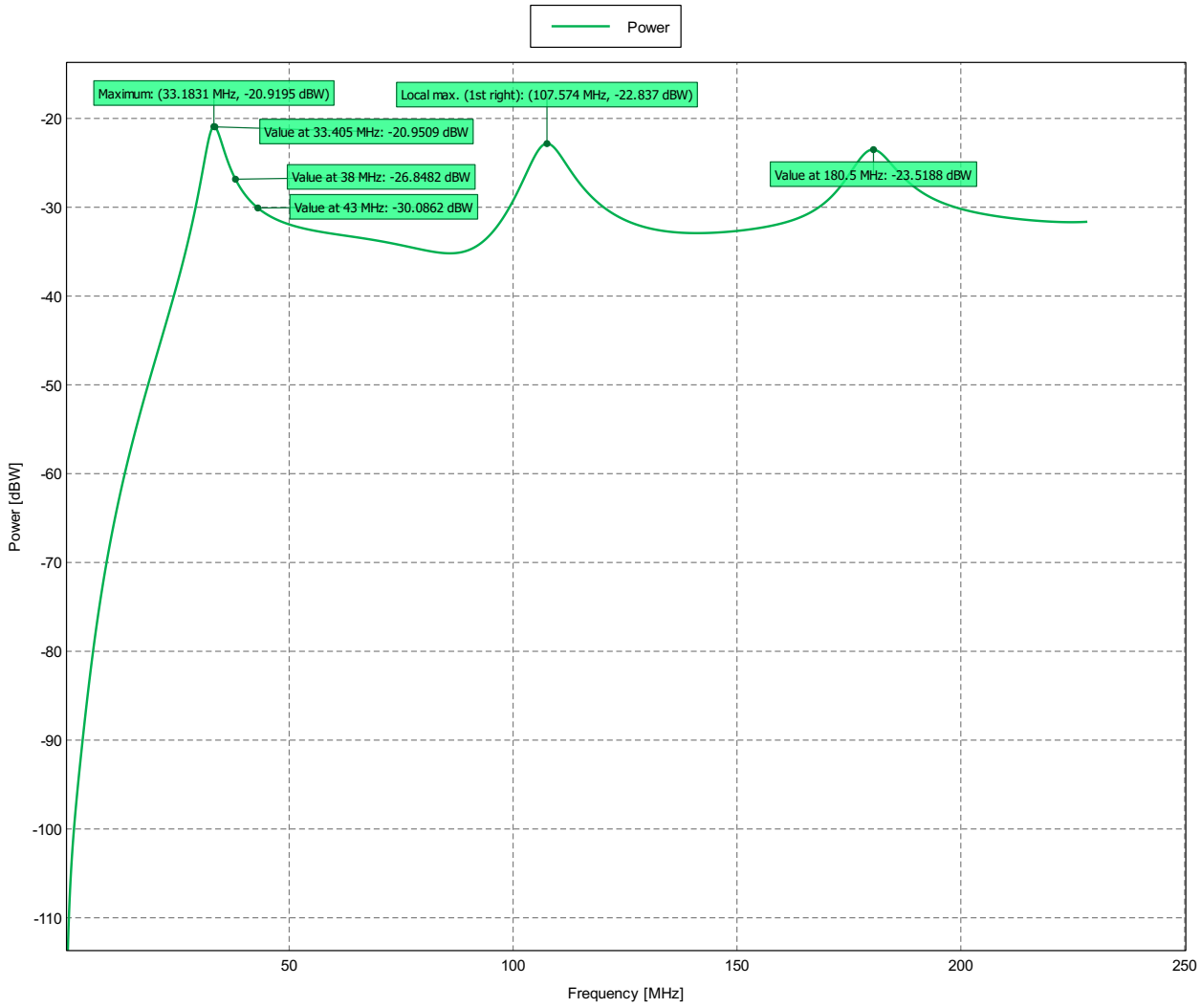

Figure 3: Active Power [dBW] - Dipolo_real

Far field: E

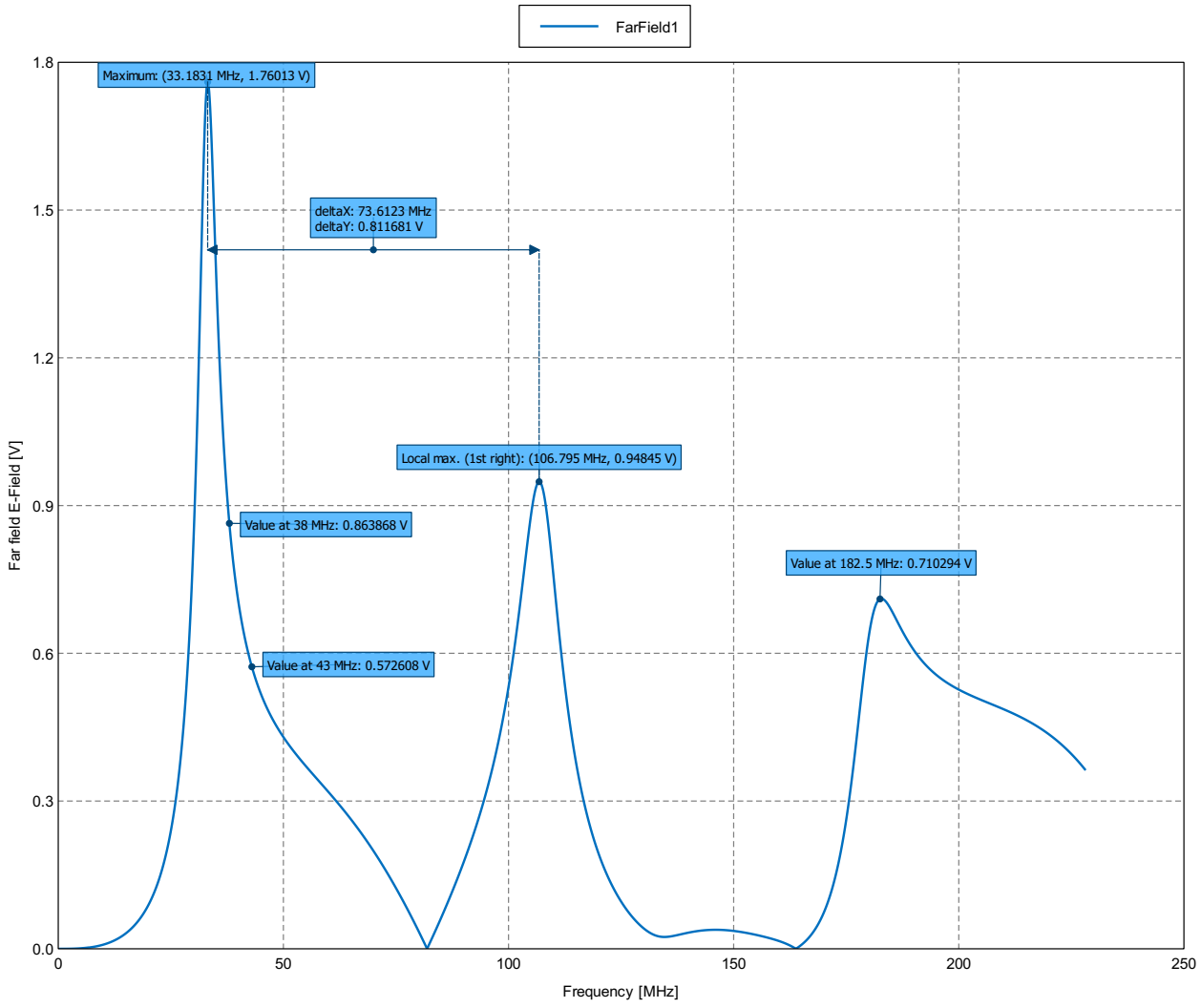

Figure 4: Total E-Field Magnitude [V] (Theta = 0 deg; Phi = 45 deg) - Dipolo_real

Far field: E db

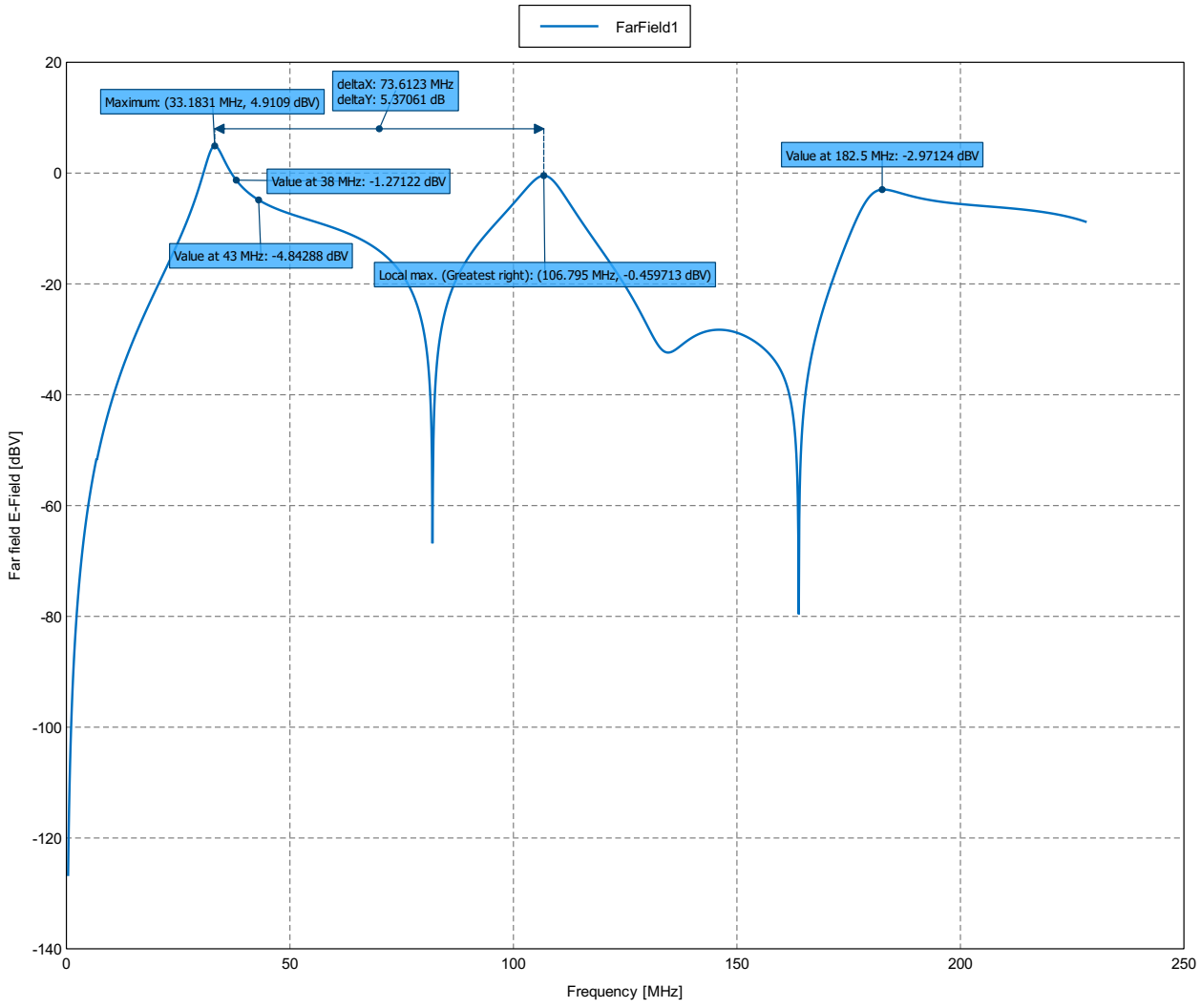

Figure 5: Total E-Field Magnitude [dBV] (Theta = 0 deg; Phi = 45 deg) - Dipolo_real

Far field: G

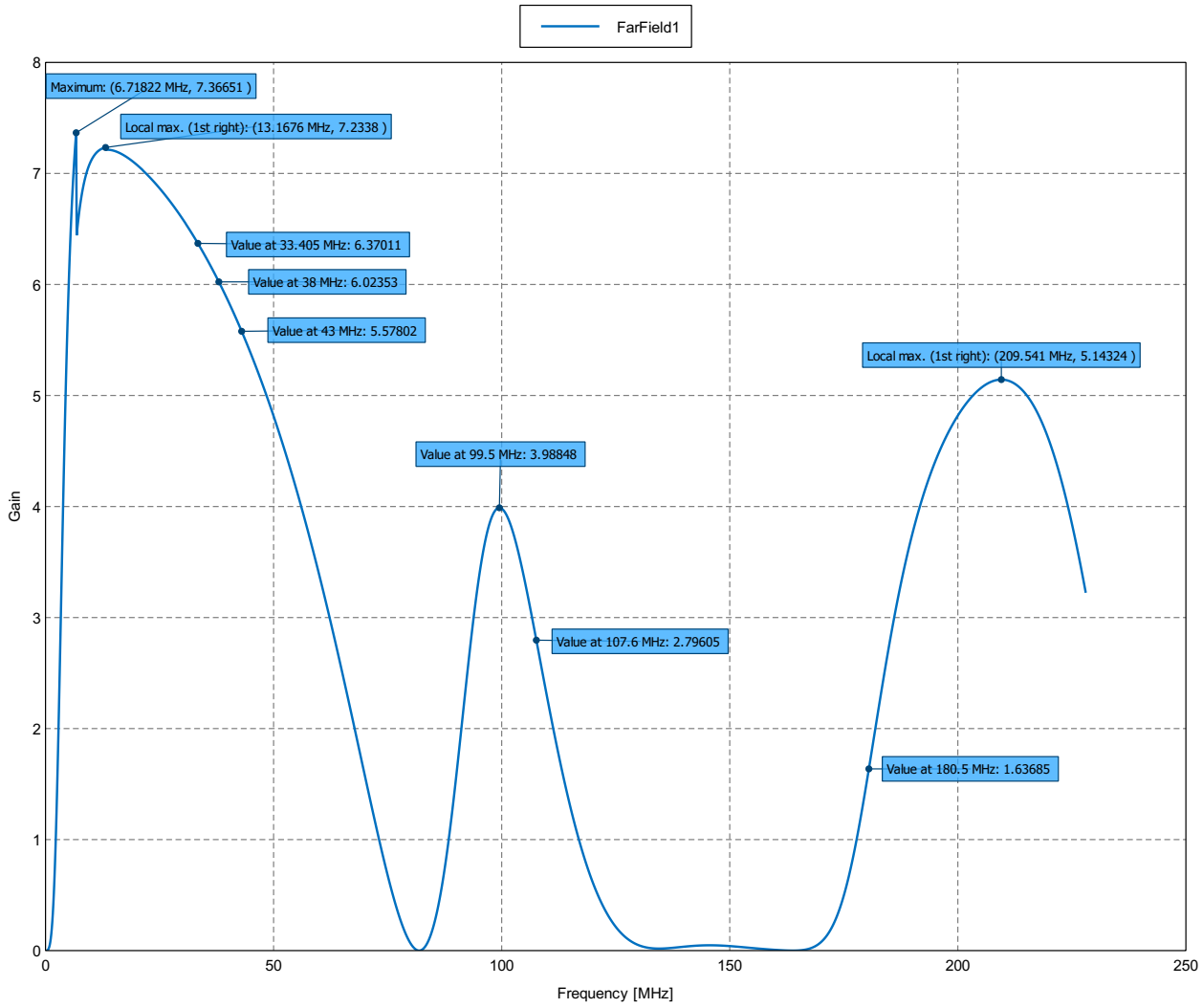

Figure 6: Total Gain (Theta = 0 deg; Phi = 45 deg) - Dipolo_real

Far field: G db

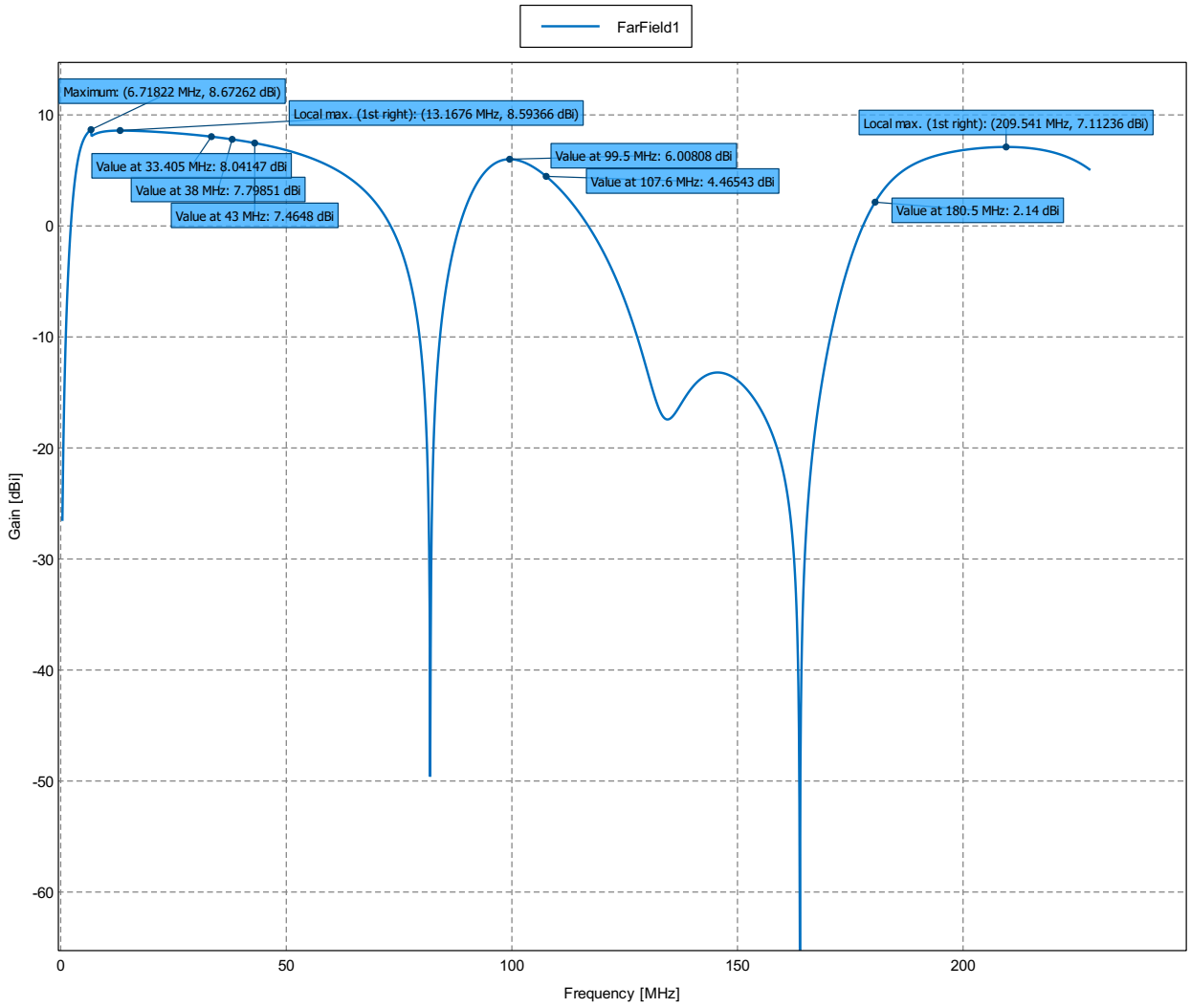

Figure 7: Total Gain [dBi] (Theta = 0 deg; Phi = 45 deg) - Dipolo_real

Far field: D

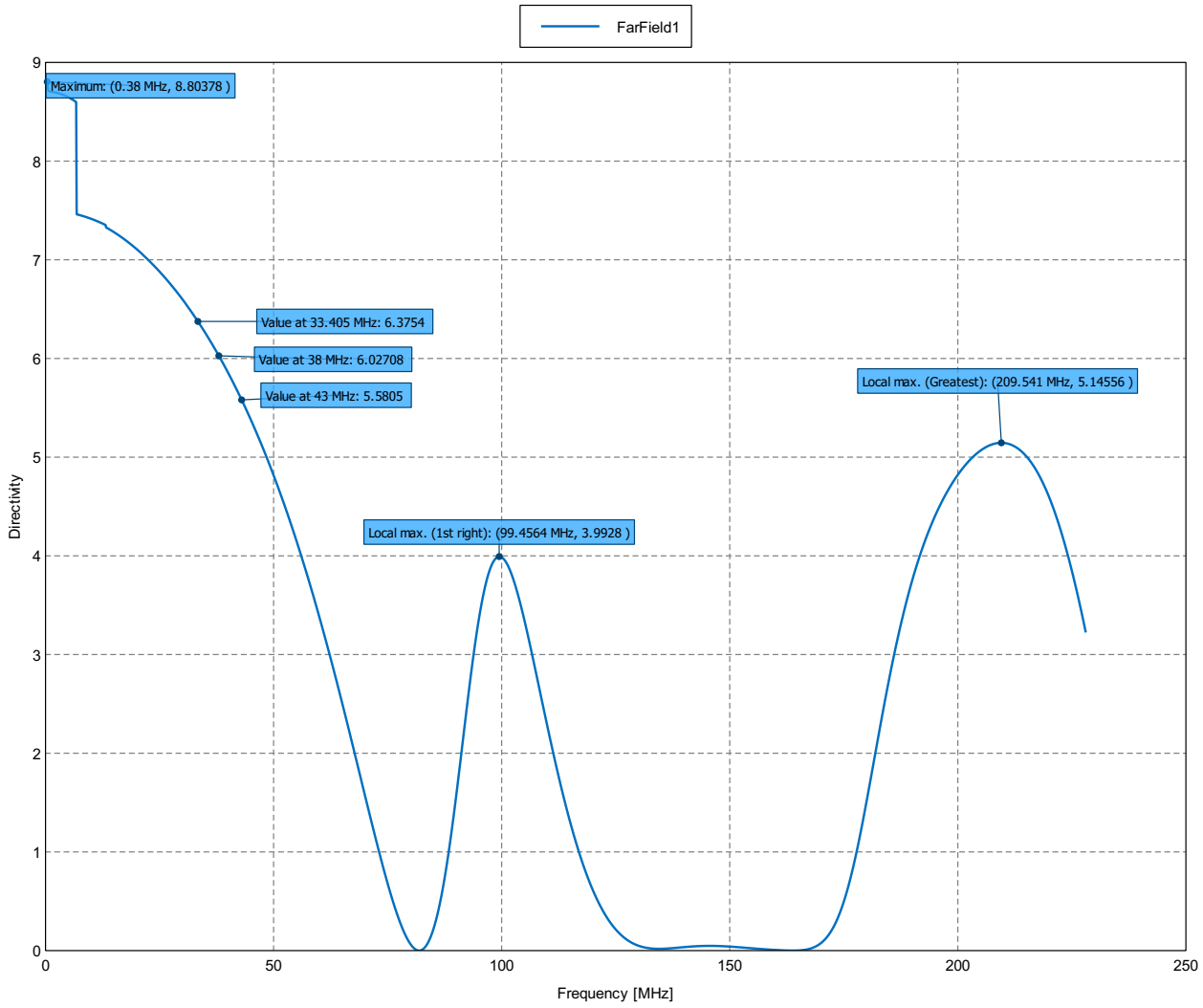

Figure 8: Total Directivity (Theta = 0 deg; Phi = 45 deg) - Dipolo_real

Far field: D db

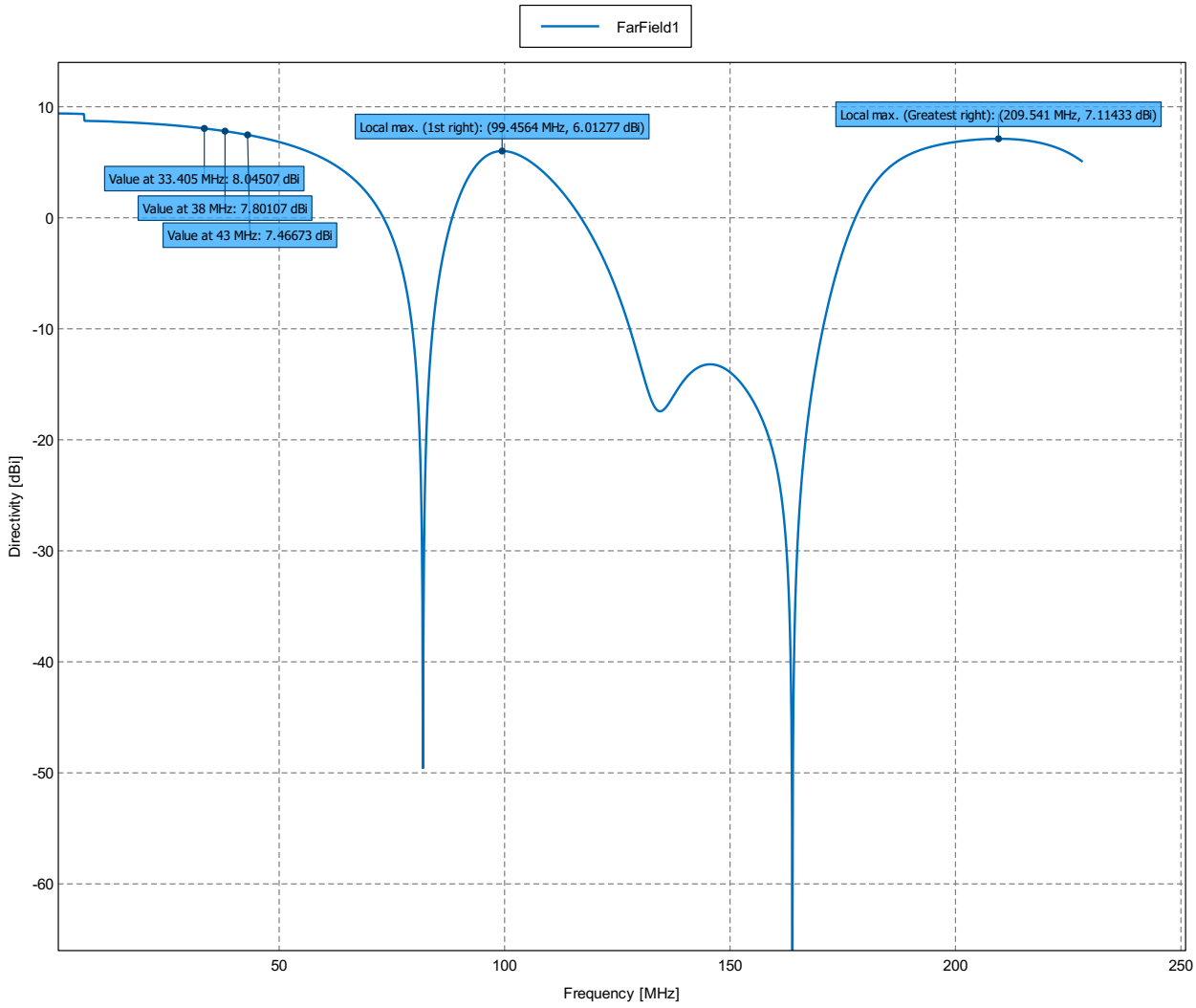

Figure 9: Total Directivity [dBi] (Theta = 0 deg; Phi = 0 deg) - Dipolo_real

E_33

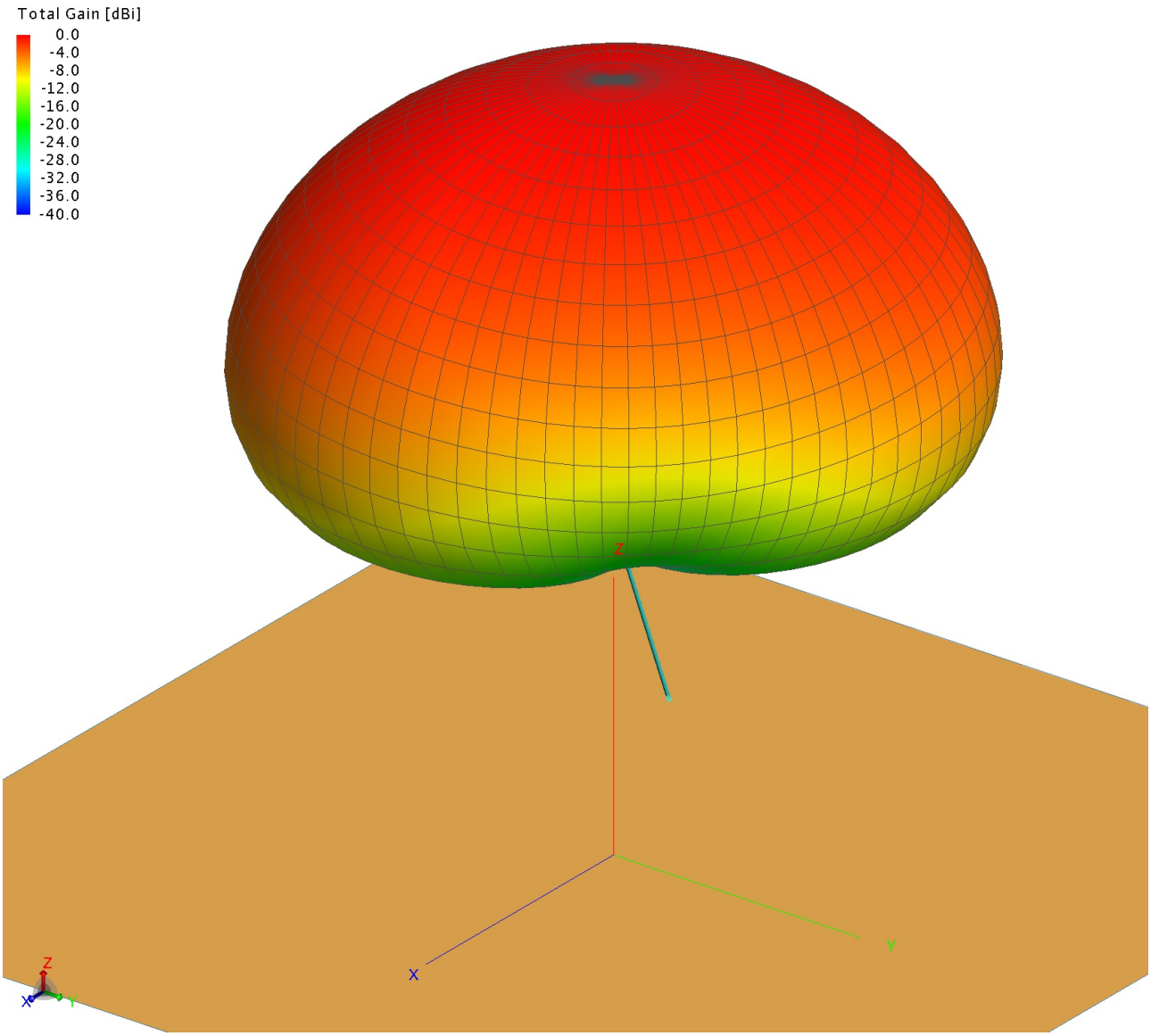

Figure 10: 3D View

G_33

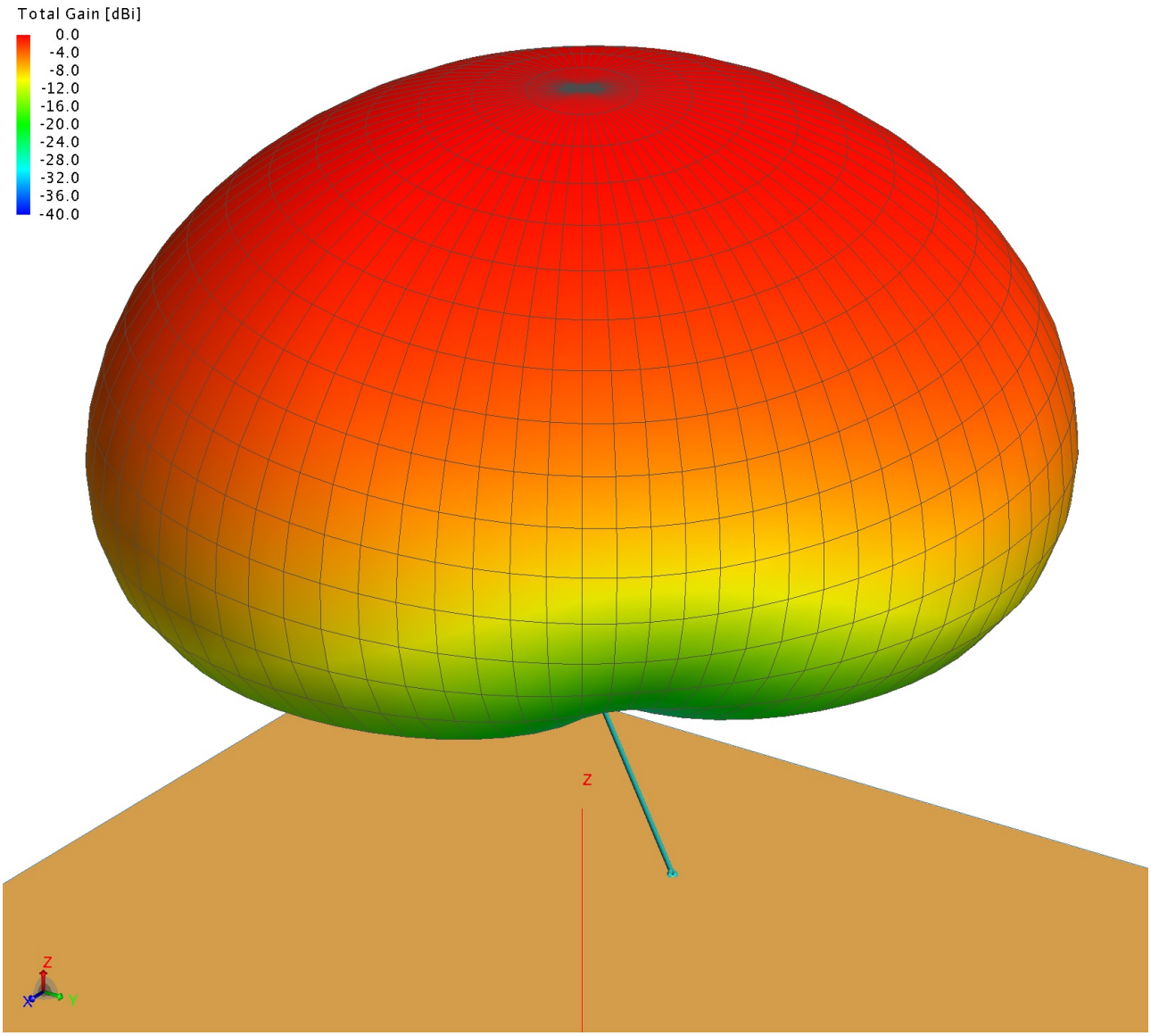

Figure 11: 3D View

D_33

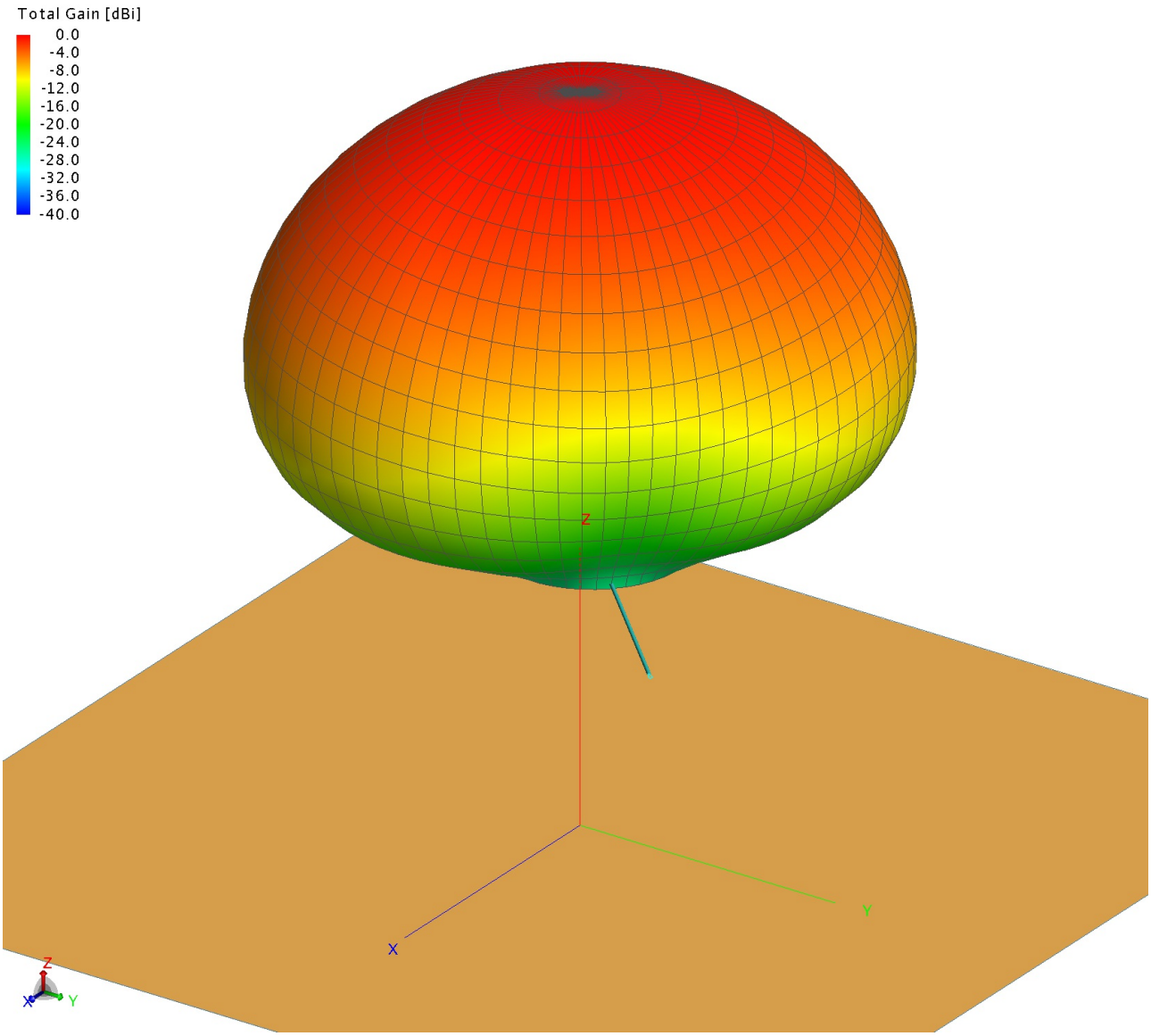

Figure 12: 3D View

FarField1: Total E-Field Magnitude [dBV]

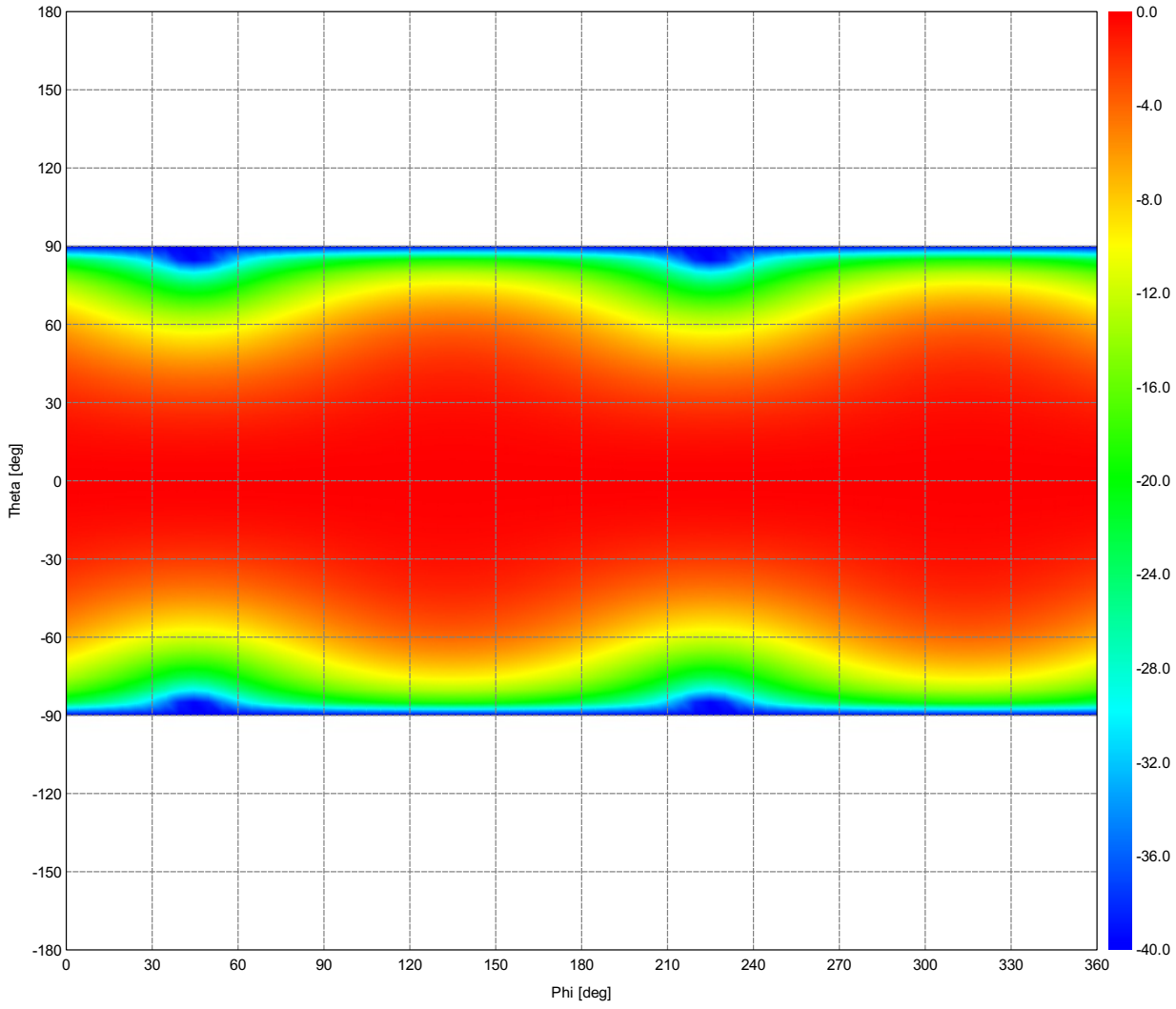

Figure 13: Total E-Field Magnitude (Frequency = 33.0719 MHz) - Dipolo_real

FarField1: Total Gain [dBi]

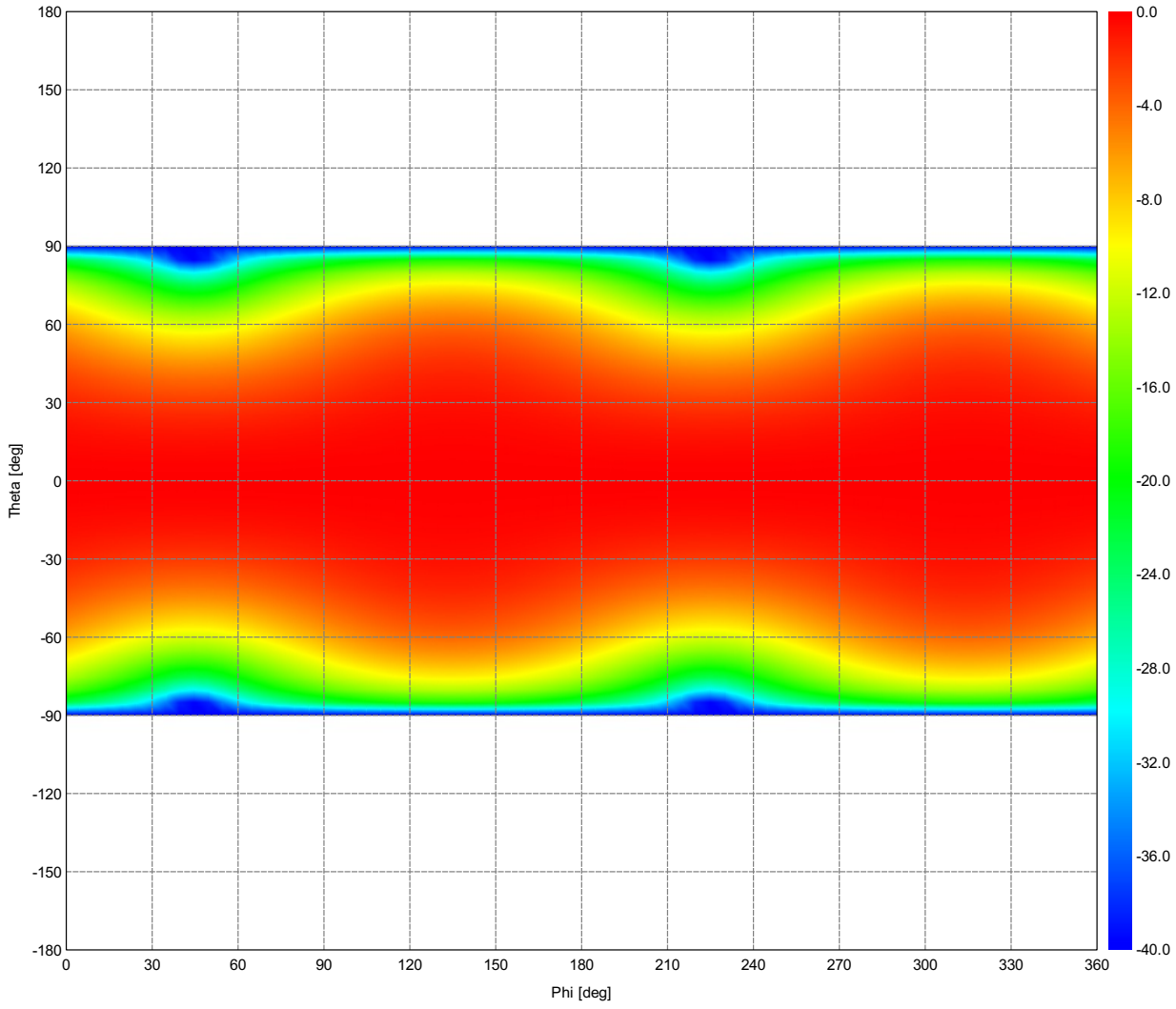

Figure 14: Total Gain (Frequency = 33.0719 MHz) - Dipolo_real

FarField1: Total Directivity [dBi]

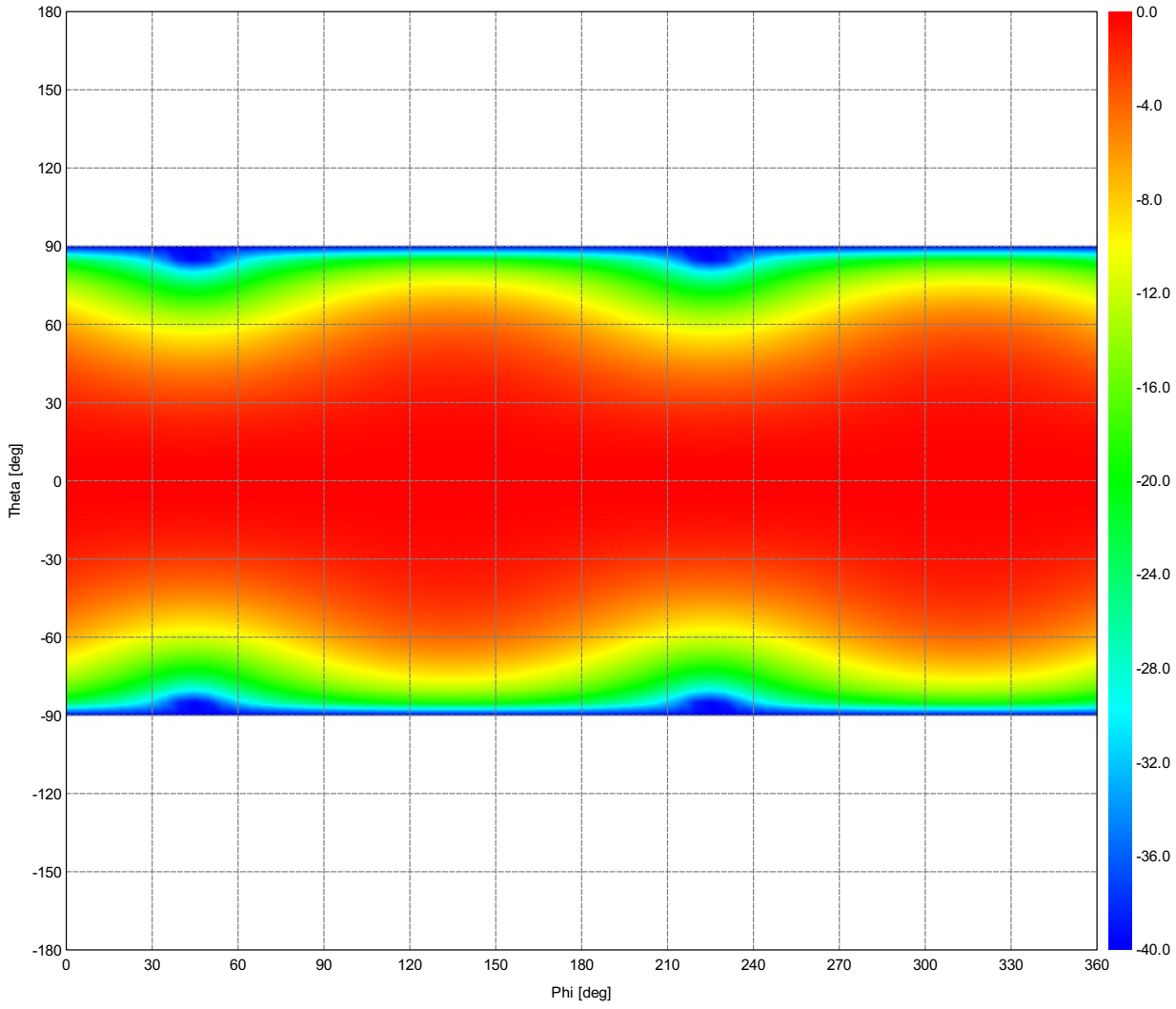

Figure 15: Total Directivity (Frequency = 33.0719 MHz) - Dipolo_real

Far field: E

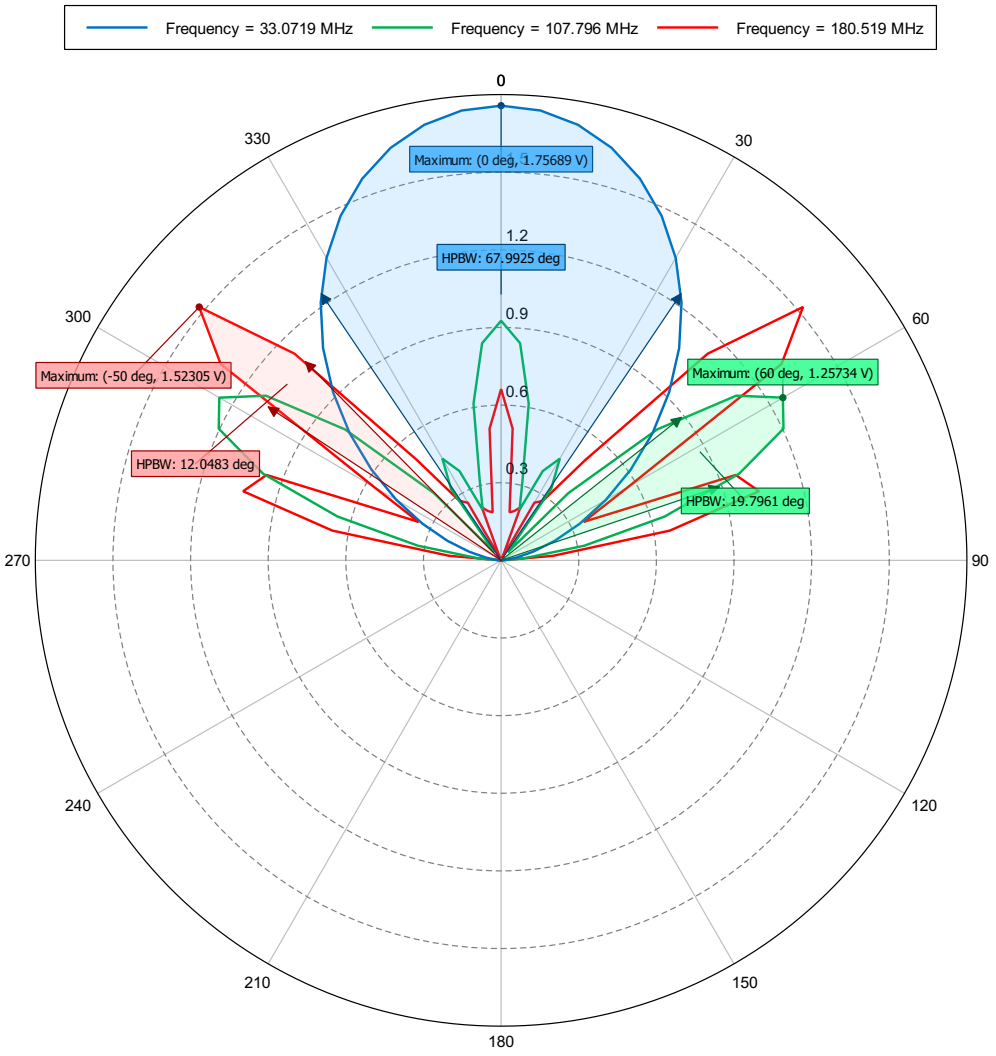

Figure 16: Total E-Field Magnitude (Phi = 45 deg) - Dipolo_real

Far field: G

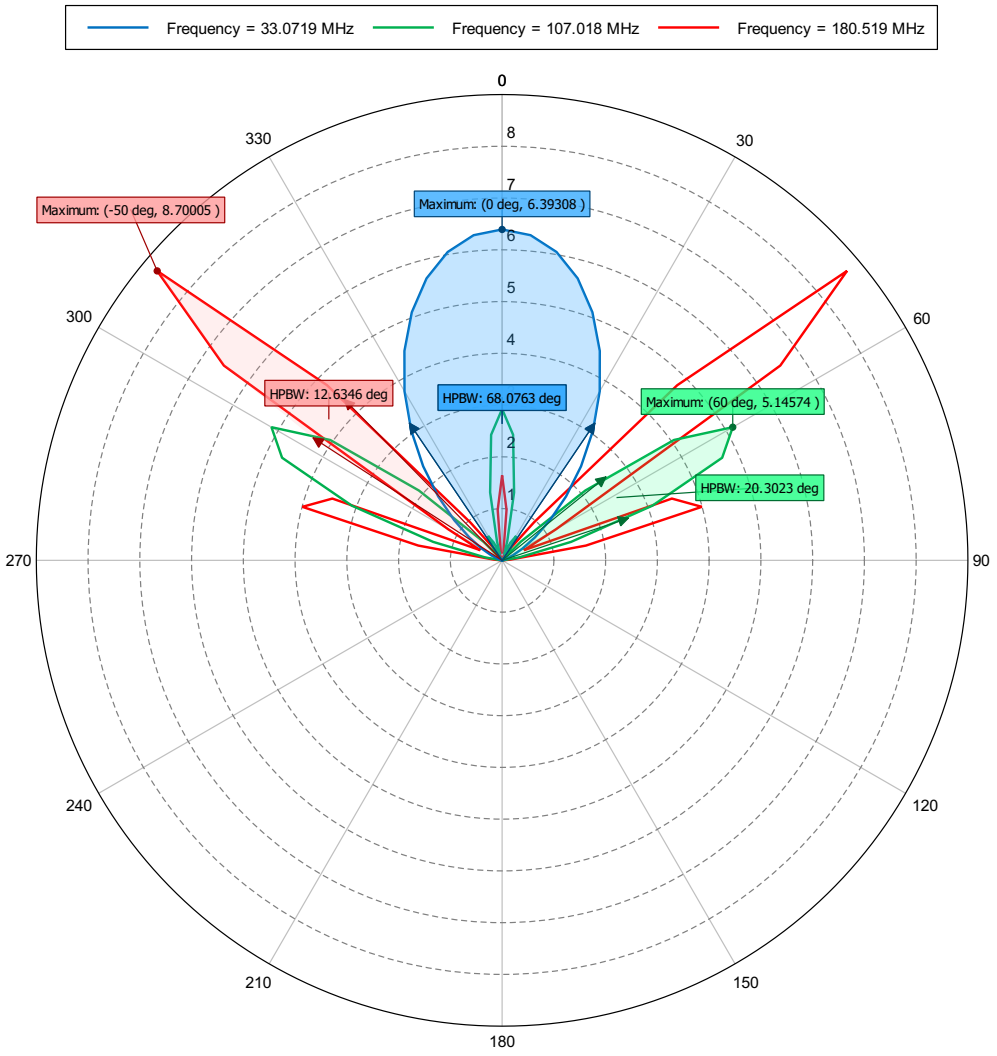

Figure 17: Total Gain (Phi = 45 deg) - Dipolo_real

Far field: D

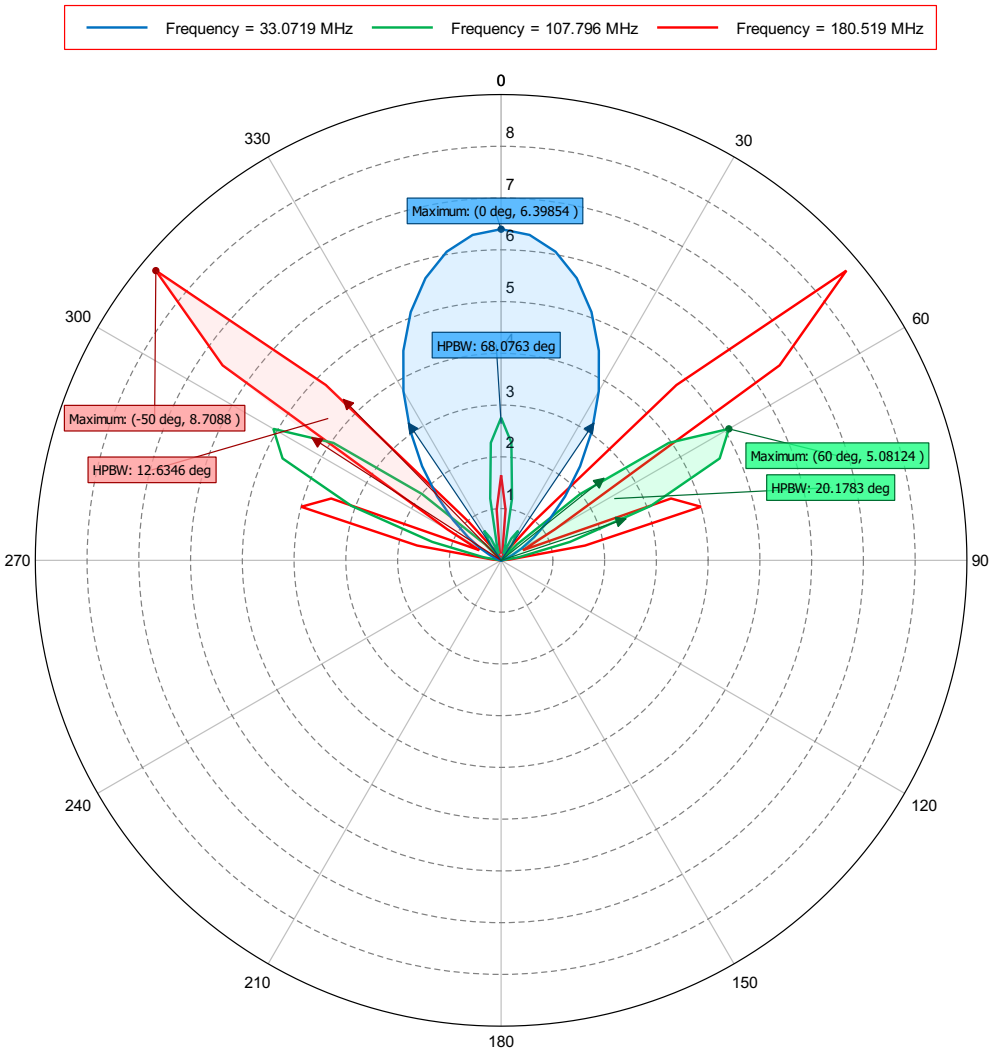

Figure 18: Total Directivity (Phi = 45 deg) - Dipolo_real

Far field: Max Gain

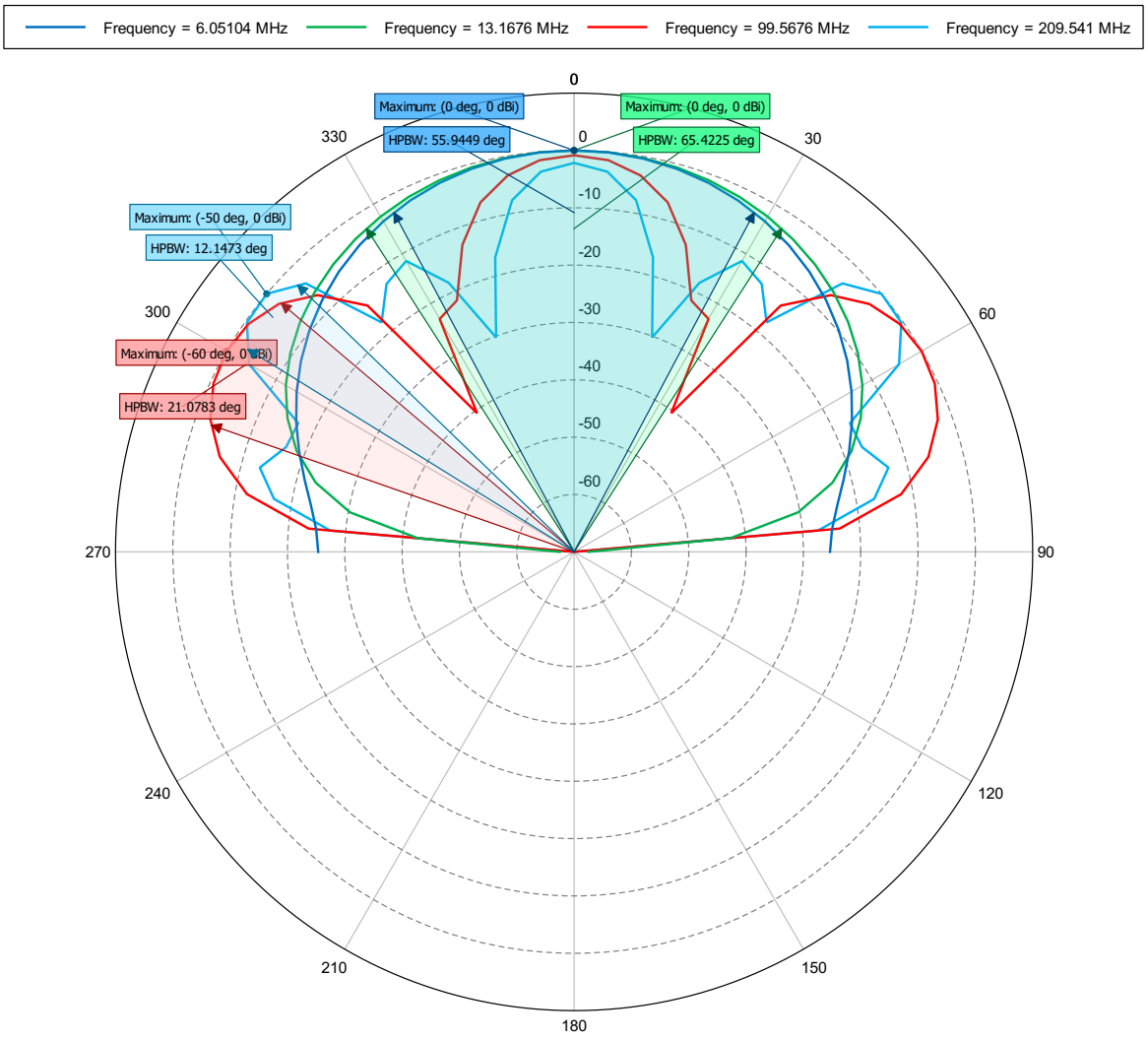

Figure 19: Total Gain (Phi = 45 deg) - Dipolo_real

Far field: BW 33-43MHz

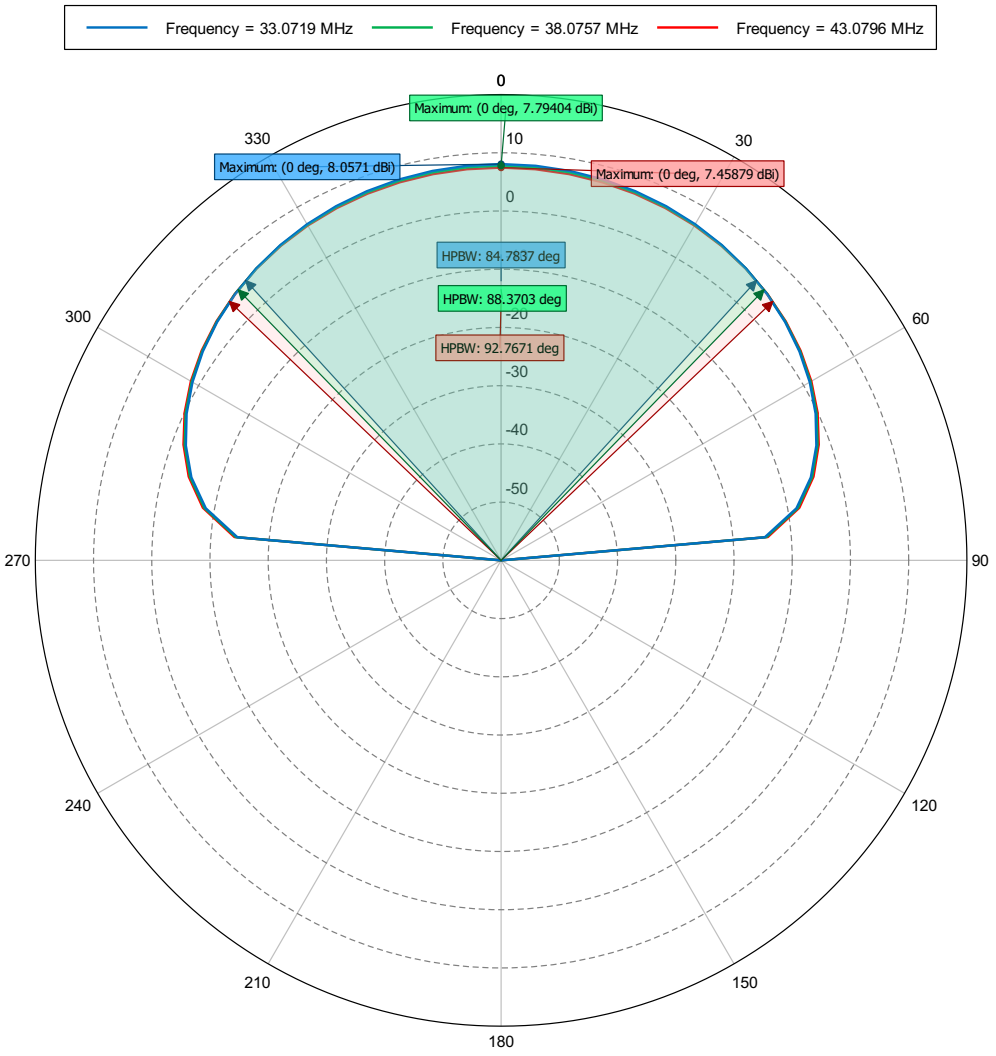

Figure 20: Total Gain (Phi = 0 deg) - Dipolo_real

Far field: BW 33-43MHz

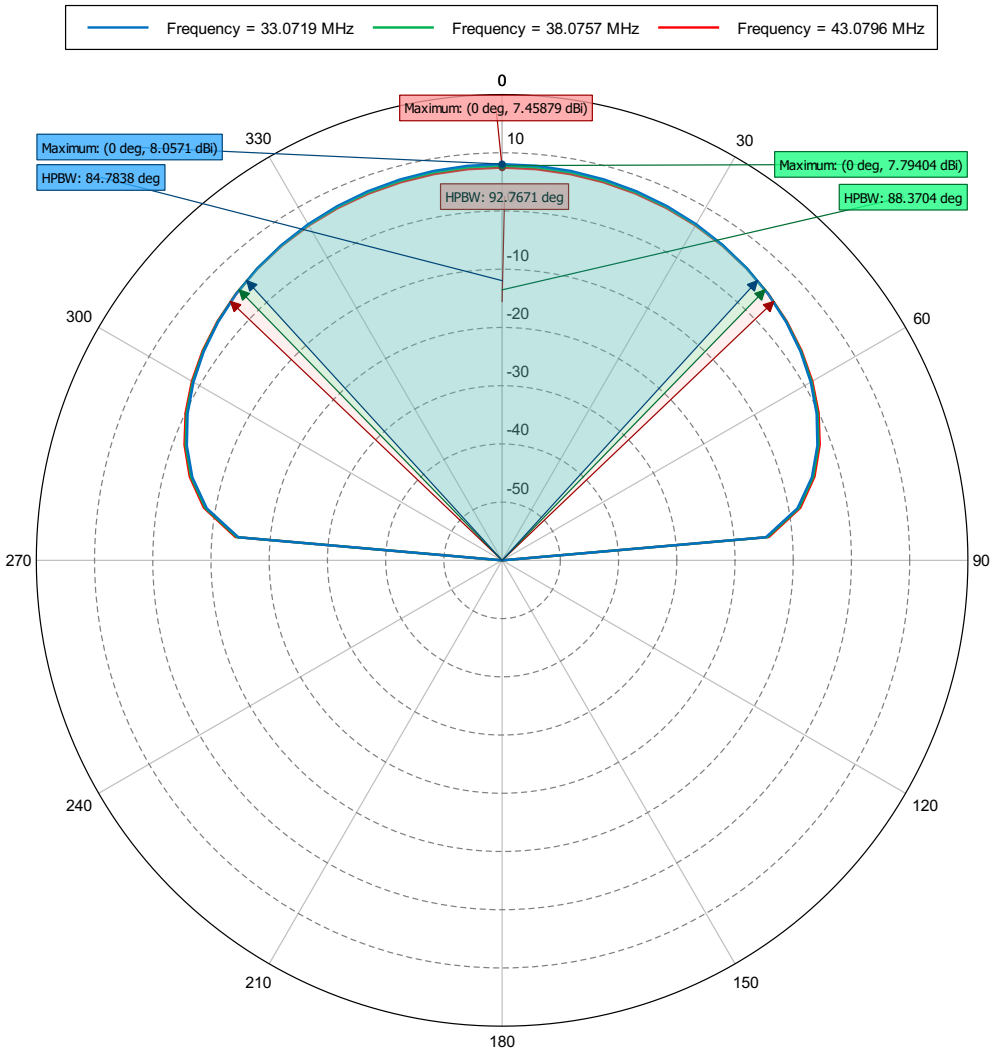

Figure 21: Total Gain (Phi = 90 deg) - Dipolo_real

Excitation

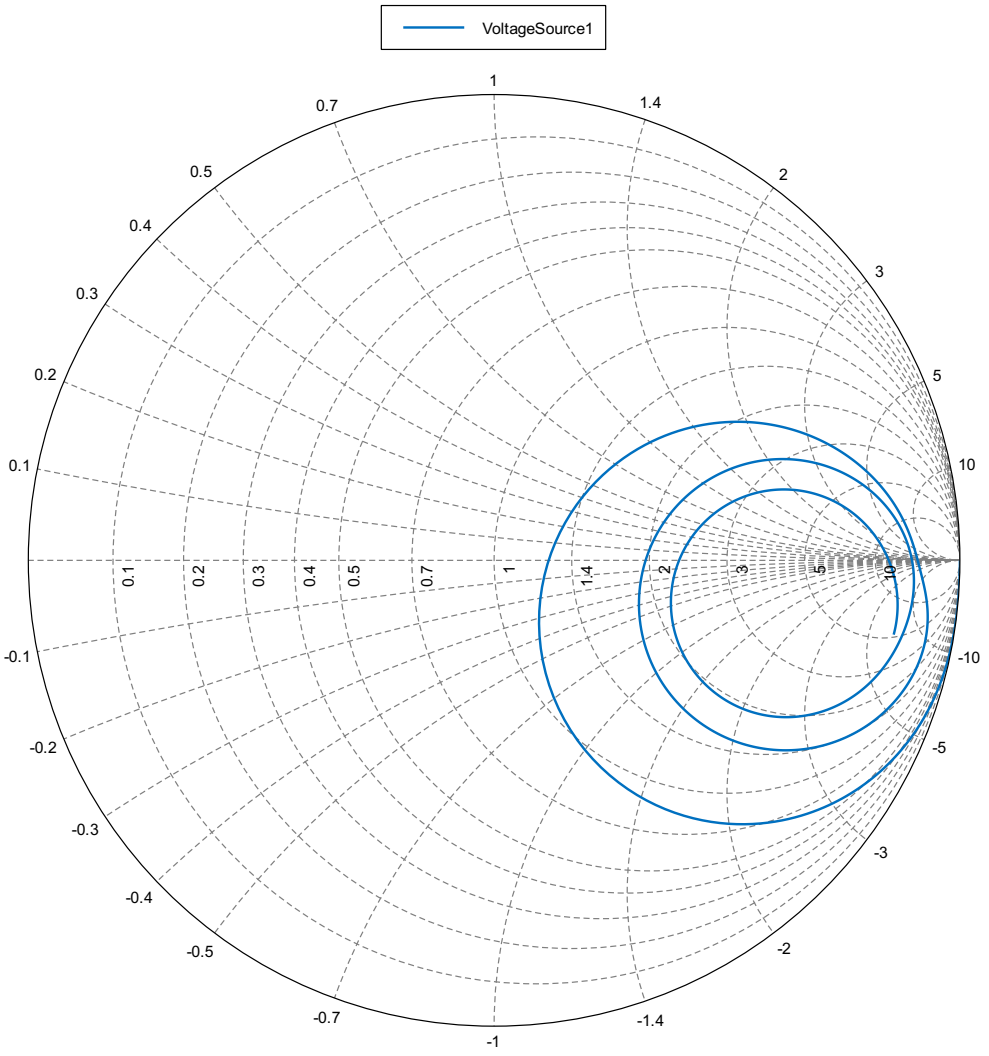

Figure 22: Impedance - Dipolo_real

Dipolo real x4 0.38-224MH

C:/Users/Cepia-beam/Documents/Feko/dipolo realista_4
2022-02-28 13:56

S-parameter

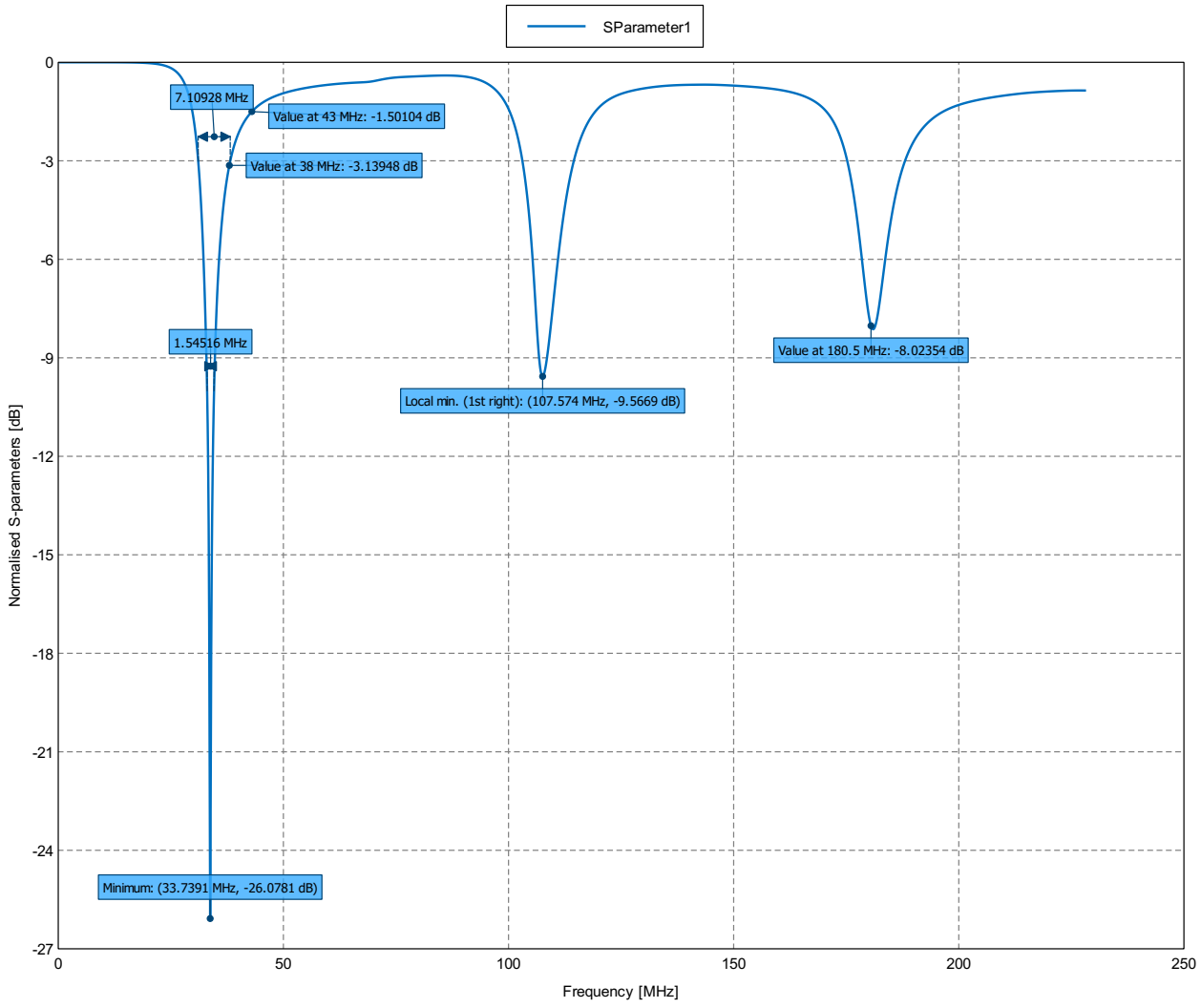

Figure 1: S-parameters Magnitude [dB] (S-parameter = S1,1) - Dipolo_real

Power

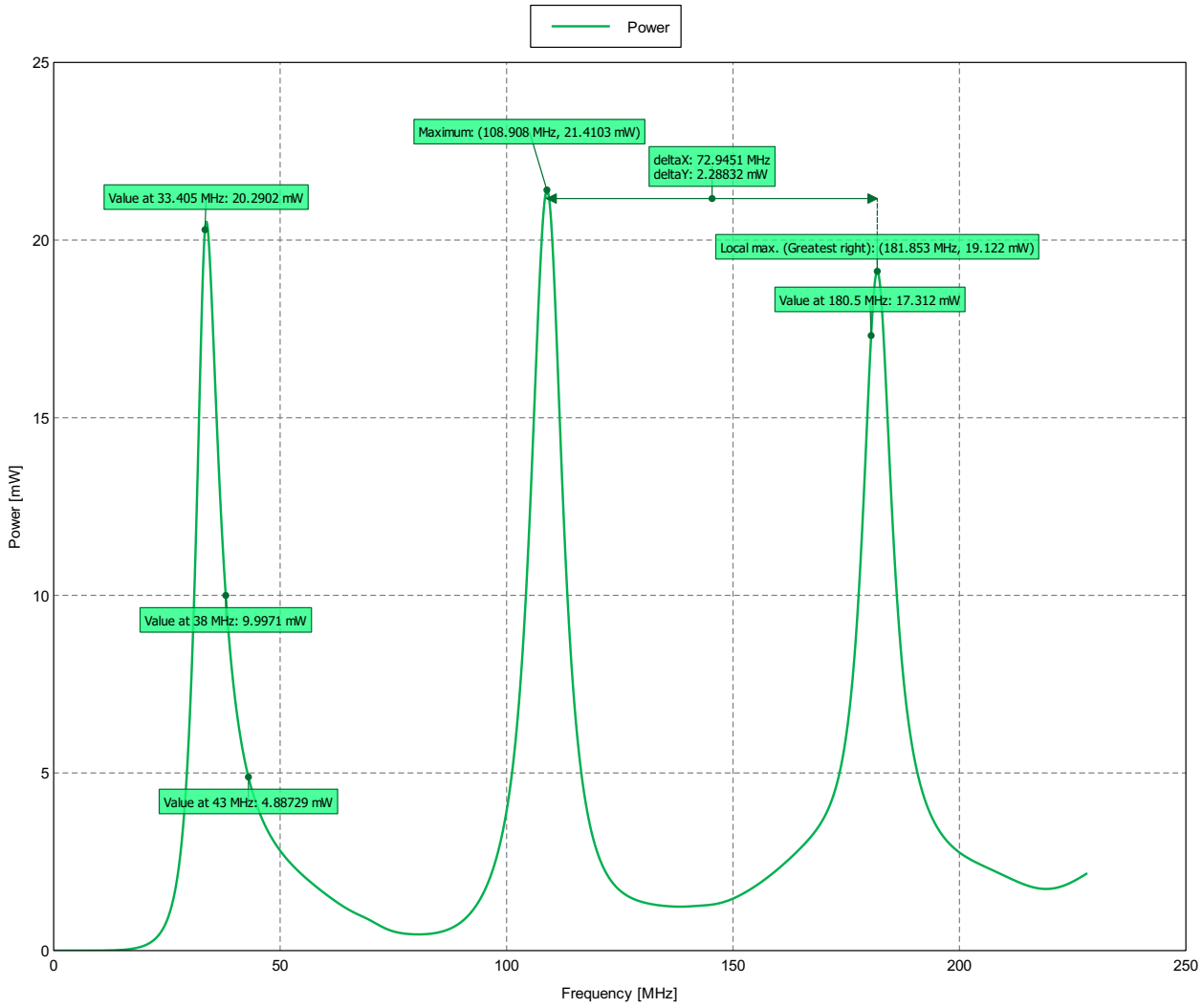

Figure 2: Active Power [mW] - Dipolo_real

Power dbW

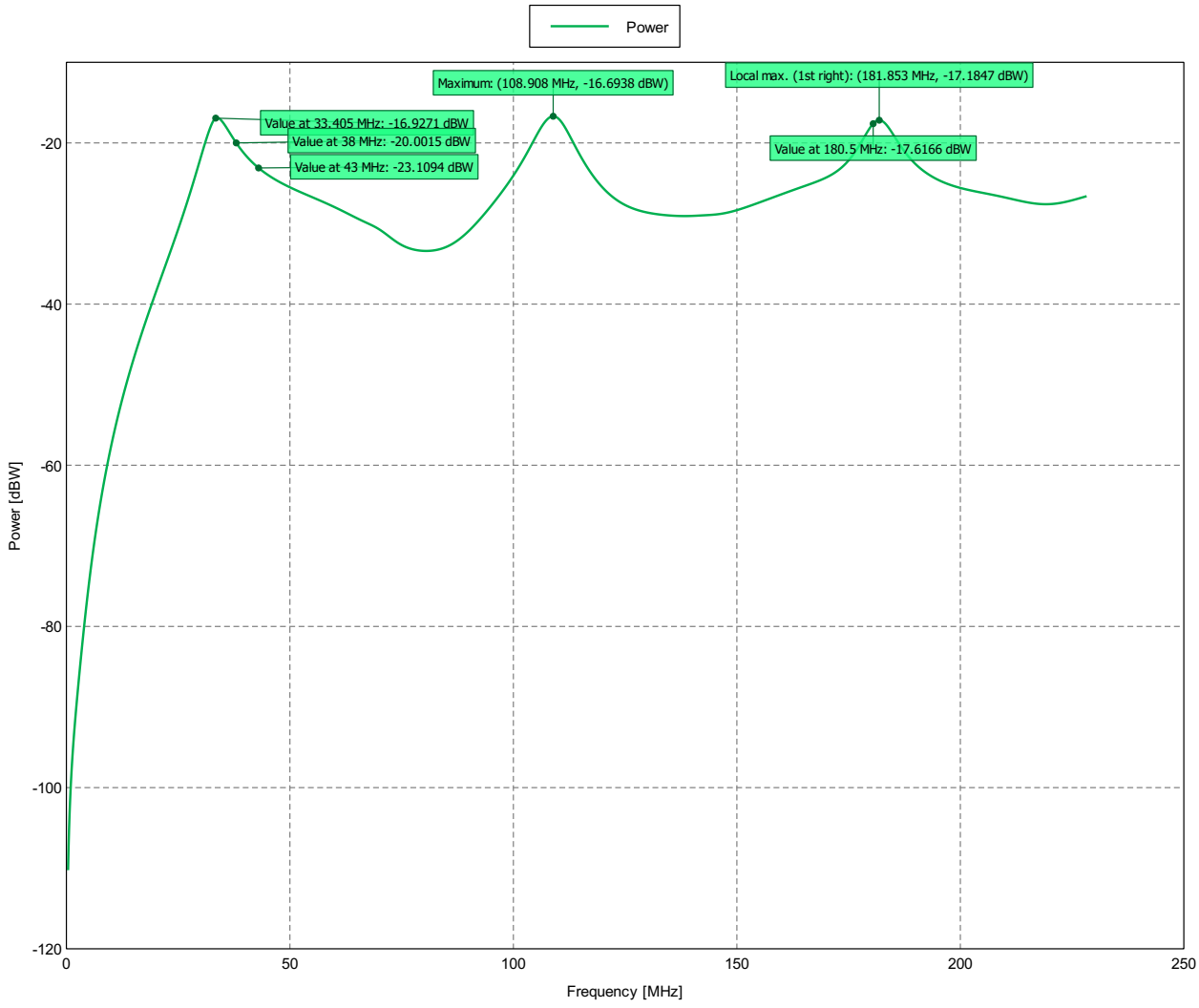

Figure 3: Active Power [dBW] - Dipolo_real

Far field: E

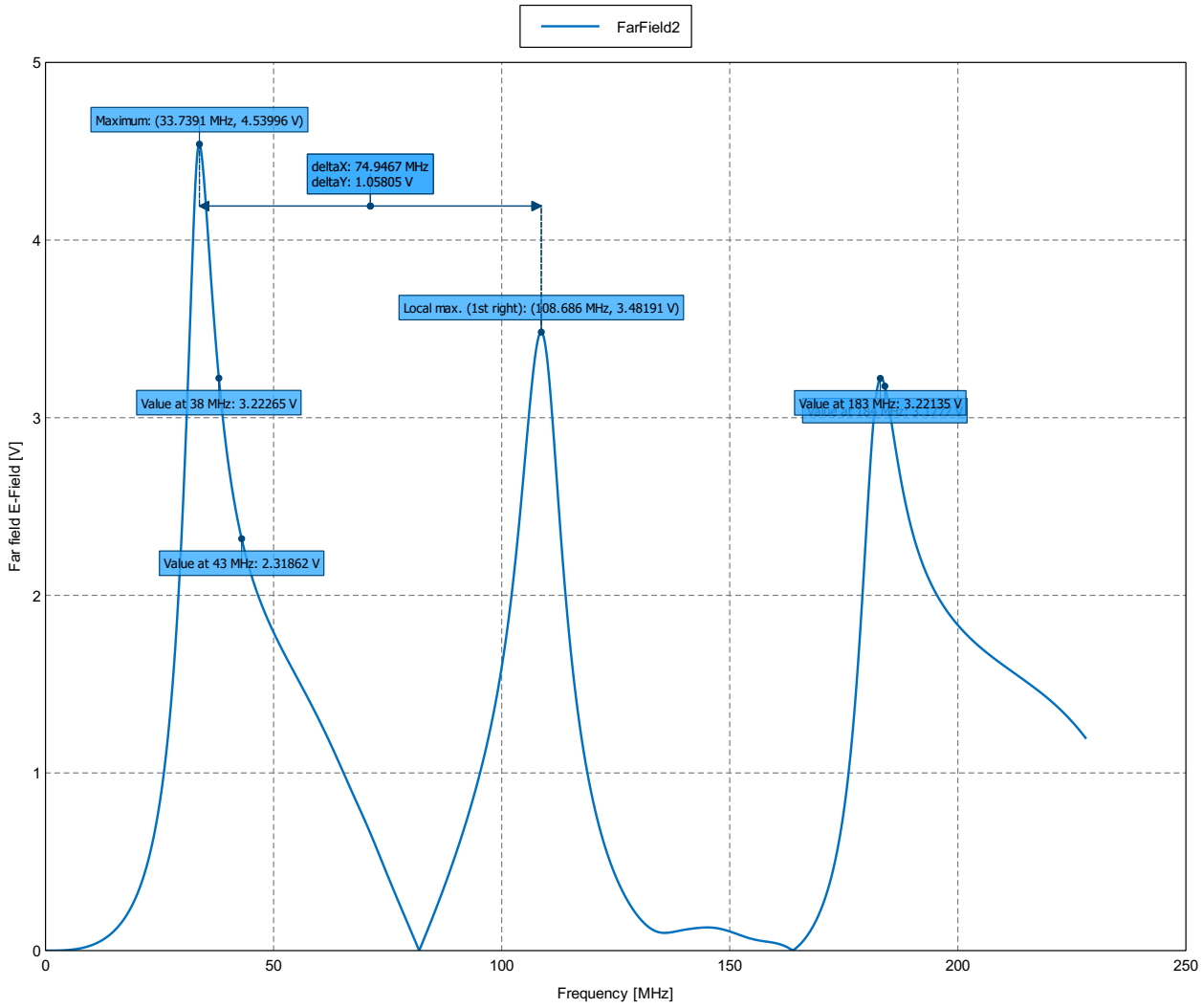

Figure 4: Total E-Field Magnitude [V] (Theta = 0 deg; Phi = 0 deg) - Dipolo_real

Far field: E db

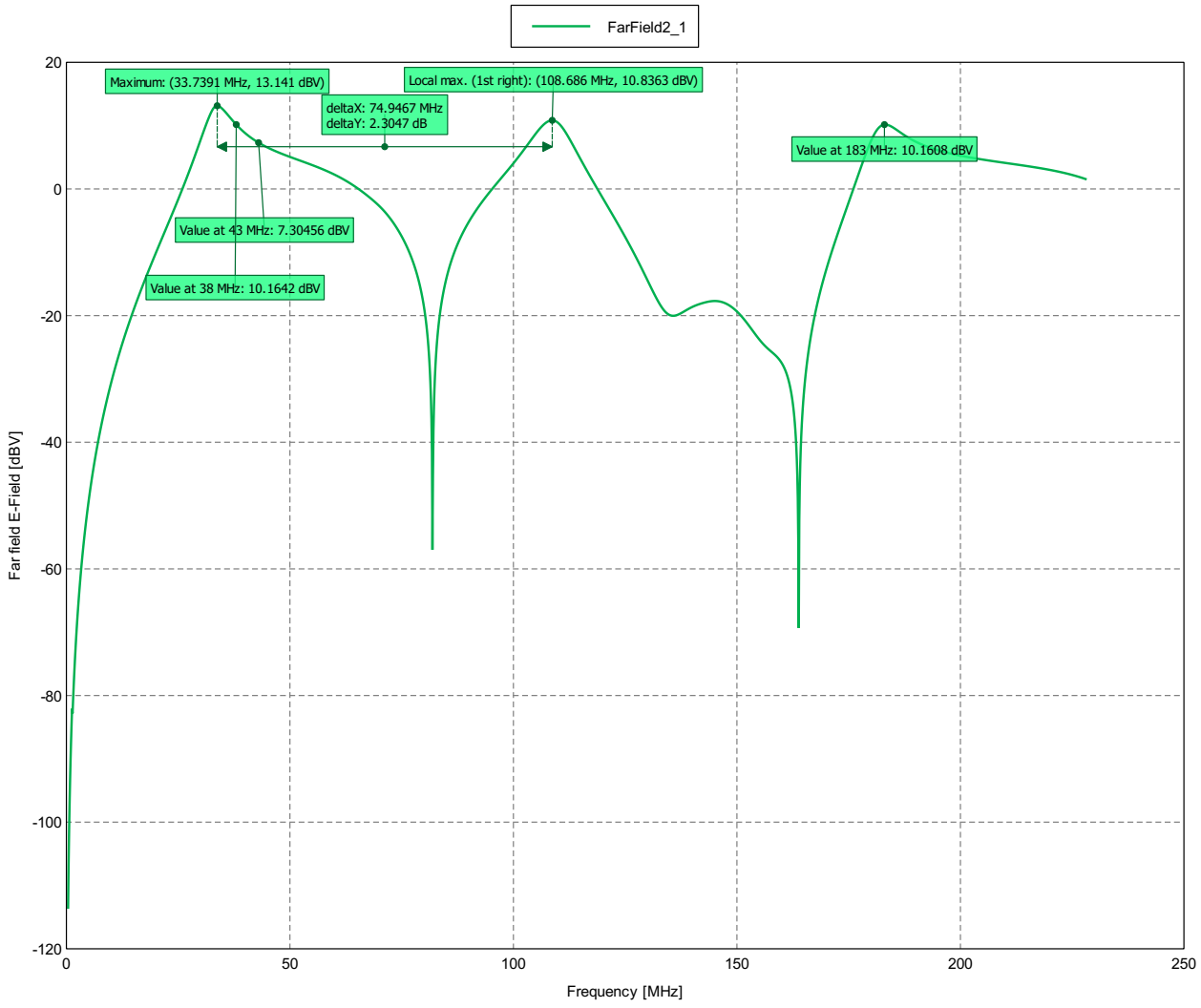

Figure 5: Total E-Field Magnitude [dBV] (Theta = 0 deg; Phi = 0 deg) - Dipolo_real

Far field: G

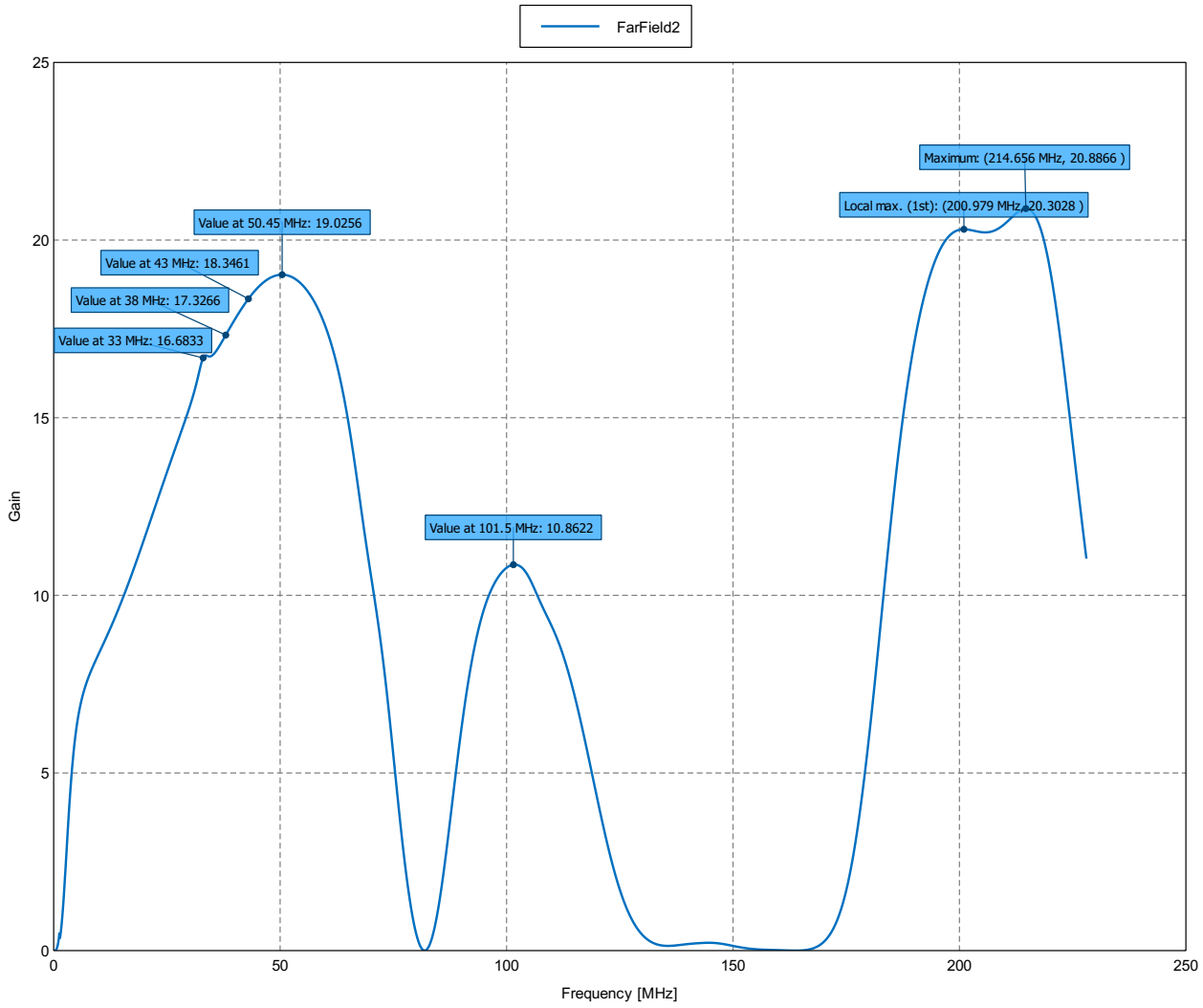

Figure 6: Total Gain (Theta = 0 deg; Phi = 0 deg) - Dipolo_real

Far field: G db

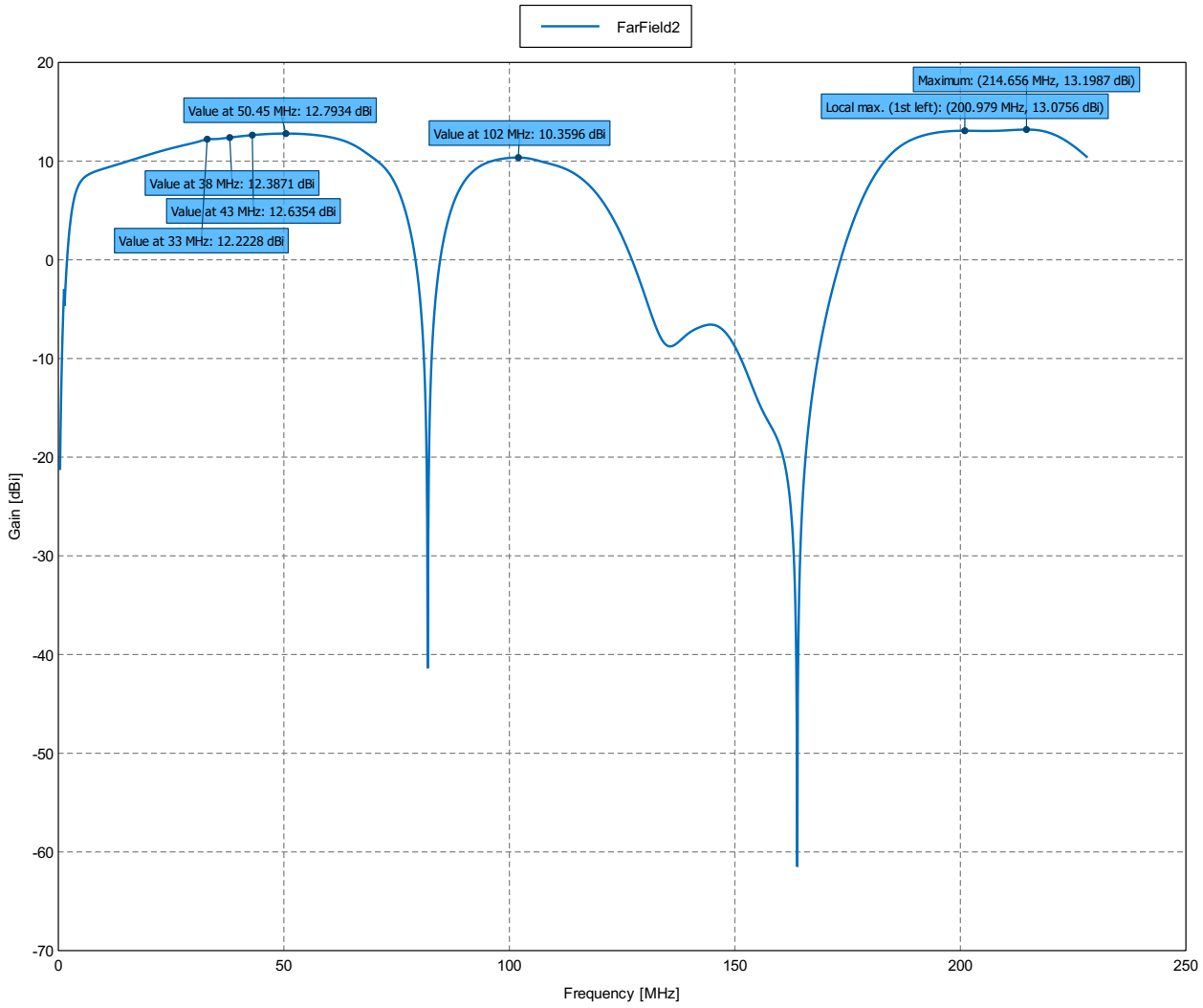

Figure 7: Total Gain [dBi] (Theta = 0 deg; Phi = 0 deg) - Dipolo_real

Far field: D

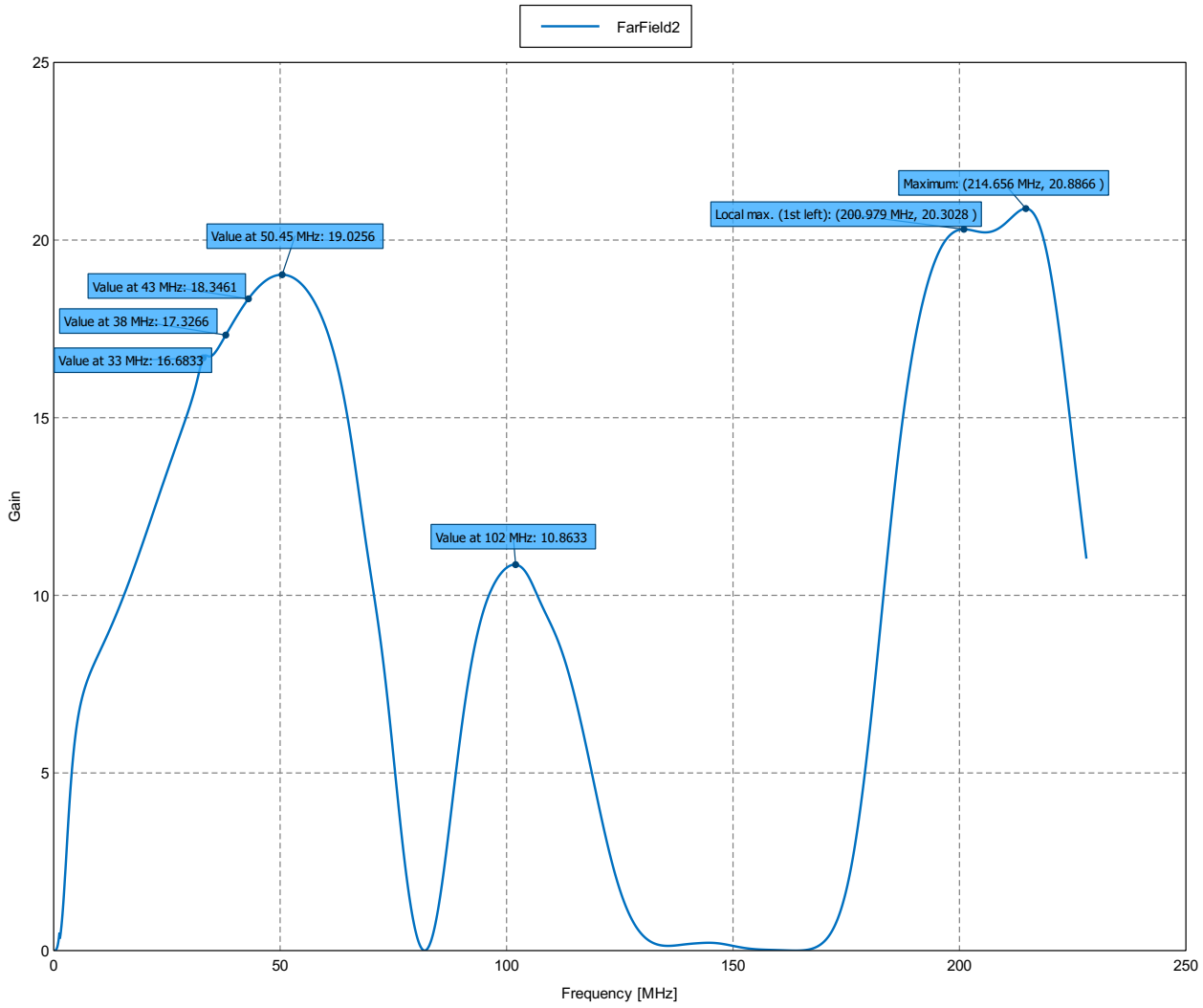

Figure 8: Total Gain (Theta = 0 deg; Phi = 0 deg) - Dipolo_real

Far field: D db

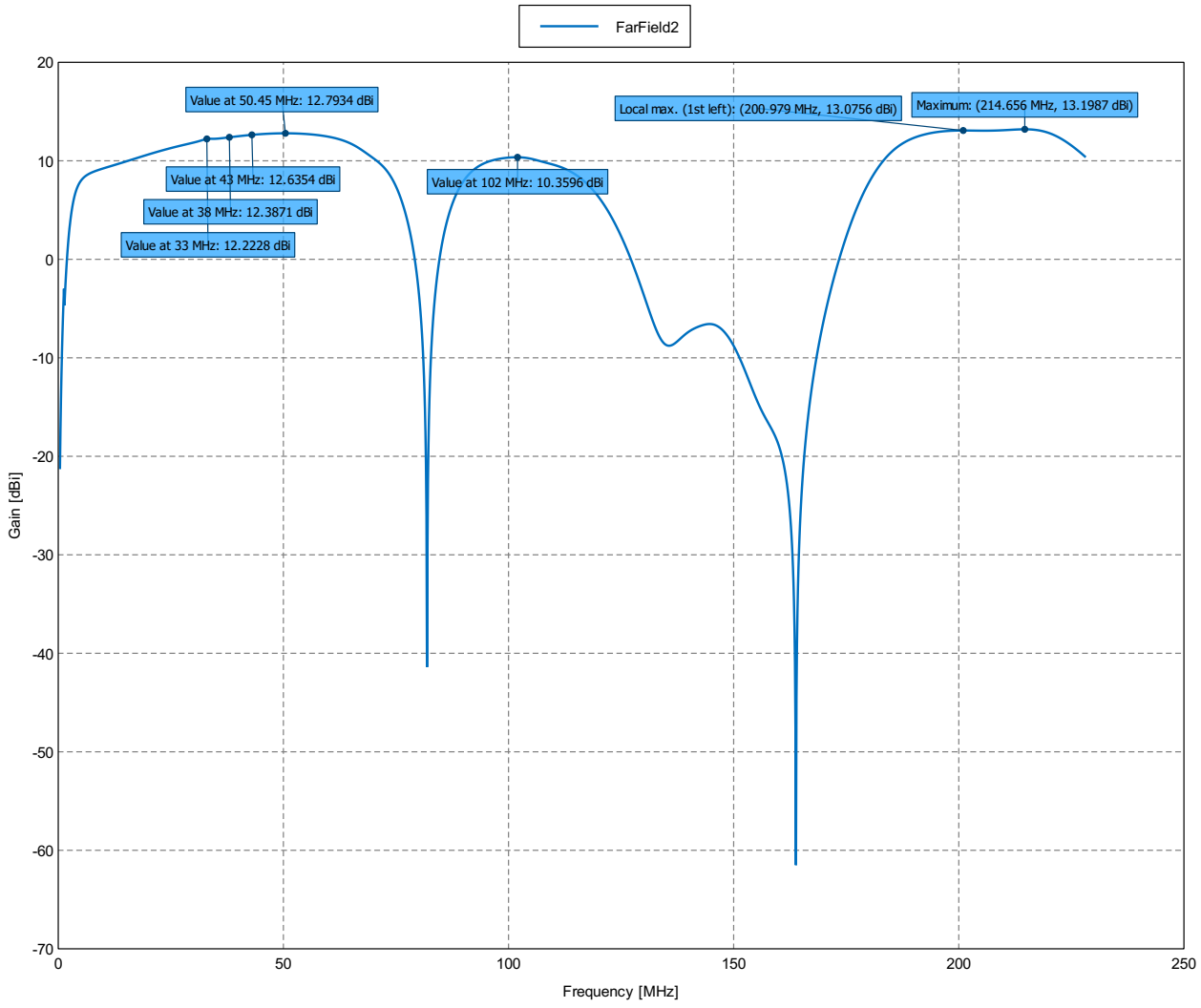

Figure 9: Total Gain [dBi] (Theta = 0 deg; Phi = 0 deg) - Dipolo_real

E_33

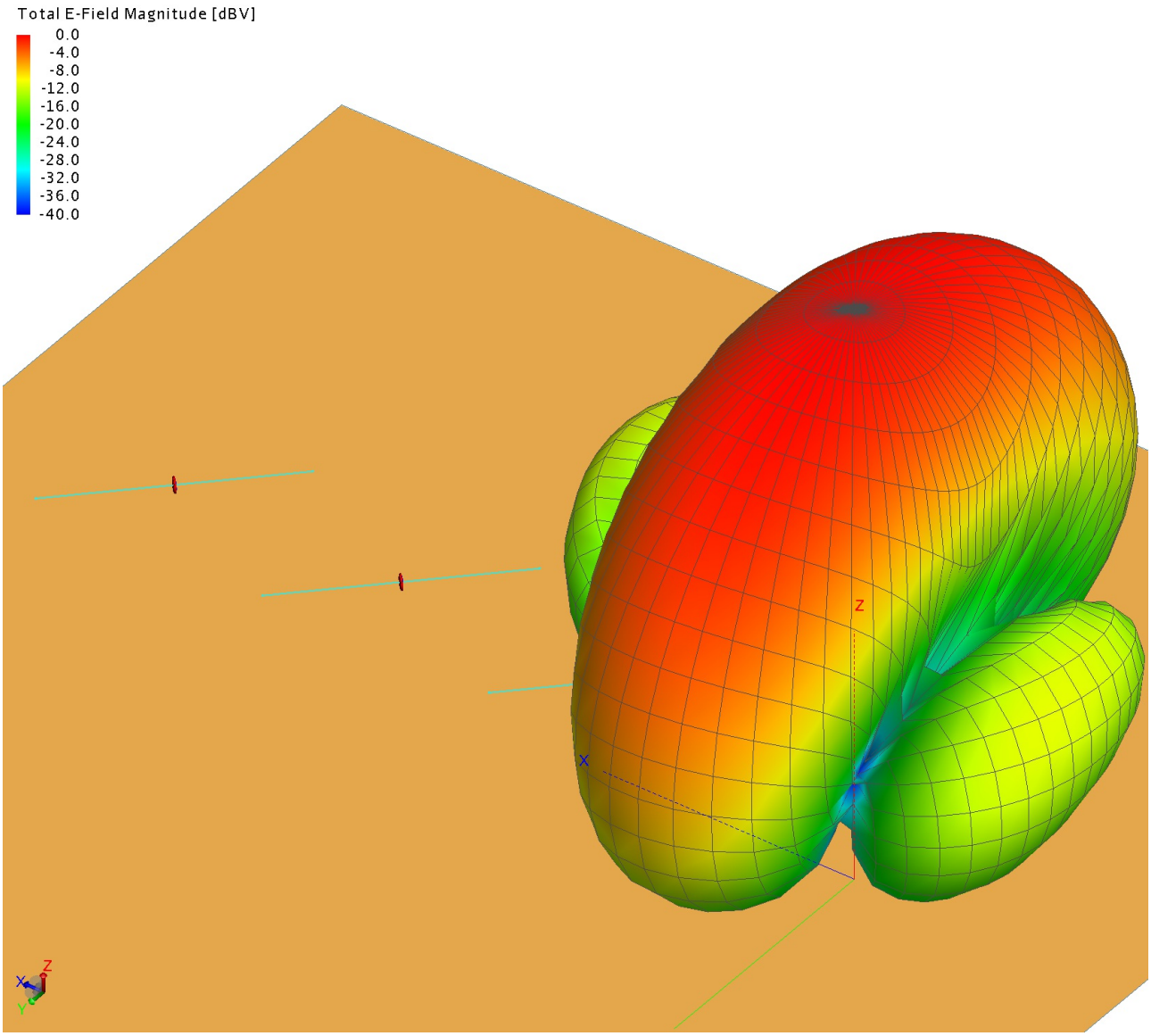

Figure 10: 3D View

G_33

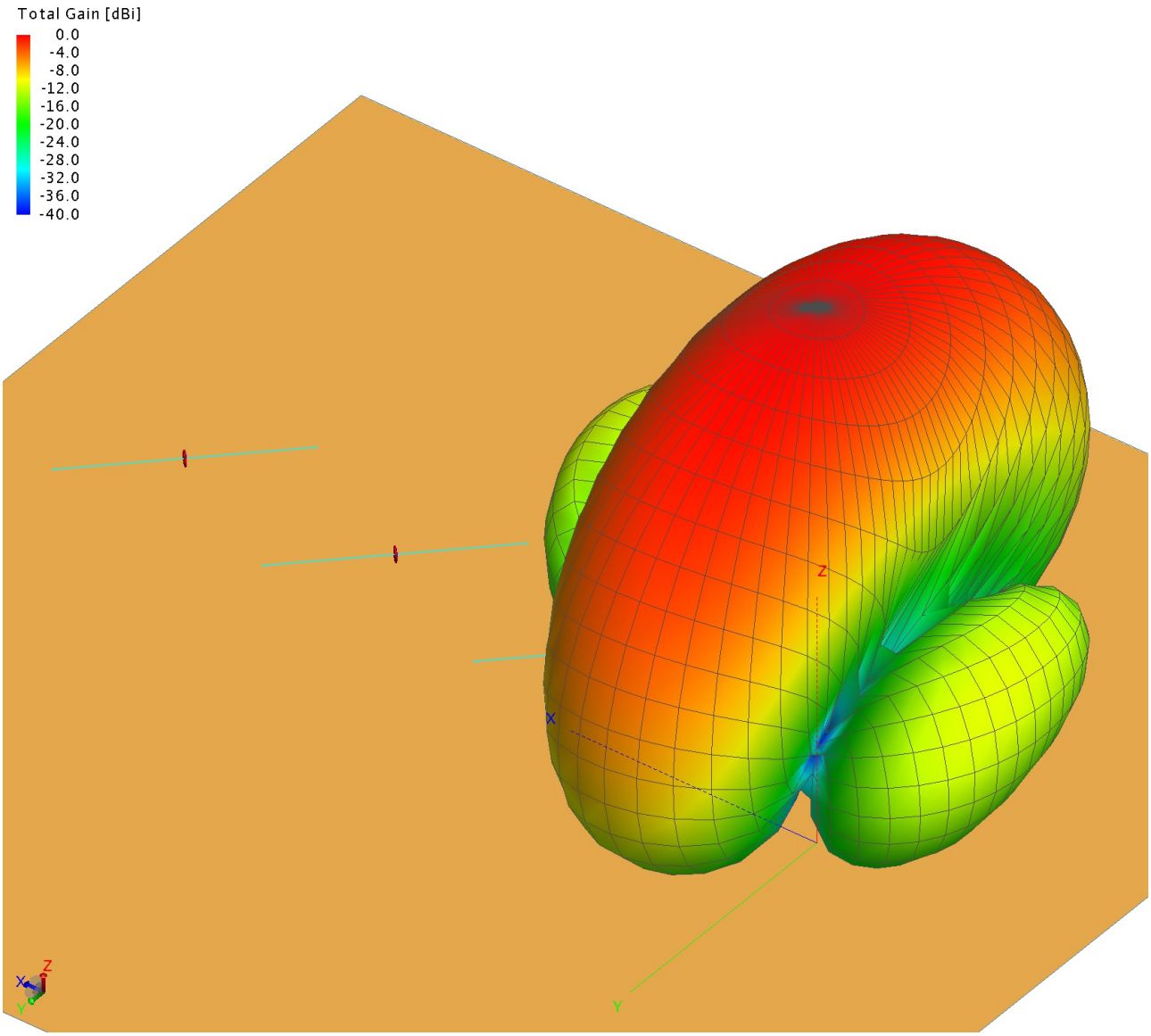

Figure 11: 3D View

D_33

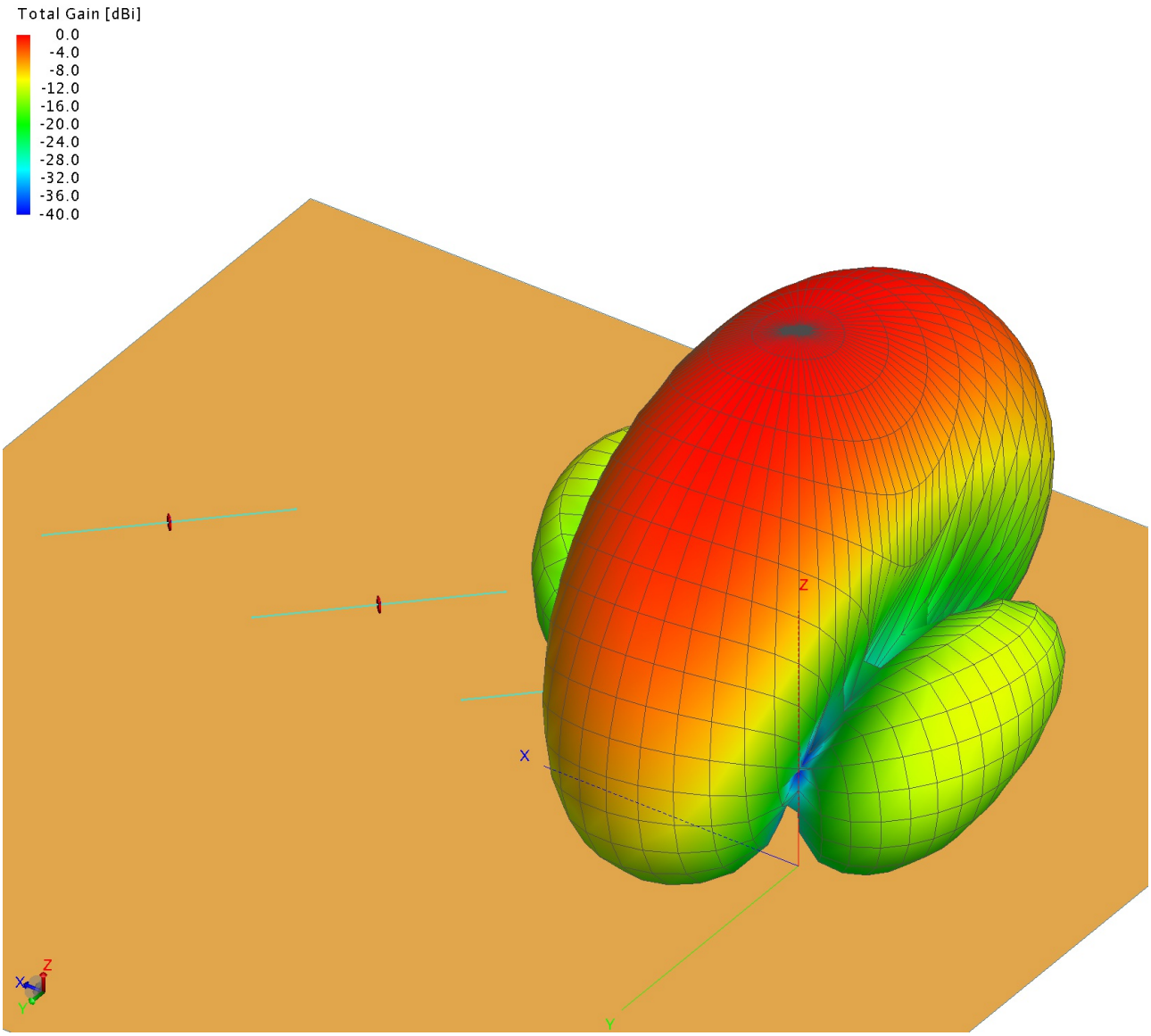

Figure 12: 3D View

FarField2: Total Gain [dBi]

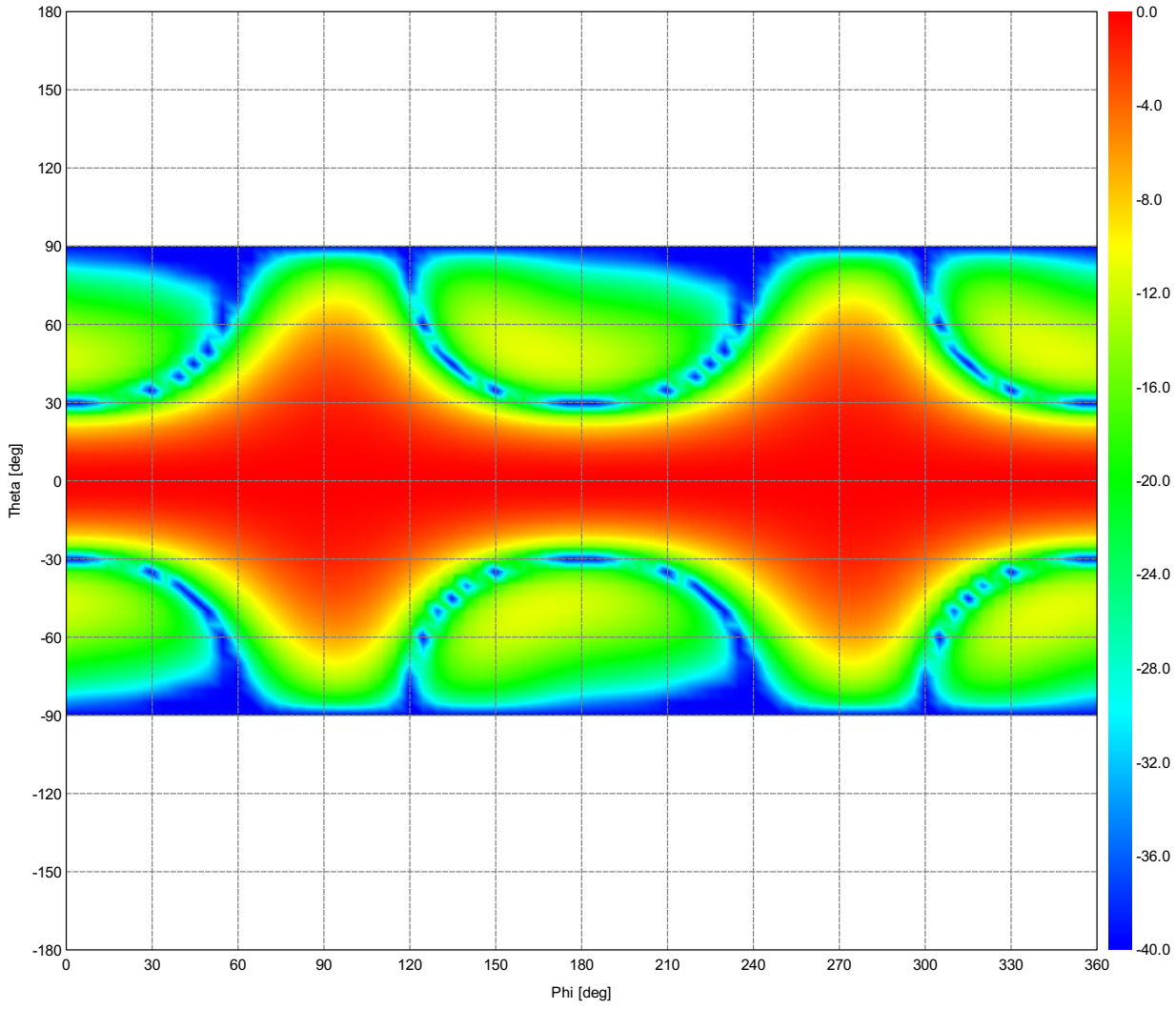

Figure 13: Total Gain (Frequency = 33.0719 MHz) - Dipolo_real

FarField2: Total Gain [dBi]

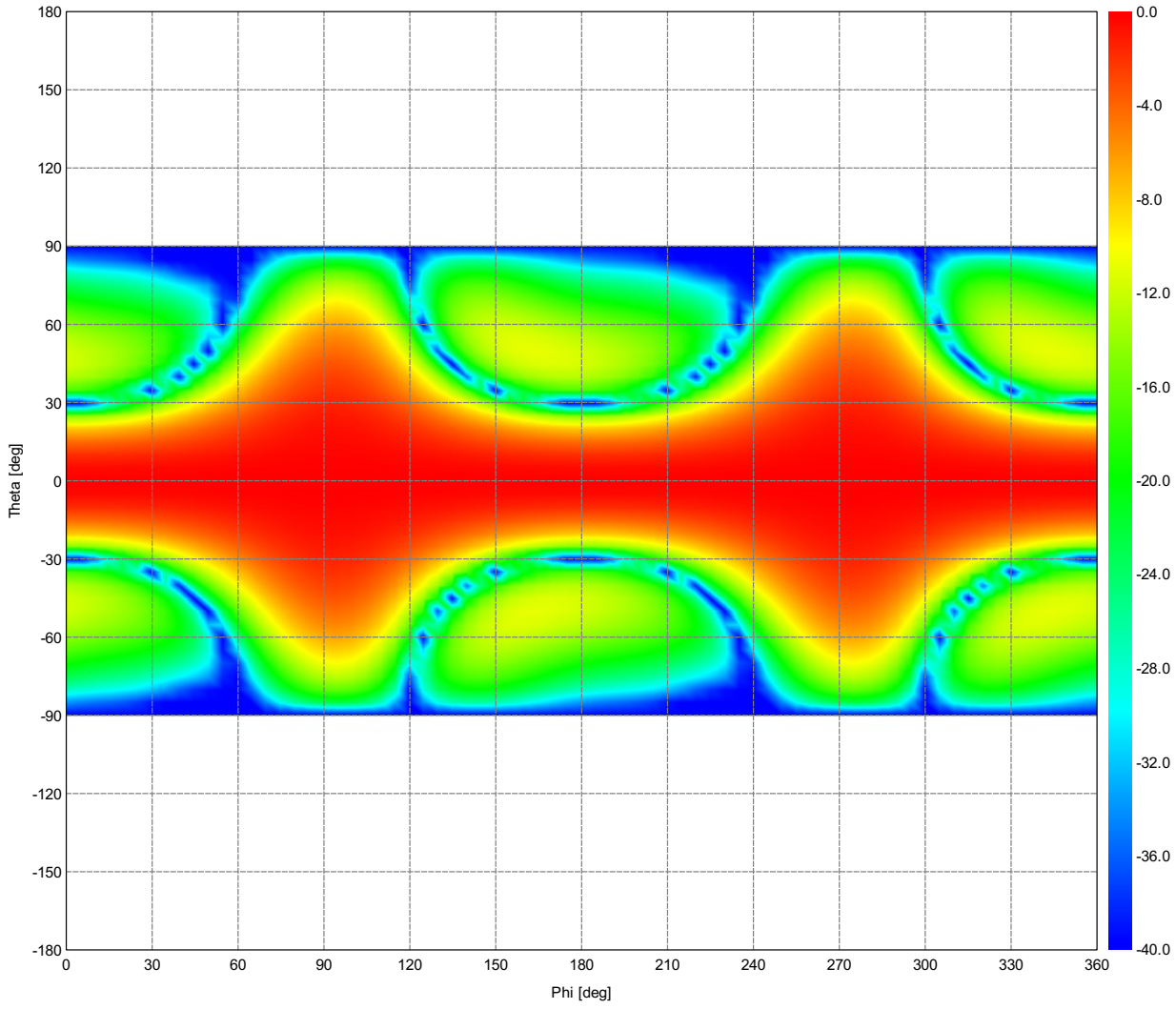

Figure 14: Total Gain (Frequency = 33.0719 MHz) - Dipolo_real

FarField2: Total Directivity [dBi]

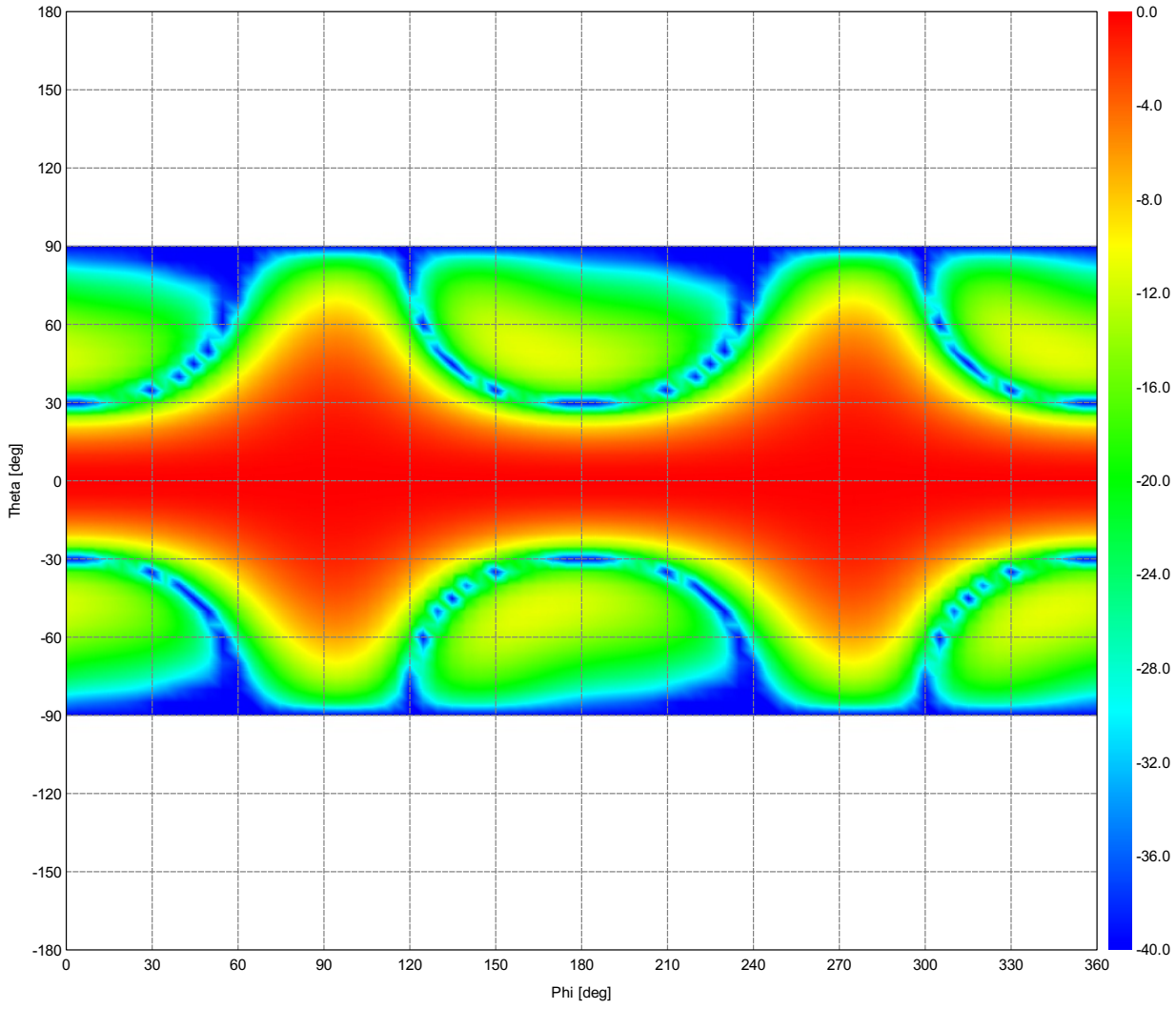

Figure 15: Total Directivity (Frequency = 33.0719 MHz) - Dipolo_real

Far field: max G

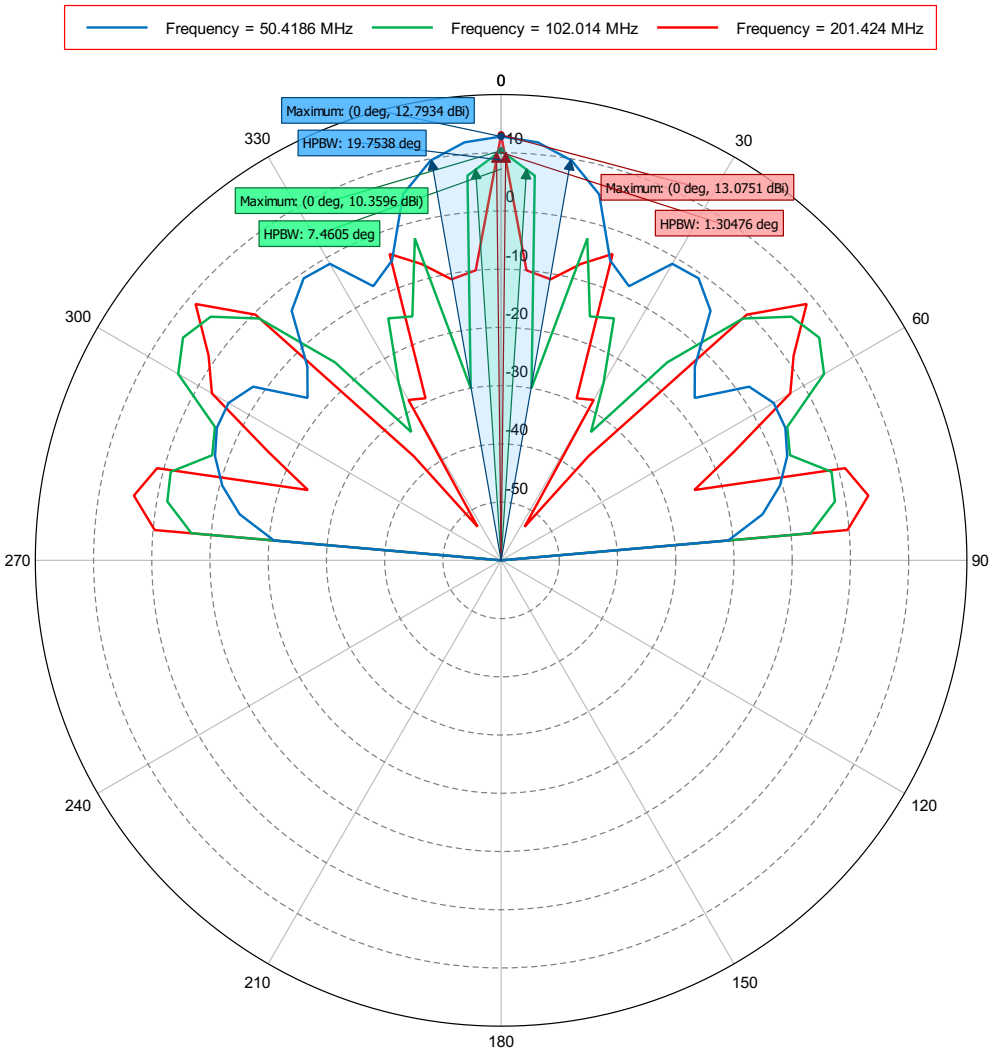

Figure 16: Total Gain (Phi = 0 deg) - Dipolo_real

Far field: G

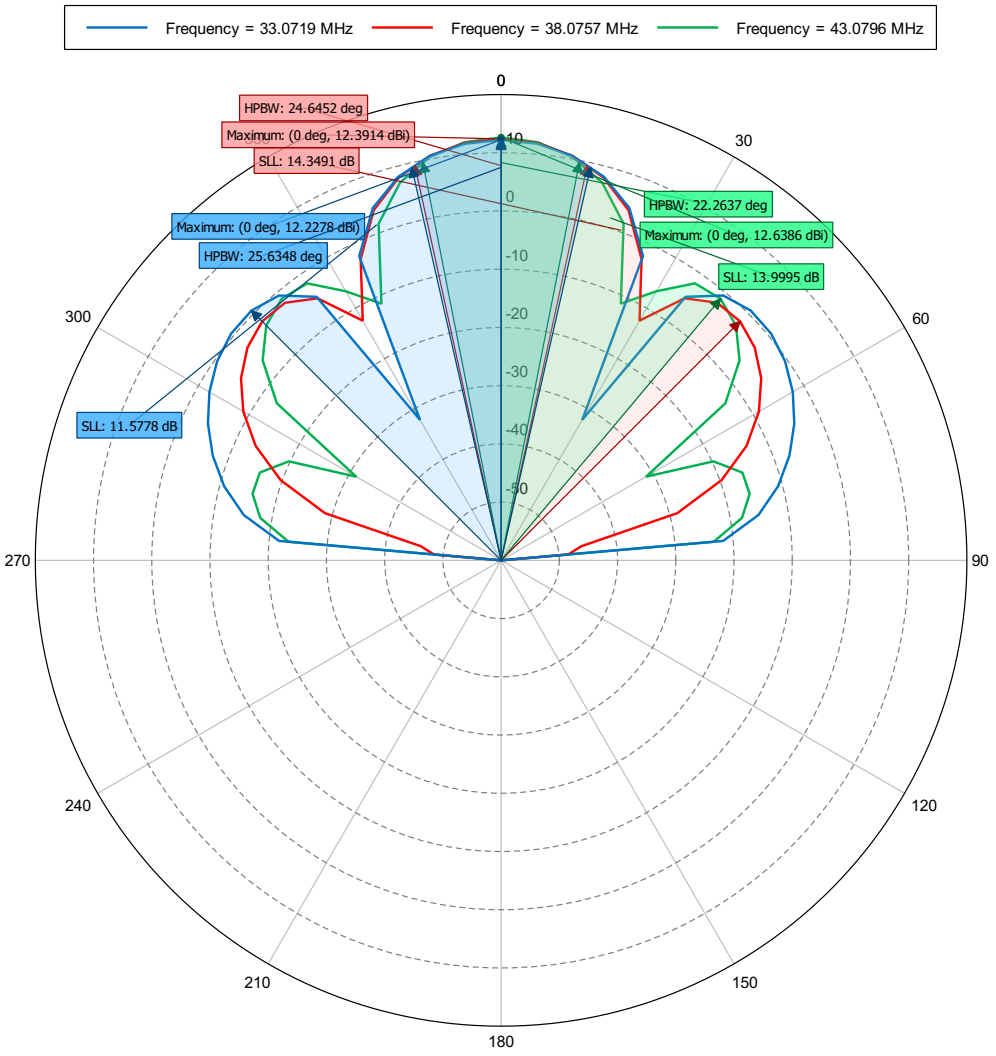

Figure 17: Total Gain (Phi = 0 deg) - Dipolo_real

Far field: G

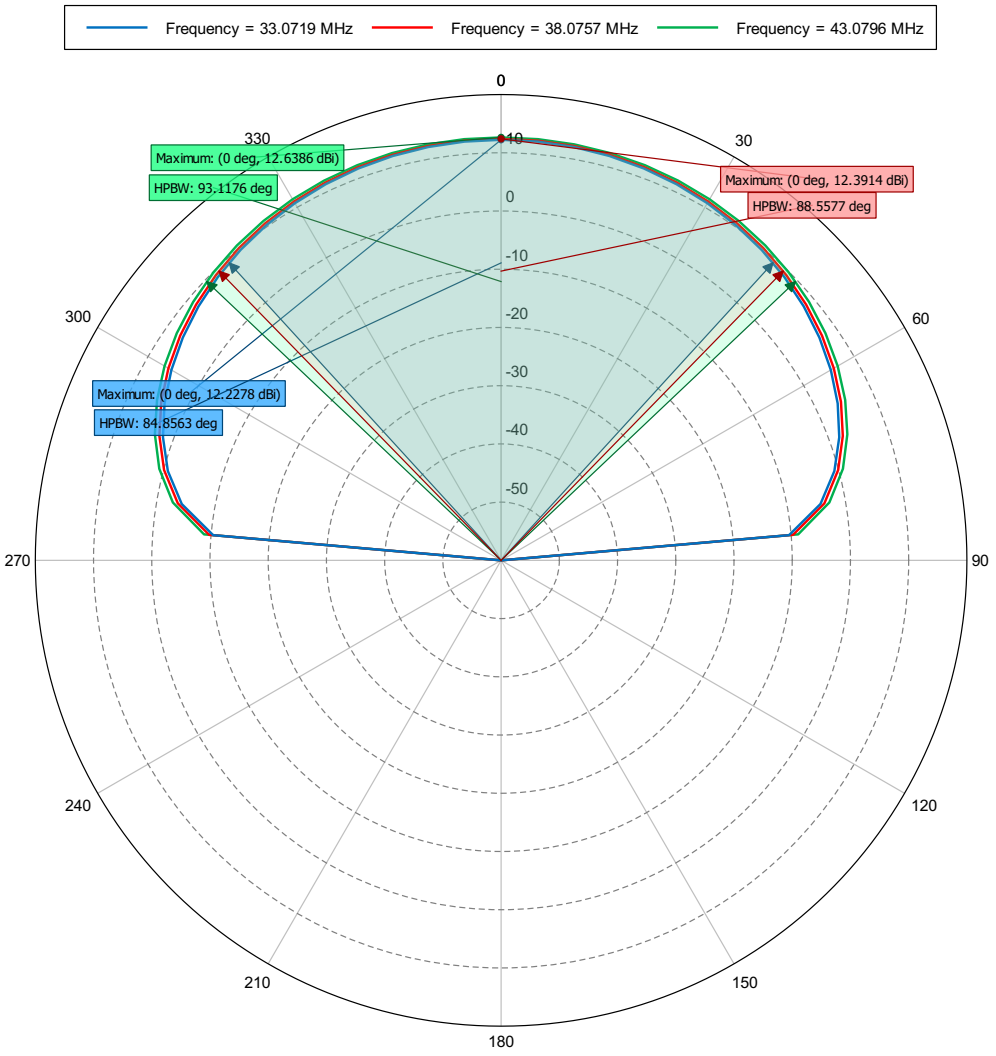

Figure 18: Total Gain (Phi = 90 deg) - Dipolo_real

Excitation

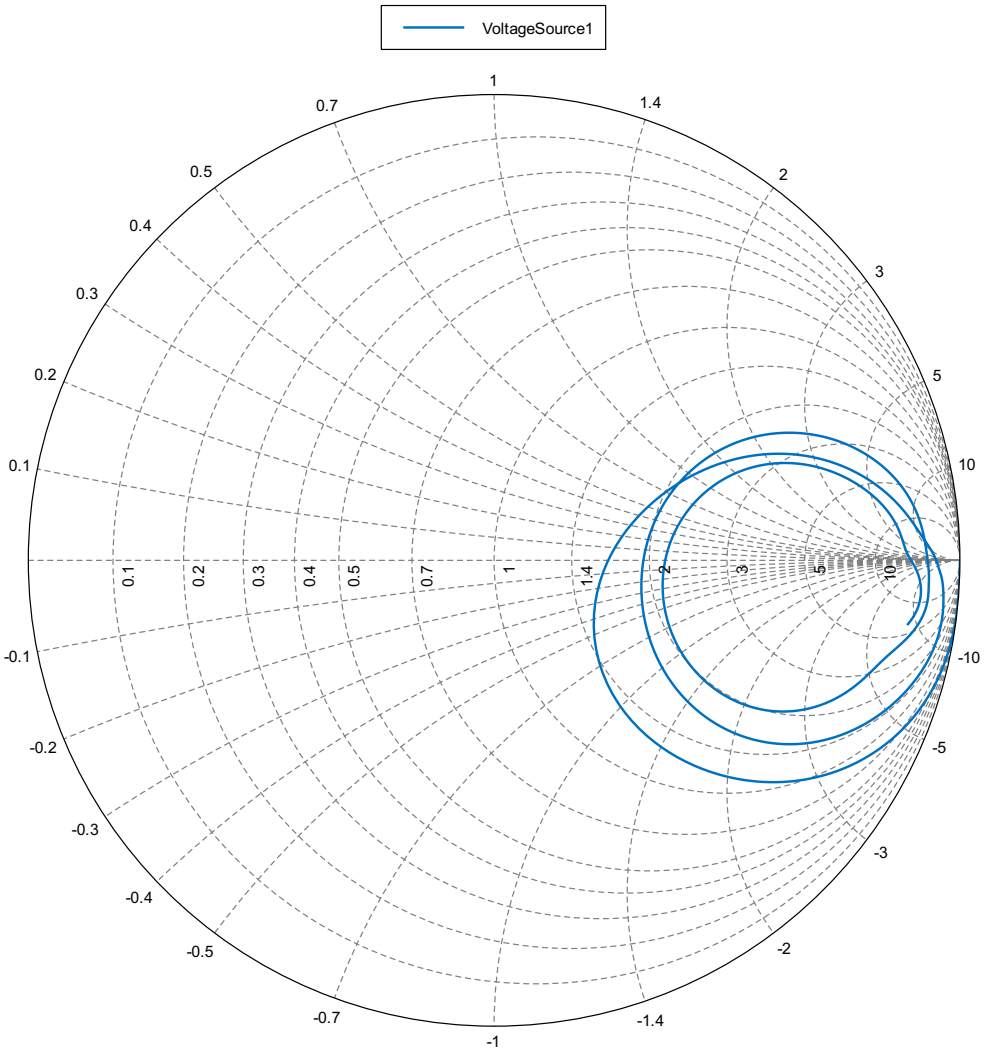

Figure 19: Impedance - Dipolo_real

Array_beamforming_001

C:/Users/Cepia-beam/Documents/Feko/dipolo realista_16
2022-02-28 13:39

theta=0,phy=0

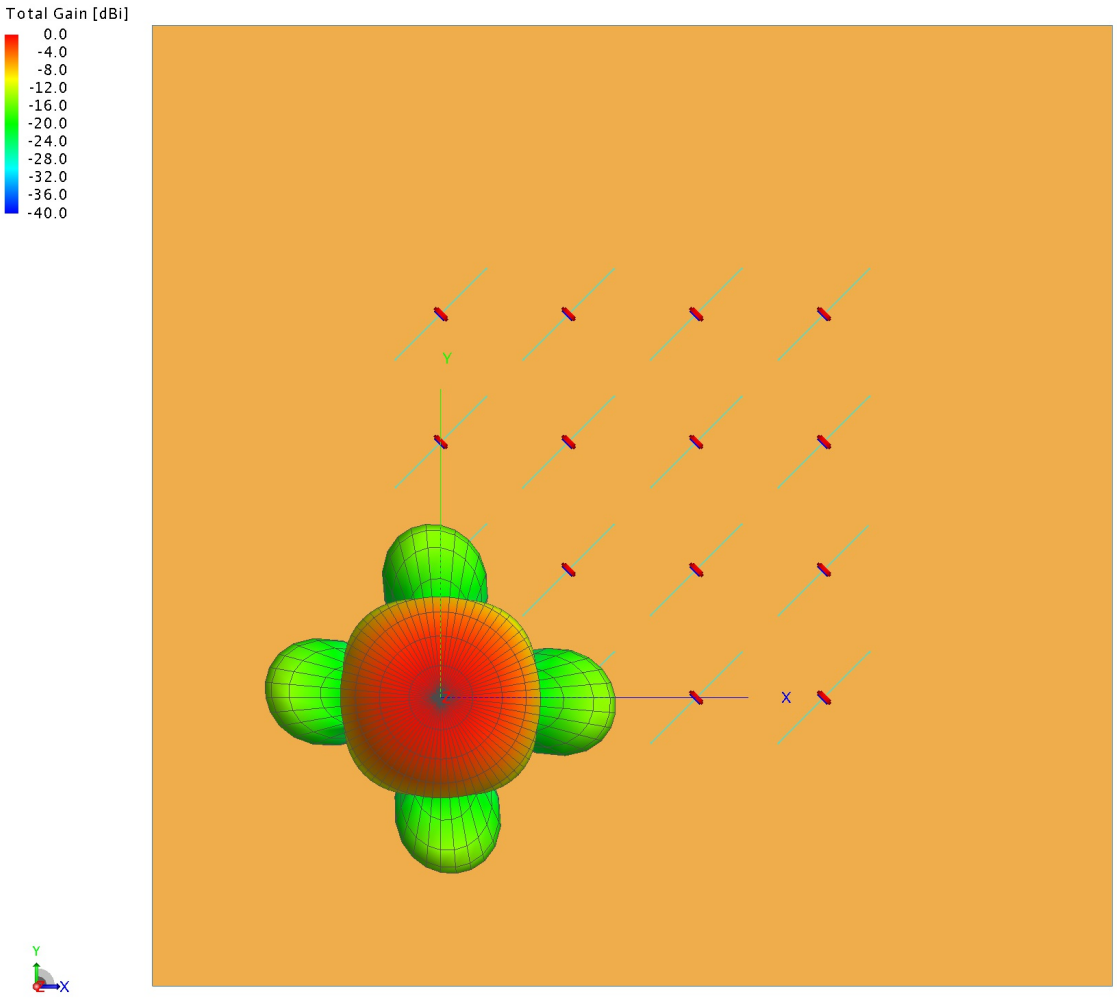

Figure 1: 3D View

theta=15,phy=0

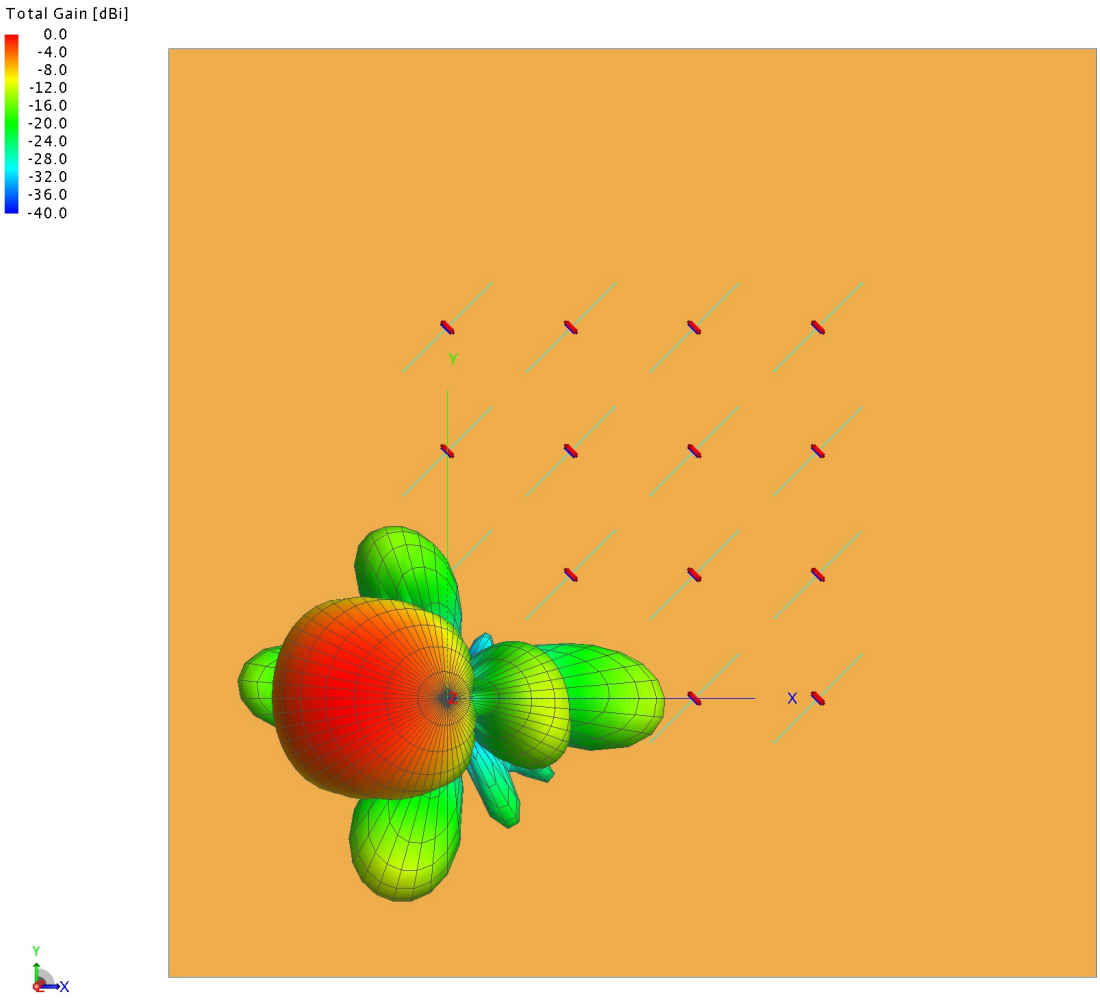

Figure 2: 3D View

theta=15,phy=45

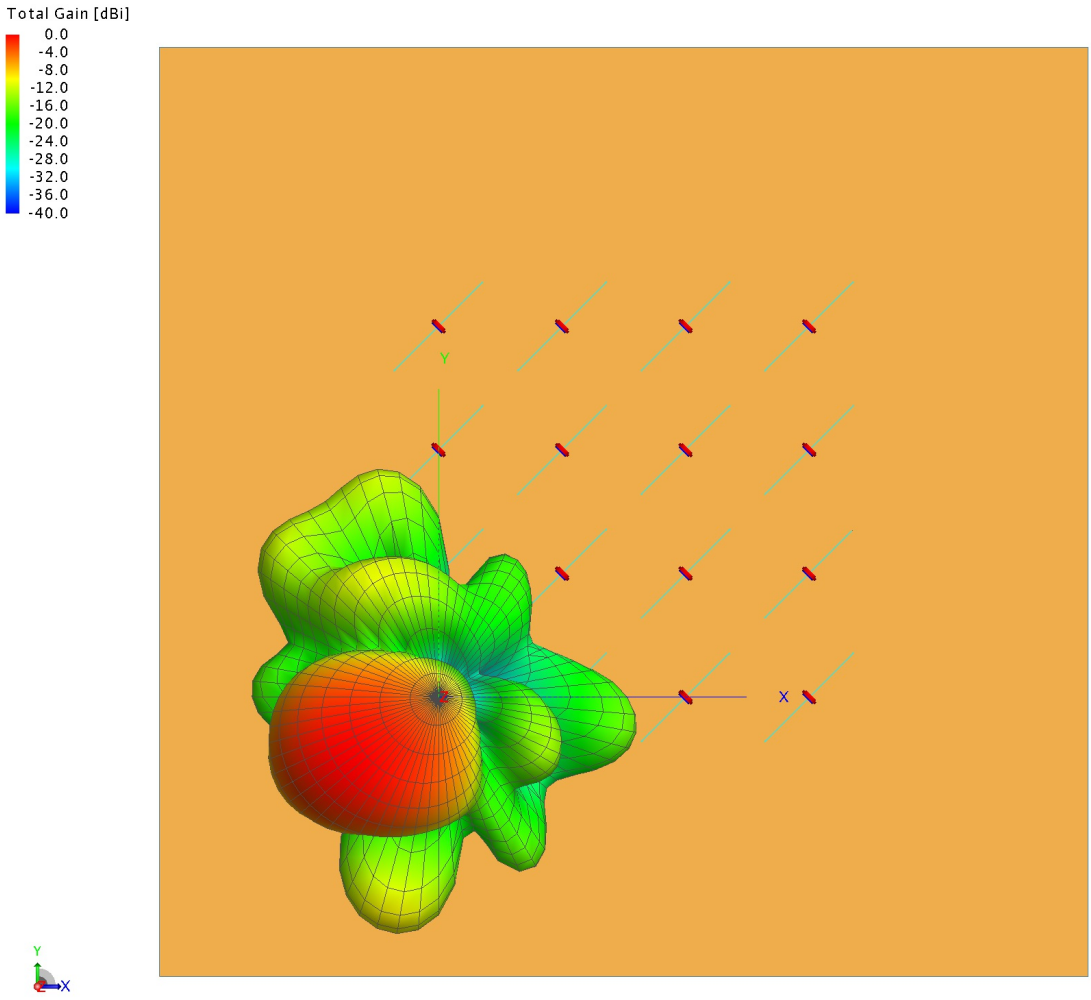

Figure 3: 3D View

theta=15,phy=90

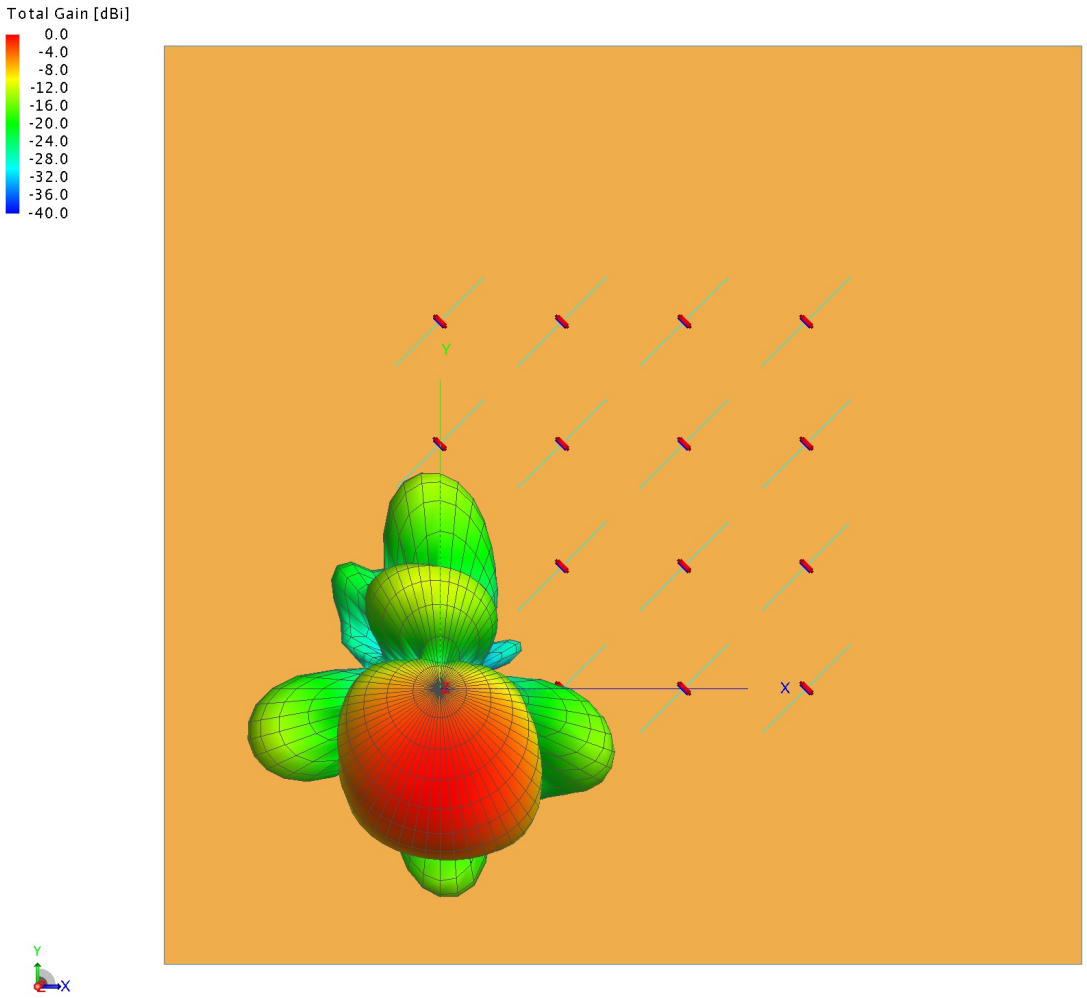

Figure 4: 3D View

theta=15,phy=135

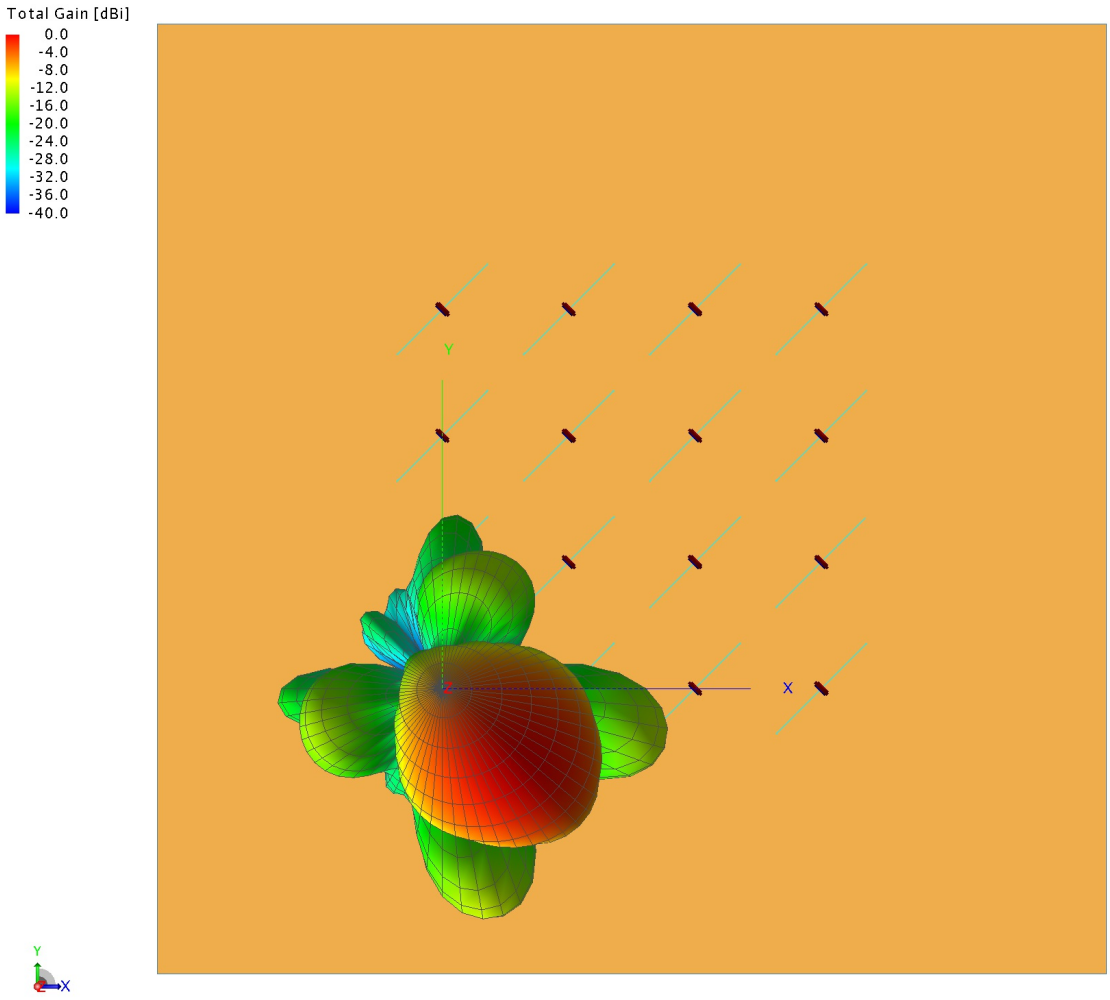

Figure 5: 3D View

theta=15,phy=180

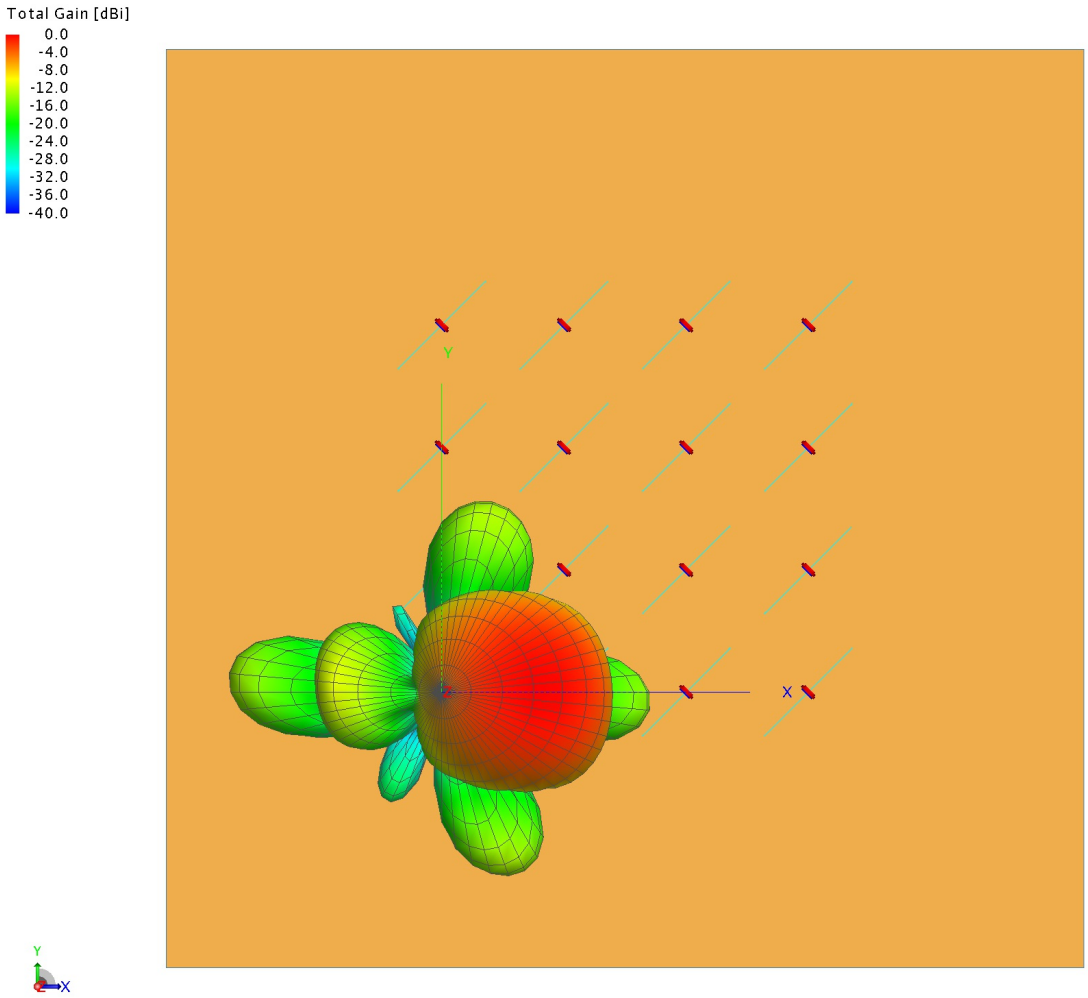

Figure 6: 3D View

theta=15,phy=225

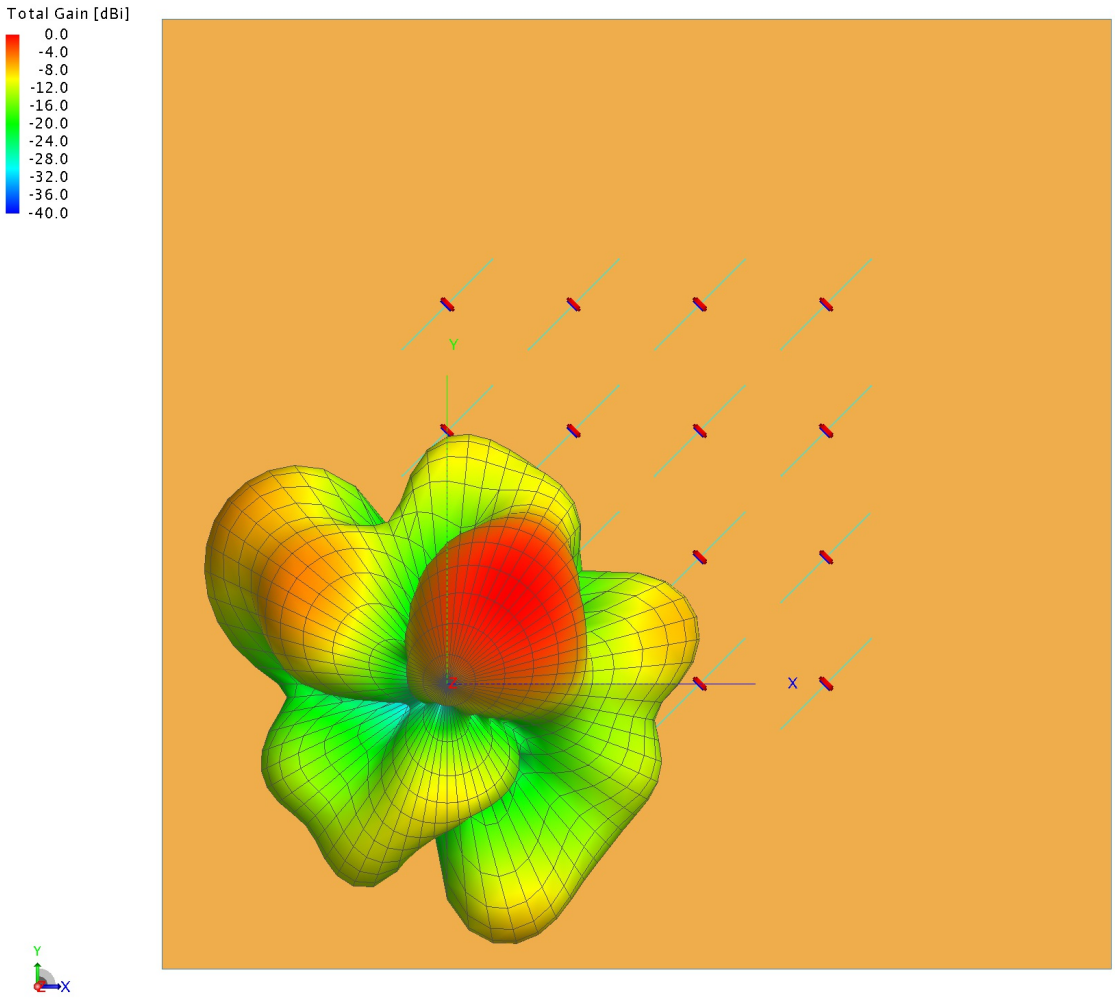

Figure 7: 3D View

theta=15,phy=270

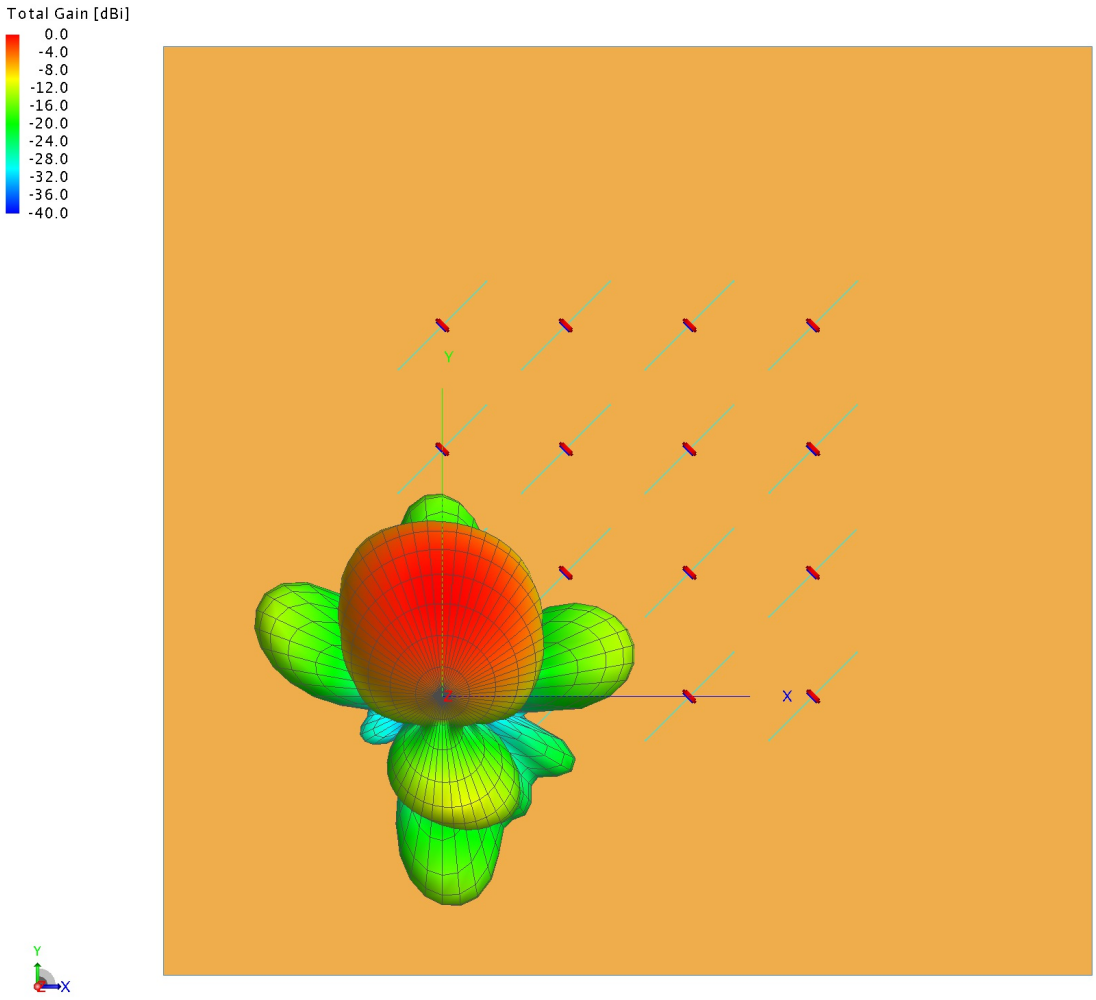

Figure 8: 3D View

theta=15,phy=315

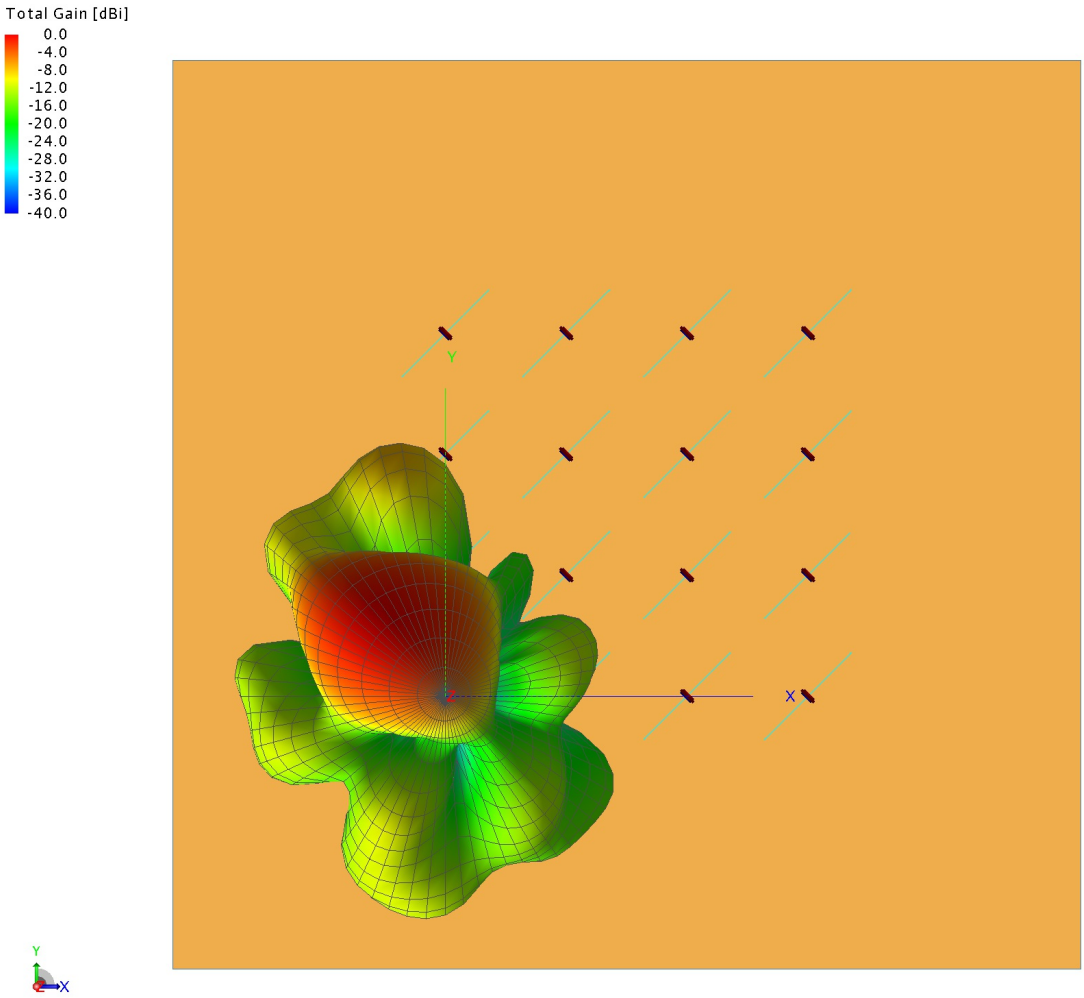

Figure 9: 3D View

theta=15,phy=360

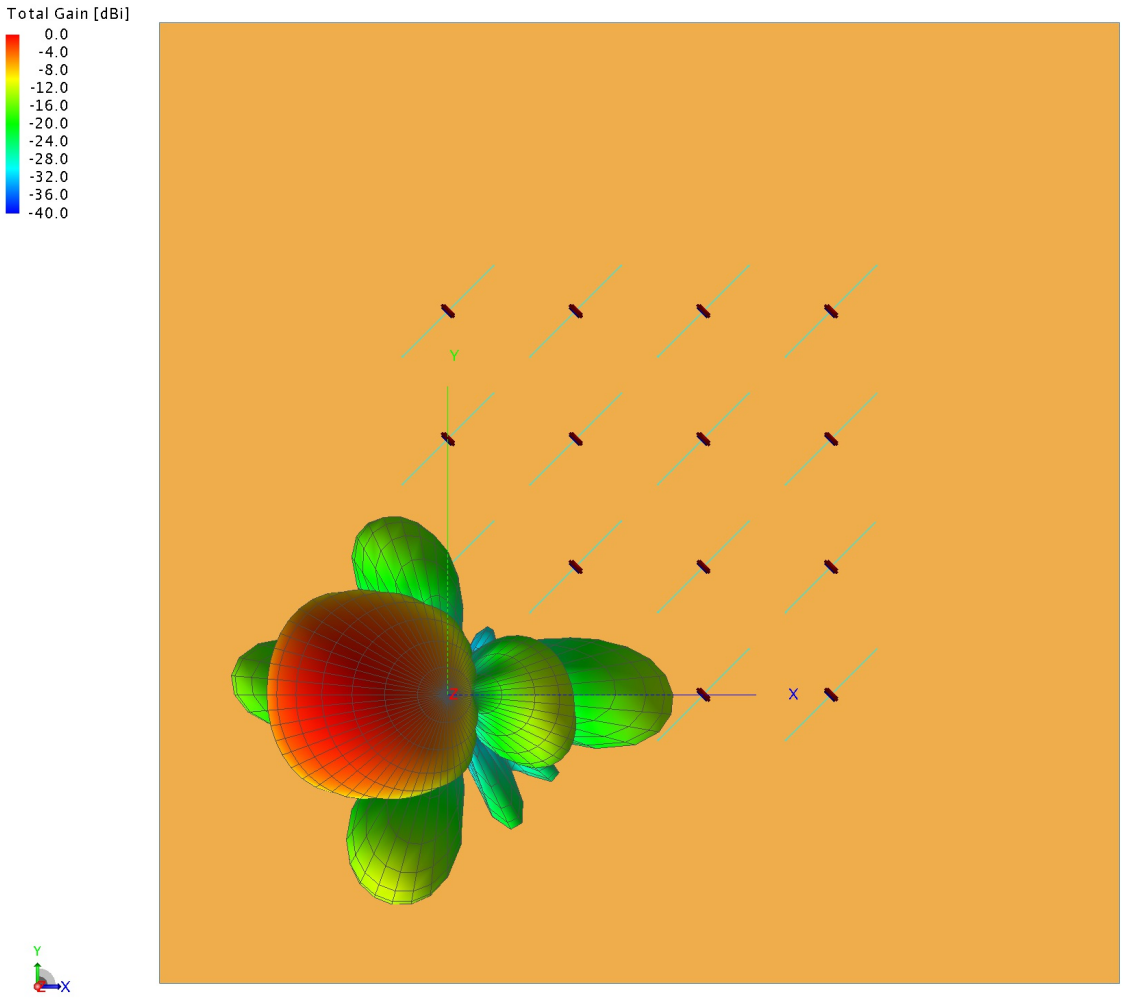

Figure 10: 3D View

theta=0,phy=0: Total Gain [dBi]

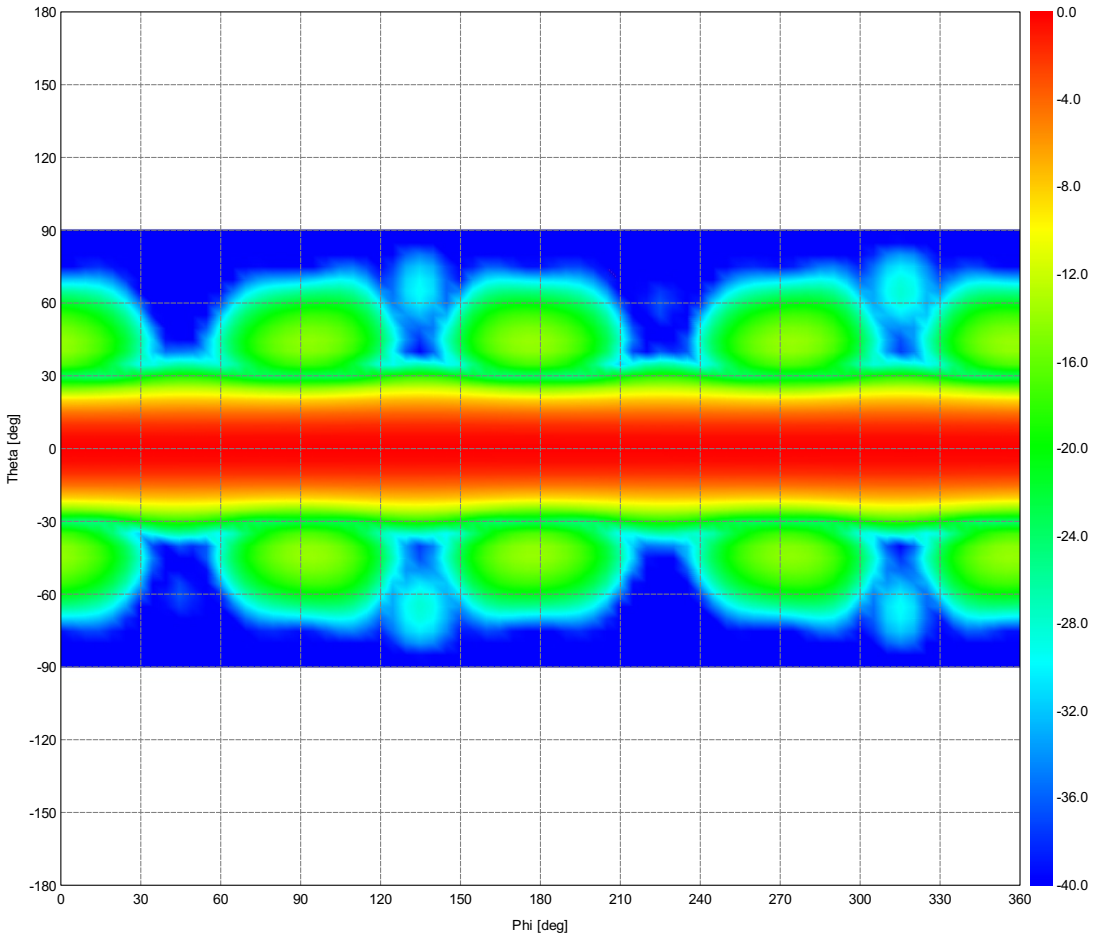

Figure 11: Total Gain (Frequency = 38.126 MHz) - Dipolo_real

theta=15,phy=0: Total Gain [dBi]

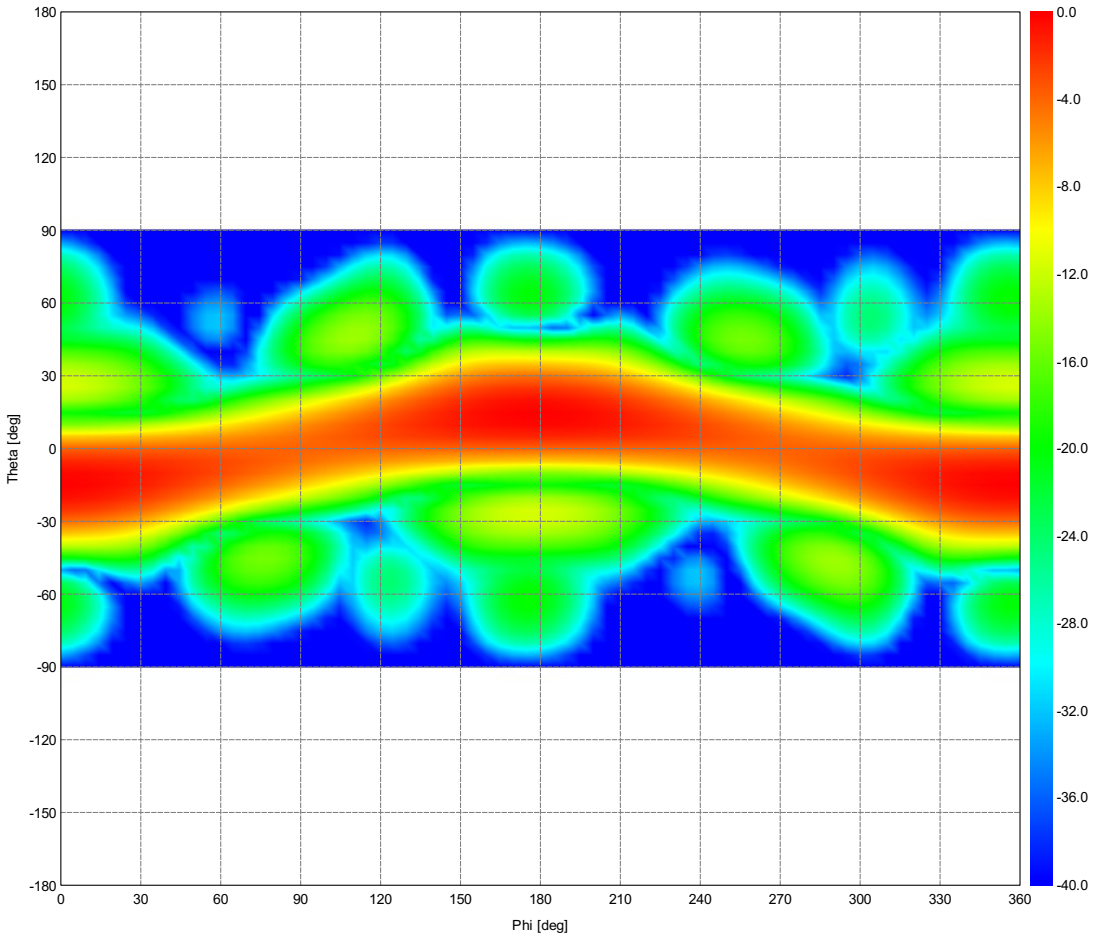

Figure 12: Total Gain (Frequency = 38.126 MHz) - Dipolo_real

theta=15,phy=45: Total Gain [dBi]

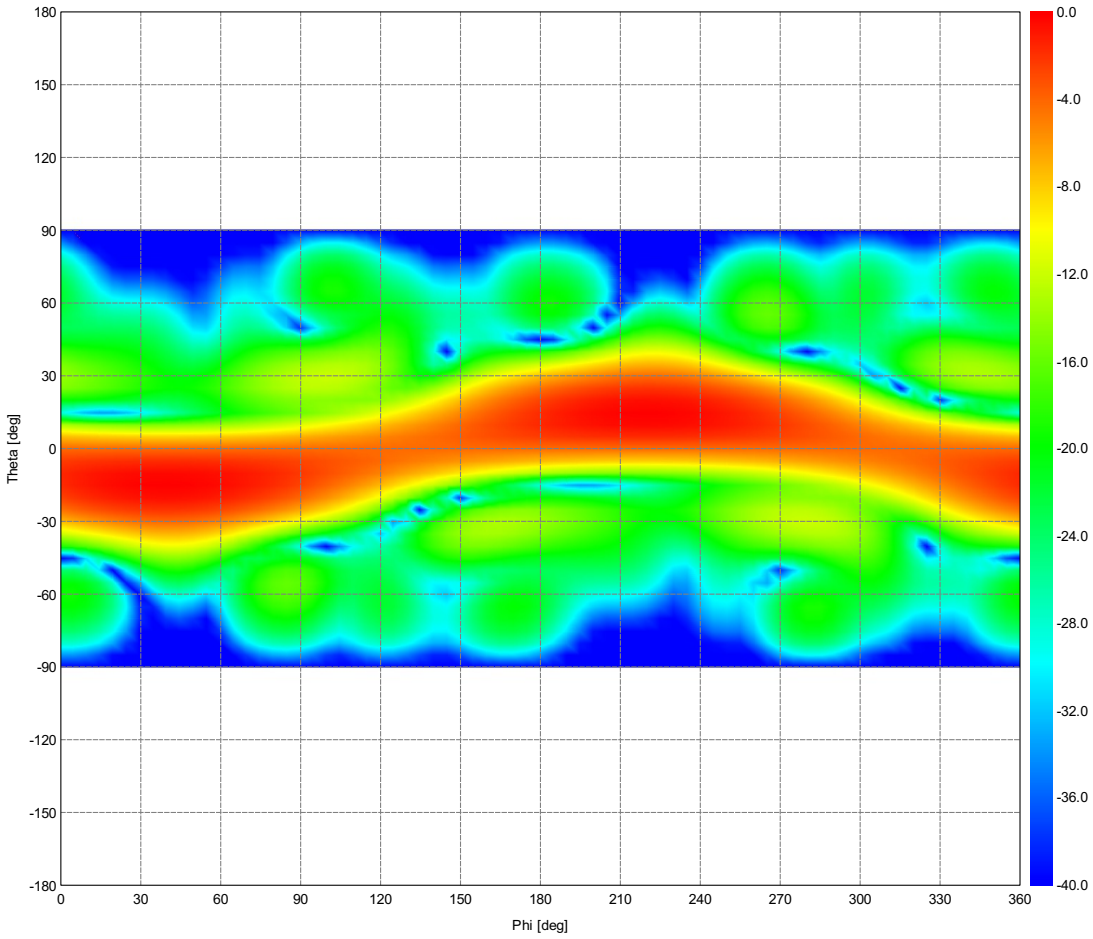

Figure 13: Total Gain (Frequency = 38.126 MHz) - Dipolo_real

theta=15,phy=90: Total Gain [dBi]

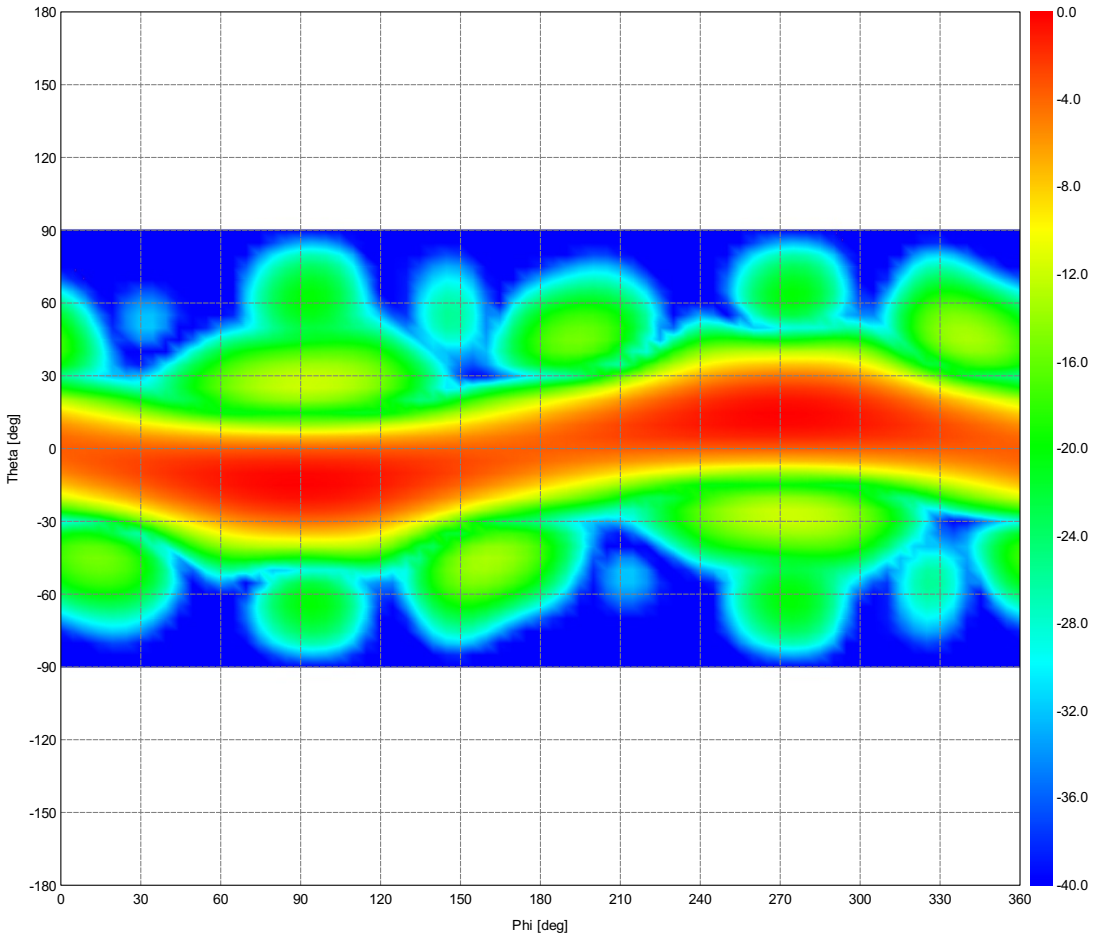

Figure 14: Total Gain (Frequency = 38.126 MHz) - Dipolo_real

theta=15,phy=135: Total Gain [dBi]

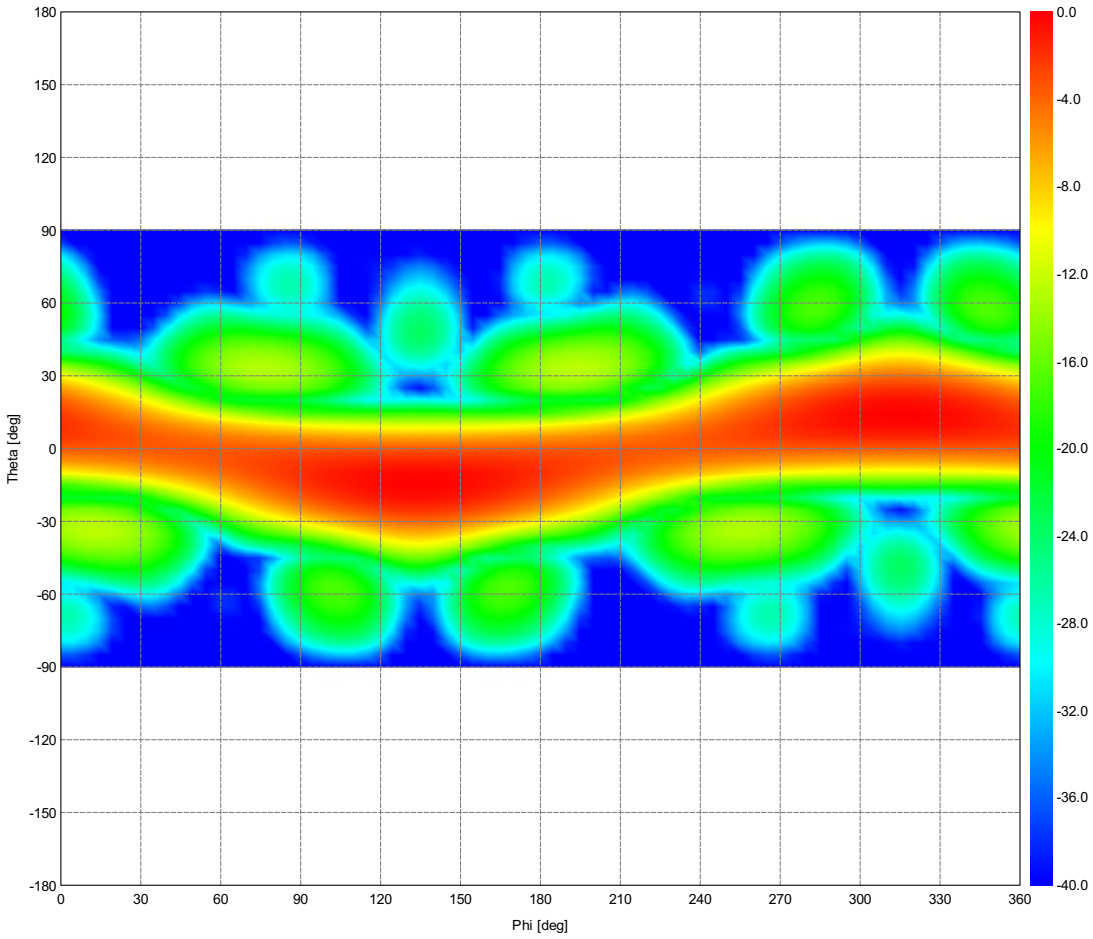

Figure 15: Total Gain (Frequency = 38.126 MHz) - Dipolo_real

theta=15,phy=180: Total Gain [dBi]

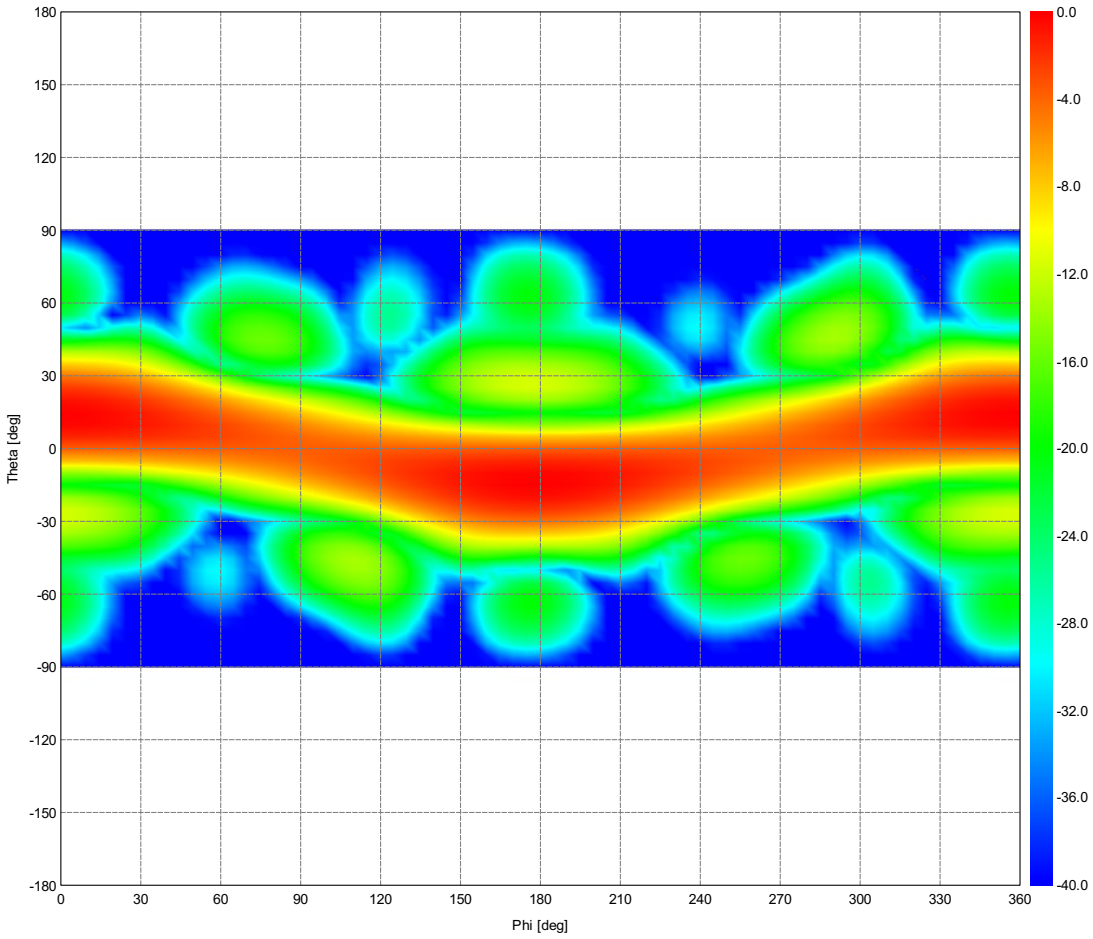

Figure 16: Total Gain (Frequency = 38.126 MHz) - Dipolo_real

theta=15,phy=235: Total Gain [dBi]

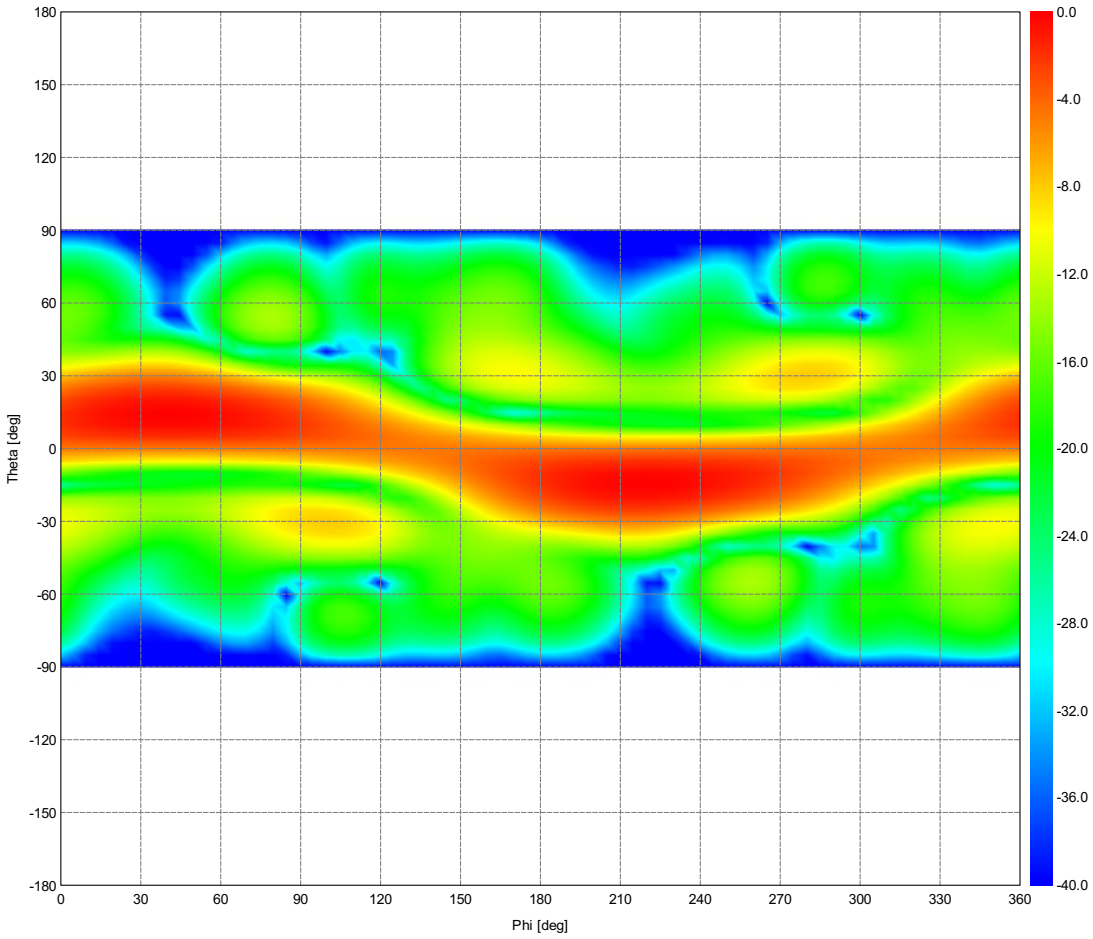

Figure 17: Total Gain (Frequency = 38.126 MHz) - Dipolo_real

theta=15,phy=270: Total Gain [dBi]

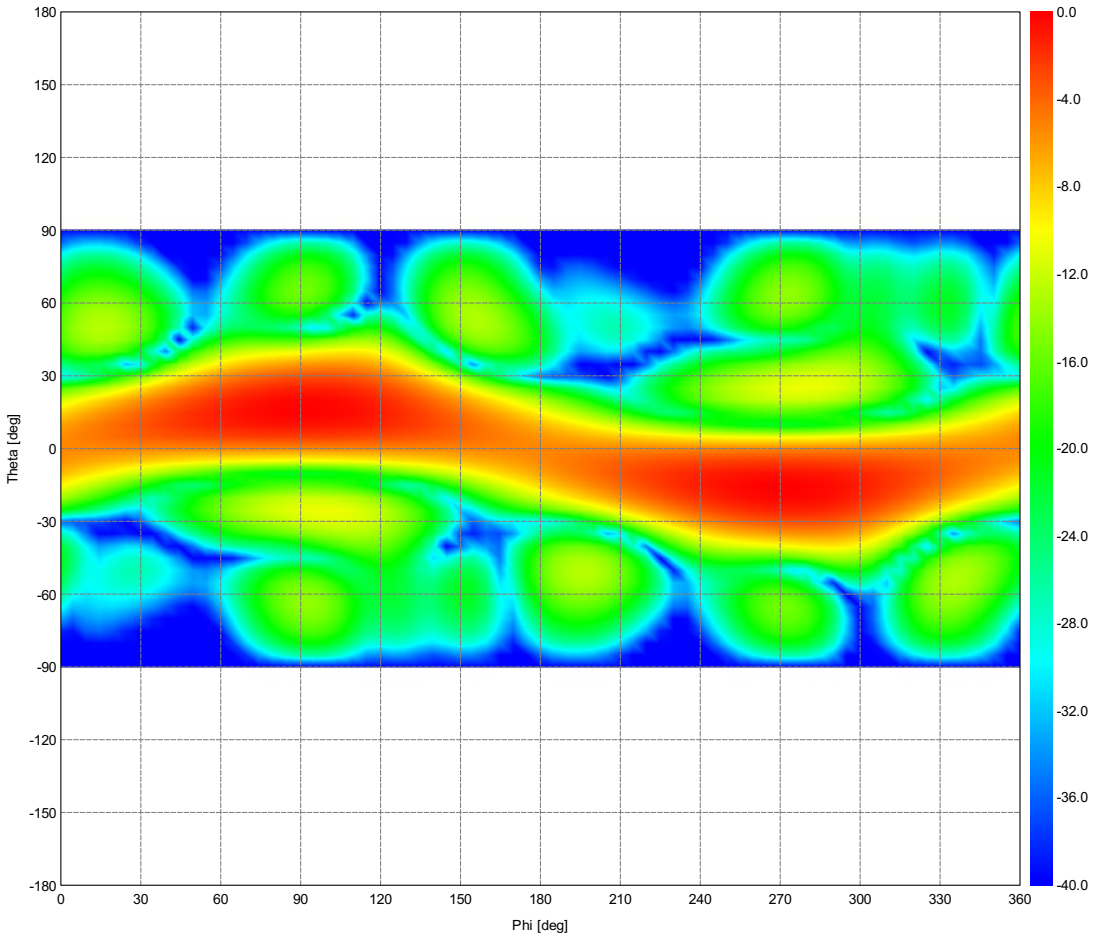

Figure 18: Total Gain (Frequency = 33.5508 MHz) - Dipolo_real

theta=15,phy=315: Total Gain [dBi]

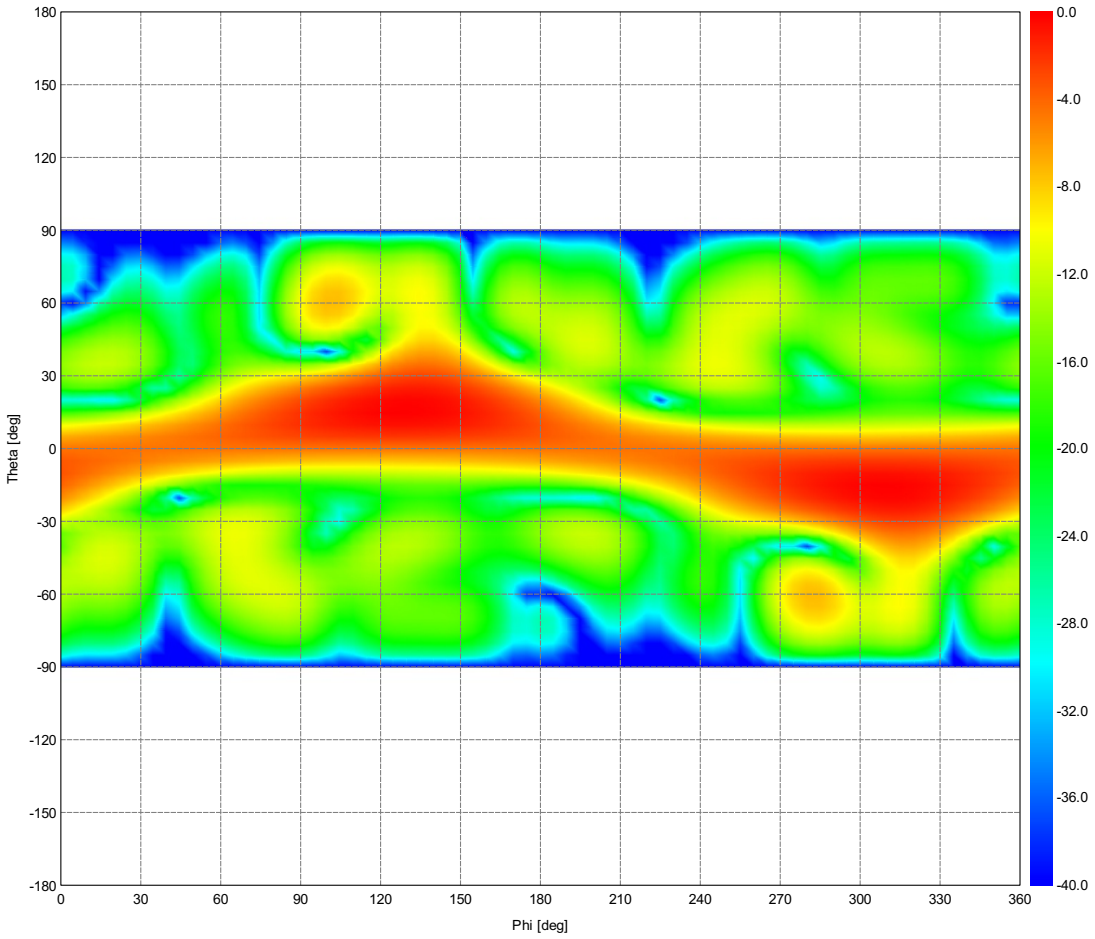

Figure 19: Total Gain (Frequency = 33.5508 MHz) - Dipolo_real

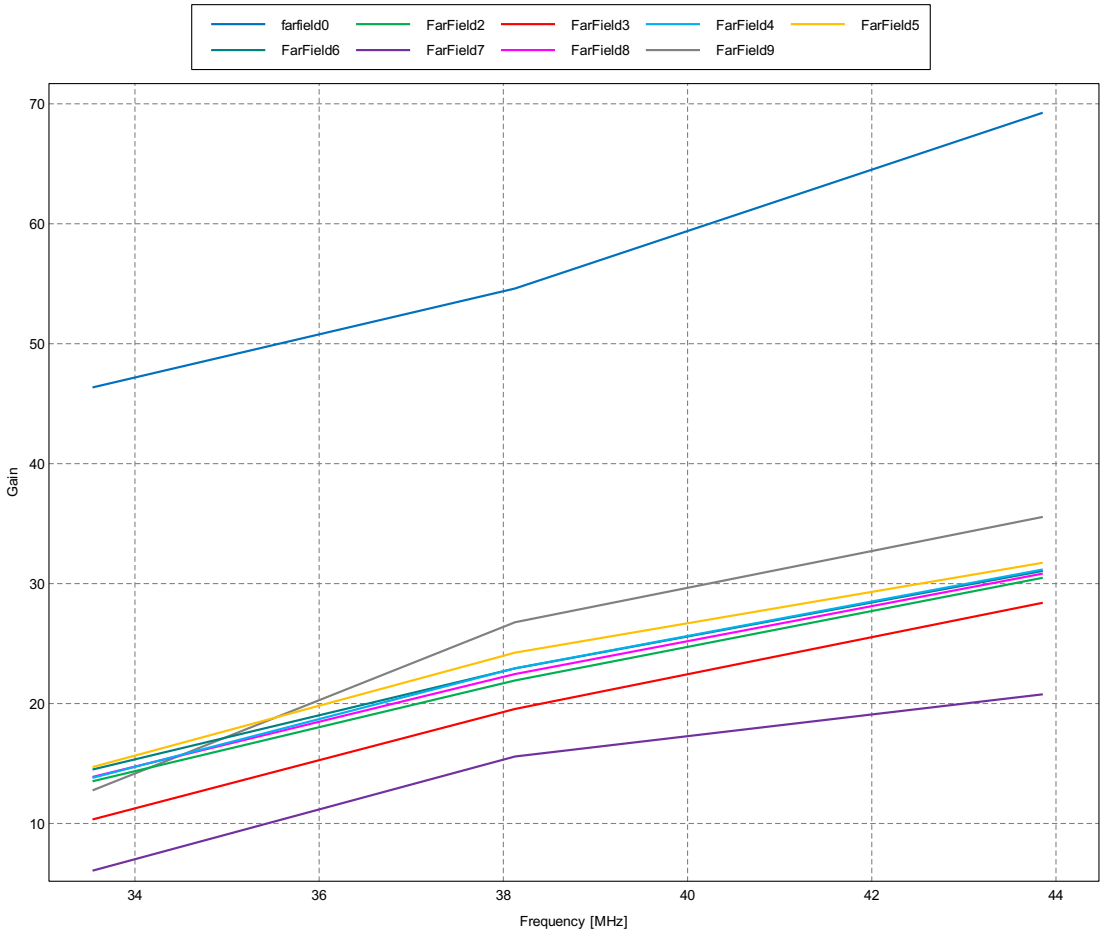

Figure 20: Total Gain (Theta = 0 deg; Phi = 0 deg) - Dipolo_real

Power

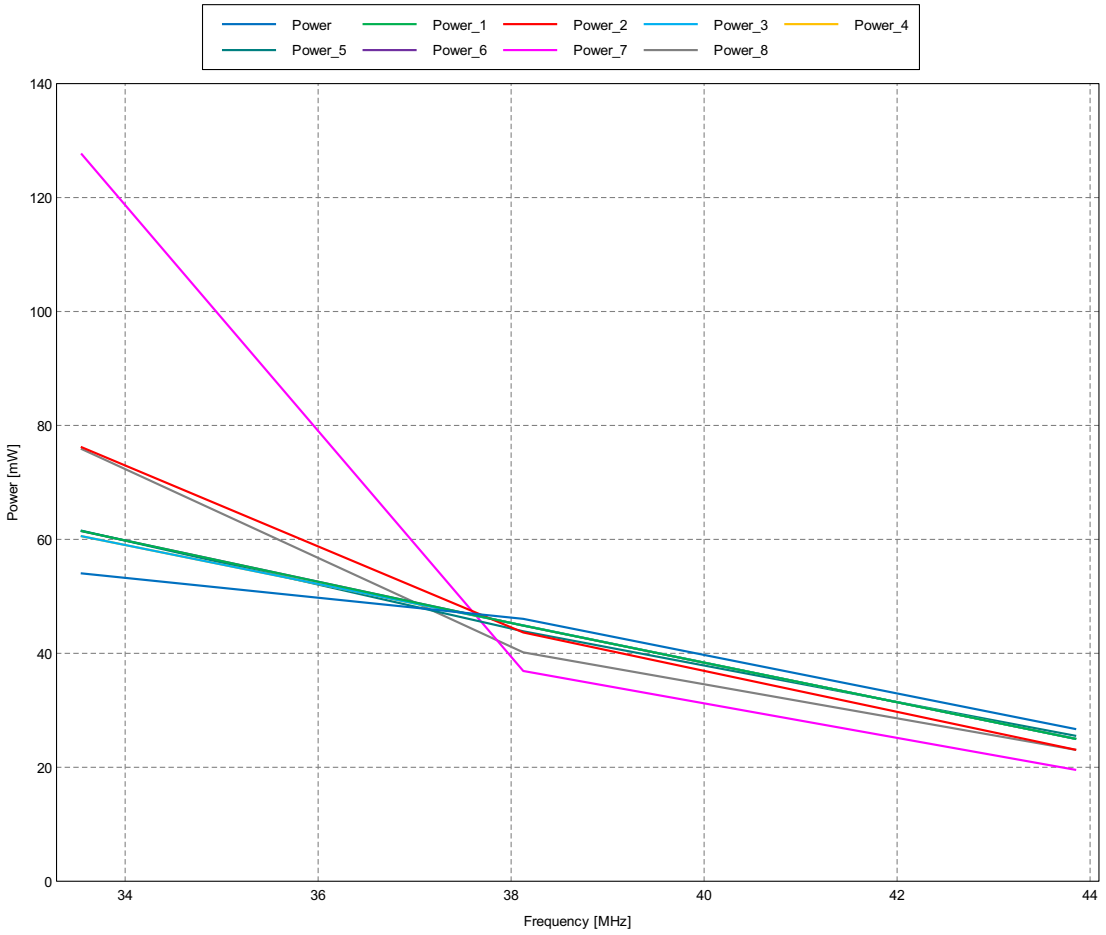

Figure 21: Active Power - Dipolo_real

theta=0,phy=0

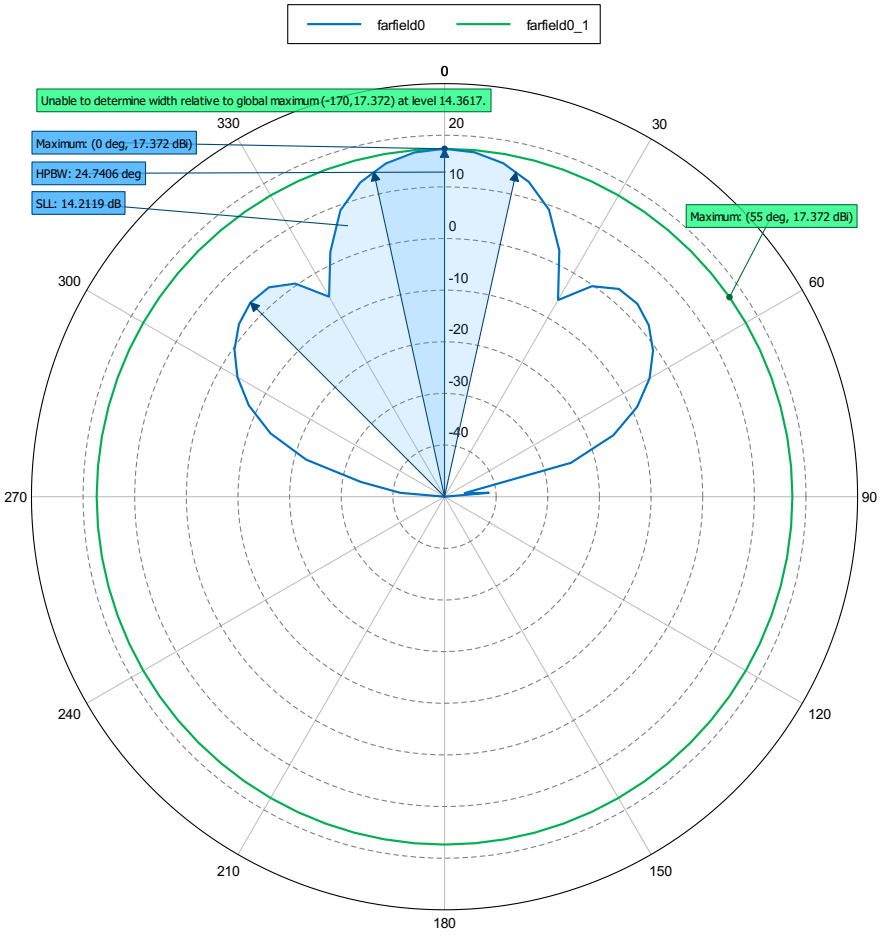

Figure 22: Total Gain (Frequency = 38.126 MHz; Theta = 0 deg; Phi = 90 deg) - Dipolo_real

theta=15,phy=0

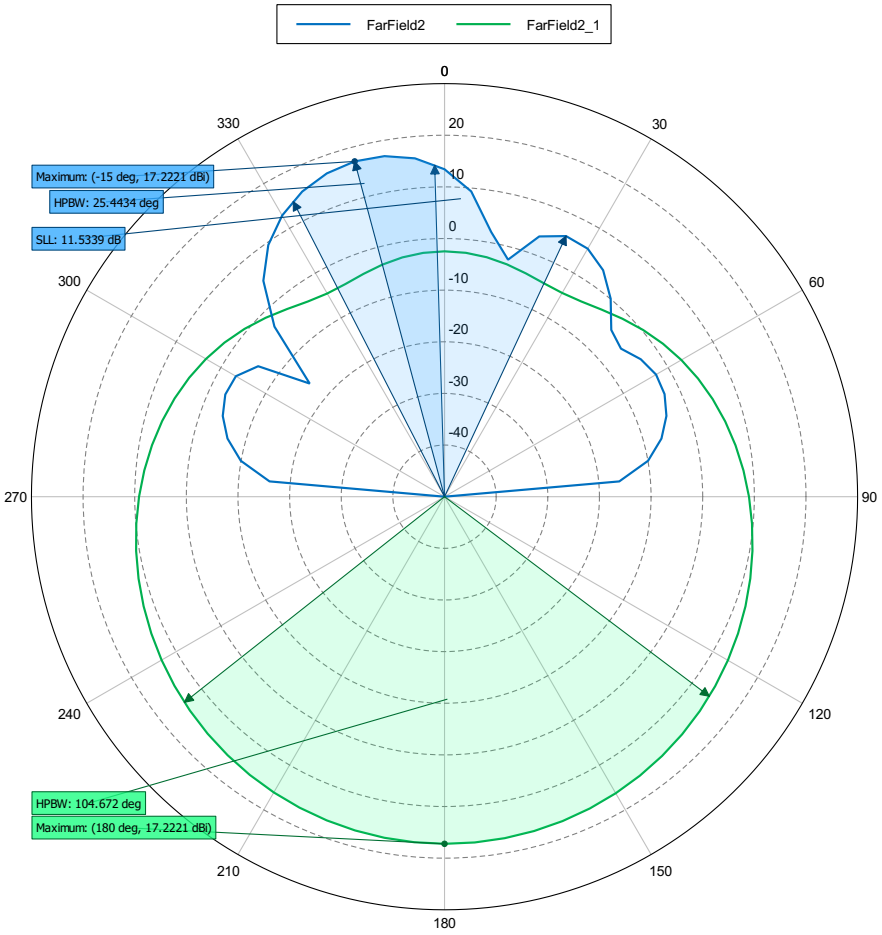

Figure 23: Total Gain (Frequency = 38.126 MHz; Theta = 15 deg; Phi = 0 deg) - Dipolo_real

theta=15,phy=45

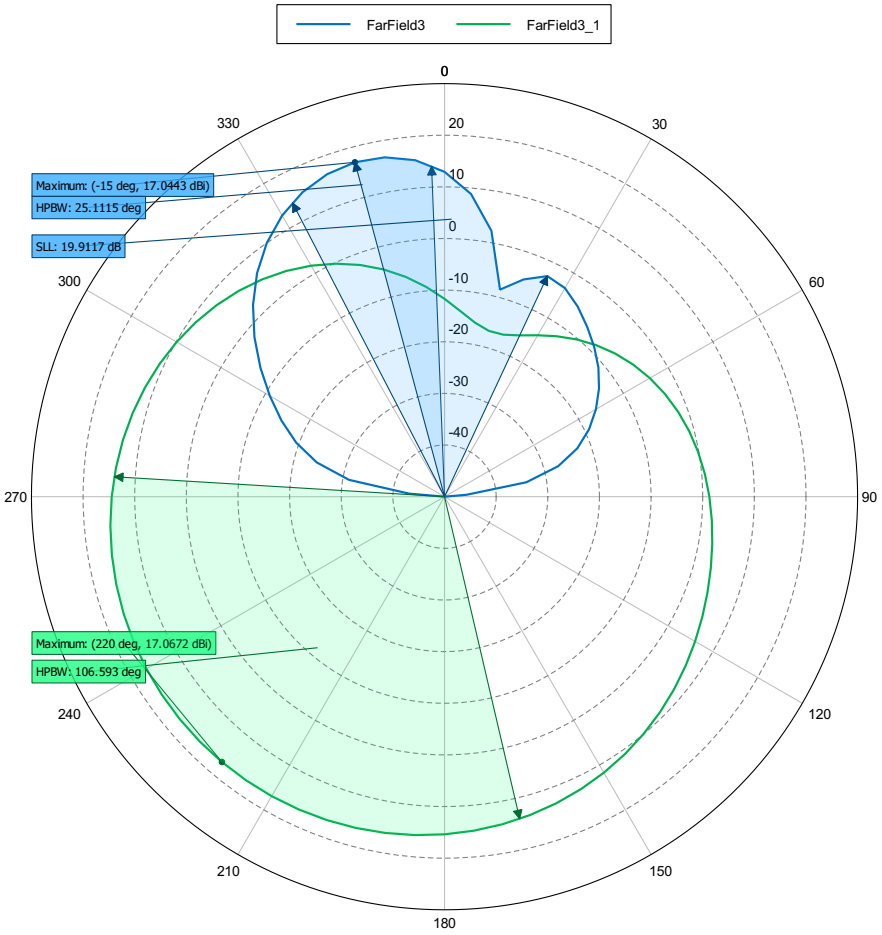

Figure 24: Total Gain (Frequency = 38.126 MHz; Theta = 15 deg; Phi = 45 deg) - Dipolo_real

theta=15,phy=90

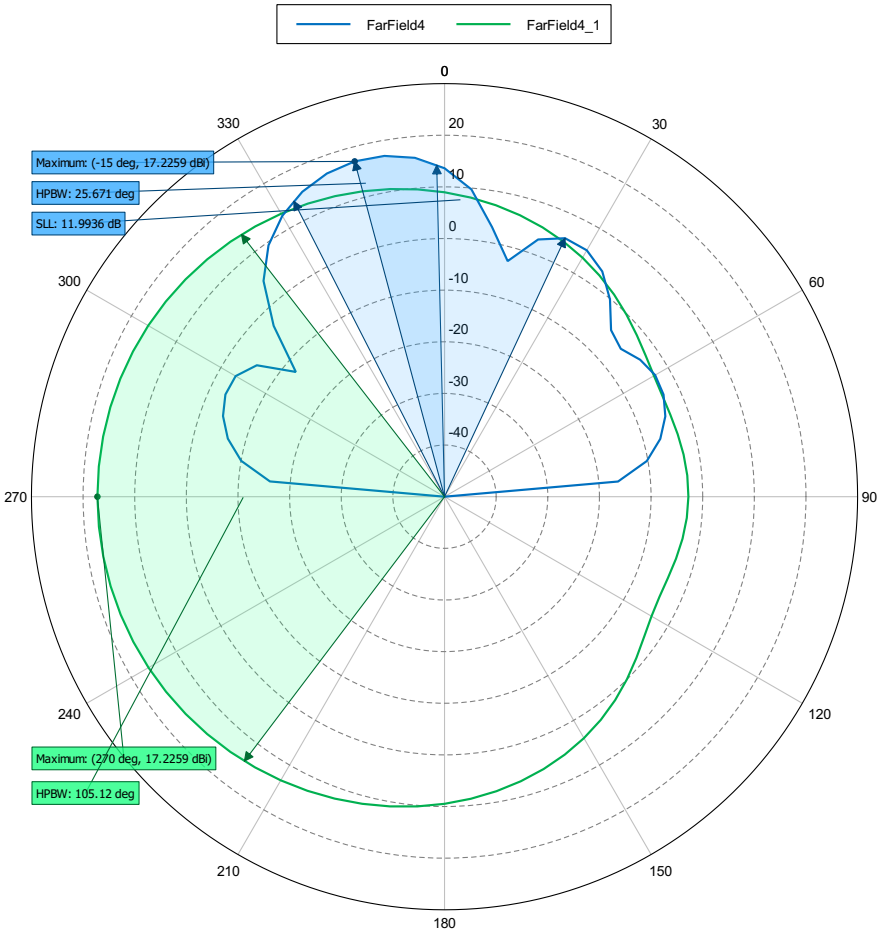

Figure 25: Total Gain (Frequency = 38.126 MHz; Theta = 15 deg; Phi = 90 deg) - Dipolo_real

theta=15,phy=135

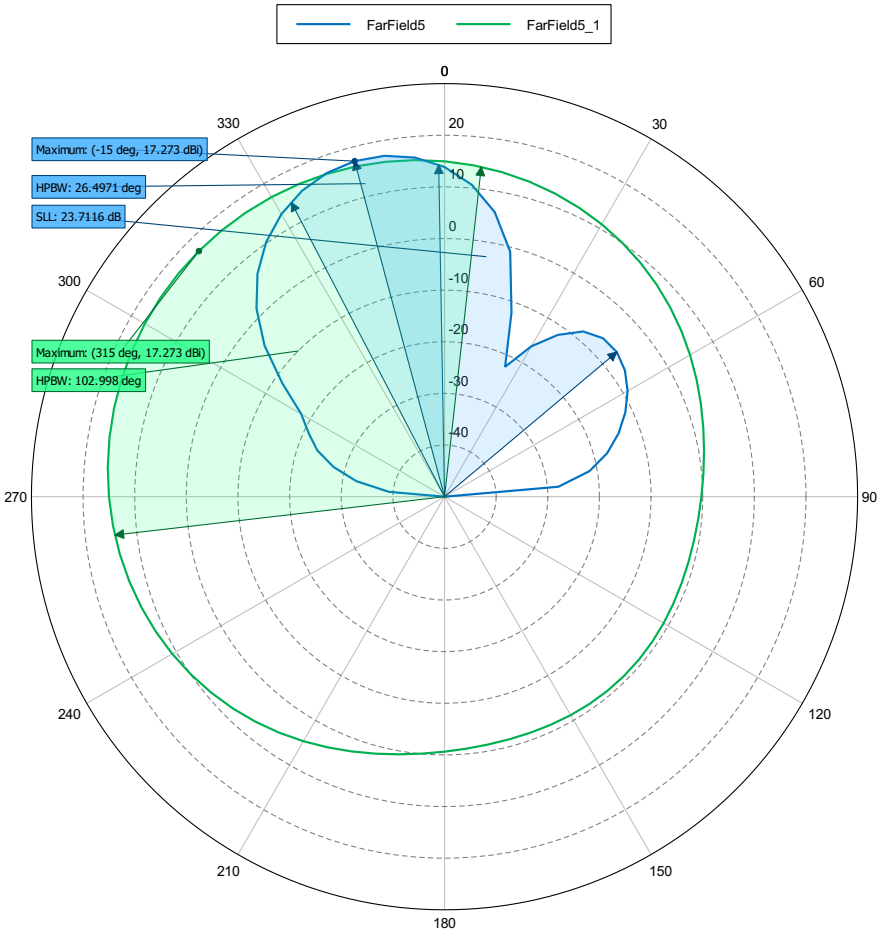

Figure 26: Total Gain (Frequency = 38.126 MHz; Theta = 15 deg; Phi = 135 deg) - Dipolo_real

theta=15,phy=180

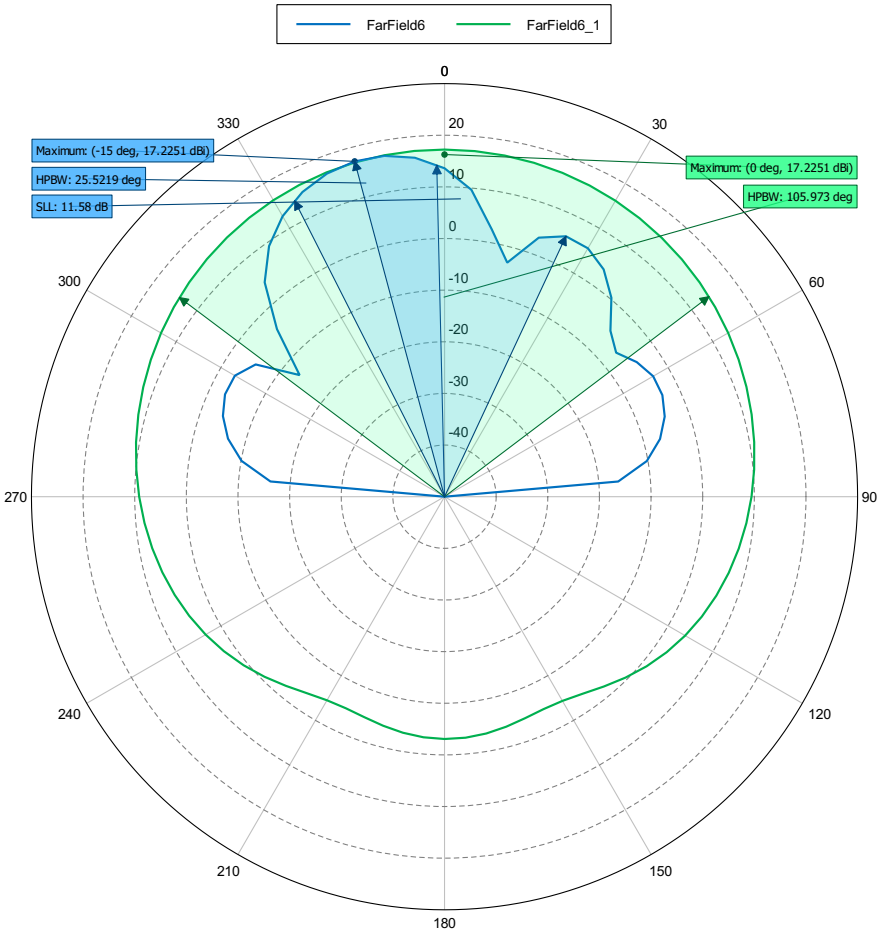

Figure 27: Total Gain (Frequency = 38.126 MHz; Theta = 15 deg; Phi = 180 deg) - Dipolo_real

theta=15,phy=225

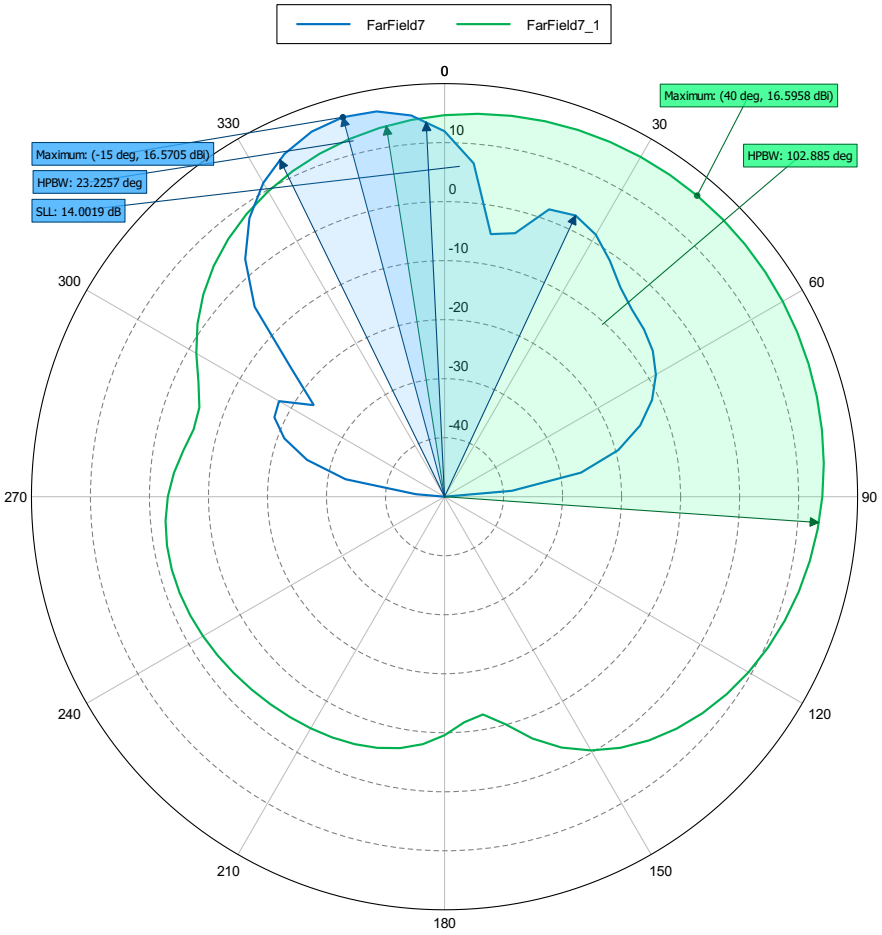

Figure 28: Total Gain (Frequency = 38.126 MHz; Theta = 15 deg; Phi = 225 deg) - Dipolo_real

theta=15,phy=270

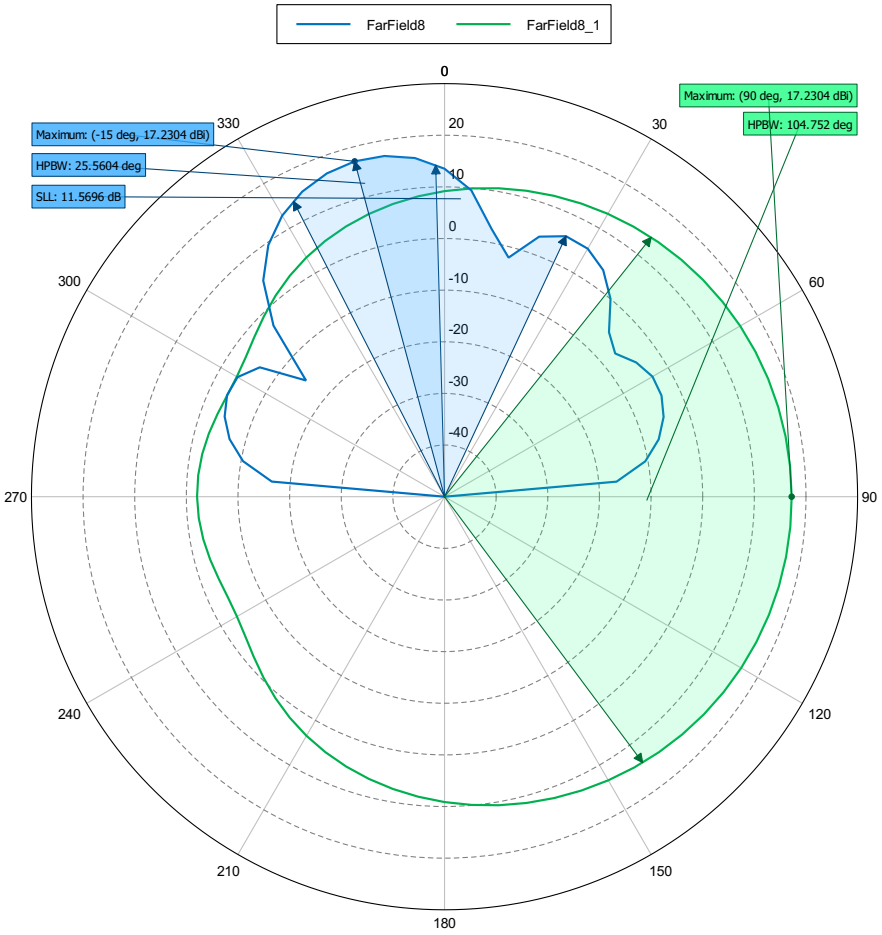

Figure 29: Total Gain (Frequency = 38.126 MHz; Theta = 15 deg; Phi = 270 deg) - Dipolo_real

theta=15,phy=315

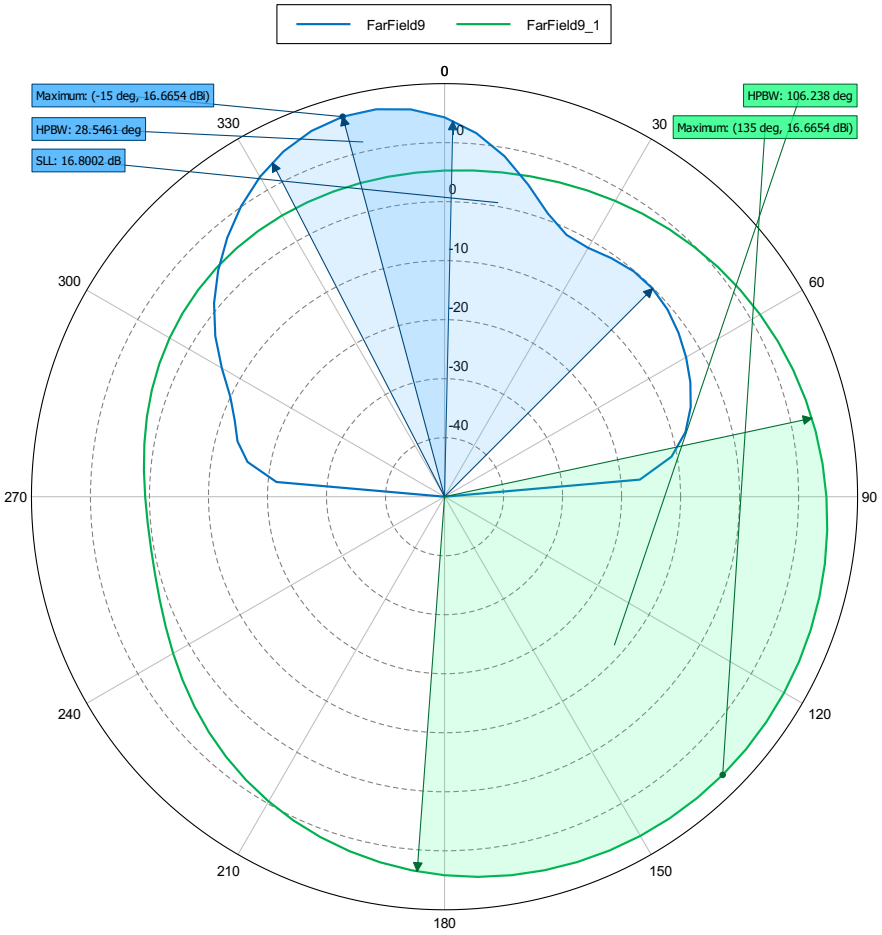

Figure 30: Total Gain (Frequency = 38.126 MHz; Theta = 15 deg; Phi = 315 deg) - Dipolo_real

Chapter 6

Quotes

www.pc-express.cl
Tecnología y Servicios a su alcance.

COTIZACION Nº 90.539

Fecha Emisión: **23 de Marzo de 2018**

Señor(es): **RODRIGO REEVES**

R.U.T.: **13.321.296-5**

Email: **Gonza2486@gmail.com**
Cond. de Pago: **Efectivo Contado**
Cond. de Entrega: **Entrega Inmediata**

Vendedor: **Blas Eduardo Gonzalez M.**
Email: **blas@pc-express.cl**

CODIGO	CANTIDAD	DESCRIPCION DEL PRODUCTO	GARANTIA	UNITARIO	TOTAL
7186	1	PROCESADOR AMD RYZEN 7 1700X 3.4 GHZ 8 CORE 20MB WOF NO FAN sAM4 P/N YD170XBCAEWOF	1 año	283.950	283.950
7386	1	PLACA MADRE B350 TOMAHAWK sAM4	6 meses	67.143	67.143
6957	2	MEMORIA DDR4 CRUCIAL BALLISTIX SPORT LT 8GB 2400 RED P/N BLS8G4D240FSE	1 año	58.739	117.479
7696	1	DISCO INTEL DE ESTADO SOLIDO SSD 2.5" 256GB MODELO 545S P/N SSDSC2KW256G8X1958660	1 año	55.378	55.378
4535	1	DISCO DURO SATA 3.5" 1TB WESTERN DIGITAL 64MB BLUE P/N WD10EZEX	1 año	26.555	26.555
7491	1	GABINETE COUGAR ARCHON P/N 385MM50.0001	3 meses	21.765	21.765
2786	1	FUENTE DE PODER EVGA 600W CERTIFICADA 80 PLUS P/N 100-W1-0600-K1	6 meses	32.689	32.689
7541	1	TARJETA DE VIDEO GEFORCE MSI GT 1030 2GB AERO P/N GEFORCE GT 1030 AERO ITX 2G OC	3 meses	56.218	56.218
6476	1	KIT TECLADO Y MOUSE GENIUS USB KM-130	6 meses	7.479	7.479
7230	1	VENTILADOR ENERMAX ETS-N31-02 FULL SOCKET - AM4 READY	3 meses	25.126	25.126
7629	1	MONITOR SAMSUNG 24" CURVO P/N LC24F390FHLXZS	1 año	97.395	97.395

OBSERVACIONES

Condiciones Generales
Consulte por descuentos de acuerdo a su forma de pago.
Cotización valida por 72 horas o hasta agotar stock.

Depósitos en nuestra cuenta corriente a nombre de:
PC EXPRESS COMPUTACION LTDA.
RUT 76.828.940-9
BANCO SANTANDER - CUENTA CORRIENTE 6838944
Mandar correo a contabilidad@pc-express.cl

DESCUENTO	
NETO	791.177
I.V.A. 19%	150.324
TOTAL	941.501

DIGICOM ELECTRONICS
EMS Solutions
ISO-9001:2008 ISO 13485:2003

7799 Pardee Lane
Oakland, Ca. 94621
Phone: 510-639-7003
Fax : 510-639-7090

April 13, 2018
QUOTE # 10172

TO : Rodrigo Reeves
CePIA, Astronomy Department
Universidad de Concepción, Chile
Phone: +56 41 220 3476
Cell: +56 9 6218 2062
Skype: rreevesd

We are pleased to submit the following quote regarding your inquiry.

Quantity 1, ADC16X250_Coax, unit cost $2,000.0
Includes modified front panel faceplate.

EXPECTED DELIVERY: 4 WEEKS ARO ESTIMATE
Shipping: FOB Origin, Oakland, CA.
If there are any question, please let us know.
Thank you for your inquiry,
Regards,
M.OHADY
MFG. MGR.
Email: mo@digicom.org

Cotizacion Sistema Analogico

Componentes	Características	Link DIgikey	Precio unitario digike	Precios por 10u	Precios 100u	Cantidades totale	Unidades	Decenas	centenas	Total unidades	Total decenas	Total decenas
orden5_39_bw_10_9												
inductores												
390 nH	1%	https://www.digikey.com/produc	0.44	3.82	27.31	50	0	0	1	0	0	27.31
51 nH	2%	https://www.digikey.com/produc	0.31	2.76	18.98	50	0	0	1	0	0	18.98
910nH	1%	https://www.digikey.com/produc	0.44	3.82	27.31	25	0	5	0	0	19.1	0
Condensadores							0		0	0	0	0
43 pF	1%	https://www.digikey.com/produc	0.77	5.68	38.94	50	0		1	0	0	38.94
330 pF(ojalá este	1%	https://www.digikey.com/produc	0.2	1.38	6.99	50	0		1	0	0	6.99
18 pF	1%	https://www.digikey.com/produc	1.53	12.09	90.66	25	0	5	0	0	60.45	0
							0	0	0	0	0	0
							0	0	0	0	0	0
Amplificador emp	TB-411-8A+						0	0	0	0	$0.00	0
Amplificador		https://www.minicircuits.com/W	1.25	12.5	115	65	0	0	1	0	0	115
CHK	Componente critico	https://www.minicircuits.com/W	3.65	34.5	32.5	65	0	0	1	0	0	32.5
C1 nad C2	libre de resonancia para altas frequencias	https://www.digikey.com/produc	3.53	28.53	248.96	130	0	4	1	0	114.12	248.96
C3	desacople	https://www.digikey.com/produc	0.36	2.47	14.84	65	0	0	1	0	0	14.84
R2		https://www.digikey.com/produc	0.45	3.45	14.5	65	0	0	1	0	0	14.5
R1 (237)	no existe el compoenente exacto como lo solucione ?	https://www.digikey.com/produc	0.4	3.38	13.2	65	0	0	1	0	0	13.2
							0	0	0	0	0	0
Conector sma		https://www.digikey.com/produc	1.69	16.9	169	80	0	8	0	0	135.2	0
Fit trough macho		https://www.digikey.com/produc	0.24	2.22	15.41	70	0	0	1	0	0	15.41
Fit trough hembra	(no deberían ser necesarios	https://www.digikey.com/produ	0.27	0.255	0.218					0	0	0

Componentes	Características	Link DIgikey	Precio por RF
orden5_39_bw_10_9			
inductores			
390 nH	1%	https://www.digikey.com/product-detail/en/murata-ele	0.88
51 nH	2%	https://www.digikey.com/product-detail/en/murata-ele	0.62
910nH	1%	https://www.digikey.com/product-detail/en/murata-ele	0.44
Condensadores			0
43 pF	1%	https://www.digikey.com/product-detail/en/kemet/CBI	1.54
330 pF(ojalá este	1%	https://www.digikey.com/product-detail/en/murata-ele	0.4
18 pF	1%	https://www.digikey.com/product-detail/en/american-	1.53
			0
			0
Amplificador emp	TB-411-8A+		0
Amplificador		https://www.minicircuits.com/WebStore/dashboard.ht	3.75
CHK	Componente critico	https://www.minicircuits.com/WebStore/dashboard.ht	10.95
C1 nad C2	libre de resonancia para altas frequencias	https://www.digikey.com/product-detail/en/knowles-d	21.18
C3	desacople	https://www.digikey.com/product-detail/en/taiyo-yude	1.08
R2		https://www.digikey.com/product-detail/en/stackpole-	1.35
R1 (237)	no existe el compoenente exacto como lo solucione ?	https://www.digikey.com/product-detail/en/panasonic	1.2
			0
Conector sma		https://www.digikey.com/product-detail/es/rf-solutions	3.38
Fit trough macho		https://www.digikey.com/product-detail/es/mill-max-m	0.48
Fit trough hembra	(no deberían ser necesarios	https://www.digikey.com/product-detail/es/mill-max-m	0
		Total usd	48.38
		Total clp	32915.333
Fr4	http://www.maxelectronica.cl/pcb/170-placa-pcb-fr-4-fibra	6500	Precio relativo por RI 1625
e=4.7	Compra en Chile	65000	RF(todo unitario) 34540.333

Totales	0	328.87	546.63
Encargo USD	875.5	Encargo CLP	595646.425

Precio Total (Encargo más RF4)
660646.425

Precio dolar(11-7-19)
680.35

total 20 RF (considerando 4 completos de prueba, no es precio total del encargo)
690806.66

Cotizacion Sistema Analogico

Componentes	Precio unitario digikey	Precios por 10u	Precios 100u	Cantidades totales Consider	Unidades	Decenas	centenas	Total unida	Total decenas	Total decenas
orden5_39_bw_10_9										
inductores										
390 nH	0.44	3.82	27.31	50	0	0	1	0	0	27.31
51 nH	0.31	2.76	18.98	50	0	0	1	0	0	18.98
910nH	0.44	3.82	27.31	25	0	0	1	0	0	27.31
Condensadores					0	0	0	0	0	0
43 pF	0.77	5.68	38.94	50	0	0	1	0	0	38.94
330 pF(ojalá este	0.2	1.38	6.99	50	0	0	1	0	0	6.99
18 pF	1.76	13.89	104.17	25	0	0	1	0	0	104.17
					0	0	0	0	0	0
					0	0	0	0	0	0
Amplificador empaquetado					0	0	0	0	$0.00	0
Amplificador	1.25	12.5	115	65	0	0	1	0	0	115
CHK	3.65	34.5	325	65	0	0	1	0	0	325
C1 nad C2	3.76	30.3	236.34	130	0	4	1	0	121.2	236.34
C3	0.38	2.97	17.8	65	0	0	1	0	0	17.8
R2	0.54	4.17	17.55	65	0	0	1	0	0	17.55
R1 (237)	0.3	3.65	14.27	65	0	0	1	0	0	14.27
					0	0	0	0	0	0
Conector sma	1.74	17.4	174	80	0	0	1	0	0	174
Fit trough macho	0.24	2.22	15.41	70	0	0	1	0	0	15.41
Fit trough hembr	0.27	0.255	0.218					0	0	0
		Precio por RF					Totales	0	121.2	1139.07
							Encargo US	1260.27	Encargo CLP	857424.6945